Improvement of cloud radar products for fog surveillance networks : fog life cycle analyses and calibration methodologies

Felipe Toledo Bittner

INSTITUT POLYTECHNIQUE DE PARIS

NNT : 2021IPPAX029

Thèse de doctorat

Improvement of cloud radar products for fog surveillance networks: fog life cycle analyses and calibration methodologies

Thèse de doctorat de l'Institut Polytechnique de Paris
préparée à École Polytechnique

École doctorale n°626 École doctorale de l'Institut Polytechnique de Paris (EDIPP)
Spécialité de doctorat : Mécanique des fluides et des solides, acoustique

Thèse présentée et soutenue à Palaiseau, le 25.05.2021, par

FELIPE TOLEDO-BITTNER

Composition du Jury :

Riwal Plougonven Directeur adjoint de recherche, LMD (UMR-8539)	Président
Christine Lac Ingénieur ICPEF Météo-France, CNRM (UMR-3589)	Rapporteur
Herman Russchenberg Full professor TU-Delft, TU Delft Climate Institute	Rapporteur
Céline Cornet Professor Université Lille 1, LOA (UMR-8518)	Examinatrice
Pauline Martinet Chercheur Météo-France, CNRM (UMR-3589	Examinatrice
Martial Haeffelin Ingénieur de recherche CNRS, IPSL (FR-636)	Directeur de thèse
Jean-Charles Dupont Physicien adjoint UVSQ, IPSL (FR-636)	Co-encadrant (Invité)
Julien Delanoë Maître de conférences UVSQ, LATMOS (UMR-8190)	Co-encadrant (Invité)

Résumé

La réduction de la visibilité causée par le brouillard a un coût significatif pour les activités civiles et économiques, notamment pour celles liées aux transports de surface, maritimes et aériens. Par conséquent, l'amélioration des méthodes de surveillance et de prévision du brouillard est un sujet de recherche actif et important.

Récemment, il a été mis en évidence que la télédétection des variables de la couche de brouillard en utilisant des radars nuages peut fournir des informations importantes sur ses processus. Ce fait, associé au développement d'une nouvelle génération de radars nuages à faible coût, a ouvert la possibilité du développement de stations de surveillance du brouillard, sur des lieux d'intérêt comme les aéroports ou les autoroutes. Cependant, certains obstacles doivent être surmontés avant la mise en place d'un réseau de surveillance du brouillard à grande échelle. Dans cette thèse, nous identifions et abordons les questions suivantes :

1.- Actuellement, la compréhension des processus du brouillard permet une quantification des variations temporelles de ses variables macroscopiques, telles que le contenu d'eau liquide intégré (LWP) et la hauteur du sommet du brouillard. Bien qu'utiles, ces informations sont insuffisantes pour discerner la tendance de dissipation du brouillard. Il reste nécessaire d'identifier des variables diagnostiques avec des seuils définis, qui pourraient être utilisées comme indicateurs de la tendance de dissipation du brouillard. Ainsi, la thèse commence par présenter un nouveau modèle conceptuel décrivant le contenu en eau liquide et la structure verticale de brouillards adiabatiques. Ce modèle est développé à partir d'observations de 80 événements de brouillard, enregistrés pendant 7 ans à l'Observatoire Atmosphérique SIRTA. Le modèle est capable de prédire le LWP du brouillard avec une erreur quadratique moyenne de 10,5 g m-2, en utilisant des mesures de la hauteur du sommet de la couche de brouillard et de la visibilité, température et pression à la surface, et fournit également deux variables diagnostiques : le contenu en eau critique (CLWP) du brouillard et le réservoir de contenu en eau (RLWP) du brouillard. Le CLWP est la quantité minimale de contenu en eau liquide intégré nécessaire pour remplir une couche de brouillard d'une épaisseur connue, tandis que le RLWP est l'excès d'eau qui doit être retiré de la colonne de brouillard pour qu'il y ait dissipation à la surface. Les deux variables peuvent être estimées en temps réel à partir d'observations in-situ et de télédétection, parmi lesquelles nous soulignons l'utilisation des radars nuage et des radiomètres micro-ondes.

Ces variables contribuent à un nouveau paradigme pour la prévision de la dissipation du brouillard, basé sur l'observation de l'état et des processus dans l'ensemble de la colonne de brouillard, et pourraient compléter les schémas actuels basés sur les mesures de visibilité en surface. Plus précisément, il a été constaté que lorsque la visibilité en surface est inférieure à 600 m, la probabilité de dissipation dans une période de temps donnée change de manière significative en fonction de la valeur du RLWP du brouillard. Par exemple, la probabilité de dissipation à l'horizon de 90 minutes, lorsque la visibilité est inférieure à 250 m, est très faible (5%) lorsque le RLWP est supérieur à 20 g m-2, mais augmente fortement (50%) lorsque le RLWP devient négatif.

2 - L'étalonnage des radars de nuages est un sujet non résolu, qui doit être abordé pour exploiter

un réseau de surveillance du brouillard qui s'appuie sur des observations de télédétection. Pour faire progresser le modèle conceptuel de brouillard décrit ci-dessus, des meilleures restitutions de propriétés microphysiques sont nécessaires. Elles sont actuellement limitées par les difficultés liées à l'étalonnage des radars nuage. En plus, des mesures étalonnées sont essentielles pour effectuer des études comparatives en utilisant des données provenant de différents sites, ce qui est essentiel pour améliorer notre compréhension du brouillard et pour généraliser les résultats du modèle conceptuel. Par conséquent, cette thèse recherche une stratégie de calibration qui pourrait s'appliquer sur un réseau de surveillance du brouillard, en utilisant les résultats de deux campagnes d'étalonnage de radars nuage réalisées en 2018 et 2019 à l'observatoire atmosphérique SIRTA, dans le cadre du développement de l'infrastructure de recherche ACTRIS.

La stratégie comprend deux étapes : la première est l'étalonnage d'un radar de référence transportable, avec une procédure qui fournit une estimation fiable de l'incertitude d'étalonnage. La seconde étape consiste à transporter cet instrument étalonné vers d'autres sites d'observation, afin de transférer son étalonnage à d'autres radars.

La calibration du radar de référence (un radar de type BASTA mini, développé par le laboratoire LATMOS) est réalisée à l'aide d'une méthode reproductible développée au cours de la thèse, basée sur l'utilisation de réflecteurs en coin. Cette méthode permet d'identifier et d'estimer indépendamment l'impact de chaque source de biais et d'incertitude. Ceci a permis de calculer l'incertitude pour les expériences réalisées, qui était de 2 dB, et d'identifier la principale source d'incertitude, qui est l'utilisation d'un modèle théorique pour calculer la surface équivalente radar du réflecteur.

Comme la méthode permet l'estimation individuelle de l'incertitude introduite par chaque source, elle a été utilisée pour comparer quantitativement les performances de différents montages expérimentaux, et pour identifier les éléments qui devraient être améliorés. Notre étude a montré que des améliorations dans la caractérisation du réflecteur de référence pourraient permettre une diminution de l'incertitude d'étalonnage jusqu'à un minimum théorique de 0,4 dB.

La méthodologie développée pour le transfert d'étalonnage est basée sur la comparaison de mesures simultanées de nuages par des radars colocalisés. Après environ deux semaines d'échantillonnage continu, il a été possible de transférer l'étalonnage du radar de référence (radar BASTA mini) à un radar nuage de marque RPG 94 GHz non étalonné. Les différences de sensibilité des radars utilisés rendent impossible le transfert de l'étalonnage basé sur les données brutes. Une nouvelle méthodologie de traitement des données a été développée pour rendre comparable la distribution des mesures des deux radar et quantifier l'incertitude introduite dans le transfert de calibration, en plus de celle de la calibration du radar de référence. Dans nos expériences, cette incertitude supplémentaire était de 0,9 dB. Des stratégies pour réduire davantage cette incertitude, et pour appliquer cette méthode à des radars dans différentes bandes de fréquences, sont également discutées.

Abstract

Visibility reduction caused by fog has a significant cost on civil and economic activities, especially for those related with surface, marine and aerial transportation. Therefore, the improvement of fog monitoring and forecasting methods are a relevant research topic.

Recently, it has been discovered that remote sensing of the fog layer with cloud radars could provide valuable information about fog processes. This fact, paired with the development of new generation low-cost cloud radars, have opened the possibility to the creation of fog surveillance stations on places of interest such as airports or highways. However, some obstacles must be overcome before the foundation of a large-scale fog surveillance network.

In this thesis we identify and address the following issues:

1.- At present, the understanding of fog processes enables a quantification of temporal variations of its macroscopic variables, such as the liquid water path and the fog top height. Albeit useful, this information is insufficient to discern fog dissipation tendency. It remains necessary to identify diagnostic variables with defined thresholds, that could act as indicators of fog dissipation tendency. Hence, the thesis begins by presenting a new conceptual model describing the liquid water content and vertical structure of adiabatic fog. This model is developed based on observations of 80 fog events, registered during 7 years at the SIRTA Atmospheric Observatory. The model is able to predict fog LWP with a RMSE of 10.5 g m-2, based on measurements of cloud top height and surface visibility, temperature and pressure, and also provides two diagnostic variables: the Critical Liquid Water Path (CLWP), and the Reservoir Liquid Water Path (RLWP). The CLWP is the minimum amount of liquid water path necessary to fill a fog layer of a known thickness. Meanwhile, the RLWP is the excess of water that must be removed from the fog column to have dissipation at the surface. Both variables can be estimated in real time from in-situ and remote sensing observations, among which we highlight the use of cloud radars and microwave radiometers.

These variables contribute to a new paradigm for fog dissipation forecasting, based on the observation of the status and processes in the whole fog column, and could complement current schemes based on surface measurements of visibility. Specifically, it was found that, when visibility is below 600 m, the probability of dissipation in a given time period changes significantly depending on fog RLWP value. For example, the probability of dissipation in 90 minutes, when visibility is less than 250 m, ranges from 5% when the RLWP is more than 20 g m-2, to 50% when the RLWP is negative.

2.- Cloud radar calibration is an unsolved topic, which must be addressed to have a fog surveillance network based on remote sensing observations. Further improvements of the proposed fog conceptual model would require better micro-physical retrievals, currently limited by the difficulties involved in cloud radar calibration. Additionally, calibrated measurements are essential to perform comparative studies using data from different sites, which is essential to improve our understanding of fog and to generalize the conceptual model results. Therefore, this thesis researches a calibration strategy that could be applied for a complete fog surveillance network, based on the results of two cloud radar calibration campaigns performed in 2018 and 2019 at the SIRTA atmospheric observatory, as part of the development of the

ACTRIS research infrastructure.

The strategy comprises two steps: the first is the calibration of a portable reference radar with a procedure that provides a reliable estimation of uncertainty. The second step is to transport this calibrated instrument to other observation sites, to transfer its calibration to other radars.

The calibration of the reference radar (a BASTA mini, developed by the LATMOS laboratory) is done using a repeatable method developed during the thesis, based on the use of corner reflectors. The methodology enables the identification and independent estimation of the impact from each source of bias and uncertainty. This enabled the calculation of the uncertainty for the performed experiments, which was of 2 dB, and the identification of the main uncertainty source, which is the use of a theoretical model to calculate the reflector radar cross section.

Since the method enables the individual estimation of the uncertainty introduced by each source, it was used to quantitatively compare the performance of different experimental setups, and to identify the elements that should be further improved. In our case, we concluded that improvements in the characterization of the reference reflector could enable a decrease of calibration uncertainty down to a theoretical minimum of 0.4 dB.

The methodology developed for calibration transfer is based on the comparison of simultaneous measurements of clouds with the radars in the proximity of each other. After approximately two weeks of continuous samples, it was possible to transfer the calibration from the reference radar (BASTA mini) to an uncalibrated 94 GHz RPG cloud radar. Differences in the sensitivity of the radars involved makes the calibration transfer based on raw data impossible. Therefore, it was necessary to develop a new data processing methodology. This method enables the quantification of the uncertainty introduced in the calibration transfer, in addition to that in the reference radar calibration. In our experiments, this additional uncertainty was of 0.9 dB. Strategies to further reduce this uncertainty, and to apply this method for radars in different frequency bands, are also discussed.

Acknowledgements

I thank the company Météomodem and the Laboratoire de Météorologie Dynamique (LMD) for providing the funding and excelent conditions to make this work possible. I would also like to acknowledge the Association Nationale Recherche Technologie (ANRT), for making this CIFRE convention possible. Additionally, I thank the strong support and funding from the European Union's Horizon 2020 research and innovation programme, under grant agreement No 654109 (ACTRIS project), for the research of cloud radar calibration methodologies.

I also thank the Institut Polytechnique de Paris (IPP), the Institut Pierre-Simon Laplace (IPSL), the Laboratoire Atmosphères et Observations Spatiales (LATMOS), the SIRTA atmospheric observatory, and the COST Action PROBE project, supported by COST (European Cooperation in Science and Technology). All these institutions provided support that was instrumental in making this work possible.

I thank my thesis Jury, composed of Riwal Plougonven, Christine Lac, Herman Russchenberg, Céline Cornet and Pauline Martinet, for the time invested in the review, and for your comments on my thesis work.

I would like to especially thank my excelent team of advisors: Martial Haeffelin, Julien Delanoë and Jean-Charles Dupont. The three were always very and committed and available to share their knowledge and experience when needed, and this was essential when facing the inherent challenges that appear in research work. They were key influences in my training as a scientist, and I learned a lot from them, both scientifically and professionally. It was always a pleasure to exchange ideas and discuss with you all, and you were important in making my PhD an enjoyable and enriching experience. I would also like to thank Martial for establishing this research project, for believing in me, and for his invaluable help when facing administrative challenges.

Besides my advisors, other people were very important for my development as a scientist, and for making this work possible. I would like to especially thank Eivind Waersted for his effort in transfering what he learnt in his thesis, which was key to start my fog research from a good position. I also want to especially thank Susana Jorquera, for her very significant contribution in the development of methods to transfer the calibration between different cloud radars. Other key people that helped me in different ways, including interesting discussions and hard field work, are: Jean-François Ribaud, Johan Parra, Patricia Delville, Marc-Antoine Drouin, Sylvain Cros, Olivier Atlan, Christophe Boitel, Jiapeng Yin, Roberto Rondanelli, Cristóbal Garrido, Christophe Le Gac, Jean-Paul Vinson, Damien Vignelles and Patrick Charpentier. I also thank the ACTRIS CCRES team, and everyone who participated in the cloud radar calibration campaigns. I believe this project is in the hands of very capable people, with the vision and the skills required to make this project succesfull. I whish you all the best in your careers.

Finally, I would like to thank all my friends, my family, and especially my wife, for their infinite patience and support in this stage. This would not have been possible without you. Again, my most sincere thanks.

Contents

1 Introduction **9**

1.1 Foreword . . . 9
1.2 Fog definition . . . 11
1.3 Life cycle of radiation and stratus-lowering fog . . . 11
1.4 Fog remote sensing . . . 13
1.5 Cloud radars . . . 16
1.6 The radar equation . . . 17
1.7 Cloud radar calibration . . . 20
1.8 Thesis context and objectives . . . 22

2 Use of remote sensing measurements to study fog LWP and CTH, and to derive new diagnostics of fog dissipation tendency **25**

2.1 Introduction . . . 25
2.2 Study of fog LWP and CTH using remote sensing measurements and a new conceptual model . . . 26
2.3 Use of conceptual model variables as indicators of fog dissipation tendency . . . 59
2.3.1 Surface visibility and RLWP during fog . . . 59
2.3.2 Temporary fog dissipation . . . 61
2.3.3 Statistics of visibility and RLWP versus fog dissipation tendency . . . 63
2.4 Synthesis . . . 66

3 Cloud radar calibration using corner reflectors **71**

3.1 Introduction . . . 71
3.2 Published paper: Absolute calibration method for frequency-modulated continuous wave (FMCW) cloud radars based on corner reflectors . . . 72
3.3 Geometrical RCS simulator . . . 96
3.3.1 Maximum theoretical RCS of the corner reflector . . . 97
3.3.2 Calculation of the corner reflector RCS for a given incidence angle . . . 97
3.3.3 Calculation of the effective reflector RCS considering antenna pattern . . . 98
3.4 Misalignment impact in calibration using corner reflectors . . . 99
3.4.1 Estimation of the misalignment bias . . . 100
3.5 Synthesis . . . 102

4 Cloud radar calibration transfer **105**

4.1 Introduction . . . 105
4.2 Calibration transfer principle . . . 106
4.3 Methodology . . . 108

4.3.1 Experimental setup . . . 108
4.3.2 Data selection . . . 109
4.3.3 Data cleansing . . . 109
4.3.4 Calibration transfer . . . 113
4.4 Results of the 2019 calibration experiment . . . 115
4.5 Synthesis . . . 118

5 Conclusions and Perspectives **121**
5.1 The role of LWP and CTH in fog life cycle . . . 122
5.2 Cloud radar calibration . . . 124
5.3 Perspectives . . . 127

Bibliography **131**

Chapter 1

Introduction

1.1 Foreword

Fog research is motivated by its significant impact on civil and economic activities. The visibility reduction caused by fog can cause costly delays and increase the accident rate on surface, marine and aerial transportation activities, with a cost of millions of dollars every year (e.g. Croft et al. (1995); Gultepe et al. (2007)). Accidents associated with fog have also resulted in injury or death for the people involved, especially in land traffic accidents (Croft et al., 1997; Abdel-Aty et al., 2011)). These issues explain, for example, recent studies carried out to improve fog forecasting in airports such as Paris, Melbourne or Cape Town (Bergot et al., 2015; Boneh et al., 01 Oct. 2015; Veljović et al., 2015).

The extinction of visible radiation caused by fog also has an impact on solar energy production. Fog reduces the amount of solar radiation reaching the surface, decreasing total electricity production, and making this production more variable and uncertain (e.g. Yao et al. (2018); Nilo et al. (2020)). This increases the challenges for grid operators, in charge of balancing energy production with the demand, hampering the grid cost optimization (Ela et al., 2013).

These sectors would benefit from better forcastings of fog evolution in time and space (e.g. Tardif and Rasmussen (2007)). However, its complexity arising from the wide range of physical and chemical processes involved, and the subtleties in the inner balance of these processes, makes fog forecasting particularly difficult (Steeneveld et al., 2015; Román-Cascón et al., 2016a). Hence, a better understanding of fog processes is essential to improve fog forecasting (Haeffelin et al., 2013).

Recent studies show that collocated remote and in-situ real time measurements can be used to improve the quantification of fog processes driving the evolution of fog layers locally (e.g. Dupont et al. (2012); Wærsted et al. (2019)). Cloud radars enable retrievals of macro and microphysical fog properties such as fog top height, and high resolution profiles of fog reflectivity and doppler velocity (Delanoë et al., 2016; Bell et al., 2021). Lidars are used to track the hydration of aerosols and the inferior limit of low stratus clouds (Kotthaus et al., 2016; Haeffelin et al., 2016b). Microwave radiometers, when combined with cloud radars to detect clouds above the fog layer, can be used for fog liquid water path retrievals (Wærsted et al., 2017).

The aforementioned issues and new findings indicate that it could be interesting to establish more observation sites at places heavily affected by fog. In previous years, an important factor restricting the amount of fog remote sensing stations was the high cost of the instruments involved. However, recent technological developments in the last decade have allowed a sharp decrease in their cost, specially for microwave radiometers and cloud radars (Rose et al., 2005; Delanoë et al., 2016; Aguirre et al., 2020). These developments are already driving the creation of cloud remote sensing networks worldwide. In

Europe, this has led to the foundation of the Cloudnet project (Illingworth et al. (2007)), and later of the European Aerosol, Clouds and Trace Gases Research Infrastructure ACTRIS (Pappalardo, 2018). The ACTRIS infrastructure already has 15 cloud remote sensing stations, equipped with most of the instruments necessary to track fog processes, and this number is expected to grow in the future. Although ACTRIS is in its implementation phase, some stations have already provided several years of high quality data for fog and cloud studies (Haeffelin et al., 2016a).

Therefore, the establishment of a network of fog monitoring stations located at critical places of interest is viable. Such network would already provide useful information on fog status and processes (e.g. Wærsted et al. (2017)), however, we have identified two challenges that must be addressed to significantly increase their benefit.

At present, there is significant progress on the research of the physical processes that impact fog evolution (e.g. Gultepe et al. (2007); Haeffelin et al. (2010); Wærsted et al. (2017)). However, there is still a lack of diagnostic variables, besides surface visibility, that could be compared against definite thresholds to quantify fog dissipation tendency. Zhou and Ferrier (2008) has advanced in this topic, by identifying threshold values for turbulence that indicate when fog formation can occur, and when fog dissipation is imminent. These results are very valuable, yet they are restricted to thin radiation fog, and cannot be used for developed adiabatic fog. Thus, the first challenge addressed by this thesis is to research for diagnostic variables that could be used to quantitatively assess fog status and dissipation tendency. This study is done using 7 years of fog observations at the SIRTA atmospheric observatory, located in Palaiseau, France (Haeffelin et al., 2005).

Another identified need is to have reliable calibration methods for the monitoring station instruments. Since lidars and microwave radiometers already have operation and calibration guidelines (e.g. Kotthaus et al. (2016); Kazama et al. (1999); Marke et al. (2016)), we decide to focus on cloud radars. Cloud radar calibration is essential to perform microphysical retrievals with these instruments (Ewald et al., 2019). For example, calibration deviations of 1 decibel, which has already been observed for different observation sites in Europe (Protat et al. (2009)), can introduce uncertainties in liquid water and ice content estimation of about 15-20% (Fox and Illingworth, 1997; Ewald et al., 2019). Besides, radar calibration has been a long-standing challenge. The lack of universal calibration methods introduces the need for continuous research for solutions, tailored for each use case (Süsskind, 1985; Atlas, 2002). Therefore, the second challenge is to develop a calibration solution for cloud radars, that could be applied in a fog monitoring network comprising several observation sites. The research on calibration methods was conducted during two cloud radar calibration campaigns, carried out in 2018 and 2019 at the SIRTA observatory, in the framework of the ACTRIS infrastructure developments.

The introduction chapter is structured as follows: Section 1.2 presents the definition of fog. Section 1.3 presents the life cycle of radiation and stratus lowering fog, which are the most common fog types observed at the SIRTA observatory (Dupont et al., 2016). Section 1.4 presents how remote sensing measurements with cloud radars, microwave radiometers and ceilometers could assist in the study of fog layers. Section 1.5, explains the operating principle and features of cloud radars. Section 1.6) introduces the equations used for radar calibration and reflectivity retrievals. Section 1.7) presents a state of the art summary of cloud radar calibration. Finally, the thesis context and objectives are elaborated in section 1.8.

1.2 Fog definition

According to the glossary of the American Meteorological Society, fog is defined as the presence of suspended water droplets in the atmosphere close to the surface, reducing visibility below 1 km (American Meteorological Society, 2012). Fog is a special case of cloud, in which the base reaches the surface. As with clouds, fog visibility reduction is mostly driven by the mie scattering interaction between visible light and the suspended water droplets (Wallace and Hobbs, 2006). Mie scattering deviates light in different directions as a beam passes, resulting in a net light extinction for this particular beam, even if the total light energy of the system remains constant.

Visibility is a measure of the distance at which an object or light can be discerned from the background. This definition is quantified by using the concept of contrast. Equation (1.1) describes how visual contrast C_v is a function of the extinction coefficient α_{ext} and the length of the beam path d (Duntley, 1948). The maximum value of contrast in this formulation is $C_v = 1$, which is reached by an ideally black object against a white background. As Eq. (1.1) shows, contrast can decrease down to 0, depending on distance and the extinction coefficient.

$$C_v = \exp^{-\alpha_{ext} \cdot d} \tag{1.1}$$

The Comission on Illumation proposed $C_v = 0.05$ as the inferior limit of constrast that allows the distinction of an object (Hautiere et al., 2006). By imposing this lower limit on contrast in Eq. (1.1), we get the Koschmieder formula (Eq. 1.2). In this formula, VIS represents the visibility, and corresponds to the maximum distance at which an object can be distinguished.

$$VIS = -\frac{\ln 0.05}{\alpha_{ext}} = \frac{3.0}{\alpha_{ext}} \tag{1.2}$$

The Koschmieder formula assumes makes several assumptions: first, the atmosphere is illuminated homogeneously. Second, the extinction coefficient and the scattering function do not vary spatially. Third, the object is ideally black and is viewed against the horizon. Fourth, the eye of the observer has a constant contrast threshold. To test the sensitivity of this formulation to variations in the hypotheses, Horvath (1971) calculated the errors that would arise from non ideal conditions. He concluded that the Koschmieder Formula can be used to calculate the extinction coefficient from observed visibilities with an error of less than about 10 per cent under non ideal conditions, by performing a proper selection of the visibility markers. This result indicates that this visibility formulation is robust enough to be applied for the fog case. Therefore, when fog is present, the visibility decrease below 1 km can be measured by using the extinction coefficient, which should be greater than 3.0 km^{-1} for the visible wavelengths.

We observe that this definition of fog is based exclusively on surface observations. This is useful from an operational point of view, but it does not consider the vertical complexity of fog layers. In the next section we explore the phenomenon of fog in more detail, understanding it as an atmospheric layer partly composed of suspended water droplets, which evolves and has a life cycle.

1.3 Life cycle of radiation and stratus-lowering fog

The droplets that make up fog appear because supersaturated air conditions cause aerosol activation near the surface. These droplets grow to the size of micrometers and are responsible for reduced visibility in foggy conditions. Air supersaturation can be caused by a temperature decrease, an increase of the water vapor content or a combination of both (Yau and Rogers, 1996).

Fog is categorized according to the mechanisms that cause its formation. There is a wide range of fog types, among which we count radiation fog, stratus lowering fog, upslope fog, precipitation fog, advention

fog, and others. This thesis focuses on radiation and stratus lowering fog, and therefore the next lines explain more in detail the characteristics of these two fog types, however a description of other fog types can be found in Gultepe et al. (2007); Tardif and Rasmussen (2007). We focus on these two fog types because they are the most frequent at the SIRTA atmospheric observatory (Dupont et al. (2016)), which is located in a continental, mid-latitude site near Paris, France (Haeffelin et al., 2005).

Radiation fog forms when air near the surface is cooled until reaching supersaturation. This fog type usually appears during clear-sky conditions, at night, when the temperature decrease is driven by radiative cooling of the surface (Haeffelin et al., 2010). Figure 1.1 (a) shows how these conditions form an stable layer with a deepening inversion, as radiative cooling continues (Smith et al., 2018). The stable profile suppresses turbulence, avoiding an excessive moist dilution in the layer which could inhibit supersaturation (Zhou and Ferrier, 2008; Haeffelin et al., 2013).

If conditions are propice for droplet growth, a thin fog layer forms and deepens within the surface inversion (Fig. 1.1 (b)). This stage of the fog life-cycle is referred to as shallow stable radiation fog (Smith et al., 2018). At this stage fog is not optically thick, and therefore liquid water condensation due to radiative cooling happens everywhere in the liquid layer, but is mostly driven by surface cooling (Wærsted et al., 2017). This keeps the temperature profile stable during this stage.

Eventually, if fog liquid water path reaches approximately 30 g m^{-2}, fog becomes optically thick to infrared radiation (Wærsted et al., 2017). This displaces the main location of radiative cooling to the fog top (Price, 2011). Cool air from the fog top sinks, eventually reaching the surface. This, when combined with the stop in surface cooling, erodes the stability of the boundary layer, evolving it to a saturated adiabatic temperature profile (Smith et al., 2018). When fog reaches the adiabatic profile, it becomes adiabatic fog (Fig. 1.1 (c)). In adiabatic fog, stability is close to neutral, enabling rapid vertical mixing that couples the surface with the fog top (Price, 2011; Porson et al., 2011).

Meanwhile, stratus-lowering fog forms when a low stratus base descends until reaching the surface. Mechanisms that have been found to produce this phenomenon are an increase in cloud liquid water

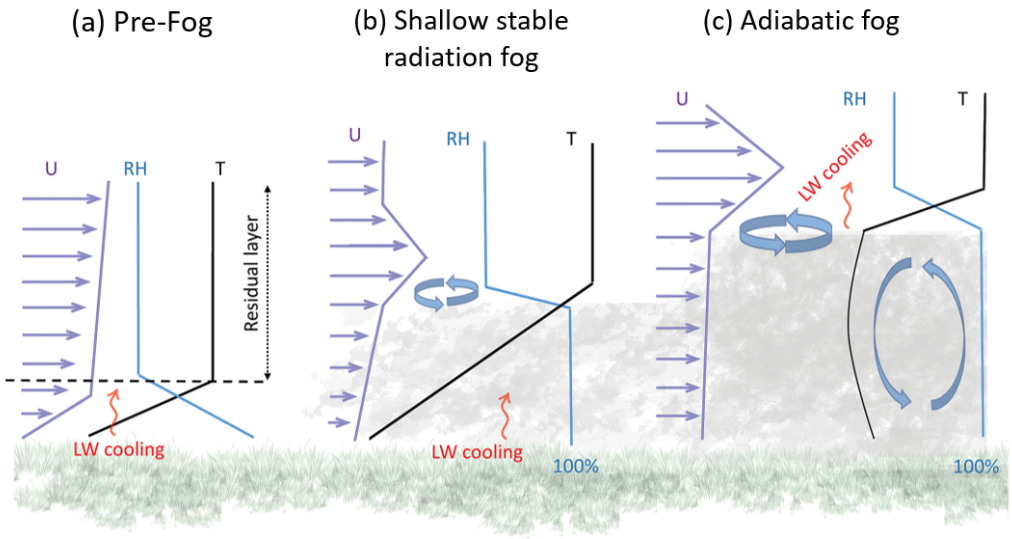

Figure 1.1: Figure showing the typical life cycle of radiation fog. A detailed description of the conditions indicated in each panel can be found in text. The vertical axis represents height with respect to the surface in green. The regions where radiative cooling is stronger are indicated with red arrows. The curved blue arrows represent turbulent mixing. U is the wind speed profile, T is the temperature profile and RH is the relative humidity profile. Illustration adapted from Smith et al. (2018).

due to cloud-top radiative cooling, cloud descent due to subsidence and moistening of the sub-cloud layer due to drizzle evaporation (Koračin et al., 2001; Dupont et al., 2012). Observations of stratus and stratocumulus adiabaticity , based on observations of their thickness and liquid water path, indicate that these cloud types are approximately well mixed (Slingo et al., 1982; Albrecht et al., 1990; Cermak and Bendix, 2011; Merk et al., 2016; Braun et al., 2018). Therefore, stratus-lowering should behave as adiabatic fog from its formation (as in Fig. 1.1 (c)). However, it is worth noting that this assertion cannot be verified with complete certainty, since at present there is a lack of similar studies relating thickness, liquid water path and adiabaticity for fog.

The dissipation of shallow radiation fog tends to happen shortly after sunrise. Meanwhile, deep adiabatic fog tends to last longer, and sometimes persists throughout the day (Price, 2011; Smith et al., 2018). Shallow radiation fog does not shelter the surface from sun radiation as efficiently as opaque adiabatic fog, leading to stronger layer heating from the surface. This, paired with their lower liquid water path with respect to adiabatic fog, explains why shallow radiation fog tends to dissipate earlier and often through evaporation (Tardif and Rasmussen, 2007; Haeffelin et al., 2010). Shallow fog is also more susceptible to dissipation due to increased turbulence (Zhou and Ferrier, 2008).

Contrastingly, most adiabatic fog events observed at the SIRTA observatory dissipate by lifting of the cloud base, without a complete evaporation of the cloud and sometimes even without a previous decrease in their liquid water path (Wærsted, 2018). This phenomena has also been widely observed in LES simulations of adiabatic fog (e.g. Nakanishi (2000); Bergot (2013); Mazoyer et al. (2017); Smith et al. (2018); Wærsted et al. (2019)). Wærsted et al. (2019) observed in LES simulations of real fog cases, that base lifting happened earlier when there was a weak stratification above the boundary layer, even when the liquid water path was increasing. They hypothesized that this may be caused by a faster entrainment at fog top that accelerates the boundary layer growth, lifting the cloud from the surface.

Wærsted (2018) goes beyond and, based on previous work by Cermak and Bendix (2011), proposed a conceptual model to estimate the minimum amount of liquid water path needed to fill a fog layer of a given thickness. He referred to this minimum value as the critical liquid water path. He then tested this model with data from real fog cases, and found that when the liquid water path decreased below the critical value, fog base lifted. Since this concept showed promising results for some case studies, we believe that it should be studied further. Specifically, these results suggest that the relationship between fog thickness and liquid water path may be key to explain fog dissipation.

1.4 Fog remote sensing

Fog evolution is driven by physical processes that occur at different locations of the layer. At the surface level, fog exchanges water with the surface through droplet deposition and impaction on vegetation and other obstacles (Katata, 2014). In addition, the surface exchanges latent and sensible heat with the fog. When the surface is moist, the water vapor evaporation at the surface contributes to increasing the condensation rate of the liquid layer, delaying fog dissipation (Wærsted et al., 2019). Additionally, when fog is not present, or when it is not opaque to long wave radiation, the long-wave cooling of the surface contributes to the liquid water condensation of the first stages in radiation fog, by reducing the temperature of the surrounding air (Haeffelin et al., 2010). When fog is opaque to long wave radiation, the surface can act as a sensible heat source, specially after sunrise (Price, 2011). This combined with radiative cooling of the fog top generates turbulence though buoyancy, distabilizing the temperature profile (e.g. Nakanishi (2000)).

Other important processes happen at fog top. The entrainment of drier air from above the fog layer produces sensible and latent heat fluxes, and depending on the humidity and inversion strength, it can

have a variable impact on the depletion of fog liquid water content (Wærsted et al., 2019). Entrainment, and large scale subsidence, also influence the vertical development of the fog layer (Wærsted et al., 2019). Besides, as mentioned in section 1.3, it has also been observed that fog top height and liquid water path may be key variables to understand fog dissipation. All these results indicate that it is necessary to observe both the surface and the vertical profile of fog, to have a comprehensive view of the processes that drive its evolution and dissipation.

However, the observation of the fog top has been historically difficult. In some cases, satellite data, ground remote-sensing instruments or atmospheric soundings could be used to provide approximations of fog top height, but these instruments were expensive and their data was not always available Román-Cascón et al. (2016b). Fortunately, new developments in remote sensing instruments in the recent years are modifying this situation. Newer generations of ground-based cloud radars and microwave radiometers now allow a continuous monitoring of the entire fog layer, remotely, and with decreasing costs.

Cloud radars are active remote sensing instruments, that emit a signal in a frequency susceptible to interact with liquid droplets of the size normally found in clouds. This interaction causses backscattering of the radar signal, that is received and processed at the radar end to retrieve properties such as object distance, reflectivity and doppler velocity. These three measurements enable, for example, the remote observation of cloud boundaries, the estimation of cloud liquid water or ice content versus range, and the retrieval of axial wind speed versus range (e.g. Sekelsky and McIntosh (1996); Kato et al. (2001); Protat et al. (2007)). Besides, recent technological improvements have significantly reduced the cost of these radars (Delanoë et al. (2016); Aguirre et al. (2020)), enabling continuous observations of boundary layer clouds at a growing number of sites (e.g. Illingworth et al. (2007); Haeffelin et al. (2016a); Pappalardo (2018)).

As is introduced in section 1.1, accurate microphysical retrievals require a reliable calibration. Yet, the development of calibration methods for radars remain a challenge, in part by its active instrument nature. Since the research of cloud radar calibration is a main subject of this thesis, we include a more comprehensive explanation of their working principle and calibration in the following sections.

Microwave radiometers (MWR) are passive remote sensing instruments, that sample the brightness temperature of incoming radiation at discrete spectral bands. These measurements are combined with inversion methods to retrieve information about meteorological variables (Solheim et al., 1998). MWR used in cloud remote sensing usually have one channel close to the 22.235 GHz water vapor absorption line, combined with another channel in an "atmospheric window" (frequency outside the absorption lines of atmospheric gasses), tipically at 36.5 or 90.0 GHz (Rose et al., 2005). These atmospheric windows are also used by cloud radars, and are shown in Fig 1.3 (b). Two channel measurements enable liquid water path and integrated water vapor retrievals. In addition, the use of multiple channels around the water vapor absorption line and the oxygen line (at 60 GHz) enable the retrieval of vertical atmospheric profiles of temperature and humidity (absolute and relative), with a vertical resolution of tens or hundreds of meters depending on altitude and the radiometer characteristics (Cadeddu et al., 2002; Ware et al., 2003). MWR and cloud radars can also be used synergestically to provide liquid water content profiles of clouds, when the radar is correctly calibrated (e.g. Frisch et al. (1998); Löhnert et al. (2001)). Technical research in MWR have already provided reliable and robust calibration guidelines (Kazama et al., 1999; Marke et al., 2016), and a reduction on their cost that makes it viable for observation networks (Rose et al., 2005).

Automatic Lidars and Ceilometers (ALC) are other useful instruments for fog remote sensing. ALC are active optical instruments, which emit laser pulses and sample their backscatter to retrieve information about suspended particles and the extinction profile of the atmospheric column. Because their wavelength interacts with atmospheric aerosols and cloud liquid water droplets, ALC are used to retrieve information of the aerosol profile, boundary layer dynamics and cloud base height (e.g. (Kotthaus

et al., 2016)). ALC have the advantage of being standard instruments, widely available in airports and atmospheric research facilities (Costa-Surós et al., 2013). However, this instrument has the disadvantage of being strongly attenuated by cloud droplets. Thus, they usually cannot provide information about the upper limit of clouds or fog layers. Despite this, ALC have been used to perform retrievals of cloud droplet number concentration and effective radius (Martucci and O'Dowd (2011)), and to track the hygroscopic growth of condensation nuclei before fog formation (Haeffelin et al., 2016b).

Figure 1.2 shows an example of remote sensing measurements taken during a fog event that took place in December of 2015, at the SIRTA atmospheric observatory. Panel (a) shows visibility measurements 4 meters above the surface, which are used to identify fog formation and dissipation time.

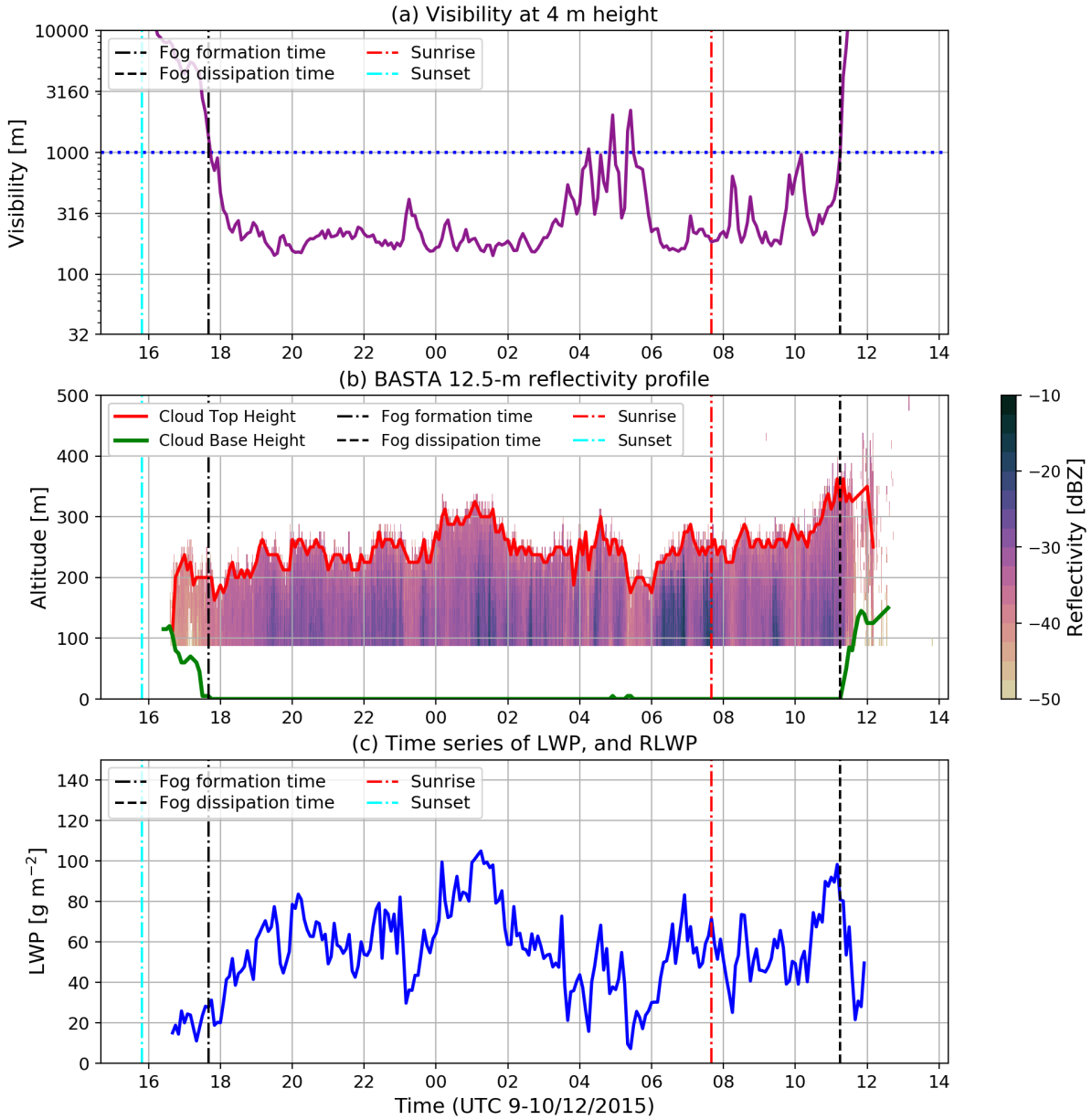

Figure 1.2: Example of remote sensing measurements of a fog layer measured during the 9th and 10th of December of 2015, at the SIRTA atmospheric observatory. Panel (a) shows the visibility time series of the fog event. Panel (b) shows cloud top height and reflectivity measurements performed using a cloud radar, and cloud base height measurements taken with a ceilometer. Panel (c) shows fog liquid water path, measured using a microwave radiometer.

Panel (b) shows reflectivity measurements with a vertical resolution of 12.5 m, taken with the cloud radar. This panel also shows cloud top height (CTH), detected using the reflectivity signal, and cloud base height tracked using the ceilometer. The combination of radar and ceilometer measurements indicate that the cloud forms by night, between 100 and 200 meters above the surface. This probably happens by the hygroscopic growth of aerosols, due to radiative cooling at the surface. The ceilometer also shows that the liquid layer gradually extends downards, until reaching the surface at the time of fog formation.

Panel (c) shows the evolution of the LWP of the fog layer. Since LWP is the total amount of water in the vertical column, it may contain contributions from clouds other than fog. Therefore, the cloud radar is used to verify that there are no clouds above the fog layer at the time of the measurements (not shown). We observe that the LWP has a value of approximately 20 g m^{-2} before and at fog formation time. Then, it rapidly grows reaching values as high as 80 g m^{-2} two hours later. This large LWP indicates that fog is probably opaque to infrared radiation and adiabatic at the time (Wærsted et al., 2017). Cloud top height oscilates close to 250 meters until 05:00 UTC, when we observe a sudden decrease of LWP accompained by a short-lived lifting of the cloud base, as evidenced by cloud base height and visibility observations.

Finally, both LWP and CTH incrase sharply before dissipation, at 11:15 UTC, when visibility rises above 1000 meters. The ceilometer indicates that dissipation happens by lifting of the fog base, probably associated with the increase in CTH (Wærsted et al., 2019). LWP and radar measurements also indicate that the cloud layer remains for about one hour after dissipation.

This example helps us see how remote sensing instruments make continuous monitoring of the fog layer possible, extending observations beyond the surface and providing a more comprehensive view of fog evolution.

1.5 Cloud radars

Radars are electromagnetic sensors for the detection and location of remote reflecting objects. Based on The Radar Handbook (Skolnik (2000)), the radar operating principle can be summarized as follows:

- The radar radiates electromagnetic energy from an antenna to propagate in space.
- Some of the radiated energy is intercepted by a remote reflecting object, also referred to as target.
- The incident energy interacts with the target and is reradiated in many directions.
- Some of the reradiated energy (echo) travels back and is received and is received by the radar antenna.
- The radar receiver amplifies and processes the signal to decide if there is detection of target echoes. When echoes are detected, the target location and other information is retrieved (for example, the target Radar Cross Section or its Doppler Velocity).

Cloud radars follow the same principle. What differentiates cloud radars from other radar types, is that the emission frequencies that they use interact with cloud particles in the Rayleigh scattering regime. The scattering regime of radiation with a given wavelength λ that incides on spheric particles of diameter D, can be inferred by using the size parameter x, in Eq. (1.3). If $x < \approx 0.1$, the Rayleight scattering approximation becomes valid. In this regime, the radar cross section of the particles is proportional to their diameter, and radiation is approximately evenly scattered in all directions. Besides, when $x > \approx 100$, the geometrical optics approximation becomes valid. Lastly, when the x value is between these two extremes, the radiation-particle interaction is better described by the Mie scattering theory (American Meteorological Society, 2012; Wallace and Hobbs, 2006).

$$x = \frac{\pi D}{\lambda} \tag{1.3}$$

Cloud radars usually operate at the Ka or W band, centered around 35 and 95 GHz respectively. This gives a wavelength of 9 and 3 mm respectively. Since the maximum diameter of liquid cloud droplets is of approximately 50 μm (Hudson and Yum (1997)), the maximum size parameter of cloud radars is of approximately $x = 0.017$ and $x = 0.05$ for Ka and W band respectively, enabling the use of the Rayleigh approximation. This is illustrated in Fig. 1.3 (a), including the scattering regime for other types of atmospheric particles. The explanation of why are these two frequencies are preferred can be found in Fig. 1.3 (b). Here we observe that the 35 and 95 GHz frequencies fall in two local minimums of atmospheric absorption. This significantly reduces attenuation with respect to other wavelengths in the millimeter range.

This section explained why cloud radars operate in the millimeter wavelength range. The next section explains the radar equation, which relates the backscattered power from an object with its radar cross section or reflectivity, for discrete or distributed targets respectively.

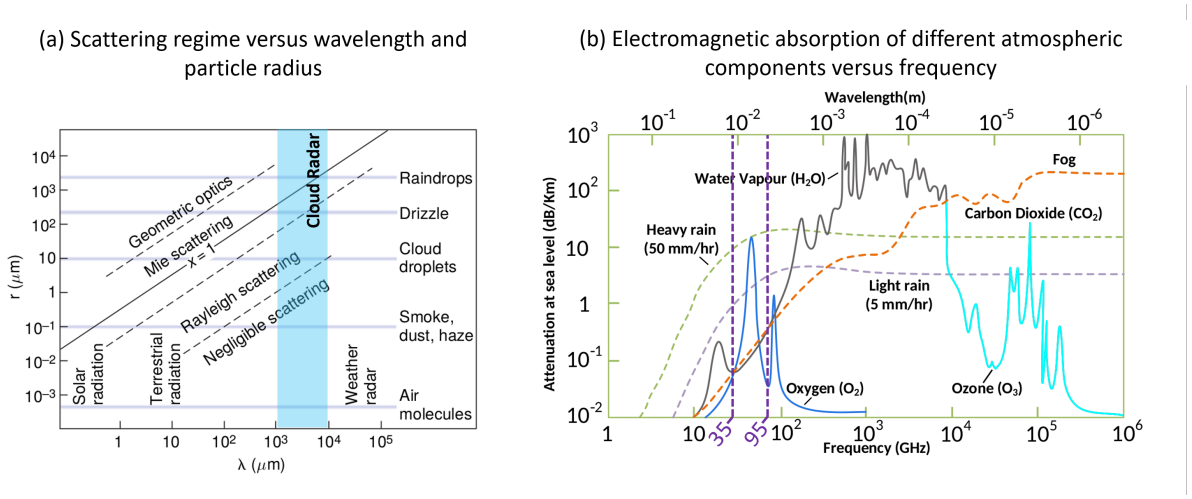

Figure 1.3: (a) Scattering regime depending on wavelength λ and particle radius r. Cloud radars usually operate within the wavelengths delimited by the light blue rectangle, where the interaction with cloud droplets is in the Rayleigh Scattering regime. Illustration adapted from Wallace and Hobbs (2006). (b) Electromagnetic absorption of different atmospheric constituents versus frequency. The two most common operating frequencies for cloud radars are indicated by purple dotted lines. Illustration adapted from Britannica (2017).

1.6 The radar equation

Here we describe how to derive the radar equation of a Frecuency Modulated Continuous Wave (FMCW) radar. This equation enables the estimation of cloud droplet reflectivity based on power measurements. The calibration terms involved in this retrieval are also derived and explained in this section.

FMCW cloud radars emit a continuous carrier wave with a constant power, which is modulated to perform a frequency sweep. This frequency sweep is known as chirp, and enables the estimation of the range from which a signal is reflected, by comparing in real time the emitted and received signal frequencies. This contrasts with the ranging method used by pulsed radars, in which range is estimated from the flying time of discrete pulses (Skolnik, 2000). Both radar types also enable the estimation of the particles doppler speed by measuring phase shifts in the echoed signal. The main advantage of FMCW radars is that they can be implemented using only solid state components, which operate using

less power and have a lower cost when compared with the components of magnetron based pulse radars. The BASTA-mini radar used in this study is an example of a W band FMCW radar (Delanoë et al., 2016).

The use of the FMCW principle is independent of the reflectivity calibration terms, and therefore this is not the focus of this section. However a detailed explanation of the FMCW principle can be found in Brooker (2005); Delanoë et al. (2016); Suleymanov (2016). We would also like to clarify that the reasoning presented in the following lines to derive the radar equation can also be applied to pulse radars. The difference is that in pulse radars it is necessary to consider a pulsed energy emission and the transmitter bandwidth in the radar power budget (Skolnik, 2000; Bringi and Chandrasekar, 2001).

The radar equation is derived by studying the physical power budget of a signal. The following derivation is based on Yau and Rogers (1996); Skolnik (2000). First, the radar transmitter emits a signal that enters the transmitter antenna with a power p'_t. Second, assuming that radar antennas are oriented in the direction of observation, an object at a distance r would receive a power density of $P_{rec}(r)$ (Eq. (1.4)). When the transmitter antenna is aligned with the target, G_t represents the maximum antenna gain. The attenuation proportional to r^2 appears because power density decreases due to the spread of the wave front (Balanis, 2016).

$$P_{rec} = p'_t \frac{G_t}{4\pi r^2} \tag{1.4}$$

Third, the traveling wave interacts with a target of a given Radar Cross Section (RCS) Γ. The RCS of an object can be understood as the equivalent cross-sectional area a sphere should have to reflect the same amount of incident power back to the radar receiver. The units to represent RCS are of m^2 in the linear scale, and of dBsm in the decibel scale ($1\ dBsm = 10\log_{10}(\Gamma(m^2))$). Because of this interaction, the target backscatters an amount of power proportional to its RCS, given by P_{refl} in Eq. (1.5).

$$P_{refl} = p'_t \frac{G_t}{4\pi r^2}\Gamma \tag{1.5}$$

Fourth, the backscattered wave travels towards the radar. If the radar has two parallel antennas, and the reflecting object is much farther than antenna separation, the instrument is operating in full antenna overlap conditions. This means that both antenna gain lobes are superimposed, and therefore the effective gain lobe of both antennas will be equivalent to the multiplication of the individual antenna patterns (Balanis, 2016). Thus, the receiver antenna gain can be calculated directly from its aperture $A_p = G_r\lambda^2/4\pi$ (G_r being the receiver antenna maximum gain). Including this term, and the spread of the electromagnetic wave by traveling the distance r a second time, we get that the power at the receiver antenna output should be that of $P'_r(r)$, indicated in Eq. (1.6).

$$P'_r(r) = \frac{G_t p'_t}{4\pi r^2} A_p \frac{1}{4\pi r^2}\Gamma = \frac{G_t G_r \lambda^2 p'_t}{(4\pi)^3 r^4}\Gamma \tag{1.6}$$

Equation (1.6) is known as the general radar equation. This equation relates the RCS Γ of a target with remote measurements of its backscattered power.

However, in most use cases it is necessary to make additional considerations before using Eq. (1.6) to measure the RCS of an object. This is because in general, radar operators do not know the exact physical power emitted and received by the antenna. What they commonly know is the nominal emitted power, and the received power measured at the receiver end, after several amplification and signal processing stages. Therefore, radar operators work with power variables defined by the pair $p'_t = p_t/L_t$ and $P_r(r) = P'_r(r)/L_r$, where L_t and L_r represent the total loss introduced by the radar internal components. This loss is the product of all loss terms divided by all the gain terms in the emitter and receiver chains. If losses are greater than 1, the physical emitted power p'_t will be smaller than the nominal emitted power

p_t, and the measured power $P_r(r)$ will be smaller than the physical received power $P'_r(r)$. Conversely, if the loss terms are between 0 and 1, we have a net system gain and the emitted and received power will be greater than the physical value. For radars, it is usual to have a total transmitter loss $L_t > 1$ because the nominal emitted power is clearreferenced with respect to the power amplifier output, just before the antenna, and the electromagnetic wave is then affected by losses in the waveguides, at the antenna input and when crossing the radome (Anagnostou et al., 2001). On the contrary, radar receivers usually have a total loss $L_r < 1$, having the net effect of amplifying the signal. This increases the instrument sensitivity, enabling the detection of weaker reflections from farther objects.

Another term that must be included in the radar equation, specially when using millimeter wave signals, is the atmospheric attenuation $l_{at}(r)$. As Fig. 1.3 shows, cloud radars operate in local minimums of atmospheric attenuation. Yet, even if this means that attenuation losses will be lower than for other intermediate frequencies, it is not neglible. For example, at SIRTA, these losses can reach values of ≈ 0.8 dB km^{-1} for an horizontal beam. Atmospheric attenuation can be calculated using a radiative transfer model for millimeter waves, such as the one published by Liebe (1989). When internal radar losses and atmospheric attenuation from traveling the distance r twice are introduced in the general radar equation, we get the radar equation used to perform RCS retrievals (Eq. (1.7)).

$$P_r(r) = \frac{G_t G_r \lambda^2 p_t}{L_r L_t (4\pi)^3} \frac{\Gamma}{l_{at}^2(r) r^4} \tag{1.7}$$

Equation (1.7) can be separated in radar internal parameters and environment dependent variables. This leads to the definition of a RCS calibration term C_Γ, in Eq. 1.8, which can be used to calculate the RCS of a target at a distance r with Eq. (1.9).

$$C_\Gamma = \frac{L_t L_r (4\pi)^3}{G_t G_r \lambda^2 p_t} \tag{1.8}$$

$$\Gamma(r) = C_\Gamma \; l_{at}^2 r^4 P_r(r) \tag{1.9}$$

Radar Equivalent Reflectivity Equation

Retrieving the RCS of a target is enough for many radar applications. However, for cloud radars, the main interest is in the retrieval of radar equivalent reflectivity Z_e. This parameter links backscattered power with the microphysics of a volume filled with small scatterers, such as water droplets or ice crystals. To derive the formulation of radar equivalent reflectivity, or simply reflectivity, it is necessary to consider the RCS of a volume filled with liquid or ice particles with a given size distribution.

Assuming that particles are approximately spherical, that their diameter D has a size distribution per unit volume of $N(D)$, that the particles backscatter radiation in the Rayleigh regime and that the total RCS per unit volume is equal to the sum of each particle contribution, we get that the total cross section per unit volume is of γ_v, shown in Eq. (1.10). $K^2 = (\epsilon_r - 1)^2/(\epsilon_r + 2)^2$ is the dielectric factor, which depends on the complex relative permittivity ϵ_r of the particles (Yau and Rogers, 1996).

$$\gamma_v = \frac{\pi^5 K^2}{\lambda^4} \int_0^\infty N(D) D^6 dD \tag{1.10}$$

Power samples of a FMCW radar will be retrieved for discrete range points, separated by the range resolution δr. These points are known as gates. If the radar uses antennas with a Gaussian beam shape, and a beamwidth θ (in radians), each gate will have the effective sampling volume $V(r)$ indicated in Eq. (1.11).

$$V(r) = \frac{\pi \delta r}{2\ln(2)} \left(\frac{r\theta}{2}\right)^2 \tag{1.11}$$

Therefore, and by assuming a uniform droplet size distribution in the radar sampling volume, we get that the RCS of a distributed target at a distance r will be of $\Gamma_v = \gamma_v \cdot V(r)$. By replacing Γ with Γ_v in Eq. (1.7), we obtain the relationship of Eq. (1.12)).

$$P_r(r) = \frac{G_t G_r \pi^3 \theta^2 p_t \delta_r}{512 \ln(2) L_r L_t \lambda^2} \frac{K^2}{l_{at}^2(r) r^2} \int_0^\infty N(D) D^6 dD \tag{1.12}$$

Reflectivity Z_e is defined from the latter term of Eq. (1.12). As can be seen in Eq. (1.13), reflectivity is proportional to the sixth power of the particles diameter. Additionally, reflectivity is usually expressed in mm^6 m^{-3} units due to the values commonly found in clouds (e.g. Fox and Illingworth (1997)).

$$Z_e = \int_0^\infty N(D) D^6 dD \ [m^6 m^{-3}] = 10^{18} \int_0^\infty N(D) D^6 dD \ [mm^6 m^{-3}] \tag{1.13}$$

By rearranging Eq. 1.12, using the Z_e definition in mm^6 m^{-3} units, we get Eqs. (1.14) and (1.15). These equations can be used to retrieve the reflectivity of an air parcel filled with liquid or ice droplets. As in the RCS radar equation, we regroup the radar dependent elements into a specific reflectivity calibration term C_Z. This term depends almost exclusively on radar properties, with the exception of the dielectric factor K which must be estimated from hypotheses or additional measurements (Sassen, 1987).

$$Z_e(r) = C_Z \ l_{at}^2(r) r^2 P_r(r) \tag{1.14}$$

$$C_Z = \frac{8\ln(2)\lambda^4 10^{18}}{\theta^2 \pi^6 K^2 \delta r} C_\Gamma \tag{1.15}$$

Additionally, it is common to express Eq. (1.14) in decibel scale by applying $10\log_{10}(\cdot)$ on both sides of the equation. When this expression is used, the units of reflectivity are modified to $dBZ = 10\log_{10}(mm^6 m^{-3})$. The RCS and reflectivity equations in decibel scale are written as Eqs. (1.16) and (1.17) respectively. Power is mW (dBm in decibel scale), r is in meters and the atmospheric attenuation is in dB ($10log_{10}(l_{at}) = L_{at}$). Under this formulation, C_Γ units are of m^{-2} mW^{-1} and C_Z units are mm^6 m^{-5} mW^{-1}.

$$\Gamma(r)[dBsm] = 10\log_{10}(C_\Gamma) + 2L_{at}(r)[dB] + 40\log_{10}(r[m]) + P_r(r)[dBm] \tag{1.16}$$

$$Z_e(r)[dBZ] = 10\log_{10}(C_Z) + 2L_{at}(r)[dB] + 20\log_{10}(r[m]) + P_r(r)[dBm] \tag{1.17}$$

$$\tag{1.18}$$

The retrieval of the calibration terms C_Γ and C_Z is one of the two axes of this thesis. The next section introduces approaches currently used for their retrieval and their limitations. Chapter 3 presents our solution to estimate these terms.

1.7 Cloud radar calibration

Cloud radar calibration is necessary to perform the retrieval of physical quantities from backscattered power measurements. As Eqs. (1.9) and (1.14) show, it is necessary to know the RCS and reflectivity calibration terms (C_Γ and C_Z respectively) to perform RCS and reflectivity measurements. However,

calibration research efforts, begining with the radar invention during the first half of the 20th century, have not yet provided a reliable and universally aplicable calibration method (Süsskind, 1985; Atlas, 2002). Different radar configurations require different approaches.

The main reason is that it is hard to calculate the total power budget of radar systems, due to their active nature and their large number of components. Radar components are distributed in three main subsystems: the transmitter, the antenna, and the receiver. Each of these subsystems is composed of serveral discrete components with their respective interconnections and interactions (Chandrasekar et al., 2015; Ewald et al., 2019). Consequently, internal radar calibration, calculated as the product of each individual component gain and loss terms (Eqs. (1.8) and (1.15)) have been found to cause RCS and reflectivity biases in the order of units of decibel. For example, Anagnostou et al. (2001) has found biases of up to 7 decibels when comparing reflectivity measurements of the Tropical Rainfall Measuring Mission satellite with ground based precipitation radars. Similarly, comparisons with the satellite-based cloud radar CloudSat have found systematic differences of two 2 decibels between cloud radars based in europe (Protat et al., 2009). Biases of this magnitude are not neglibible, since calibration errors of just 1 decibel would introduce uncertainties of 15%–20% in liquid water and ice content retrievals (Fox and Illingworth, 1997; Ewald et al., 2019).

The afforementioned difficulties motivated the research of alternative calibration methods which could characterize the complete radar system at once. They are known as 'end-to-end' calibration methods, and rely on the use of discrete or distributed targets with known RCS or reflectivity respectively (Chandrasekar et al., 2015). The calibration principle relies on Eqs. (1.9) and (1.14). Equation (1.9) shows that the RCS calibration term C_Γ can be retrieved by measuring the power backscattered from a target with a known RCS, positioned at a known distance. Alternatively, the reflectivity calibration term C_Z can be retrieved by sampling a distributed target with known reflectivity, with Eqs. (1.14). Since the RCS and the reflectivity calibration terms are linked by Eq. (1.15), in theory it suffices to get one calibration term to calculate the other.

The discrete targets used for the RCS calibration (also known as point targets), have simple geometrical shapes that enable the calculation of their radar cross section from theoretical principles. Commonly used shapes are spheres, triangular and square thriedres (corner reflectors) and cylinders, among others (Brooker, 2006; Doerry and Brock, 2009). When using discrete targets, manufacturing accuracy is critical. Errors of some degrees in the angles of trihedres can introduce biases in the order of decibels with respect to theoretical RCS calculations, specially for millimeter wavelengths (Garthwaite et al., 2015). This method, however, has been widely tested, even using different setups such as balloons or drones (Atlas and Mossop, 1960; Bergada et al., 2001; Yin et al., 2019), and has enabled a comprehensive study of uncertainty for X band (8-12 GHz) and lower frequency radars (Garthwaite et al., 2015; Chandrasekar et al., 2015; Yin et al., 2019).

Alternative approaches using active reflectors have been tested, to reduce the impact of environmental clutter. These active devices measure the radar power and return signals with a shifted frequency, to make it distinguishable from the background (Brunfeldt and Ulaby, 1984; Atlas, 2002). However, they require an internal calibration and an assesment of their antenna alignment before being useful as references. They are not exempt from system alignment errors neither.

Distributed targets have also been used to calibrate cloud radars. Hogan et al. (2003) calibrated a W band radar by using rain as a reference, by taking advantage of the approximately constant 19 dBZ reflectivity for rain rates between 3 and 10 mm $h^{\breve{}1}$. In this study, Hogan et al. (2003) also found that a thin layer of rainwater on the radome produced a two-way loss of 9 to 14 dB, which was later avoided by operating the radar at a low elevation angle and employing a shelter to keep it dry. Another calibration excercise with rain was done by Myagkov et al. (2020), where he used the self-consistency method of polarimetric radar variables and a comparison with the droplet size distribution mesured

by an in-situ distrometer to estimate the calibration terms of a W band radar. The self-consistency method requires polarimetric and doppler spectrum measurements, which impose additional challenges in radar design and calibration (Ryzhkov et al., 2005), however provides good calibration results, with an uncertainty within 0.7 dB. The main limitation is that this approach requires the use of a scanning radar with polarimetric and doppler spectrum capabilities, increasing the instrument cost. Therefore, these instruments are not available at all sites. Meanwhile, Myagkov et al. (2020) shows that calibration using a disdrometer can provide a calibration uncertainty within 0.9 dB for rain rates below 4 mm h^{-1}. This method can be used by vertical, non-polarimetric radars as long as they have a strong enough blower to keep the radome dry.

Other distributed targets that can be used for calibration are clouds. Ewald et al. (2019) validated the calibration of their Ka-band cloud radar HAMP MIRA, on board of the German research aircraft HALO, by comparing cloud measurements with two other W band radars (RASTA and CloudSat). His conclusions indicated that these comparisons must consider differences in signal attenuation, arising from different gas and liquid water absorption between the operating frequencies, and in the scattering regime of each radar when interacting with the hydrometeors. After a careful data selection, Ewald et al. (2019) was able to validate the calibration of their HAMP MIRA with an uncertainty of 1 decibel, showing that calibration transfer between radars, using clouds as common targets, may be a practical calibration approach.

1.8 Thesis context and objectives

This thesis is positioned in the context of a scientific-industrial collaboration between the Laboratoire de Météorologie Dynamique (LMD) of the Institut Polytechnique de Paris (IPP) and the company Météomodem SAS.

Fog studies are an active research topic for the LMD and for its atmospheric observatory, the SIRTA. This interest arises from the previously mentioned scientific challenges involved, regarding the identification and quantification of fog processes and the forecasting of fog evolution. The laboratory already has a large number of publications about the study of fog processes ((Haeffelin et al., 2010, 2013; Dupont et al., 2016, 2018; Wærsted et al., 2017, 2019)), and has developed the fog formation nowcasting tool PARAFOG (Haeffelin et al., 2016b). PARAFOG is running continuously at SIRTA, and in Roissy, Orly and Agen airports[1]. In addition, the SIRTA observatory is involved in the development of the ACTRIS cloud remote sensing network (Pappalardo, 2018). It is foreseen that the SIRTA observatory will become a National Facility of ACTRIS to provide cloud remote sensing measurements.

The teams at IPSL, LATMOS and LMD involved in cloud remote sensing are also developing new services to improve the cloud remote sensing data quality at European scale. This is done as part of the ACTRIS Topical Center for Cloud Remote Sensing (CCRES). Among these services, cloud radar calibration guidelines are of high interest for all ACTRIS cloud remote sensing national facilities. This implies that improved cloud radar calibration methods must be developed.

On the side of the company Météomodem, the main interest is the development of fog assessment products that could benefit from the relatively low cost of their last generation BASTA cloud radars, with the long term goal of creating a network of fog monitoring stations for airports or other relevant sites. Additionally, the company is interested in developing calibration methodologies for the cloud radars of these networks, to guarantee their performance.

BASTA cloud radars are developed in a partnership between Météomodem and the LATMOS laboratory of Guyancourt, France (Delanoë et al., 2016). These radars use the Frequency Modulated

[1]PARAFOG diagnostics can be accessed free of charge at the url `https://www.lmd.polytechnique.fr/sirta/parafog/index.html`

Continuous Wave (FMCW) emission principle, which enables a significant reduction of costs and radar size by enabling the use of solid state components instead of magnetrons. BASTA radars can measure reflectivity and doppler velocity of hydrometeors up to 18 km of height with different resolution and integration modes.

This congruence of interests, and the antecedents presented in the introduction, led to the formulation of this thesis project and of its objectives. The objectives of the thesis are:

1. To better understand the relationship between liquid water path (LWP) and cloud top height (CTH) in fog layers, and their roles on fog evolution and dissipation. To demonstrate how remote sensing measurements can support the investigation of these relationships.

2. To improve the quality of fog remote sensing measurements, in particular the unresolved issue of cloud radar calibration, considering the needs of fog monitoring networks.

For objective 1, we studied 7 years of fog measurements collected at the SIRTA atmospheric observatory. We focus this study on fog layers that reach a CTH of at least 85 meters, to enable its observation using the vertical BASTA cloud radar of the SIRTA observatory (lower CTH values are within the radar blind zone). Because our observations mostly comprise the vertical column, we neglect the effect of horizontal advection or heterogeneities, focusing mostly on the vertical fog structure. Since previous studies show that fog top height (CTH) and liquid water path (LWP) may be key variables to understand fog evolution and dissipation (Wærsted (2018)), we orient the research of objective 1 with the following questions:

1. What is the relationship between LWP and CTH in fog layers?

2. How are these variables related with the fog life cycle?

3. How can remote sensing measurements be used to support fog LWP and CTH studies?

4. Can LWP and CTH provide an indicator of fog dissipation tendency?

These questions are addressed in Chapter 2. Questions 1, 2 and 3 are studied in section 2.2. There we propose a conceptual model relating fog LWP with its CTH, surface visibility and adiabaticity. The model provided a coherent framework to study the relationship between these meteorological variables, and enabled the identification of fog status indicators. These results are presented in a publication submitted to the Copernicus Atmospheric Chemistry and Physics Journal, which is currently under peer-review (Toledo et al., 2021). Question 4 is addressed in section 2.3. Here we study how the indicator variables identified ealier could be used to assess fog dissipation tendency.

For objective 2, we planned and performed two cloud radar calibration campaigns at the SIRTA observatory. The calibration campaigns took place in May of 2018 and March of 2019 in the framework of the ACTRIS infrastructure development, and lasted about two months each. In these campaigns we tested several calibration approaches, in order to determine an appropriate strategy to calibrate the cloud radars of the fog monitoring network. The experiments involved the use of the BASTA radar, among other instruments and equipment brought by several national and international contributors. The teams involved in these campaign were the LATMOS and LMD laboratories of France, the TU-Delft University of the Netherlands, the spanish University of Granada, the german University of Cologne, the british University of Reading, the romanian INOE institute, and the companies Météomodem, METEK and RPG GmbH.

The antecedents presented in section 1.7, and practical considerations discovered when planning and executing the experiments, led us to develop a two step calibration strategy: First, to calibrate a

reference radar using a reference corner reflector, since this method has the potential of providing an absolute reflectivity calibration with a thorough characterization of uncertainty. Second, to use this radar as a reference, to calibrate other radars in the network. This strategy led to the following research questions:

1. How can cloud radar calibration and its uncertainty be determined using corner reflectors?
2. How can cloud radar calibration be transferred, and what is the uncertainty of this procedure?

Chapter 3 addresses question 1. Here we study how to use corner reflectors to calibrate cloud radars, and how to quantify bias and uncertainty sources. This chapter is based on an article published in the Atmospheric Measurement Techniques journal (Toledo et al., 2020). The method was developed and tested during 2018 and 2019 calibration campaigns, using a scanning BASTA mini cloud radar.

Chapter 4 addresses question 2. This chapter presents a calibration transfer methodology for radars in the W band, based on the comparison of simultaneous cloud measurements. The method is illustrated using data from the 2019 calibration campaign, where a BASTA mini is used as a reference to calibrate a 94 GHz RPG cloud radar. This chapter also presents how to quantify the uncertainty of the calibration method, and the considerations that must be made when transferring calibration between radars with different sensitivity.

Finally, the general conclusions of the thesis, and the perspectives for future work, are presented in chapter 5.

Chapter 2

Use of remote sensing measurements to study fog LWP and CTH, and to derive new diagnostics of fog dissipation tendency

2.1 Introduction

In section 1.3 we introduced the fog life cycle, understanding fog as a layer with the presence of liquid water droplets, existing between the surface and the temperature inversion. Previous research (Wærsted et al. (2019); Wærsted (2018)) has shown that fog top height (CTH) and liquid water path (LWP) may be important variables to describe fog evolution and dissipation, based on case studies.

To further investigate this hypothesis, we conduct a study using 7 years of remote sensing measurements of fog CTH and LWP, in addition to in-situ observations of surface visibility, temperature and pressure. This data was collected at the SIRTA atmospheric observatory located in Palaiseau, France (Haeffelin et al., 2005).

The observations are interpreted using an original conceptual model for fog layers, which relates the liquid water path of fog to its geometrical thickness and the liquid water content at the surface. This conceptual model made the study of fog adiabaticity possible, by considering the singular conditions that fog has with respect to other clouds. For example, the fact that fog has a solid boundary at the surface, or that it can exist in opaque and non-opaque regimes.

Following the objectives of the thesis, the conceptual model is used to derive key diagnostic parameters of fog dissipation tendency. The first parameter, defined as the critical liquid water path (CLWP), indicates the minimum amount of LWP that is necessary to fill a fog layer of a given thickness and reduce surface visibility to 1000 meters. The second parameter is the reservoir liquid water path (RLWP), which is defined as the difference between fog LWP and CLWP. The RLWP is a quantitative measure of the amount of LWP that must be removed before dissipation can occur, for a given fog thickness. When the RLWP becomes negative, the LWP is less than the CLWP and therefore fog dissipates. We also demonstrate that RLWP is a function of fog CTH and LWP, and that it can be depleted by variations in either of these parameters.

Finally, we also include a study on the information that RLWP and visibility can contribute to the assessment of fog dissipation tendency. We identify conditions in which RLWP behaves independently

of visibility, acting as an independent variable to characterize fog status. We also perform calculations of fog dissipation probability within different time ranges, as a function of visibility and RLWP, and identify the limitations of this approach.

The conceptual model formulation and its study is the object of a publication submitted to the Atmospheric Chemistry and Physics journal, which is currently under review (Toledo et al., 2021). This publication is included in section 2.2 of this chapter. In this document, section 2 explains the formulation of the conceptual model and of the CLWP and RLWP variables. Section 3 presents the measurements and methodology used to construct and evaluate the conceptual model. Section 4 shows fog adiabaticity results, and compares the conceptual model LWP predictions with historical observations. Section 5 uses case studies to exemplify how conceptual model variables enable us to understand fog evolution, and present statistical results of fog behavior during its formation, middle life and dissipation phases. Section 6 present the conclusions of the article. Then we present our study about the use of RLWP and visibility in the assessment of fog dissipation tendency, in section 2.3, followed by a synthesis of this chapter in section 2.4.

2.2 Study of fog LWP and CTH using remote sensing measurements and a new conceptual model

A New Conceptual Model for Adiabatic Fog

Felipe Toledo[1], Martial Haeffelin[2], Eivind Wærsted[3], and Jean-Charles Dupont[4]

[1]Laboratoire de Météorologie Dynamique, École Polytechnique, Institut Polytechnique de Paris, 91128 Palaiseau, France
[2]Institut Pierre Simon Laplace, École Polytechnique, CNRS, Institut Polytechnique de Paris, 91128 Palaiseau, France
[3]Laboratoire de Météorologie Dynamique, École Polytechnique, Institut Polytechnique de Paris, 91128 Palaiseau, France.
Current affiliation: The Norwegian Meteorological Institute, Henrik Mohns Plass 1, 0313, Oslo, Norway
[4]Institut Pierre-Simon Laplace, École Polytechnique, UVSQ, Université Paris-Saclay, 91128 Palaiseau, France

Correspondence: Felipe Toledo (ftoledo@lmd.polytechnique.fr)

Abstract.

Visibility reduction caused by fog can be hazardous for human activities, especially for the transport sector. Previous studies show that this problem could be mitigated by improving nowcasting of fog dissipation. To address this issue, we propose a new paradigm which could potentially improve our understanding of the life cycle of adiabatic continental fogs, and of the conditions that must take place for fog dissipation.

For this purpose, adiabatic fog is defined as a layer filled with suspended liquid water droplets, extending from an upper boundary all the way down to the surface, with a saturated adiabatic temperature profile. In this layer, the liquid water path (LWP) must exceed a critical value, the critical liquid water path (CLWP). When the LWP is less than the CLWP, the amount of fog liquid water is not sufficient to extend all the way down to the surface, leading to a surface horizontal visibility greater than 1 km. Conversely, when the LWP exceeds the CLWP, the amount of fog water is enough to reach the surface, inducing a horizontal visibility less than 1 km. The excess water with respect to the critical value is defined as the reservoir liquid water path (RLWP).

The new fog paradigm is formulated as a conceptual model that relates the liquid water path of adiabatic fog with its thickness and surface liquid water content, and allows the critical and reservoir liquid water paths to be computed. Both variables can be tracked in real time using vertical profiling measurements, enabling a real time diagnostic of fog status.

The conceptual model is tested using data from seven years of measurements performed at the SIRTA observatory, combining cloud radar, microwave radiometer, ceilometer, scatterometer and weather station measurements. In this time period we found 80 fog events with reliable measurements, with 56 of these lasting more than three hours.

The paper presents the conceptual model and its capability to derive the LWP from the fog CTH and surface horizontal visibility with an RMS uncertainty of 10.5 g m^{-2}. The impact of fog liquid water path and fog top height variations on fog life cycle (formation to dissipation) is presented based on four case studies, and statistics derived from 56 fog events. Our results, based on measurements and an empirical parametrization for the adiabaticity, validate the applicability of the model. The calculated reservoir liquid water path is consistently positive during the mature phase of fog, and starts to decrease quasi monotonously about one hour before dissipation, reaching a near-zero value at the time of dissipation. Hence, the reservoir

liquid water path and its time derivative could be used as indicators of the life cycle stage, to support nowcasting of fog dissipation.

1 Introduction

Fog occurs due to multiple processes that lead to water vapor saturation in the air close to the surface. Water vapor saturation can be caused by a reduction of air temperature, due to radiative cooling, turbulent heat exchange, diffusion, adiabatic cooling through lifting, advection. It can also occur by air moistening, due to water evaporation from the surface, evaporation of drizzle, advection of moist air, and vertical mixing (Brown and Roach, 1976; Gultepe et al., 2007; Dupont et al., 2012). On the contrary, fog dissipates as a result of warming and drying of the air near the surface, and also through the removal of droplets by precipitation (Brown and Roach, 1976; Haeffelin et al., 2010; Wærsted et al., 2017, 2019).

Stable fog and adiabatic fog should be distinguished because radiative, thermodynamic, dynamic and microphysical processes are significantly contrasted in the two types of fog. In a stable fog layer, the equivalent potential temperature increases with height, which inhibits vertical mixing. The surface is therefore weakly coupled with the fog top. Stable fog remains shallow and contains small amounts of liquid water, limiting the radiative cooling of the fog layer. In contrast, in an adiabatic fog the stability is close to neutral, enabling rapid vertical mixing, so that the surface and fog top are strongly coupled (Price, 2011; Porson et al., 2011). An adiabatic fog behaves similarly to stratocumulus clouds on top of convective boundary layers (Cermak and Bendix, 2011). The processes of adiabatic fogs have been studied extensively in the past with large-eddy simulation (LES) and numerical weather prediction (NWP) models (Nakanishi, 2000; Porson et al., 2011; Bergot, 2013, 2016; Wærsted et al., 2019).

An adiabatic fog or stratiform cloud cools at its top from emission of long wave radiation, which destabilises the cloud and leads to convective mixing. When the cloud is coupled with the land surface, the destabilising process can be further strengthened by heat fluxes from below due to soil heat (Price, 2011). A thermal inversion develops right above the cooling cloud fog top and limits the coupling between the cloud and free atmosphere above. The thermal inversion defines the upper boundary of the adiabatic fog. The lower boundary of the stratiform cloud layer varies in time and space depending the amount of liquid water present in the cloud. For the adiabatic fog, the lower boundary is defined by the surface and is therefore fixed. Hence a fog layer may not grow geometrically deeper when the amount of liquid water increases.

Cermak and Bendix (2011) define fog and stratiform clouds based on cloud layer top altitude and liquid water content that follows a sub-adiabatic profile. A fog layer is thus defined as a stratiform cloud that contains sufficient liquid water to reach down to the surface.

Wærsted et al. (2019) showed using a large eddy-simulation model and remote sensing measurements that dissipation of fog can occur due to both reduction of liquid water content of the fog layer and increase of fog top height. Dissipation is defined here as removal of fog droplets leading to visibility increasing above 1 km at screen-level height. The simulations reveal a similar behavior as proposed by Cermak and Bendix (2011). For a given fog top height, if the liquid water path contained in the

fog layer becomes insufficient, the fog base lifts from the ground, which can be interpreted as fog dissipation through lifting into a stratiform cloud.

In adiabatic clouds, the thickness can be approximated from liquid water path. Brenguier et al. (2000) state that liquid water path is proportional to the square of cloud thickness. A precise quantification of the relationship between fog thickness and fog liquid water path is lacking in the literature.

In this article we present a conceptual model that relates the liquid water path of adiabatic fog to its geometrical thickness and surface liquid water content. The conceptual model enables an estimation of the minimum amount of column liquid water that is necessary to reach a visibility less than 1000 meters at the surface, defined as the critical liquid water path, and a calculation of the excess water that enhances fog persistence, defined as the reservoir liquid water path. The model also enables a quantification of the impact of liquid water path and geometrical thickness variations on the reservoir, a characteristic that could be later used to improve fog forecasting tools.

The conceptual model theory is explained in Section 2. In Section 3, we present all measurements used to construct and evaluate the conceptual model. In Section 4 we derive a parametrization for fog adiabaticity using historical data, and we compare the conceptual model predictions with fog thickness, liquid water path and surface liquid water content observations. In Section 5 we present case studies to exemplify how conceptual model variables enable us to understand fog evolution, and statistical results of fog behavior during its formation, middle life and dissipation phases.

2 Fog Conceptual Model

2.1 Fog LWP Conceptual Model

The hypothesis of this work is that when a fog layer is well-mixed, the persistence or not of fog at surface level will be determined by vertically integrated quantities of the whole fog layer, and in particular the integrated liquid water content. To test this hypothesis we develop a unidimensional model for a fog column, based on previous models for stratus clouds.

For stratus clouds, cloud Liquid Water Content (LWC) increases with height can be modelled using Eq. (1) (Betts, 1982; Albrecht et al., 1990; Cermak and Bendix, 2011). In this equation, z is the vertical distance above the Cloud Base Height (CBH), which increases until reaching the Cloud Top Height (CTH). $\Gamma_{ad}(T,P)$ is the negative of the change in saturation mixing ratio with height for an ideal adiabatic cloud, and $\alpha(z)$ is the local adiabaticity, defined as the ratio between the real and the ideal adiabatic liquid water content change with height. $\Gamma_{ad}(T,P)$ is a quantity that depends on the local temperature T and pressure P. The equation used for its calculation can be found in appendix A.

$$\frac{dLWC(z)}{dz} = \alpha(z)\,\Gamma_{ad}(T,P) \tag{1}$$

This model can also be applied for well mixed fog layers, where the adiabatic profile assumption is valid. Fog layers that are radiatively opaque will cool almost exclusively at the fog top and therefore tend towards static instability, which causes mixing through convective turbulence. During day time, convection is reinforced by sensible heat release from the surface.

This mixing induces the formation of a saturated adiabatic temperature profile in fog layers (Roach et al., 1976; Boutle et al., 2018; Wærsted et al., 2019).

However, there is one key difference in fog layers that must be considered when integrating (1). In stratus clouds, it is assumed that the LWC at the cloud base is zero, because condensation is starting gradually from unsaturated air, and therefore there is a smooth transition between dry and moist air.

This smooth transition does not occur in fog layers. In this case, the cloud base is fixed by the surface height, and has a possitive LWC. These characteristics are the reason for the visibility reduction at the surface. It is worth noting that for adiabatic fog, the surface presence could produce a larger accumulation of LWC with respect to other clouds of the same thickness. This could happen because in this fog type, water vapor condensation can occur rapidly at the fog top, due to radiative cooling (e.g. Wærsted et al. (2017)), and this LWC would be redistributed in a layer of a fixed vertical extent. Vertical redistribution would happen because in adiabatic fog, the stability is close to neutral and therefore vertical circulation caused by surface heating, or cloud top radiative cooling, are possible (Smith et al., 2018).

Thus, when integrating Eq. (1) it is necessary to account for a non-zero Surface Liquid Water Content (LWC_0). Since fog (and stratus clouds) are shallow, their LWC increases with height, and $\Gamma_{ad}(T,P)$ can be assumed constant for the whole layer (Albrecht et al., 1990; Braun et al., 2018). This leads to the LWC formulation of Eq. (2).

$$LWC(z) = \int_{z'=0}^{z'=z} \alpha(z')\, \Gamma_{ad}(T,P)\, dz' + LWC_0 \tag{2}$$

The blue curve of Fig. 1 (a) illustrates how LWC behaves in well mixed fog. For most of the fog layer thickness, LWC increases with height due to upward motions of moisture from the surface and within the cloud (Oliver et al., 1978; Manton, 1983; Walker, 2003; Cermak and Bendix, 2011). Then, when approaching fog top from below, the LWC change with height decreases until becoming a net reduction of LWC near the top. This decrease is due to entrainment of dry-air at the top, which leads to a quick decline in droplet size and LWC (Brown and Roach, 1976; Roach et al., 1982; Driedonks and Duynkerke, 1989; Hoffmann and Roth, 1989; Boers and Mitchell, 1994; Cermak and Bendix, 2011).

Fog LWP is defined as the integral of LWC(z) in the fog column (Eq. 3a). Its formulation as a function of adiabaticity is presented in Eq. (3b), where z is the height above the surface. Since in fog the CBH is always at the surface, fog thickness is completely defined by its CTH.

$$LWP = \int_{z=0}^{z=CTH} LWC(z)\, dz \tag{3a}$$

$$= \int_{z=0}^{z=CTH} \left(\int_{z'=0}^{z'=z} \alpha(z')\, \Gamma_{ad}(T,P)\, dz' + LWC_0 \right) dz \tag{3b}$$

$$LWP = \frac{1}{2} \alpha_{eq}\, \Gamma_{ad}(T,P)\, CTH^2 + LWC_0\, CTH \tag{3c}$$

To simplify the calculation of the integral in Eq. (3b), which requires the knowledge of the adiabaticity profile $\alpha(z)$, we introduce the Equivalent Adiabaticity α_{eq} term. The Equivalent Adiabaticity is defined as the constant adiabaticity value that would give the same LWP value, when replacing $\alpha(z')$ in Eq. (3b). The equivalent adiabaticity enables the definition of the Fog Conceptual Model LWP, in Eq. (3c).

The Conceptual Model LWP has the same value as Fog LWP, but its LWC(z) profile is different because it uses a constant adiabaticity value. This difference is illustrated in Fig. 1 (a). Fog LWP is the light blue surface, bound by the fog LWC curve with varying adiabaticity with height. Whereas, the Conceptual Model LWP corresponds to the dashed area. Its LWC increases linearly with height because of the constant adiabaticity value. This figure shows that both Fog and the Conceptual Model have the same Surface LWC for a given LWP value. Considering that surface LWC can be linked to visibility, this implies that for a given fog LWP value, the Conceptual Model should predict realistic visibility values at the surface.

In our study, α_{eq} is estimated using a parametrization derived from 7 years of fog observations at the SIRTA observatory (see Sect. 4.2). It is worth mentioning that this parameter is also defined in literature as the in-cloud mixing parameter β (e.g. Betts (1982); Cermak and Bendix (2011)), which is equivalent to α_{eq} and can be easily transformed using the rule $\alpha_{eq} = (1 - \beta)$.

2.2 Critical and Reservoir LWP

Wærsted (2018) found that fog dissipation by lifting of its base is explained by a deficit in LWP considering a given fog thickness. This motivated the definition of a Critical Liquid Water Path (CLWP), which is the minimum amount of LWP needed for a cloud to reach the surface, and reduce horizontal visibility below 1000 meters.

CLWP is formulated from Eq. (3c), assuming a Critical Liquid Water Content LWC_c at the surface. LWC_c is the LWC that would cause a 1000 meters visibility, calculated using the parametrization derived by Gultepe et al. (2006) (appendix B). This parametrization indicates that the LWC_c has a value of $\approx 0.02\ gm^{-3}$.

$$CLWP = \frac{1}{2}\alpha_{eq}\,\Gamma_{ad}(T,P)\,CTH^2 + LWC_c\,CTH \tag{4}$$

When fog is present, its LWP value must be always larger than the CLWP. This property motivates the definition of an additional parameter, the Reservoir Liquid Water Path (RLWP). RLWP is a quantitative metric on how far fog is from dissipation, and is calculated using Eq. (5).

$$RLWP = LWP - CLWP = LWP - \frac{1}{2}\alpha_{eq}\,\Gamma_{ad}(T,P)\,CTH^2 - LWC_c\,CTH \tag{5}$$

The relationship between CLWP and RLWP is illustrated in Fig. 1 (b). In this case, we have a fog with a given cloud top height CTH and a liquid water content LWP, that are associated with a liquid water content LWC_0 at the surface. This LWC is greater than the critical value LWC_c, because visibility is less than 1000 m. The CLWP of this fog, indicated by the red surface to the left, is calculated using Eq. (4). Its value indicates the minimum LWP that fog can have before reducing surface LWC below its critical value, which could cause an increase of visibility above 1000 meters. All excess liquid water above the

(a) Relationship between Fog and Conceptual Model LWC and LWP

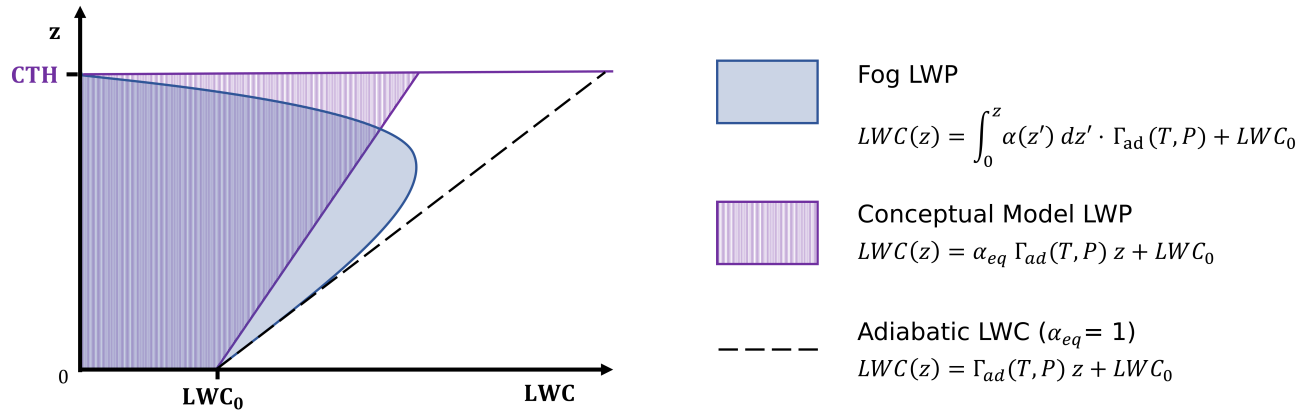

(b) Conceptual Model Critical and Reservoir LWP

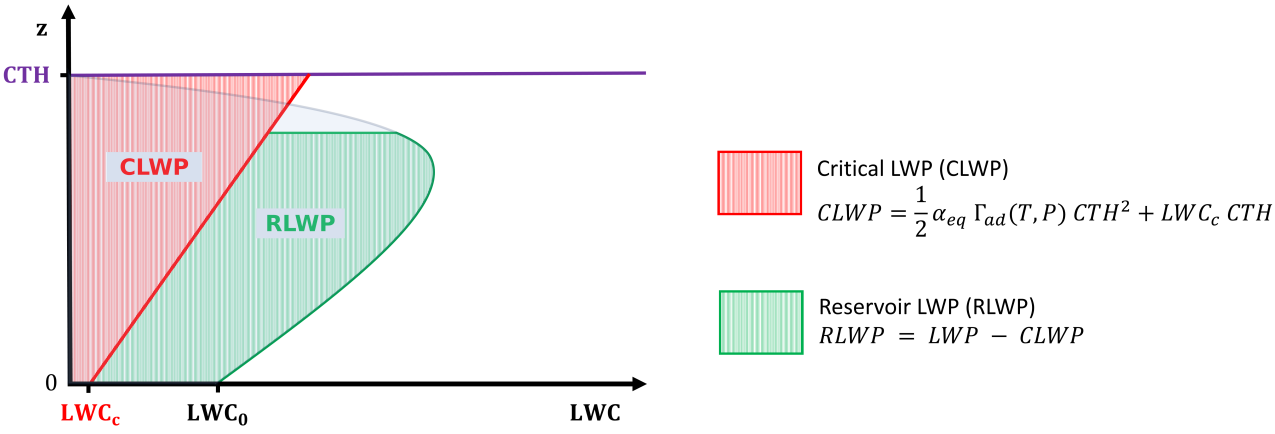

Figure 1. (a) Illustration of the relationship between Fog, Conceptual Model and adiabatic LWC with vs height. In all cases LWC changes with height from its surface value until reaching fog top (CTH). Fog and Conceptual Model LWP have the same value. (b) Representation of the Critical LWP (CLWP) and Reservoir LWP (RLWP) with respect to fog LWP. CLWP is predicted LWP value that fog should have when visibility equals 1000 meters at the surface (with an associated suface LWC defined as LWC_c). RLWP is the difference between fog and the CLWP, and represents the excess water that enables fog persistence.

CLWP value creates the RLWP, indicated by the green surface to the right, and corresponds to all the excess LWP that must be removed before fog can dissipate at the surface.

3 Dataset and Data Treatment Methodology

The dataset used to study the Conceptual Model formulation consists on seven years of fog observations made at the SIRTA atmospheric observatory, from July of 2013 to March of 2020 (Haeffelin et al., 2005). This observatory is located 156 m above sea level, approximately 20 km south of Paris (48°43'N, 2°12'E) in a location with a relatively high fog incidence (about 30 fog events per year).

The observatory data must be treated to transform raw measurements into Conceptual Model variables. Section 3.1 indicates which instruments are used in this study, Sec. 3.2 describes how fog events are detected, and how their formation and dissipation time is identified, and Sec. 3.3 explains the processing of raw observations into Conceptual Model variables.

After data treatment, an additional data quality control stage is performed to remove from the data pool the fog cases with measurements taken under non optimal conditions. The criteria used is explained in Sec. 3.4. A summary of the complete data processing is shown in Fig. 2.

3.1 Observations

The SIRTA observatory is equipped with a large array of instruments, tailored for observing fog and fog processes (Haeffelin et al., 2010; Wærsted, 2018). A subset of these instruments is selected for studying the proposed conceptual model, based on the required inputs. These instruments are listed in Table 1.

Data from three remote sensing instruments is used: a CL31 Ceilometer, a BASTA Cloud Radar and a HATPRO Microwave Radiometer. The CL31 is a widely used instrument for Cloud Base Height (CBH) detection, with a vertical resolution of 15 meters (Kotthaus et al., 2016). In this study it is used to retrieve the CBH of low stratus clouds preceding fog events, and to track CBH lifting during temporary or definitive dissipation of the fog layer.

The Cloud Radar BASTA is a 95 GHz FMCW radar used to retrieve vertical profiles of cloud reflectivity, up to 12 km of height (Delanoë et al., 2016). It operates continuously alternating between 12.5, 25 and 100 m resolution modes every 12 seconds. The 12.5 m mode has the highest vertical resolution and therefore it is used to retrieve fog CTH. Meanwhile, the 100 m mode is the most sensitive and reaches the highest altitude of 12 km, and therefore is used to detect the presence of clouds above the fog layer.

The multi-wavelength microwave radiometer (MWR) HATPRO measures the integrated LWP of the atmospheric column. The manufacturer specified uncertainty of the LWP product is of $\pm$ 20 g m^{-2}, but for relatively small LWP ($<$ 40 g m^{-2}), investigations indicate that the uncertainty is within $\pm$ 5-10 g m^{-2}, at least when the fog forms in clear sky so that a possible time-independent bias can be corrected for (Marke et al., 2016; Wærsted et al., 2017). When no other cloud is present above the fog layer, LWP measured by the MWR will correspond to fog LWP. Thus, MWR and Cloud Radar data can be combined to perform reliable fog LWP retrievals.

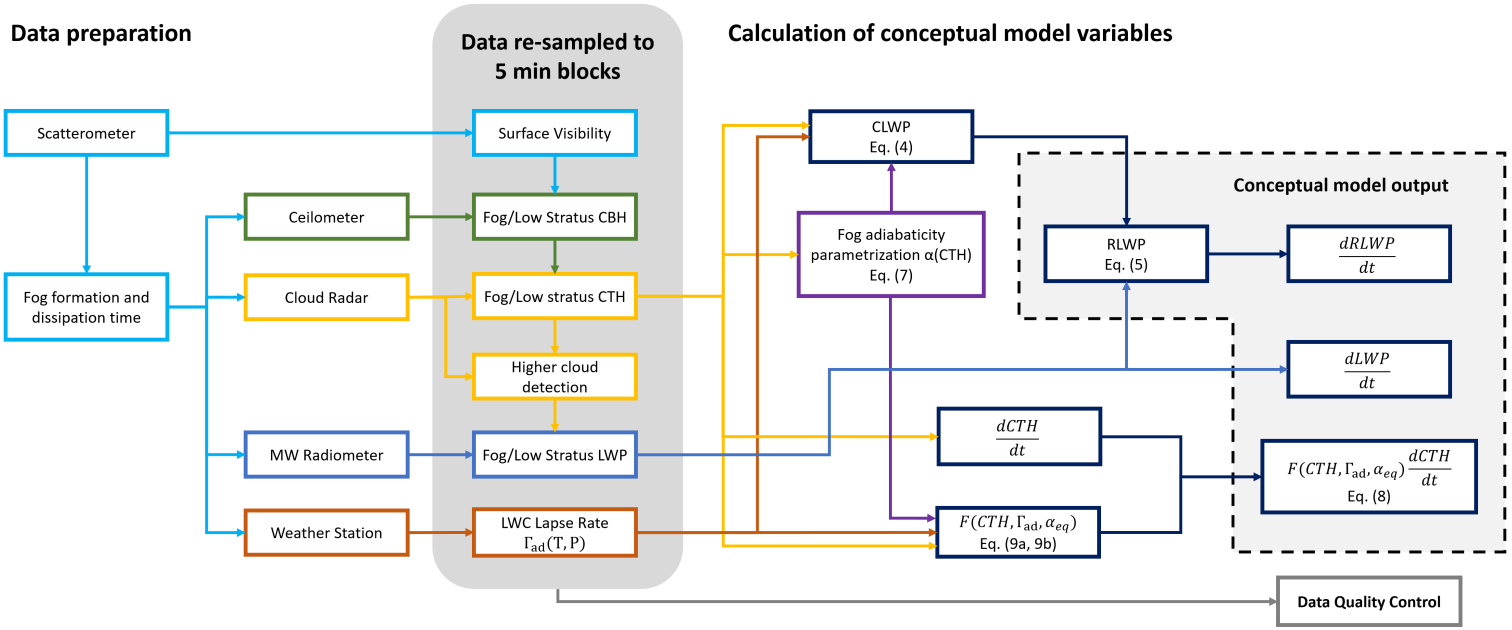

Figure 2. Summary of the data treatment and calculation methodology. The procedure can be separated in three main stages: First, data preparation consists in identifying fog periods from historical visibility measurements, and in gathering raw instrumental information for these periods. Second, data is re-sampled and homogenized into 5 minute time blocks. First order products such as fog CTH, LWP, among others are calculated. Third, the data treated in the second stage is used to calculate conceptual model variables. An additional data quality control stage is included, to check if the variables of each identified period were retrieved under reliable operating conditions of the instruments.

These remote sensing instruments are complemented by a weather station 2 meters above the surface, and two Scatterometers, at 4 and 20 meters above the surface. The weather station provides the thermodynamic data necessary to calculate the saturated adiabatic lapse rate $\Gamma_{ad}(T, P)$, and the 4-m scatterometer provides the visibility data used to detect fog events and to calculate fog LWC at the surface. Visibility data is also used to complement the CL31 CBH estimation for very low cloud layers.

Table 1. List of instruments and measurements used in this study.

Instrument	Measured Quantity	Vertical Range (RA) and Resolution (RE)	Time Res.
905 nm Ceilometer *Vaisala CL31*	Attenuated backscatter (m^{-1} sr^{-1})	RA 0-7600 m, RE 15 m	60 s
14-Ch. Microwave Radiometer *RPG HATPRO*	Liquid Water Path (g m^{-2})	Integrated column	60 s
95 GHz FMCW Cloud Radar *BASTA*	Radar Equivalent Reflectivity (dBZ)	RA 85-6000 m, RE 12.5 m RA 100-12000 m, RE 100 m	12 s 12 s
550 nm Scatterometer *Degreane DF320/DF20+*	Visibility (m)	4 m above ground 20 m above ground	60 s 60 s
Thermometer *Guilcor PT100*	Air Temperature (K)	2 m above ground	60 s
Barometer *Druck RPT410F*	Surface Pressure (Pa)	2 m above ground	60 s

3.2 Fog event detection

Fog periods are identified using a scheme based on previous work done by Tardif and Rasmussen (2007); Wærsted et al. (2019). This method requires the re-sampling of the surface visibility time series to 5 minute blocks. Each 5 min block is assigned a "fog" or "clear" value, depending on the distribution of visibility in its time period. A block is assigned the "fog" value when more than half of the visibility measurements are less than 1000 m, and is assigned "clear" otherwise.

After asigning values to each block of the complete visibility time series, we analyze groups of five consecutive blocks in a sliding manner. These five contiguous blocks are defined as a construct, and its value is positive when the central and at least two other are fog blocks, and negative otherwise.

A fog event forms when a positive construct is encountered, with a formation time defined as the central time of the first fog block in the construct. Conversely, a fog event dissipates when the last positive construct is followed by either a negative construct or three consecutive clear blocks. Fog dissipation time is set as the central time of the block immediately after the last fog block in the last positive construct. Fog events separated by less than 1 hr are merged, and all fog events lasting less than 1 hr are discarded. This algorithm provides the formation and dissipation time of 217 fog events between July 2013 and

March 2020. It's worth noting that this method, based on visibility measurements only, does not classify the fog type. Hence, all fog types are considered in this study.

3.3 Data processing

After identifying the fog events, it is necessary to process raw measurements from the instruments into information that can be used by the conceptual model. To study the conceptual model variables during fog events, and the time period surrounding them, observational data is automatically processed and re-sampled to 5 min time blocks, covering the period from 3 hours before fog formation to 3 hours after fog dissipation.

CBH is retrieved using a threshold value of $2{\cdot}10^{-4}$ $\mathrm{m}^{-1}\mathrm{sr}^{-1}$ on the CL31 attenuated backscatter measurements, following the method of Haeffelin et al. (2016). When the liquid layer is closer than 15 m to the ground, the CL31 cannot identify the CBH anymore and therefore the Scatterometer measurements are checked, setting the CBH as 0 m when visibility drops below 1000 m. Both CBH and visibility measurements are averaged to five minute time blocks, matching the blocks used by the fog detection algorithm.

The Cloud Radar is used to retrieve fog CTH and to detect the presence of higher clouds above the fog layer, based on its vertical reflectivity profile (Wærsted et al., 2019). To retrieve CTH, reflectivity signals in each radar gate are analyzed, starting from the gate closest to the CBH and checking one gate at a time, going upwards. CTH is estimated as the height of the gate under the first gate where no cloud signal is detected. A gate is considered to have a valid cloud signal if more than half of the reflectivity samples in a five minute time block are not removed by the automatic noise filtering algorithm of the radar (Delanoë et al., 2016). As with CBH, time blocks used in CTH retrievals match those defined for fog detection.

A limitation of this method is that the minimum detectable CTH is of 85 meters. Under this height, radar interference becomes very significant, making the differentiation between a valid cloud signal and noise very difficult. In this situation the CTH retrieval is not possible, and therefore the associated time block would not have a valid CTH value.

Radar data is also used to create a flag indicating the possible presence of liquid clouds above the fog layer when another valid signal is observed above fog CTH, within the first kilometer for the 12.5 m resolution mode, or within the first 6000 m for the 100 m resolution mode. This flag is used in LWP retrievals, as explained below.

The HATPRO Microwave Radiometer performs LWP retrievals of fog every 60 s, which are then averaged and re-sampled to the 5 min time block grid. Additionally, when a given time block has an associated flag indicating the possible presence of higher liquid clouds, the LWP sample is declared not valid. This is done to ensure that the LWP samples are reliable, by avoiding a possible fog LWP overestimation when liquid clouds are present.

Time series of surface temperature and pressure are all averaged to match the 5 minute time blocks. The saturated adiabatic lapse rate $\Gamma_{ad}(T, P)$ is calculated for each of these time blocks using these measurements and the equations in appendix A.

In this scheme, it is important to note that to have a valid sample of conceptual model variables in a given 5 min time block, the block must have valid measurements of fog CTH, LWP, surface visibility, and surface temperature and pressure. Therefore, it is possible to have fog cases without valid samples of conceptual model variables for some time periods. We decided to use

these cases (if they comply with the data quality control of Sect. 3.4), and to consider all the samples with valid conceptual model calculations for the statistical analyses.

3.4 Data quality control

After data treatment is complete for all automatically detected fog events, a manual check is done to remove cases where data is unreliable. This happens when instruments operate under non optimal conditions, or when the upper liquid cloud flagging algorithm did not work correctly.

This control consist on accepting or removing complete fog cases and their associated dataset. A fog case is removed from the data pool if measurements taken when the fog takes place comply with at least one of the following criteria:

1. Data is taken during or after strong precipitation: Strong precipitation wet the Microwave Radiometer radome, leading to unreliable LWP retrievals for an unpredictable period of time that can last up to hours, even when following all maintenance instructions (Görsdorf et al., 2020). Additionally, strong rain leads to difficulties in identifying the fog CTH because the strong reflectivity from rain hides the weaker returns from suspended fog droplets.

2. There are no valid data blocks: No CTH or LWP retrievals could be made for the given fog event. This can happen when fog is thinner than 85 meters, or when liquid clouds are present above fog for the complete event duration.

3. Fog and Cloud borders are not well identified: In some cases the automatic cloud border detection algorithm fails, leading to unfiltered LWP retrievals with liquid clouds above, or to a bad estimation of fog CTH when upper clouds are too close to the fog layer. The latter can be seen in the radar data as multilayer fog formed by the union of two previously independent cloud layers. This situation departs from the single well mixed layer assumption, and therefore the conceptual model is not applicable.

The quicklooks for the accepted and rejected fog cases are available in the article supplementary material. After this stage we end with 80 valid fog cases and 137 rejected cases, where 50 were removed because of criterion 1, 69 because of criterion 2 and 18 because of criterion 3. These 80 valid fog cases have at least one valid sample of conceptual model variables (see Sect. 3.3), which are then used in the next stages of data analysis and results.

4 Data Analysis and Results

4.1 Fog Adiabaticity

A key parameter in the calculation of the CLWP is the Equivalent Fog adiabaticity α_{eq} (Eq. (4)). This parameter has been previously studied in literature for boundary layer stratocumulus and stratus clouds, where typically observed values of α_{eq} range between 0.6 and 0.9 (Slingo et al., 1982; Boers et al., 1990; Boers and Mitchell, 1994; Braun et al., 2018). In this situation, clouds have an adiabatic profile and are buoyant (Betts, 1982). Buoyancy is important because it is necessary to have dissipation by lifting of the fog base.

Hence, it is interesting to study whether these adiabaticity values also apply to fog, which is a special cloud case with a solid lower boundary at the surface. Therefore, we use the complete database to calculate α_{eq} by closure, with Eq. (6). This equation is an inversion of the conceptual model formulation of Eq. (3c), and enables an estimation of the adiabaticity while correcting the impact of the LWC accumulation at the fog base. We only perform α_{eq} retrievals when visibility is below 2000 m, in order to remain close to fog conditions.

$$\alpha_{eq}^{closure} = \frac{2(LWP - LWC_0\, CTH)}{\Gamma_{ad}(T,P)\, CTH^2} \tag{6}$$

Figure 3 (a) shows the resulting equivalent adiabaticity $\alpha_{eq}^{closure}$ versus CTH and LWP. The results indicate that $\alpha_{eq}^{closure}$ increases for greater values of LWP and CTH. In addition, negative adiabaticity values are found for lower LWP values, specially below 30 g m^{-2}.

To study this behavior in more detail, Figure 3 (b) shows a boxplot with the statistics of $\alpha_{eq}^{closure}$ for different LWP ranges. Here we observe that negative adiabaticity values become frequent when the LWP is below the 30-40 g m^{-2} range, until occuring for more than half of the samples when the LWP is below 20 g m^{-2}.

This can be explained by considering that fog with LWP less than 30 g m^{-2} is not optically thick (Wærsted et al., 2017). Under this condition, the liquid water condensation happens everywhere in the liquid layer, but it is mostly driven by surface cooling. This process is associated with stable atmospheric conditions, where vertical mixing is almost neglibile (Zhou and Ferrier, 2008). Under this regime, the LWC will be distributed according to the cooling and condensation rate at each height, and therefore it is possible to have situations where surface LWC is greater than LWC values above, especially during radiation fog formation. This situation would lead to the observed negative α_{eq} values.

When fog LWP surpasses the 30-40 g m^{-2} range, its adiabaticity converges to 0.7, which, as stated in the previous lines, is a value consistent with a value consistent with typical observations of boundary layer stratocumulus (Slingo et al., 1982; Boers et al., 1990; Boers and Mitchell, 1994; Cermak and Bendix, 2011; Braun et al., 2018). This can be explained because fog gradually becomes opaque to infrared radiation when its LWP surpasses 30 g m^{-2}(Wærsted et al., 2017). In this scenario, LWC generation is mostly driven by radiative cooling at the fog top. This radiative cooling induces a temperature gradient between the fog top and the surface, leading to convective motions. An increase in the intensity of convection will be correlated with an increase in fog CTH, because the additional energy would enhance boundary layer development. Then, as fog becomes deeper, it is expected that the relatively stronger convective motions associated would drive the vertical liquid water mixing closer to what is observed in boundary layer clouds. This result and theory also indicate that dissipation by base lifting should happen when the LWP is at or above the 30-40 g m^{-2} range, when the layer is adiabatic and buoyant.

Finally, we can also observe that adiabaticity sometimes reaches values slightly greater than 1, which can be associated with periods when fog is superadiabatic. This is possibly caused by an excess of liquid water with respect to the extent of the fog column, which may be caused by the surface presence, as introduced in Sect. 2.

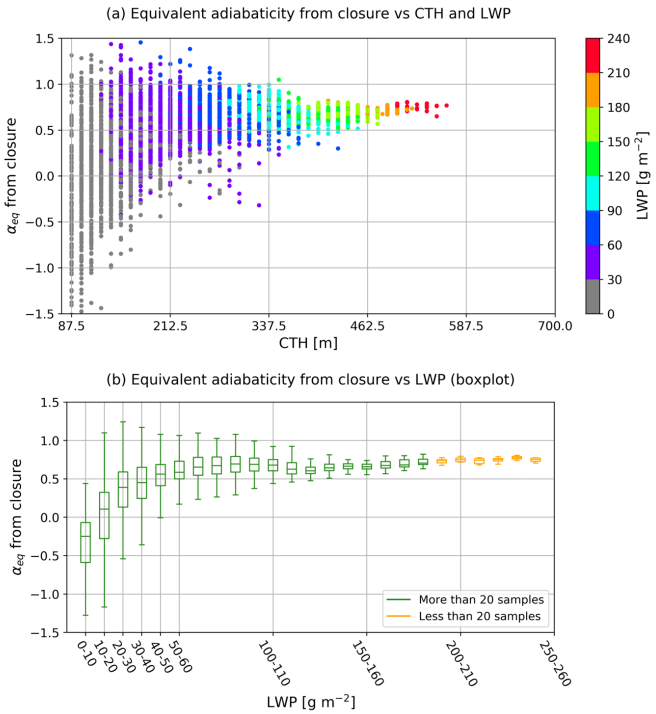

Figure 3. (a) Equivalent adiabaticity versus fog CTH and LWP. The equivalent adiabaticity is calculated by closure, using Eq. (6). (b) Boxplot of the equivalent adiabaticity, calculated by closure, for different LWP ranges. In both figures only samples with visibility below 2000 m are considered.

4.2 Adiabaticity parametrization as a function of CTH

The strong correlation between adiabaticity and CTH observed in Fig. 3 (a) suggests that α_{eq} can be parametrized as a function of CTH. The parametrization curve is calculated by minimizing the error of the model presented in Eq. (7) with respect to the median α_{eq} value at each radar range bin (see Fig. 4). To reduce uncertainty due to lack of data, only bins with more than 20 valid samples are used.

$$\alpha_{eq}(CTH) = \alpha_0 \left(1 - e^{-\frac{CTH - H_0}{L}}\right) \tag{7}$$

The retrieved value for each coefficient are $\alpha_0 = 0.65$, $H_0 = 104.3$ m and $L = 48.3$ m. These parameters come from fog statistical behavior, and can be interpreted as follows: α_0 is the equivalent adiabaticity value that fog reaches when it has completely transitioned into an adiabatic regime. H_0 is the usual height at which LWC starts to increase with height. L indicates, based on adiabaticity, that the transition from stable to adiabatic fog is possible when CTH reaches 150 meters, and very likely when CTH is above 250 meters ($H_0 + L$ and $H_0 + 3L$ respectively).

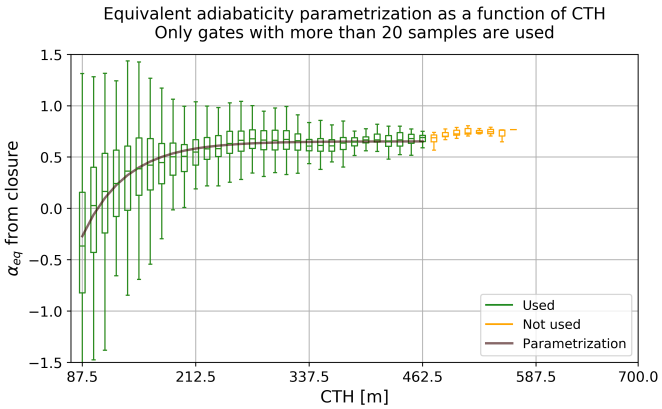

Figure 4. Boxplot with the distribution of equivalent adiabaticity for each radar CTH bin, with the derived parametrization superimposed (Eq. (7)). Equivalent adiabaticity is calculated by closure using Eq. (6). Only samples with visibility below 2000 m are considered.

In principle, the adiabaticity parametrization is valid for CTH values below 462.5 m, where the parametrization is derived. Beyond this height there is not enough data to guarantee its reliability; however it is likely that adiabaticity should remain close to the convergence value of 0.66 based on our observations and on what has been previously published in literature (Slingo et al., 1982; Boers et al., 1990; Boers and Mitchell, 1994; Cermak and Bendix, 2011; Braun et al., 2018).

4.3 Conceptual model validation

In this section we study fog statistical data to study how it behaves with respect to the conceptual model. Figure 5 (a) shows all CTH, LWP and surface LWC measurements taken when fog is present (visibility less than 1000 m). Data is separated in different temperature ranges. Modeled LWP and CLWP curves are shown. LWP and CLWP theoretical curves are calculated using Eqs. (3c) and (4) respectively, with the $\alpha_{eq}(CTH)$ parametrization derived in Sec. 4.2. Each hexagon color is given by the mean LWC_0, calculated using all the data in their respective CTH+LWP space. Hexagons with less than 5 samples within their surface are removed, since they are likely to be associated with non replicable, noisy data.

This figure shows a good agreement between the theoretical curves and observed results. Most LWP samples are higher than the critical value, as the model predicts when visibility is less than 1000 meters. Additionally, it can be seen that for a fixed CTH, LWP increases with LWC_0. This behavior seems to be well captured in the current Conceptual Model formulation, as the difference between the three lines shows (each theoretical LWP line has a different LWC_0 value, indicated in the legend).

Figure 5 (b) shows data samples taken when visibility is between 1000 and 2000 meters, as an scatterplot. As in Sec. 4.1, the 2000 m superior limit to visibility is selected, to remain close to fog conditions where the conceptual model is valid. LWP of these data samples should be less than the CLWP line for these visibility values, however we observe that sometimes they can also be larger. This can be explained by two main reasons: CLWP is calculated for a single temperature while data temperature varies within a range, and because of instrumental uncertainties. HATPRO LWP uncertainty is around 10 g m^{-2}, while radar CTH retrieval has a resolution of 12.5 m. This uncertainty is present in this retrieved data, and is also likely to be propagated

inside the $\alpha_{eq}(CTH)$ parametrization, introducing some variability in the results. However this is not deemed critical, since variability around the CLWP line is smaller than 10 g m^{-2}, and because the fog life cycle studies of Sec. 5) verify that LWP is lower than the critical value before fog formation and after fog dissipation.

Finally, we perform an evaluation on how well the Conceptual Model predicts fog LWP, based on CTH, Temperature, Pressure and surface LWC inputs. These variables are used to calculate the Conceptual Model LWP with Eq. (3c), with the $\alpha_{eq}(CTH)$ parametrization of Sec. 4.2, and compared against HATPRO LWP retrievals. Results are shown in Fig. 6. Here we can see that most samples are close to the 1-1 line for LWP values less than approximately 190 g m^{-2}. Beyond this LWP value some deviation appears, however there is not enough data available to verify if this is a systematic error of the model or on how data was taken. Despite this deviation, the good agreement between modeled and observed LWP can be seen in the linear fit, with a slope equal to 1, and in the RMSE of just 10.5 g m^{-2}, which is very close to the LWP retrieval uncertainty.

4.4 Drivers of RLWP temporal variations

Equation (5), indicates that changes in both LWP and CTH can contribute to RLWP depletion, and therefore to fog dissipation. To quantify the relative impact of LWP and CTH changes in RLWP, we calculate the time derivative of Eq. (5). By assuming constant temperature and pressure, and using the $\alpha(CTH)$ parametrization of Sec. 4.2, we obtain Eq. (8).

This equation shows that RLWP changes are proportional to LWP variations, and to CTH variations weighted by the function $F(CTH, \Gamma_{ad}, \alpha_{eq})$. This function, written explicitly in Eqs. (9a) and (9b), converts CTH variations into g m^{-2} units, and thus enables a comparison between both effects.

$$\frac{dRLWP}{dt} = \frac{dLWP}{dt} - F(CTH, \Gamma_{ad}, \alpha_{eq}) \frac{dCTH}{dt} \tag{8}$$

$$F(CTH, \Gamma_{ad}, \alpha_{eq}) = \frac{1}{2} \frac{\partial \alpha_{eq}(CTH)}{\partial\, CTH}\, \Gamma_{ad}(T,P)\, CTH^2 + \alpha_{eq}(CTH)\, \Gamma_{ad}(T,P)\, CTH + LWC_c \tag{9a}$$

$$\frac{\partial \alpha_{eq}(CTH)}{\partial\, CTH} = \frac{\alpha_0}{L} e^{-\frac{CTH - H_0}{L}} \tag{9b}$$

Equation (8) implies that RLWP depletion, and thus fog dissipation, can occur by LWP reduction and/or by CTH growth. It also indicates that it is possible to have compensating effects enhancing fog persistence, for example fog that is reducing its LWP could persist if its CTH is also decreasing (which can happen under strong subsidence). Another implication is that it is possible to have fog dissipation even if LWP is increasing quickly, through a fast increase in CTH. The case studies of Sec. 5.1 show how useful this separation between LWP and CTH effects can be, by analyzing some examples of the previously mentioned scenarios. Section 5.2.3 shows statistical results of fog RLWP, LWP and CTH time derivatives just before dissipation.

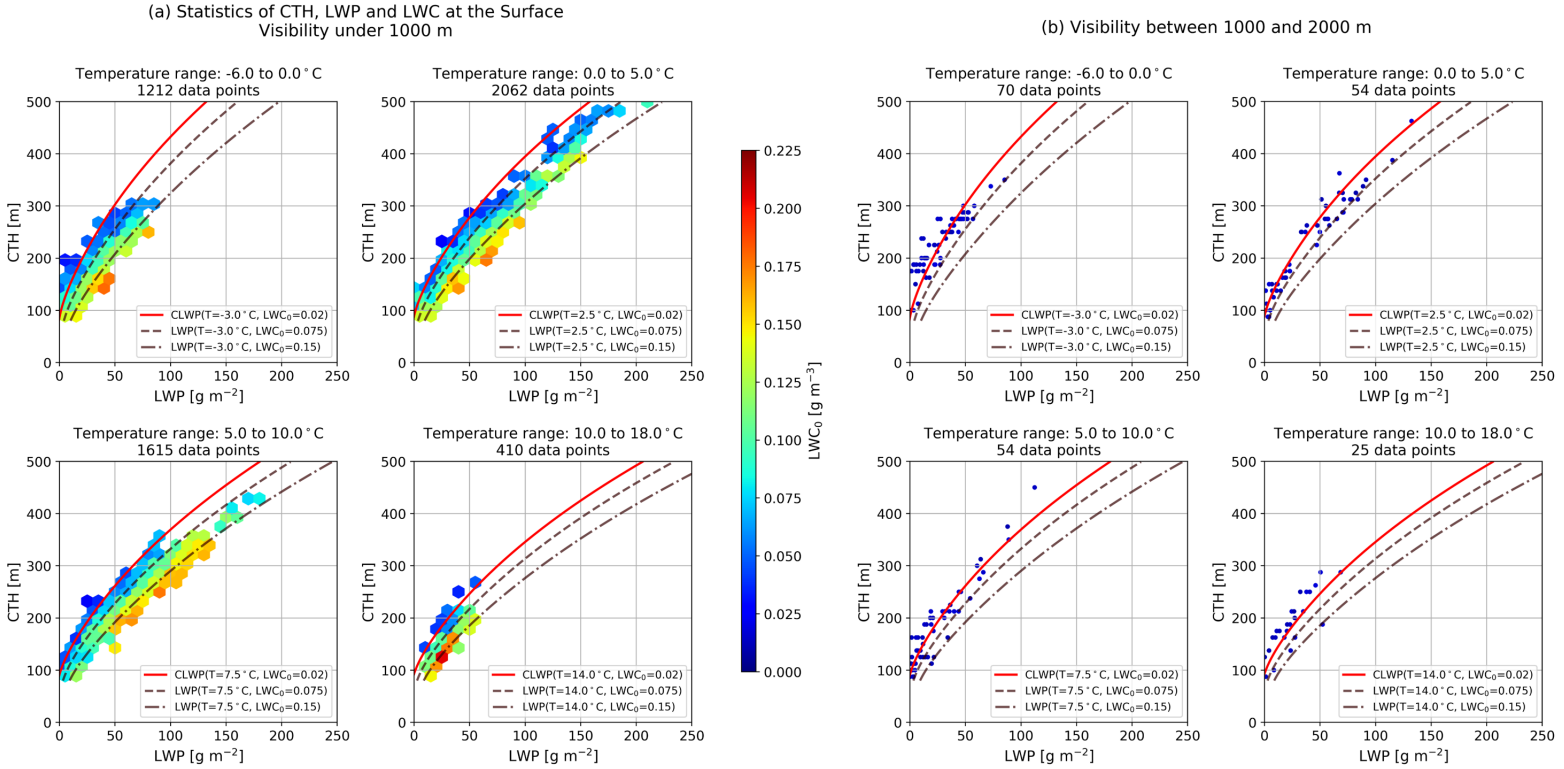

Figure 5. Observations of CTH, LWP and LWC at the surface for different temperature and visibility ranges. Data associated with visibility values below 1000 m is to the left (title (a)), while data measured with visibility values between 1000 and 2000 m is to the right (title (b)). Conceptual model theoretical LWP and CLWP lines for different conditions, indicated in the legend, are superimposed. The adiabaticity values used in the conceptual model calculation are calculated using the adiabaticity parametrization of Sec. 4.2.

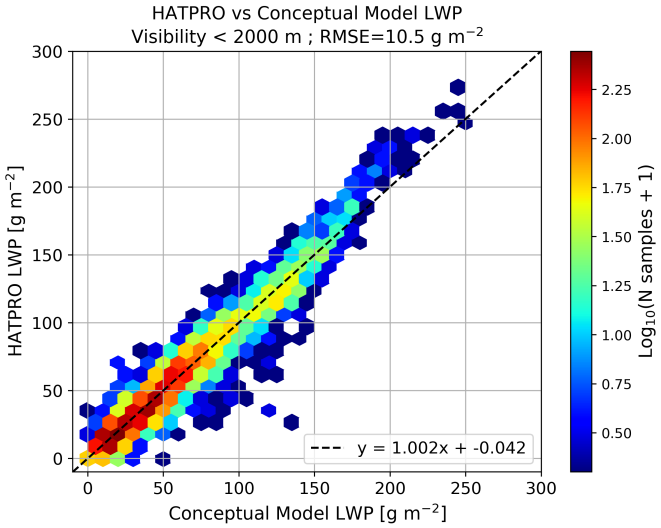

Figure 6. 2D histogram comparing HATPRO and Conceptual Model LWP values, for data retrieved when visibility is less than 2000 m. Conceptual model LWP is calculated using fog CTH, fog LWC at the surface derived from visibility, surface temperature, surface pressure and the adiabaticity parametrization of Eq. (7). Under these conditions, the conceptual model predicts LWP with an RMSE of 10.5 g m^{-2} and an almost perfect linear relationship.

5 Fog life cycle

5.1 Case studies

We present 3 case studies to illustrate the behavior and role of changes in LWP and CTH on presence of fog at the surface during the fog life cycle (Figs. 7, 8 and 9). For each case we provide a 5-panel figure that illustrates the time series of fog/stratus layer boundaries, reflectivity profile, 4-m and 20-m horizontal visibilities, the fog/stratus layer measured LWP and computed RLWP, temperature and closure adiabaticity; and the change rate of RLWP, with the individual contributions from LWP and CTH variations.

In all three cases, we observe that fog is present at the ground (4-m height visibility < 1 km) when the RLWP is greater than 0 g m^{-2}. RLWP changes at a rate of +/-10 g m^{-2} h^{-1}, with values reaching + or – 30 g m^{-2} h^{-1} at times. The LWP estimation of all case studies is done directly using the HATPRO, verifying that the radar does not detect signals from liquid clouds below 6 km of height.

Case study 1 (Fig. 7): Radiative fog occurring during fall season (31 October 2015) that forms six hours before sunrise and dissipates about three hours after sunrise at 10:25 UTC. The fog layer is about 200 m thick during the entire fog life cycle with a water content of 30-60 g m^{-2}. This LWP range and the adiabaticity values close to 0.6 indicates that fog is optically thick and can be considered as a well-mixed layer for most of its duration. The RLWP is not large, mostly near + 10 g m^{-2}, with a maximum value of 30 g m^{-2} observed 2-3 hours before sunrise. CTH changes are relatively slow during the entire fog life

cycle, with values less than 50 m h^{-1}. From 03 to 05 UTC, the CTH increases which acts as RLWP depletion of nearly -20 g m^{-2} h^{-1}, while at the same time the LWP increases with a rate reaching +50 g m^{-2} h^{-1} resulting in a net increase of RLWP. After 05 UTC, the trends in CTH and LWP reverse. The CTH subsides slowly (about -20 m h^{-1}) contributing positively on the RLWP at a rate of nearly +5-10 g m^{-2} h^{-1}, while the LWP initiates a progressive and nearly monotonous decrease of -10 g m^{-2} h^{-1} that brings the RLWP to 0 g m^{-2} at 09 UTC. The progressive drying of the fog layer is also identifiable in the closure adiabaticity value, which starts to decrease just after sunrise. After 09 UTC, the near-surface visibility initiates a rapid increase, exceeding 1 km at 10:25 UTC, time at which the entire fog layer is dissipated. The complete layer dissipation and the increasing temperature makes it highly unlikely that fog will re-form in the coming hours. Note on Fig. 7 (f) that LWP and CTH contributions to RLWP are nearly always of opposite signs, but not equal in magnitude.

Case study 2 (Fig. 8): Another radiative fog that occurs in the fall season, just a few days apart from case study 1 (26 October 2015). It forms just three hours before sunrise and dissipates about 3.5 hours after sunrise at 10:55 UTC. The fog layer is about 200 m thick during the mature phase of the fog life cycle and nearly doubles between sunrise and time of dissipation, while the water content remains above 50 g m^{-2}. After fog formation, RLWP reaches 30 g m^{-2} in about one hour and remains at this level for about 2 hours. Fog adiabaticity indicates that after the first hour from formation fog remains in a well mixed state. Around sunrise, RLWP initiates a nearly monotonous decreasing trend of -10 g m^{-2} h^{-1} that will last until fog dissipation. The negative RLWP rate is driven by the rise of CTH that contribute negatively on RLWP with a rate that exceeds -20 g m^{-2} h^{-1} only partially compensated by +20 g m^{-2} h^{-1} LWP increase rates. Oscillations in LWP and CTH contributions to RLWP are clearly visible in Fig. 8 (f). When there is strong cooling at the fog layer top, LWP and vertical circulation increase. This in turn increases the mixing with the layer above fog, resulting in a CTH increase. On the contrary, processes associated with CTH subsidence tend to decrease LWP rates (Wærsted, 2018). In this case study, the depletion of RLWP is clearly driven by the CTH increase and the fog LWP still exceeds 75 g m^{-2} at the time of dissipation.

Case study 3 (Fig. 9): Here we have a typical case of a very low stratus cloud layer with CTH near 250 m agl and an LWP that ranges 25-50 g m^{-2}. This combination leads to a negative RLWP that is insufficient for the stratus to deepen all the way to the surface. As expected for low stratus clouds, the value of closure adiabaticity is close to 0.6 for all valid samples (when visibility is less than 2000 m, to have valid conceptual model conditions with positive LWC at the surface). The stratus is present from 18:00 UTC onwards during twelve hours with a near-surface visibility of about 2-3 km. From 18 until 23 UTC, RLWP is clearly negative changing frequently from negative to positive rates of change (about +/- 5 g m^{-2} h^{-1}) as the contributions of LWP and CTH changes oscillate from positive to negative values (as also seen in Case 3). At 01 UTC, the stratus reaches a new equilibrium with an LWP hovering around 50 g m^{-2}, which brings the RLWP very close to 0 g m^{-2}. The fog CBH is then below 20 agl, as evidenced by the visibility values measured at 20 m agl (Fig. 9 (c)). Between 04:30 and 06:30 UTC, the RLWP becomes again negative and the stratus base lifts. A strong increase in LWP (+40 g m^{-2} h^{-1}) starting after 06:00 UTC leads to a positive RLWP after 06:30 UTC and the stratus layers deepens all the way to the surface. The trend in LWP reverses around 08 UTC (-20 g m^{-2} h^{-1}) while the CTH remains mostly constant hence reducing the RLWP towards 0 g m^{-2} before 10 UTC. This case study shows that the RLWP is also a good indicator of the possibility for a very low stratus layer to deepen into fog and then reversely for the fog to lift into a low stratus.

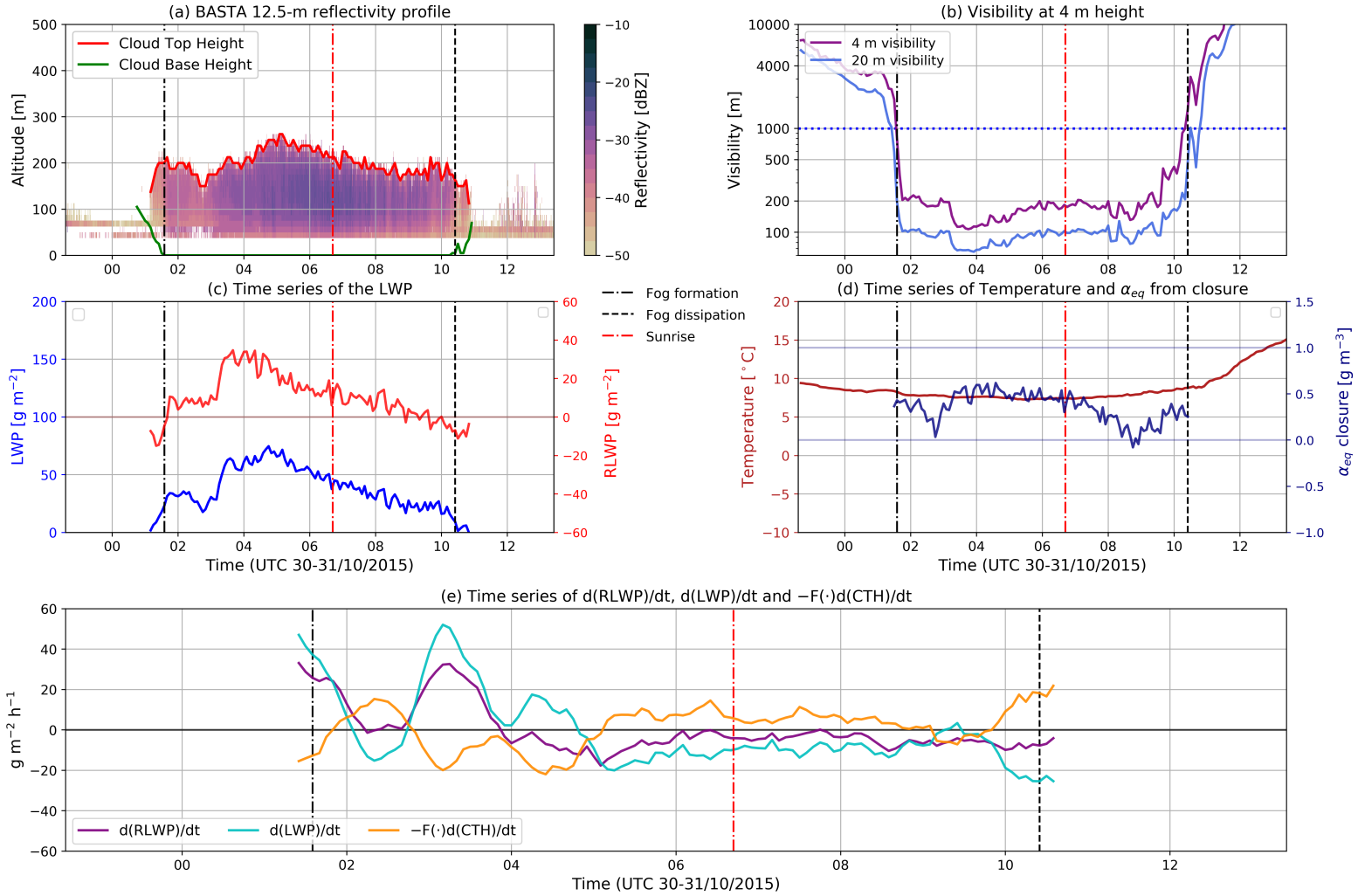

Figure 7. Case study 1. (a) Cloud Base Height (CBH), Cloud Top Height (CTH), and the cloud radar 12.5 m resolution reflectivity profile for the first 1000 m of height. (b) 4-m and 20-m horizontal visibilities. (c) Fog/Stratus layer measured LWP and computed RLWP. (d) Temperature and closure adiabaticity (calculated only when visibility is less than 2000 m). (e) Change rate of RLWP, with the individual contributions from LWP and CTH variations. In each panel, the time of fog formation and fog dissipation are clearly marked as well as the time of sunrise.

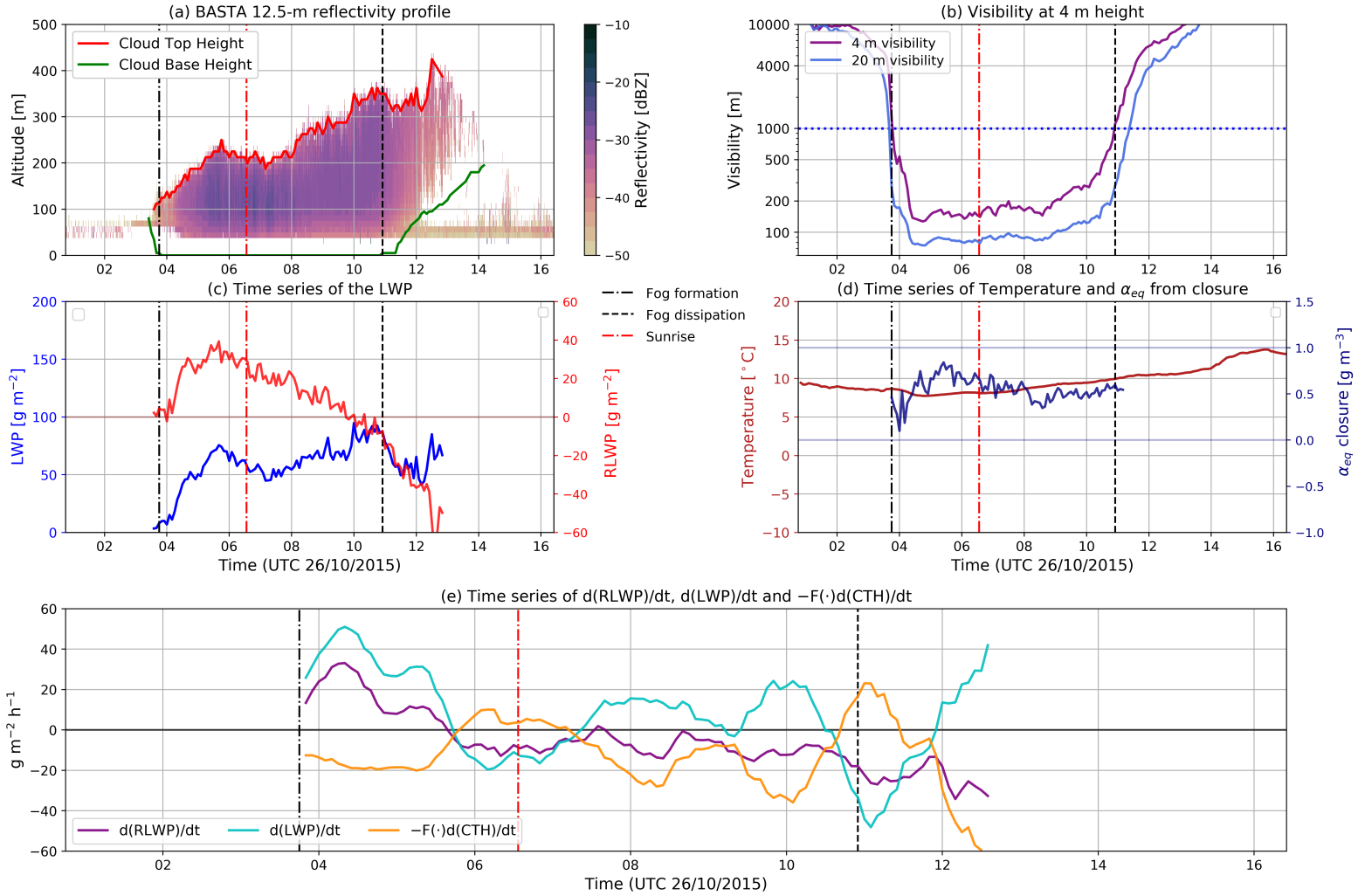

Figure 8. Case study 2. (a) Cloud Base Height (CBH), Cloud Top Height (CTH), and the cloud radar 12.5 m resolution reflectivity profile for the first 1000 m of height. (b) 4-m and 20-m horizontal visibilities. (c) Fog/Stratus layer measured LWP and computed RLWP. (d) Temperature and closure adiabaticity (calculated only when visibility is less than 2000 m). (e) Change rate of RLWP, with the individual contributions from LWP and CTH variations. In each panel, the time of fog formation and fog dissipation are clearly marked as well as the time of sunrise.

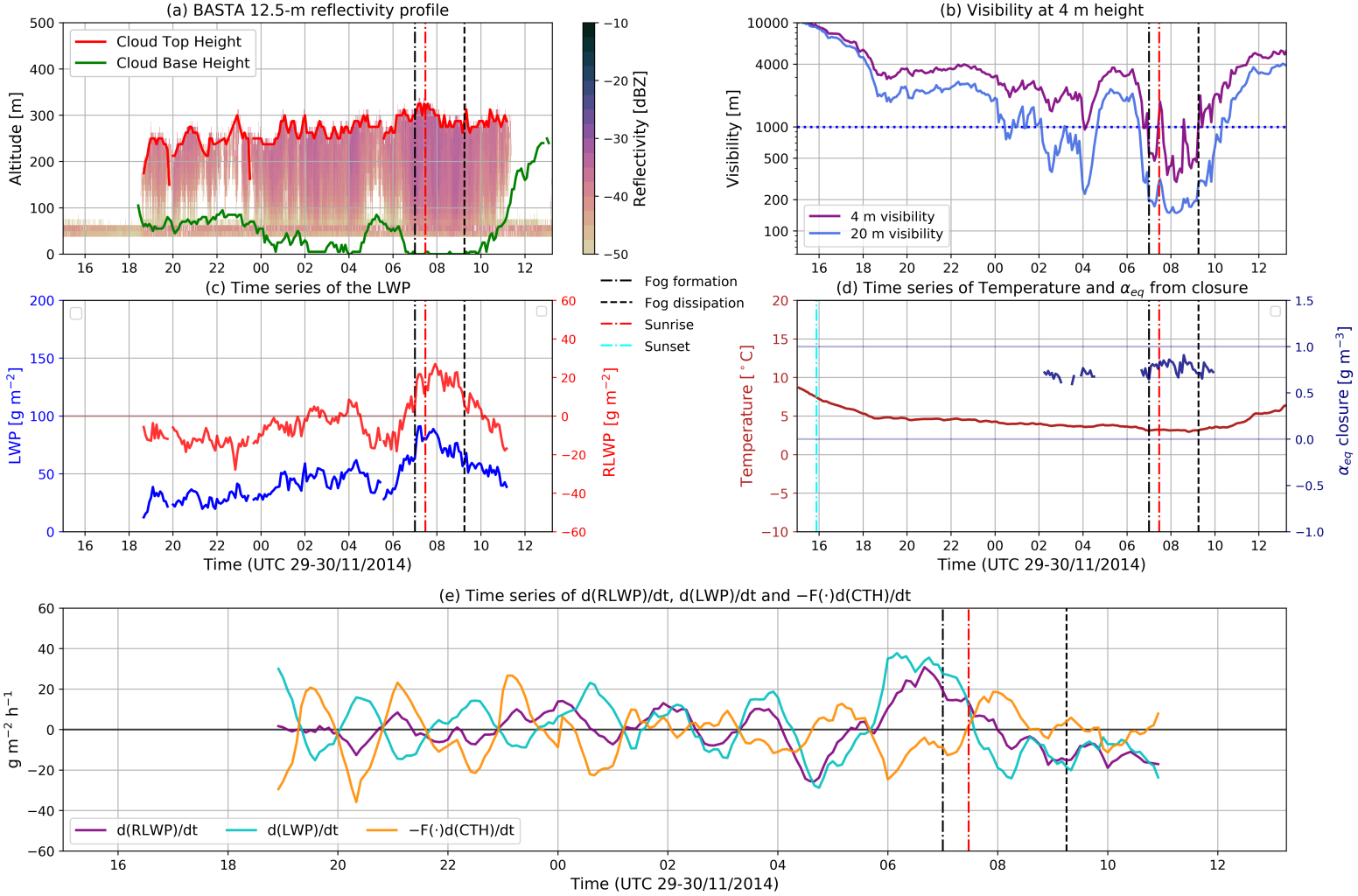

Figure 9. Case study 3. (a) Cloud Base Height (CBH), Cloud Top Height (CTH), and the cloud radar 12.5 m resolution reflectivity profile for the first 1000 m of height. (b) 4-m and 20-m horizontal visibilities. (c) Fog/Stratus layer measured LWP and computed RLWP. (d) Temperature and closure adiabaticity (calculated only when visibility is less than 2000 m). (e) Change rate of RLWP, with the individual contributions from LWP and CTH variations. In each panel, the time of fog formation and fog dissipation are clearly marked as well as the time of sunrise.

5.2 Fog life cycle statistics

Taking advantage of our large database, we study the behavior of fog RLWP and its time derivative dRLWP/dt statistically, for three different periods: fog formation, mature stage and dissipation. The objective is to identify patterns that these fog variables follow at each stage. This could lead to the development of new indicators to enhance the capabilities of fog forecasting models.

Fog formation statistics are taken between 90 minutes before and 90 minutes after the time block were fog formation is identified from visibility measurements (Sec. 3.2). Likewise, for the dissipation period the analyzed data is taken from 90 minutes before to 90 minutes after the dissipation time block. All remaining blocks between 90 minutes after fog formation, and 90 minutes before fog dissipation, are considered to be fog middle life data. Because of how the fog stages are defined, the cases included in this statistical analysis must have a duration of at least 3 hours. This is valid for 56 cases, which are used for statistical analysis in the following sections.

The time derivative of the RLWP (and the sliding mean used in Fig. 10 (b.2)) is estimated by calculating the slope of a linear fit on RLWP data within $\pm$ 30 minutes of a given time block. The retrieved slope value is declared valid only if at least 75% of the RLWP samples used in its calculation are valid.

5.2.1 Fog formation

Figure 10 (a.1) shows the statistical behavior of RLWP between 90 minutes before and 90 minutes after for formation. It can be seen that at fog formation there is a transition from negative to positive RLWP values. The relatively lower amount of samples before -35 minutes from fog formation happen because there are less fog cases were the cloud has formed that early, or that have an identifiable CTH above 85 meters. Yet, we can see that RLWP cannot be significantly lower than -10 g m^{-2} if fog will form within 30 minutes.

Additionally, in Fig. 10 (a.2) we can see that dRLWP/dt becomes positive about one hour before formation, and remains consistently positive for another hour after formation. This first hour after fog formation is when fog reservoir grows the most, reaching a change rate of 10 to 25 g m^{-2} h^{-1}, and it may be critical in establishing fog persistence for the coming hours. After this first hour, fog RLWP stabilizes around 10 to 20 g m^{-2} and the increase per hour is reduced until entering the mature stage.

All 56 fog cases lasting more than 3 hours are considered for the statistics. However, since radiation fog is formed from a shallow layer close to the surface, these cases usually do not provide valid data points because their CTH cannot be retrieved with the radar (it can only observe CTH values above 85 m). Therefore, most of the data points before and around formation time are contributed by stratus lowering fog events.

5.2.2 Fog mature stage

A histogram with RLWP values is shown in Fig. 10 (b.1). We can see that approximately 90% of the time fog has a positive RLWP value, with a median value of 20.1 g m^{-2} and reaching up to 60 g m^{-2}. Negative RLWP values in fog mature stage are explained by short-term temporary lifting of fog from the surface, most likely caused by RLWP oscilations.

Figure 10 (b.2) shows the statistics of dRLWP/dt versus the sliding mean value of RLWP. This figure shows that RLWP and its time derivative are not correlated, and that most of the time dRLWP/dt remains within $\pm$ 20 g m^{-2} h^{-1}. The very low median value of dRLWP/dt = -0.2 g m^{-2} h^{-1} shows that fog does not have a clear tendency of RLWP increase or decrease in the long term. Thus, during this stage of fog life cycle, RLWP remains positive most of the time, with variations driven by oscillations in the value of dRLWP/dt.

The statistics for this period defined as fog mature stage are derived using the 56 fog events lasting more than 3 hours. In the fog mature stage several radiation fog cases will be developed beyond 85 m of CTH, and therefore both stratus lowering and radiation fog cases contribute to the statistics.

5.2.3 Fog dissipation

In the latter stage of fog life cycle, shown in Fig. 11 (a.1), RLWP decreases consistently from positive values associated with the middle of the life cycle until reaching negative values after fog dissipation. Additionally, there are almost no RLWP samples above 30 g m^{-2} observed in the last 30 minutes before dissipation. Hence, an RLWP value above 30 g m^{-2} may be interpreted as an indicator of fog persistence.

Figure 11 (a.2) shows that the monotonous decrease in RLWP begins about 60 minutes before fog dissipation, and can commonly reach values of about -10 to -30 g $m^{-}2$ h-1. These negative values in the time derivative continue after fog dissipation, and can be explained by further lifting or drying of the remaining low stratus cloud (Wærsted et al., 2019).

To study what is the main driver of fog dissipation, Fig. 11 (b) shows the calculated dRLWP/dt, dLWP/dt and $-$F(CTH, Γ_{ad}, α_{eq})·dCTH/dt trends, defined in Sec. 4.4, using the last 60 minutes of data before dissipation. Theoretically, dissipation can only happen when the RLWP decreases, which only happens when the sum of the LWP and CTH time derivative terms is negative (Eq. (8). This matches the results of Fig. 11, which has most points in the quadrants leading to the aforementioned condition. The few points that show a RLWP increase before dissipation, to the right of the dashed line, are associated with uncertain retrievals due to low absolute RLWP values, or fast RLWP depletion in the few minutes just before dissipation (time trends are calculated using a one hour linear fits). Additionally, observations confirm that fog dissipates under the same scenarios predicted in Sect. 4.4. Here the conceptual model predicts that fog could dissipate, even when the LWP is increasing, if the RLWP reduction from layer thickening is larger (strong CTH increase). Conversely, fog can also dissipate when the LWP decreases, even when the CTH subsides. Finally, some cases dissipate with the contribution of both effects, LWP decrease and layer thickening.

6 Conclusions

This work presents a Conceptual Model for adiabatic fog that relates fog liquid water path with its thickness, surface liquid water content and adiabaticity. The model predicts that LWP can be split into two contributions: the first is proportional to the adiabaticity and the square of CTH, and the second is the product of surface LWC and CTH. The later dependency is due to

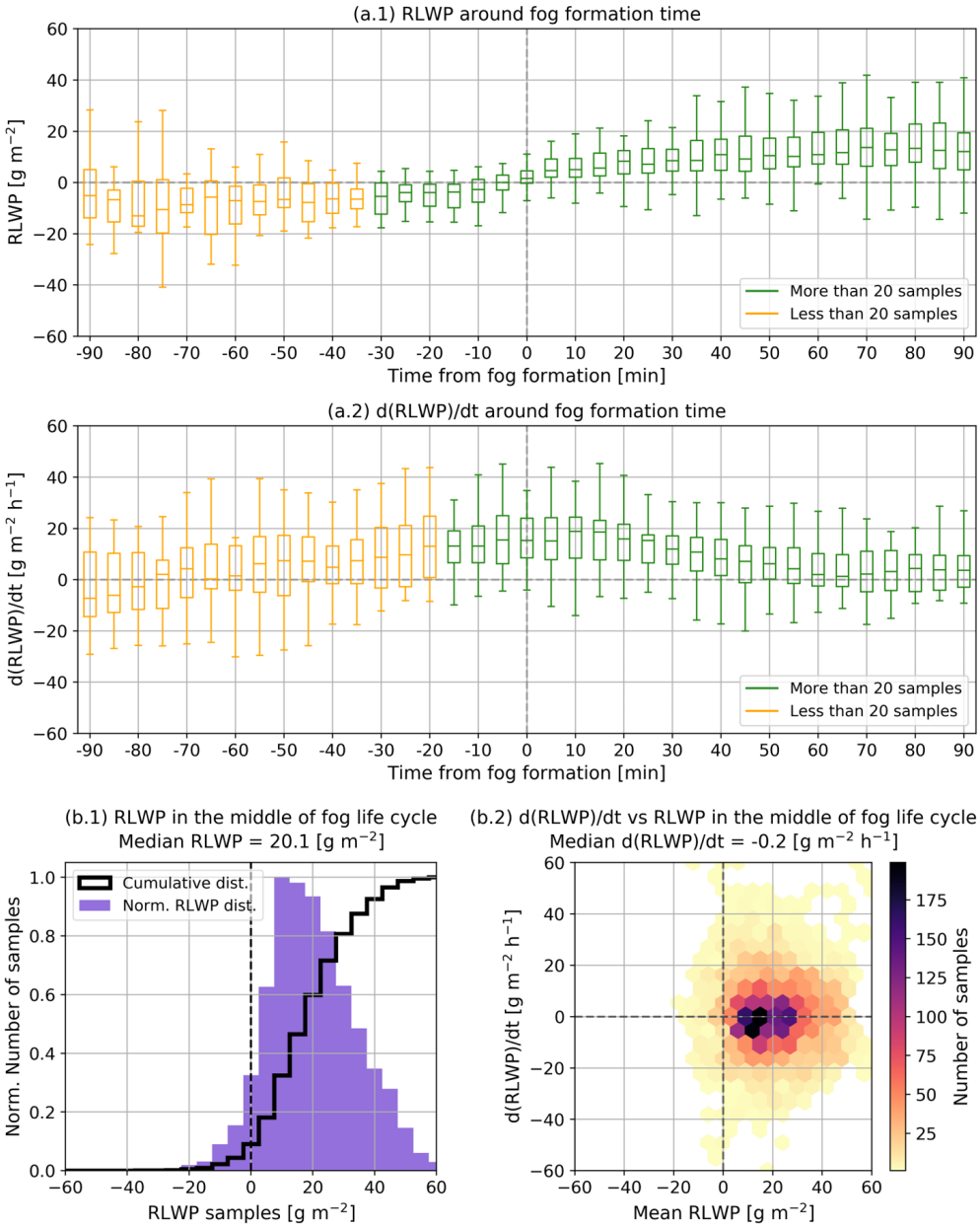

Figure 10. The boxplots of panels (a.1) and (a.2) represent RLWP and dRLWP/dt statistics for each time block 90 minutes before and after fog formation. Boxplot shows the 25th, 50th and 75th percentiles, and the maximum and minimum values. The number of samples per bin is shown in Fig. S2 of the supplementary material. Panels (b.1) and (b.2) show RLWP and dRLWP/dt statistics during fog middle life, between 90 minutes after fog formation and 90 minutes before dissipation, calculated using 4064 and 3952 samples respectively. The ordinate axis of panel (b.1) is associated with the cumulative and normalized distributions.

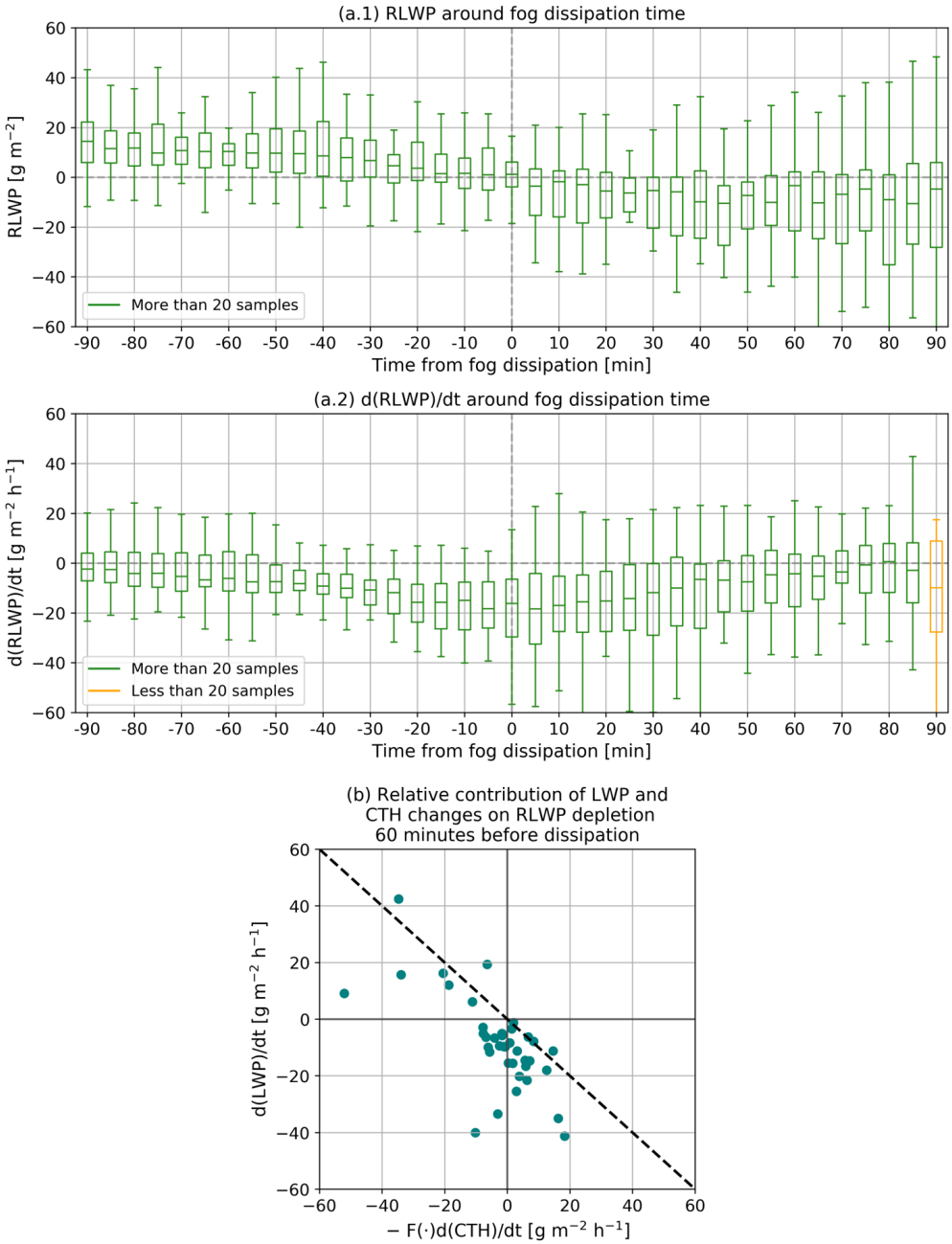

Figure 11. The boxplots of panels (a.1) and (a.2) show RLWP and dRLWP/dt statistics for each time block, 90 minutes before and after fog dissipation. These statistics are derived using 56 fog events, however there may be less than this amount of valid samples for each bin. The number of valid samples per bin is shown in Fig. S3 of the supplementary material. Panel (b) shows the impact of LWP and CTH variations in RLWP depletion, using data from the last 60 minutes before dissipation. The dashed line indicates the theoretical limit where fog dissipation is possible (only to the left of this line). In quadrants II and III cloud base lifting contributes to RLWP decrease, while in Quadrants III and IV the LWP decrease contributes to RLWP depletion. This panel contains 40 valid samples from 56 fog cases, calculated using the method explained at the beginning of Sect. 5.2

an excessive accumulation of water with respect to an equally thick cloud, which appears in fog because the surface presence limits vertical development.

This excess accumulation of water motivates the definition of two diagnostic parameters, which later will prove to be key in understanding fog evolution: the Critical LWP and the Reservoir LWP. The Critical LWP (CLWP) is the minimum amount of column water that would fill the fog layer and cause a visibility reduction down to 1000 m at the surface. The Critical LWP can be calculated using the conceptual model, by imposing a surface LWC equivalent to a 1000 m visibility. Meanwhile, the Reservoir LWP (RLWP) is the difference between fog LWP and the Critical value, and represents the excess of water that enables fog persistence. Case studies and statistical results show that the Reservoir LWP is positive when fog is present, and reaches 0 g m^{-2} at about the same time as fog dissipation.

The model is used to statistically study fog adiabaticity. Important conclusions are that thinner fog, with a LWP less than 20 g m^{-2}, have adiabaticity values below 0.6, and can even reach negative values. This happens when the fog layer is not yet opaque during the fog formation stage, when LWC distribution is not even and may be larger closer to the surface. In this situation fog is not buoyant and therefore it may not lift when the RLWP reaches 0 g m^{-2}. Conversely, when fog is developed, its adiabaticity value gets closer to previously observed values for boundary layer fog, converging at approximately 0.66 for fog with a LWP greater than 30-40 g $m^{-}2$. Here the fog layer is adiabatic, and therefore the fog base should lift when the RLWP depletes down to 0 g m^{-2}. Adiabaticity results are highly variable for LWP values between 20-30 g m^{-2}, and therefore it may be necessary to include additional observations to discern the adiabaticity of the fog layer in this LWP range.

Another result from the study of adiabaticity is an adiabaticity parametrization as a function of fog thickness, which can be used to estimate fog LWP and to perform conceptual model calculations. The estimation of fog LWP has an RMSE of 10.5 g m^{-2}, which is close to the uncertainty in LWP measurement of 10 g m^{-2}, validating the modeled dependency of the LWP on surface LWC, temperature, pressure and CTH.

The temporal derivative of the RLWP is studied, obtaining an analytic formulation that enables the quantification of the contribution of LWP and CTH variations to the depletion of the reservoir, and therefore leading to fog dissipation. This formulation, which is validated by observations, indicates that fog dissipation will depend on the ratio between LWP and CTH variations, and that fog can dissipate by lifting as long as the net RLWP trend is negative, even if 1. LWP and CTH are both increasing, 2. LWP is decreasing and CTH increasing and 3. LWP and CTH are both decreasing.

Statistical observations of the fog life cycle indicate that the RLWP increases, in general, about 60 minutes before and after fog formation. This is followed by positive RLWP values, during fog middle life, that may oscilate or vary depending on the LWP and CTH evolution. Then, about 60 minutes before dissipation, the RLWP starts to decrease consistently until reaching 0 g m^{-2} at dissipation time.

The aforementioned conclusions and the paper results indicate that the RLWP and its time derivative can be used as indicators of the fog life cycle stage, at the local scale. This enables its potential use as an additional diagnostic variable, to quantify how close fog is from dissipation. This may complement visibility measurements at key sites affected by fog, such as airports and land roads, and help improving their logistics to reduce costs and the probability of accidents (Tardif and Rasmussen, 2007).

At present, the RLWP provides an estimation, in real time, of the excess of water of fog that enables the fog layer to remain at the surface. This can already be used as a diagnostic to estimate how likely fog persistence is for the coming minutes, based on the instant RLWP value and its trend (fog dissipation nowcasting). For example, results indicate that fog will not dissipate in the next 30 min if its RLWP is greater than 30 g m^{-2}. Additionally, the RLWP must have a decreasing trend before dissipation, and therefore a positive trend would indicate fog persistence. This result could be improved by introducing forecasting tools to the conceptual model scheme. Forecasting when the RLWP will become 0 g m^{-2} would provide a proxy to predict fog dissipation by base lifting. This forecasting could be done, for example, by considering physical processes. They provide information on fog evolution, and could be used to estimate how the LWP and CTH, and thus the RLWP, will evolve in the near future (e.g. Wærsted et al. (2019)).

Another interesting perspective would be to test conceptual model calculations using the output of fog large-eddy simulations (LES). If the conceptual model variables behave as theoretically expected in these simulations, they could be used to further study the impact of microphysics or surface properties on fog adiabaticity.

Other area of interest would be to study the conceptual model at other sites with frequent fog events. When fog is adiabatic (LWP > 30-40 g m^{-2}), the observed equivalent adiabaticity results is consistent with values observed at other sites. This hints that the conceptual model could be applicable at other sites with similar fog types (continental mid-latitude fogs), with possible variations in the adiabaticity parametrization due to local conditions. This remains to be verified using real observations.

It would also be of interest to study how the direct retrieval of adiabaticity profiles from cloud radar reflectivity profiles could be used to improve the accuracy of the RLWP estimation, compared to the use of a single equivalent value.

Data availability. All data used in this study is hosted by the SIRTA observatory. Data access can be requested for free following the conditions indicated in the SIRTA data policy (https://sirta.ipsl.fr/data_policy.html).

SIRTA observatory website: https://sirta.ipsl.fr/

Data request form: https://sirta.ipsl.fr/data_form.html

Appendix A: Calculation of $\Gamma_{ad}(T, P)$

The inverse of the saturation mixing ratio change with height $\Gamma_{ad}(T, P)$ is calculated using the formulation published by Albrecht et al. (1990) and Braun et al. (2018), shown in Eq. (A1).

$$\Gamma_{ad}(T,P) = \left[\frac{(\epsilon + w_s) w_s l_v}{R_d T^2}\Gamma_w - \frac{g w_s P}{(P - e_s) R_d T}\right] \rho_d \tag{A1}$$

A description and the equations necessary to calculate each term used in the calculation of $\Gamma_{ad}(T, P)$ are given in Tab. A1.

Table A1. List of all the terms needed for the calculation of $\Gamma_{ad}(T, P)$.

Term	Definition	Calculation	Units
T	Surface temperature		K
P	Surface pressure		Pa
l_v	Latent heat of vaporization	$2.5 \cdot 10^6$	J Kg^{-1} K^{-1}
c_p	Specific heat of dry air at constant pressure	1005	J Kg^{-1} K^{-1}
g	Acceleration of gravity	9.81	m s^{-2}
R_d	Dry air ideal gas constant	287.0	J Kg^{-1} K^{-1}
R_v	Water vapor ideal gas constant	461.5	J Kg^{-1} K^{-1}
ϵ	Ratio of R_d to R_v	$\frac{R_d}{R_v}$	
e_s	Vapor saturation pressure	$611.2 \cdot \exp\left(\frac{17.67(T-273.15)}{T-29.65}\right)$	Pa
w_s	Saturation mixing ratio	$\epsilon \frac{e_s}{P-e_s}$	
ρ_d	Dry air density	$\frac{P-e_s}{R_d T}$	Kg m^{-3}
Γ_w	Moist adiabatic lapse rate	$\frac{g}{c_p}\left(1+\frac{l_v w_s}{R_d T}\right) / \left(1+\frac{\epsilon l_v^2 w_s}{R_d c_p T^2}\right)$	K m^{-1}
$\Gamma_{ad}(T, P)$		Eq. (A1)	Kg m^{-4}

Appendix B: Visibility-LWC parametrization

Surface LWC estimation from visibility measurements is done by inverting Gultepe et al. (2006) Eq. (6). This results in Eq. (B1), where LWC is Liquid Water Content in Kg m^{-3} and VIS is the visibility in meters.

$$LWC = 0.0187 \cdot 10^{-3} \cdot \left(\frac{VIS}{1000}\right)^{-1.041} \tag{B1}$$

Author contributions. FT and MH developed the conceptual model and its formulation, based on initial work by EW and MH. FT and EW developed the code used for data analysis. FT and MH defined the paper structure and content. MH and JCD manage the SIRTA observatory, which provided the used dataset. All authors reviewed the paper.

Competing interests. The authors declare that they have no conflict of interest.

Acknowledgements. We acknowledge all the SIRTA observatory technical team for their extraordinary work on retrieving long term and high quality datasets. SIRTA measurements were performed in the framework of the ACTRIS, supported by the European Commission under the Horizon 2020 – Research and Innovation Framework Programme, H2020-INFRADEV-2019-2. We also acknowledge Marc-Antoine Drouin and Cristophe Boitel of the SIRTA observatory for their help on data access. We acknowledge the french Association Nationale Recherche

535 Technologie (ANRT) and the company Meteomodem for their contribution in the funding of this work. Finally, this publication is based upon work from COST Action PROBE, supported by COST (European Cooperation in Science and Technology).

References

Albrecht, B. A., Fairall, C. W., Thomson, D. W., White, A. B., Snider, J. B., and Schubert, W. H.: Surface-based remote sensing of the observed and the Adiabatic liquid water content of stratocumulus clouds, Geophysical Research Letters, 17, 89–92, https://doi.org/10.1029/GL017i001p00089, https://agupubs.onlinelibrary.wiley.com/doi/abs/10.1029/GL017i001p00089, 1990.

Bergot, T.: Small-scale structure of radiation fog: a large-eddy simulation study, Quarterly Journal of the Royal Meteorological Society, 139, 1099–1112, 2013.

Bergot, T.: Large-eddy simulation study of the dissipation of radiation fog, Quarterly Journal of the Royal Meteorological Society, 142, 1029–1040, 2016.

Betts, A. K.: Cloud Thermodynamic Models in Saturation Point Coordinates, Journal of Atmospheric Sciences, 39, 2182 – 2191, https://doi.org/10.1175/1520-0469(1982)039<2182:CTMISP>2.0.CO;2, https://journals.ametsoc.org/view/journals/atsc/39/10/1520-0469_1982_039_2182_ctmisp_2_0_co_2.xml, 1982.

Boers, R. and Mitchell, R. M.: Absorption feedback in stratocumulus clouds influence on cloud top albedo, Tellus A, 46, 229–241, 1994.

Boers, R., Melfi, S. H., and Palm, S. P.: Cold-Air Outbreak during GALE: Lidar Observations and Modeling of Boundary Layer Dynamics, Monthly Weather Review, 119, 1132–1150, 1990.

Boutle, I., Price, J., Kudzotsa, I., Kokkola, H., and Romakkaniemi, S.: Aerosol–fog interaction and the transition to well-mixed radiation fog, Atmospheric Chemistry and Physics, 18, 7827–7840, https://doi.org/10.5194/acp-18-7827-2018, https://acp.copernicus.org/articles/18/7827/2018/, 2018.

Braun, R. A., Dadashazar, H., MacDonald, A. B., Crosbie, E., Jonsson, H. H., Woods, R. K., Flagan, R. C., Seinfeld, J. H., and Sorooshian, A.: Cloud Adiabaticity and Its Relationship to Marine Stratocumulus Characteristics Over the Northeast Pacific Ocean, Journal of Geophysical Research: Atmospheres, 123, 13,790–13,806, https://doi.org/10.1029/2018JD029287, https://agupubs.onlinelibrary.wiley.com/doi/abs/10.1029/2018JD029287, 2018.

Brenguier, J.-L., Pawlowska, H., Schüller, L., Preusker, R., Fischer, J., and Fouquart, Y.: Radiative properties of boundary layer clouds: Droplet effective radius versus number concentration, Journal of the atmospheric sciences, 57, 803–821, 2000.

Brown, R. and Roach, W.: The physics of radiation fog: II–a numerical study, Quarterly Journal of the Royal Meteorological Society, 102, 335–354, 1976.

Cermak, J. and Bendix, J.: Detecting ground fog from space – a microphysics-based approach, International Journal of Remote Sensing, 32, 3345–3371, https://doi.org/10.1080/01431161003747505, https://doi.org/10.1080/01431161003747505, 2011.

Delanoë, J., Protat, A., Vinson, J.-P., Brett, W., Caudoux, C., Bertrand, F., Parent du Chatelet, J., Hallali, R., Barthes, L., Haeffelin, M., et al.: Basta: a 95-GHz fmcw doppler radar for cloud and fog studies, Journal of Atmospheric and Oceanic Technology, 33, 1023–1038, 2016.

Driedonks, A. and Duynkerke, P.: Current problems in the stratocumulus-topped atmospheric boundary layer, Boundary-Layer Meteorology, 46, 275–303, 1989.

Dupont, J.-C., Haeffelin, M., Protat, A., Bouniol, D., Boyouk, N., and Morille, Y.: Stratus–fog formation and dissipation: a 6-day case study, Boundary-layer meteorology, 143, 207–225, 2012.

Gultepe, I., Müller, M. D., and Boybeyi, Z.: A New Visibility Parameterization for Warm-Fog Applications in Numerical Weather Prediction Models, Journal of Applied Meteorology and Climatology, 45, 1469–1480, https://doi.org/10.1175/JAM2423.1, https://doi.org/10.1175/JAM2423.1, 2006.

Gultepe, I., Tardif, R., Michaelides, S., Cermak, J., Bott, A., Bendix, J., Müller, M. D., Pagowski, M., Hansen, B., Ellrod, G., et al.: Fog research: A review of past achievements and future perspectives, Pure and applied geophysics, 164, 1121–1159, 2007.

Görsdorf, U., Knist, C., and Lochmann, M.: First results of the cloud radar and microwave radiometer comparison campaign at Lindenberg, aCTRIS Week 2020, 2020.

Haeffelin, M., Barthès, L., Bock, O., Boitel, C., Bony, S., Bouniol, D., Chepfer, H., Chiriaco, M., Cuesta, J., Delanoë, J., et al.: SIRTA, a ground-based atmospheric observatory for cloud and aerosol research, in: Annales Geophysicae, vol. 23, pp. 253–275, 2005.

Haeffelin, M., Bergot, T., Elias, T., Tardif, R., Carrer, D., Chazette, P., Colomb, M., Drobinski, P., Dupont, E., Dupont, J.-C., et al.: PARIS-FOG: Shedding new light on fog physical processes, Bulletin of the American Meteorological Society, 91, 767–783, 2010.

Haeffelin, M., Laffineur, Q., Bravo-Aranda, J.-A., Drouin, M.-A., Casquero-Vera, J.-A., Dupont, J.-C., and De Backer, H.: Radiation fog formation alerts using attenuated backscatter power from automatic lidars and ceilometers, Atmospheric Measurement Techniques, 9, 5347, 2016.

Hoffmann, H.-E. and Roth, R.: Cloudphysical parameters in dependence on height above cloud base in different clouds, Meteorology and Atmospheric Physics, 41, 247–254, 1989.

Kotthaus, S., O'Connor, E., Münkel, C., Charlton-Perez, C., Haeffelin, M., Gabey, A. M., and Grimmond, C. S. B.: Recommendations for processing atmospheric attenuated backscatter profiles from Vaisala CL31 ceilometers, Atmospheric Measurement Techniques, 9, 3769–3791, https://doi.org/10.5194/amt-9-3769-2016, https://amt.copernicus.org/articles/9/3769/2016/, 2016.

Manton, M.: The physics of clouds in the atmosphere, Reports on Progress in Physics, 46, 1393, 1983.

Marke, T., Ebell, K., Löhnert, U., and Turner, D. D.: Statistical retrieval of thin liquid cloud microphysical properties using ground-based infrared and microwave observations, Journal of Geophysical Research: Atmospheres, 121, 14,558–14,573, https://doi.org/10.1002/2016JD025667, https://agupubs.onlinelibrary.wiley.com/doi/abs/10.1002/2016JD025667, 2016.

Nakanishi, M.: Large-eddy simulation of radiation fog, Boundary-layer meteorology, 94, 461–493, 2000.

Oliver, D., Lewellen, W., and Williamson, G.: The interaction between turbulent and radiative transport in the development of fog and low-level stratus, Journal of the Atmospheric Sciences, 35, 301–316, 1978.

Porson, A., Price, J., Lock, A., and Clark, P.: Radiation fog. Part II: Large-eddy simulations in very stable conditions, Boundary-layer meteorology, 139, 193–224, 2011.

Price, J.: Radiation fog. Part I: observations of stability and drop size distributions, Boundary-layer meteorology, 139, 167–191, 2011.

Roach, W., Brown, R., Caughey, S., Crease, B., and Slingo, A.: A field study of nocturnal stratocumulus: I. Mean structure and budgets, Quarterly Journal of the Royal Meteorological Society, 108, 103–123, 1982.

Roach, W. T., Brown, R., Caughey, S. J., Garland, J. A., and Readings, C. J.: The physics of radiation fog: I – a field study, Quarterly Journal of the Royal Meteorological Society, 102, 313–333, https://doi.org/https://doi.org/10.1002/qj.49710243204, https://rmets.onlinelibrary.wiley.com/doi/abs/10.1002/qj.49710243204, 1976.

Slingo, A., Brown, R., and Wrench, C.: A field study of nocturnal stratocumulus; III. High resolution radiative and microphysical observations, Quarterly Journal of the Royal Meteorological Society, 108, 145–165, 1982.

Smith, D. K. E., Renfrew, I. A., Price, J. D., and Dorling, S. R.: Numerical modelling of the evolution of the boundary layer during a radiation fog event, Weather, 73, 310–316, https://doi.org/https://doi.org/10.1002/wea.3305, https://rmets.onlinelibrary.wiley.com/doi/abs/10.1002/wea.3305, 2018.

Tardif, R. and Rasmussen, R. M.: Event-based climatology and typology of fog in the New York City region, Journal of applied meteorology and climatology, 46, 1141–1168, 2007.

Wærsted, E.: Description of physical processes driving the life cycle of radiation fog and fog–stratus transitions based on conceptual models, Ph.D. thesis, Paris Saclay, 2018.

Wærsted, E. G., Haeffelin, M., Dupont, J.-C., Delanoë, J., and Dubuisson, P.: Radiation in fog: quantification of the impact on fog liquid water based on ground-based remote sensing, Atmospheric Chemistry and Physics, 17, 10 811–10 835, https://doi.org/10.5194/acp-17-10811-2017, https://www.atmos-chem-phys.net/17/10811/2017/, 2017.

Wærsted, E. G., Haeffelin, M., Steeneveld, G.-J., and Dupont, J.-C.: Understanding the dissipation of continental fog by analysing the LWP budget using idealized LES and in situ observations, Quarterly Journal of the Royal Meteorological Society, 145, 784–804, https://doi.org/10.1002/qj.3465, https://rmets.onlinelibrary.wiley.com/doi/abs/10.1002/qj.3465, 2019.

Walker, M.: The science of weather: Radiation fog and steam fog, Weather, 58, 196–197, 2003.

Zhou, B. and Ferrier, B. S.: Asymptotic analysis of equilibrium in radiation fog, Journal of Applied Meteorology and Climatology, 47, 1704–1722, 2008.

2.3 Use of conceptual model variables as indicators of fog dissipation tendency

This section presents statistics of the of RLWP with respect to surface visibility. Then it presents the definition of temporary fog dissipation, and how this phenomenon limits the performance of dissipation forecasting when it is based exclusively on diagnostic variables. Finally, it concludes with a calculation of fog dissipation probability within different time ranges, as a function of RLWP and visibility.

2.3.1 Surface visibility and RLWP during fog

Surface visibility and RLWP are two variables that describe fog state. Visibility is an in-situ measurement, hence its information only represents the instrument surroundings. Contrastingly, RLWP is a variable that extracts information from the fog column state. Therefore, it should provide additional information when compared with visibility alone.

To check this hypothesis, we begin by studying the behavior of fog visibility versus RLWP. For this we plot the two histograms of Fig. 2.1. Figure 2.1 (a) shows the histogram with the distribution of both variables, using all valid data collected in the 80 fog cases selected in the article. Meanwhile, Fig. 2.1 (b) shows a histogram with the number of fog cases in which each pair RLWP-visibility appeared at least once.

We observe the range of possible RLWP values is more restricted when visibility is greater than ∼600, compared with lower visibility values. This result is understandable, because RLWP must approach zero as visibility increases, limiting the possible RLWP-visibility configurations. On the contrary, when visibility is less than ∼600 m, Fig. 2.1 (a) shows RLWP can present a large range of values, from negative to 40 or more g m^{-2}. This situation becomes more accused when visibility is under 250 m, where RLWP values ranging between 5 and 40 g m^{-2} appear with a similar frequency.

At the same time, Fig. 2.1 (b) shows that RLWP values above 20 g m^{-2} appear in a lower number of fog events. This creates an apparent contradiction with Fig. 2.1 (a), where the amount of samples above and below the RLWP of 20 g m^{-2} is similar. Since visibility and RLWP are sampled every 5 minutes, longer duration fog cases would contribute to a larger number of samples. Therefore, the large amount

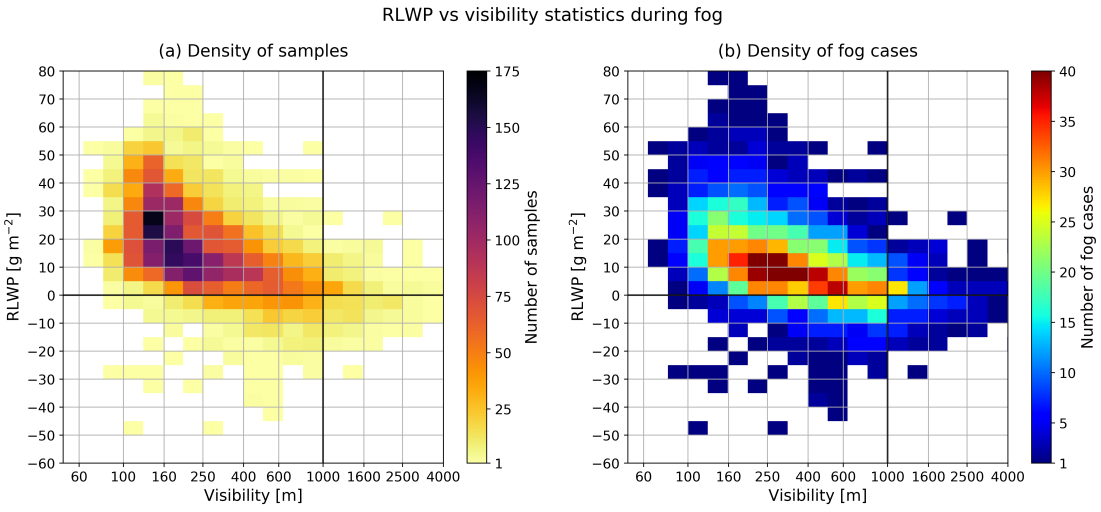

Figure 2.1: Distribution of RLWP versus visibility during fog. Panel (a) is drawn using all valid samples of the 80 fog events selected in the article. Panel (b) shows how many fog events reach the RLWP-visibility values bounded by each pixel (a fog event is counted if at least one of its RLWP-visibility samples falls within a given pixel).

of samples with RLWP above 20 g m^{-2} must come from less frequent cases, that last longer than cases with lower RLWP values.

Another observation is that, during fog, we have visibility samples reaching values greater than 1000 meters, which in principle is incompatible with fog definition. This data corresponds to a temporary dissipation event, which does not last long enough to mark the end of the fog period. Temporary dissipation is discussed in more detail in Sect. 2.3.2.

Section 4.1 of the article shows that fog adiabaticity has two regimes, depending on fog LWP. When LWP is less than 30 g m^{-2}, fog is optically thin and most of the radiative cooling and liquid water condensation happens close to the surface, under a stable atmospheric profile. On the contrary, when LWP is greater than 30 g m^{-2}, fog is optically thick and therefore radiative cooling and liquid water condensation happens mostly at fog top, generating vertical convective flows that destabilize the boundary layer.

To study if the behavior of the RLWP versus visibility statistics for these two regimes, we plot the histogram of Fig. 2.1 (a) again, but this time separating between samples with LWP less and greater than 30 g m^{-2}. Results are shown in Fig. 2.2. Panel (a) shows the statistics of data points with LWP values below 30 g m^{-2}, associated with shallow fog that is not opaque to infrared radiation. We observe that in this regime, visibility can range between $\sim$ 100-1000 meters with a RLWP generally less than 20 g m^{-2}. This can be understood from the properties of shallow fog. In this situation, the atmosphere is stable and coupling between the surface and upper layers is weak or neglibile. This, paired with the fact that radiative cooling happens predominantly close to the surface, explain why visibility can drop significantly without significant vertical development. The lack of vertical development and the low adiabaticity of shallow fog are associated with a low amount of LWP in the column, which therefore limits the maximum attainable RLWP.

This contrasts the situation of Fig. 2.2 (b), where we present the data with LWP greater than 30 g m^{-2}. Under these conditions, fog is optically thick and therefore most of the radiative cooling and liquid water condensation happens at fog top. Stability is close to neutral, coupling the fog base with its top through vertical mixing. Under these conditions, an increase in the amount of RLWP, which is a measure of the excess water sustaining fog, would imply that more water is being redistributed in the column. This larger amount of water would reduce visibility in the whole layer, including the first meters above the surface, explaining why visibility decreases systematically for larger RLWP values.

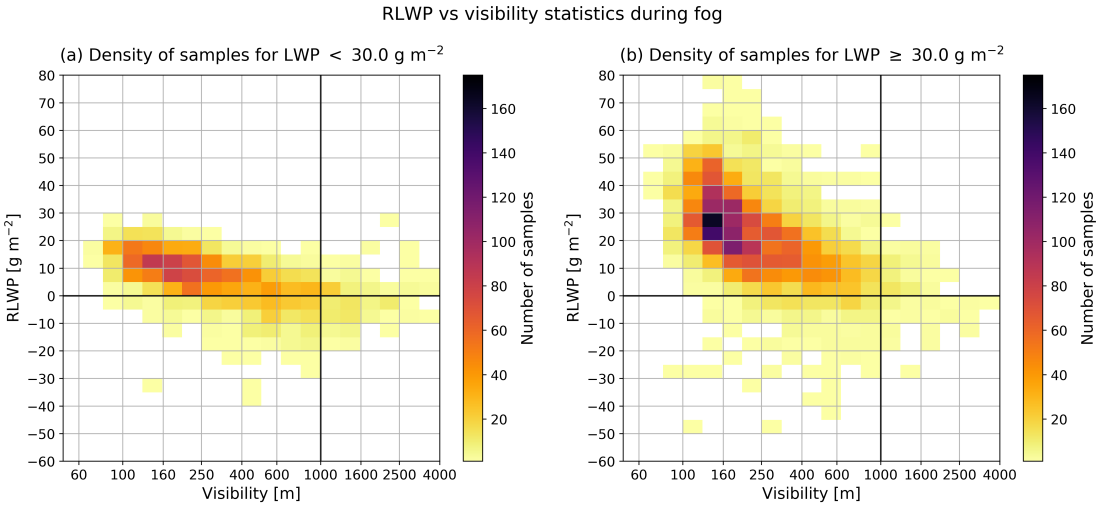

Figure 2.2: Distribution of RLWP versus visibility for (a) shallow and (b) adiabatic fog. Samples are extracted from the 80 fog events selected in the article, and classified based on their LWP value.

2.3.2 Temporary fog dissipation

In the previous section we observed that some samples, observed during fog, had surface visibility values above 1000 m (see for ex. Fig. 2.1). However, fog definition states that visibility at the surface must be less than 1000 m. The reason for which these samples appear is in the algorythm used to identify fog formation and dissipation time (based on the previous work of Tardif and Rasmussen (2007); Wærsted et al. (2019) and explained in Sect. 3.2 of the article). This algorythm declares that periods with visibility above 1000 m that last less than 60 minutes do not mark the definitive dissipation time of a fog event. Hence, periods lasting less than 60 minutes, with high visibility values ($>$ 1000 m), can remain within a detected fog event. These are defined as temporary fog dissipation periods.

Some causes of temporary dissipation are well known, yet this phenomenon is not widely discussed in literature. When radiation fog is forming, visibility may increase for short time periods due to horizontal advection of clear air patches, where fog is not yet formed due to differences in surface properties that impact humidity (Gultepe et al., 2007). Other cause for temporary dissipation is the droplet growth and subsequent decrease of LWP caused by fog drizzle (Dupont et al., 2012). Finally, we have observed that adiabatic fog can temporarily lift during a transitory LWP depletion, or a fast increase in CTH.

Figure 2.3 shows an example of a radiation fog case with temporary dissipation periods. Panel (c) shows that fog forms close to 02:30 UTC, and remains below 20 meters until approximately 05:00 UTC. Fog CTH is too low to be detected by the radar and its LWP remains very close to 0 g m^{-2} (panels (a) and (d) respectively). Within this period we observe that the 4-m visibility increased several times above 1000 meters. This likely happens because of the advection of surrounding clear air patches, as explained in previous lines. Later, around 05:45 UTC, LWP starts to increase until surpassing the $\sim$ 30 g m^{-2} associated with opaque fog at 06:00 UTC. During this period fog becomes thick enough to be observed with the radar, and we begin to have CTH, RLWP and closure adiabaticity retrievals. The latter, shown on panel (e), shows that fog becomes superadiabatic for a brief period of time ($\alpha_{eq}^{closure} > 1.0$). This happens because radiative cooling is quickly condensing a lot of water, producing a fast LWP increase (up to $\sim$55 g m^{-2} Hr^{-1}, panel (f)). Sustained liquid water generation fills the fog layer above the adiabatic limit, because the layer growth is bounded by the surface and the temperature inversion. After sunrise, at 08:00 UTC, adiabaticity drops to $\approx$ 0.6, indicating that fog is adiabatic for the rest of its duration.

During the adiabatic fog stage, there is another temporary dissipation period between 11:15 and 12:00 UTC approximately. In this case, the visibility increase is caused by a transient lifting of the fog base. Evidence for this can also be seen in the 20-m visibility timeseries of panel (c), which also increases during this time period. At the same time, RLWP decreases until reaching negative values, remaining consistent with what is expected theoretically (when the RLWP is less than 0, the LWP is not enough for fog to reach the surface). Panel (f) shows that base lifting is caused by the vertical growth of the fog layer. Effectively, a CTH increase produces a net decrease of RLWP from $\sim$ 10:45 UTC, shortly before the time of the base lifting. This vertical development is later compensated by an increase on LWP, allowing the fog layer to reach down to the surface again. This situation last until 14:00 UTC, when the fog base lifts for more than 60 minutes, marking the dissipation time of this fog period.

Temporary dissipation within fog events are a frequent phenomena. Figure 2.4 (left) shows that more than 50% of fog events have at least one of these events (45 out of 80 fog cases). Meanwhile, Figure 2.4 (right) shows that fog duration and the number of temporary dissipation periods is not strongly correlated, indicating that they are not likely to be a random event (if it were, the number of dissipation periods should be strongly correlated with fog duration). Temporary dissipation periods were detected searching for periods in fog with a visibility greater than 1000 m, that lasted between 10 and 55 minutes.

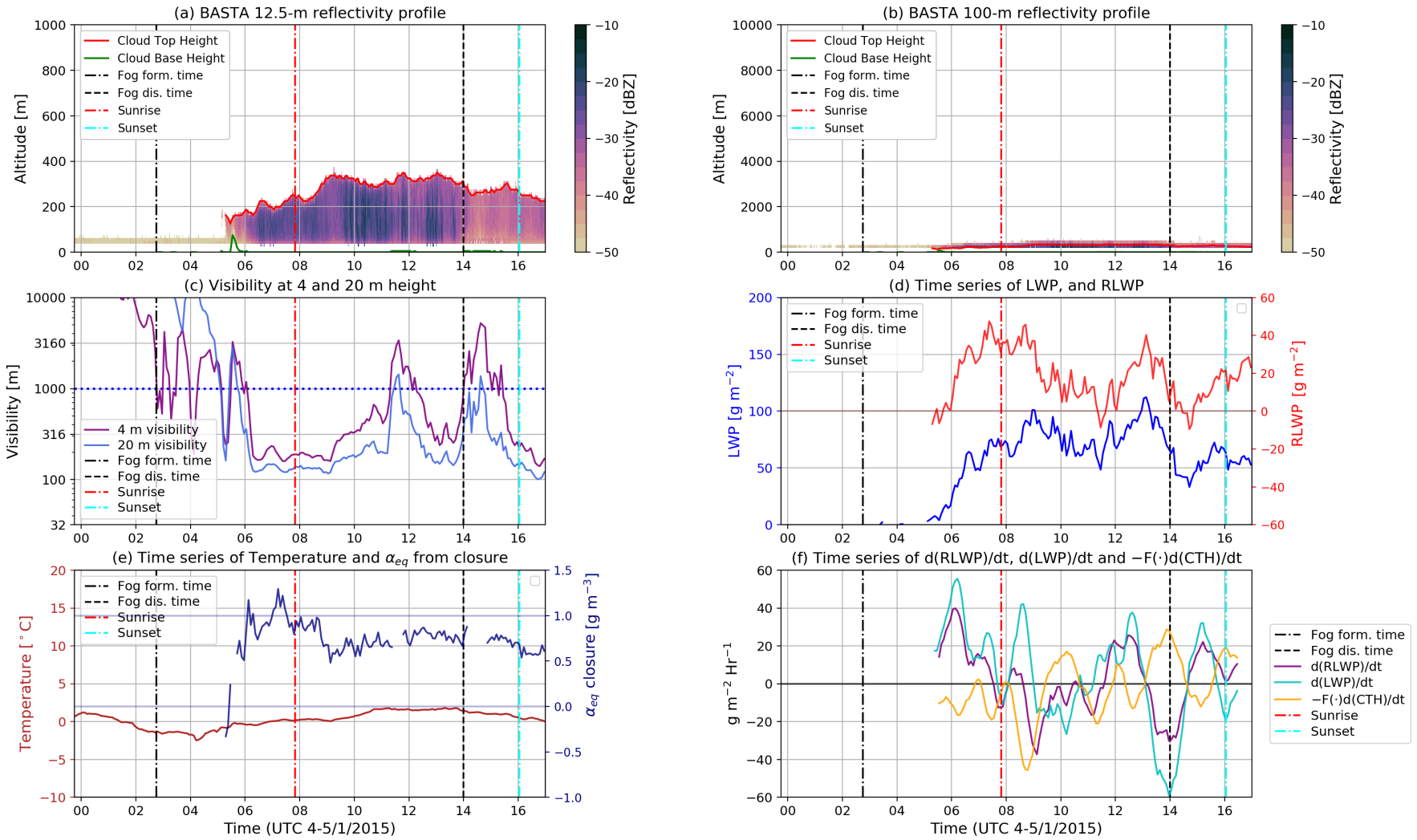

Figure 2.3: Example of a fog case with temporary dissipaton periods close to the formation time (advection of clear air in shallow radiation fog) and during its adiabatic stage (short-lived fog base lifting). Panel description: (a) Cloud Base Height (CBH), Cloud Top Height (CTH), and the cloud radar 12.5 m resolution reflectivity profile for the first 1000 m of height. (b) Cloud radar 100 m resolution reflectivity profile up to 10 km of height. (c) 4-m and 20-m horizontal visibilities. (d) Fog/Stratus layer measured LWP and computed RLWP. (e) Temperature and closure adiabaticity (calculated only when visibility is less than 2000 m). (f) Rate of change of the RLWP, with the individual contributions from LWP and CTH variations. The time of fog formation, fog dissipation, sunrise and sunset are marked in each panel.

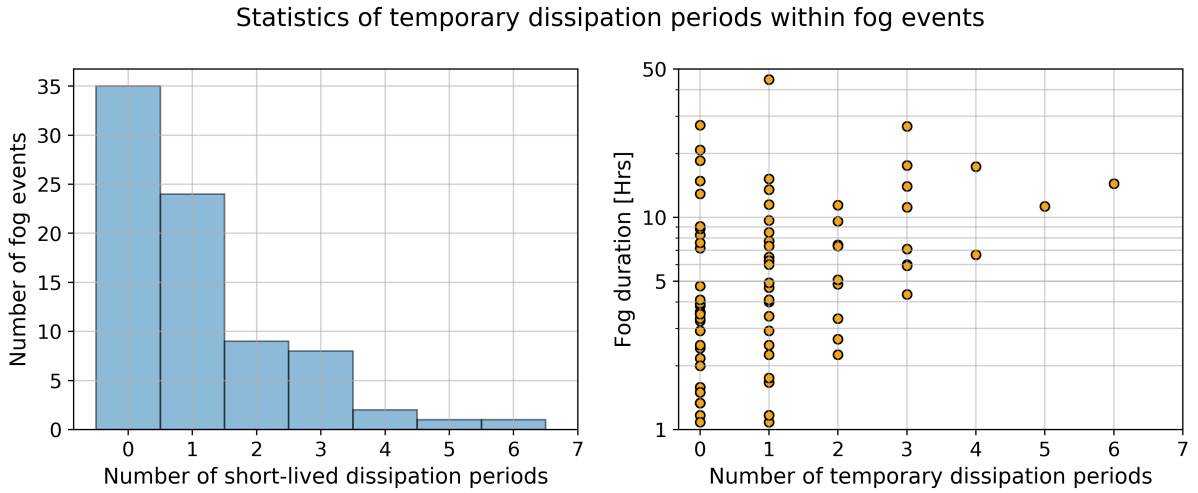

Figure 2.4: Statistics of temporary dissipation periods (surface visibility $>$ 1000 m lasting between 10 and 55 minutes within a fog event). The panel on the left shows the amount of fog events with a given number of dissipation periods. The panel on the right shows a scatterplot with the number of dissipation periods versus fog duration.

2.3.3 Statistics of visibility and RLWP versus fog dissipation tendency

Visibility and RLWP are two variables that provide information on fog status. Visibility is an in-situ measure used to define and detect fog presence at the surface. By continuity, temporary and definitive fog dissipation is preceded by increasing visibility values, until reaching and surpassing 1000 meters. Meanwhile, RLWP is a variable calculated using information from the fog column that provides a measure of the excess water that enables the persistence of adiabatic fog at the surface. As is explained in Sect. 2.2, when the RLWP is greater than 0 g m^{-2}, fog liquid water path is large enough to sustain a visibility under 1000 meters at the surface. When RLWP reaches 0 or negative values, fog LWP is not enough to fill the layer between the surface and the temperature inversion, and therefore we observe a visibility increase at the surface.

Both variables provide consistent results at dissipation time. As is shown in Fig. 11 of the article, when visibility reaches 1000 meters, the RLWP becomes 0 g m^{-2}. Contrastingly, when visibility is low we observed that RLWP provides an additional dimension that can vary independently of visibility (see Sect. 2.3.1).

This additional dimension could introduce a complementary source of information when assessing fog dissipation tendency. However, before studying statistics, we must make a consideration. From a theoretical point of view, the RLWP does not provide enough information to anticipate if dissipation will be temporary or definitive. It only provides a measure of the amount of water that must be removed before surface visibility can surpass 1000 m. Since at present we do not have enough information to estimate the duration of an incoming dissipation period, we decide to not distinguish between temporary and definitive dissipation when studying the viability of RLWP and visibility as indicators of fog dissipation tendency.

Figure 2.5 shows RLWP and visibility statistics with respect to fog dissipation tendency. Panel (a) of Fig. 2.5 shows histograms of the RLWP samples for the 10, 30, 60, 90, 120 and 180 minutes before dissipation (in red). Samples measured farther than these time periods from dissipation are presented in blue. Panel (b) shows the same statistics for visibility samples.

(a) RLWP statistics during fog: data separated according to the number of minutes before dissipation

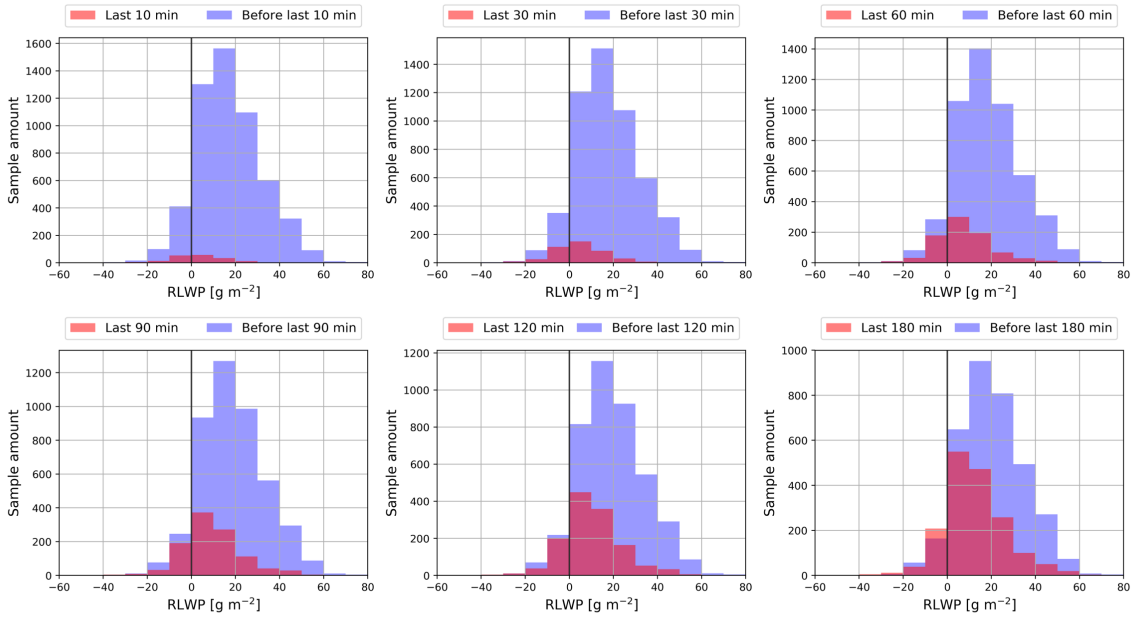

(b) Visibility statistics during fog: data separated according to the number of minutes before dissipation

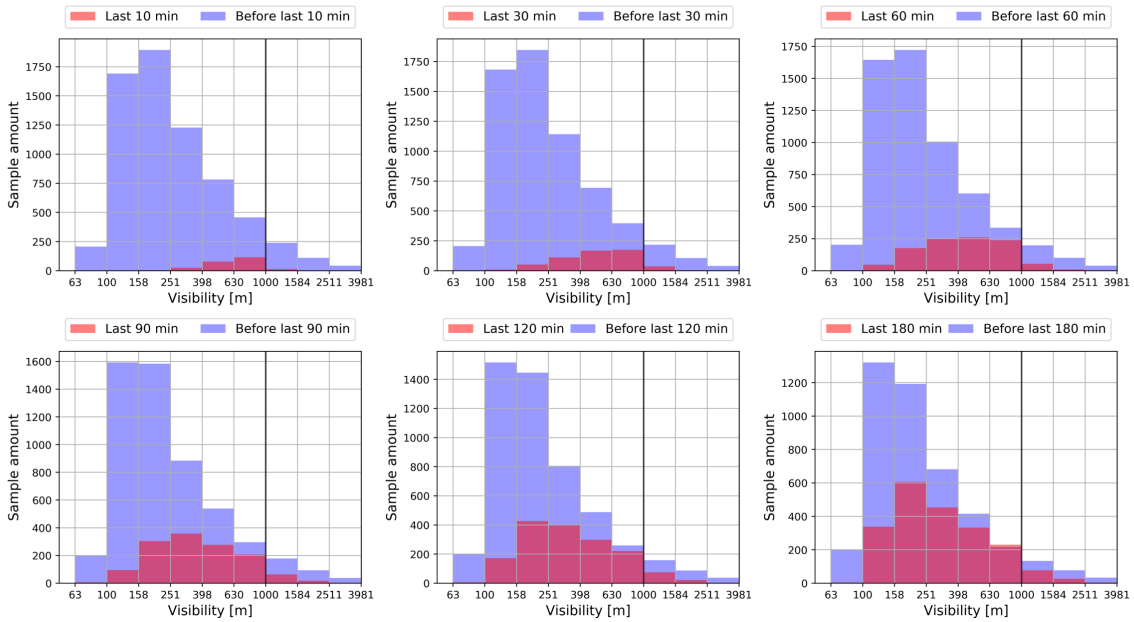

Figure 2.5: Statistics of RLWP (Panel (a)) and visibility (Panel (b)). Red histograms show data taken in the last 10, 30, 60, 90, 120 and 180 minutes before fog dissipation. Blue histograms show all samples taken before this period. Data extracted from the 80 fog events selected in the article (Sect. 2.2). No distinction is made between temporary and definitive dissipation.

On panel (a) we observe that, in general, RLWP samples distribute closer to 0 g m^{-2} for data closer to dissipation, with the mode at the 0-10 g m^{-2} bin. This is an expectable result, because the RLWP must decrease below 0 g m^{-2} when visibility increases above 1000 m.

An interesting result is that high RLWP values seem to provide information about fog persistence. Data shows that it is very unlikely to have any kind of dissipation in less than 90 minutes when the RLWP is greater than 20-30 g m^{-2}. Similarly, when RLWP is greater than 40 g m^{-2} fog is more much likely to persist for, at least, 180 additional minutes. These results indicate that RLWP could be a good indicator of fog persistence, specially for values greater than 20 g m^{-2}.

The visibility histograms on panel (b) show that when visibility is within 600-1000 meters, the chances of dissipation in the next 30 minutes is greater than 50%. When visibility is above 400 meters, the chance of dissipation in the next 60 minutes is also greater than 50%. For visibility values below 400 meters we have a high ratio of samples associated with fog persistence for at least 60 minutes, and when visibility is less than 250 meters, fog is likely to last for at least 120 additional minutes.

To study the information that visibility and RLWP can provide as indicators of fog dissipation tendency, we calculate the probability of dissipation as a function of time, for different ranges of RLWP and visibility. Probability is calculated as the ratio of samples close to dissipation versus the total amount of samples within each specified range of visibility and RLWP. The results are shown in Fig. 2.6.

When visibility is less than 250 meters, a comparison between the black dashed line (calculated for any RLWP value) and the colored lines (calculated for specific RLWP ranges) indicate that the probability of dissipation is strongly influenced by RLWP. For all time ranges, probability of dissipation increases when RLWP decreases, reaching a maximum of 60% for negative RLWP values in the 120-180 minutes time range. The 0-10 g m^{-2} is associated with smaller dissipation probabilities for most time ranges, except for 180 minutes where it converges with the negative RLWP curve. It shows dissipation probabilities of 20%, 50% and 60% for the next 60, 120 and 180 minutes respectively. The probabilities of the 10-20 g m^{-2} curve raise more slowly than those of the 0-10 g m^{-2} range, as can be seen in the dissipation probabilities of 10%, 25% and 40% for the next 60, 120 and 180 minutes respectively. The behavior of

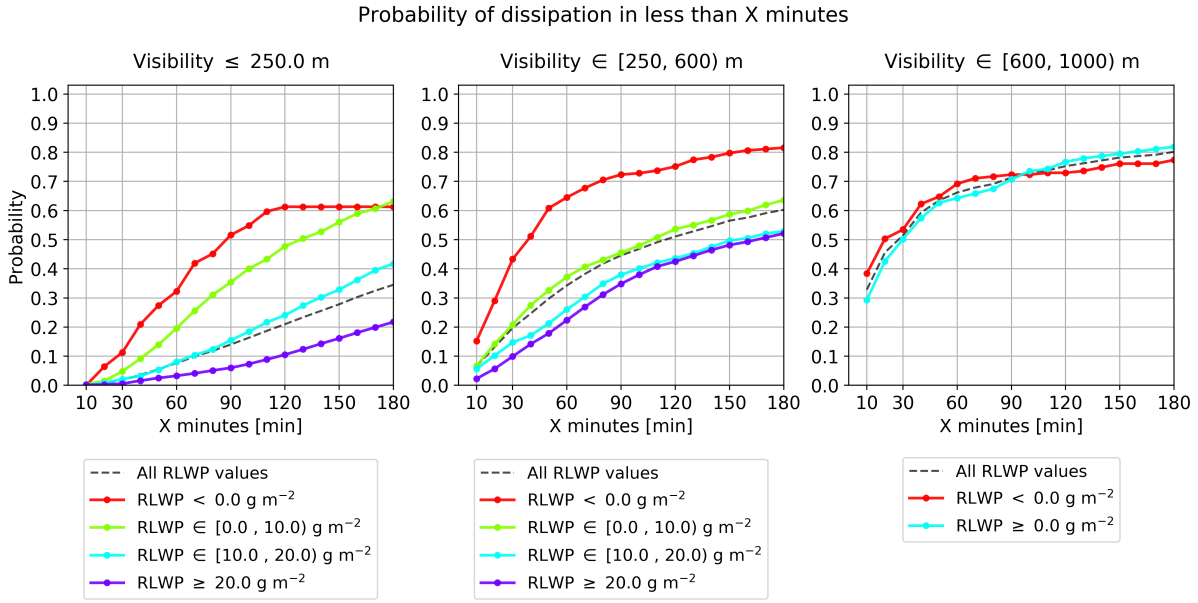

Figure 2.6: Probability of fog dissipation as a function of time, RLWP and visibility. Probability is calculated as the ratio of the samples closer than X minutes to dissipation versus the total amount of samples in the specified visibility and RLWP range. No distinction is made between temporary and definitive dissipation.

probabilities in the 10-20 g m^{-2} range also remains close to the black curve calculated using all RLWP values, indicating that dissipation probability in this RLWP range is similar to what could be obtained by using visibility alone. On the other extreme, samples with RLWP values greater than 20 g m^{-2} have less than a ∼10% chance of being within the last 120 minutes before dissipation, and less than ∼20% of being within the last 180 minutes. Thus, a visibility under 250 meters paired with RLWP values above 20 g m^{-2} are strong indicators of fog persistence for the next 2-3 hours.

For the visibility range between 250 and 600 meters, probability of dissipation is greater for all curves, with respect to the $\leq$ 250 m visibility range. Negative RLWP values provide a specially distinct signal, raising quickly from 15% to 65% in the first 60 minutes, until reaching a maximum of 70-80% for periods longer than 90 minutes. The probabilities for the 0-10 g m^{-2} range are significantly smaller than for the negative RLWP values, remaining close to the "average" black curve, with dissipation probabilities of 35%, 50% and 60% for the next 60, 120 and 180 minutes respectively. The curves for 10-20 and $\geq$ 20 g m^{-2} remain very close in this visibility range, with slighly higher dissipation probabilities for the 10-20 g m^{-2} range (differences smaller than 10%). This likely happens because of physical constraints that strongly reduce the chance of having RLWP greater than 20 g m^{-2} in this visibility range, as can be seen in Fig. 2.1.

Finally, when visibility is between 600 and 1000 meters, the impact of RLWP on the dissipation probability becomes negligible. This is likely due to the stronger correlation between these variables in this visibility range, caused by the limited number of possible configurations that visibility and RLWP can have under these conditions (see Sect. 2.3.1). Dissipation probabilities in this range are of 65%, 70% and 80% for the next 60, 120 and 180 minutes respectively.

Considering these results, we can affirm that RLWP provides additional information of fog dissipation tendency when visibility is below 600 meters. Observed differences in dissipation probability can reach up to 50% when comparing negative and high RLWP values (above 20 g m^{-2}) for this visibility range. Contrastingly, for visibilities between 600 and 1000 meters the RLWP does not provide additional information about fog dissipation tendency, due to the RLWP convergence towards 0 g m^{-2} when visibility increases to 1000 m.

2.4 Synthesis

This chapter presented our research on fog top height (CTH) and liquid water path (LWP), which led to the formulation of a new conceptual model. This model relates the liquid water path of fog with its thickness, liquid water content at the surface (LWC_0), and adiabaticity. This model is used to study fog adiabaticity, and to analyze the fog life cycle in case studies and statistically. Additionally, it provided a new insight on the causes of adiabatic fog dissipation, and on the parameters that must be tracked to assess its dissipation tendency. The main results to retain from this chapter are:

- Fog LWP can be split in two different terms: one proportional to fog adiabaticity and the square of the CTH, and another which is the product of LWC_0 with fog CTH. The first term is analog to the LWP dependency on thickness for clouds (Braun et al., 2018). The second term is fog-exclussive, and is introduced by an excessive accumulation of water caused by the temperature inversion at fog top and the presence of the surface, which limit the vertical development of the layer.

- This excess of water with respect to an adiabatic cloud motivates the definition of two diagnostic parameters:

  - Critical LWP (CLWP): this is the minimum amount of LWP required to fill the fog layer (from fog top to the surface), and reduce visibility to 1000 m at the surface.

  - Reservoir LWP (RLWP): this is the difference between the LWP and the CLWP of a fog layer. It represents the excess of water that enables fog persistence. The RLWP is positive when fog is present, and reaches 0 g m^{-2} at the time of its formation and dissipation, when the LWP equals the CLWP.

- The model is used to statistically study fog adiabaticity. Important conclusions are that thinner fog, with a LWP less than 20 g m^{-2}, have adiabaticity values below 0.6, and can even reach negative values. This happens when the fog layer is not yet opaque during the fog formation stage, when LWC distribution is not even and may be larger closer to the surface. In this situation fog is not buoyant and therefore it may not lift when the RLWP reaches 0 g m^{-2}. Conversely, when fog is developed, its adiabaticity value gets closer to previously observed values for boundary layer fog, converging at approximately 0.66 for fog with a LWP greater than 30-40 g $m^{-}2$. Here the fog layer is adiabatic, and therefore the fog base should lift when the RLWP depletes down to 0 g m^{-2}. Adiabaticity results are highly variable for LWP values between 20-30 g m^{-2}, and therefore it may be necessary to include additional observations to discern the adiabaticity of the fog layer in this LWP range.

- Fog adiabaticity is correlated with fog CTH. Thin fog (CTH $<$ 200 m) has lower and highly variable adiabaticity values, ranging from -0.5 to 0.5. Negative values are associated with shallow fog that is not opaque to infrared radiation. For CTH $>$ 200 m, adiabaticity converges to 0.6 which is a value commonly observed in adiabatic fog and boundary layer clouds.

- The previous result enabled the derivation of a parametrization to calculate adiabaticity as a function of CTH. When the parametrized adiabaticity is used in the conceptual model, combined with measurements of fog top height, surface visibility and surface temperature and pressure, we get an estimation of fog LWP with a RMSE of 10.5 g m^{-2}, which is close to the uncertainty in the LWP measurements. Additionally, data shows that the predicted LWP captures correctly the observed effect of variations on LWC_0, temperature and CTH.

- The time derivative of the Reservoir LWP is calculated analytically. Its formulation enables the separation of LWP and CTH contributions to RLWP variations. A rise in LWP increases RLWP by the same amount. A rise in CTH reduces RLWP by an amount proportional to the CTH increase, to the adiabaticity and to the inverse of the saturation mixing ratio change with height ($\Gamma_{ad}(T, P)$).

- Statistics indicate that the Reservoir LWP increases systematically from 0 g m^{-2} for the first $\approx$60 minutes of a fog event, and decreases systematically during the last $\approx$60 minutes. Between these two periods, RLWP can oscilate under compensating LWP and CTH variations, sustaining a positive RLWP during fog middle life.

- When visibility is less than approximately 600 m, RLWP is not bound by surface visibility and can range between negative and $\approx$60 g m^{-2}, acting as an independent variable to describe fog status. On the contrary, when visibility is greater than approximately 600 m, the range of possible RLWP values becomes more restricted and more correlated with visibility.

- Fog may have temporary dissipation periods, when visibility increases above 1000 m. These time periods are included in a fog event because of the algorithm used for their identification. About 60% of the 80 fog events studied have at least one temporary dissipation period.

- RLWP and visibility measurements cannot be used to forecast if dissipation will be temporary or definitive. This happens because visibility increases to 1000 meters at the same time that RLWP

decreases to 0 g m^{-2} in the minutes preceding both dissipation types (strong correlation between visibility and RLWP). Therefore, calculated dissipation probabilities do not differentiate between temporary and definitive dissipation.

- RLWP improves the assessment of the dissipation tendency when visibility is less than 600 m:
  - For visibility < 600 m: fog layers contain an excess of LWP that is larger than the CLWP. The RLWP can range between +10 and +60 g m^{-2}, depending on the fog adiabaticity. To reach fog dissipation, the fog layer much reach a RLWP of 0 g m^{-2}, either by reducing its LWP or by increasing its CTH. As decreasing RLWP takes time, for a given visibility, a fog with a larger RLWP will be more likely to persist than a fog with a small RLWP. For example, the expected dissipation probability for samples with negative RLWP, and RLWP $\geq$ 20 g m^{-2}, can differ by up to 50%.
  - For visibility > 600 m: high visibilities are associated with periods close to fog formation or dissipation. In these cases, RLWP is highly correlated with visibility, and therefore it does not provide additional information about fog persistence or dissipation tendency.

- It is important to study how the variables of the conceptual model contribute to the uncertainty in the estimation of the CLWP, since uncertainties in the CLWP propagate directly to the RLWP. Therefore, we use the theory of error propagation to quantify the total uncertainty in the estimation of the CLWP and the contribution of each variable.

  As a reminder, the equation used to calculate the CLWP (previously presented in section 2.2) is:

$$CLWP = \frac{1}{2}\alpha_{eq}(CTH)\Gamma_{ad}(T,P)CTH^2 + LWC_cCTH \tag{2.1}$$

  The estimated uncertainty for each term is presented in the following lines:

  - CTH uncertainty is of 6.25 m, which is half the vertical resolution of the radar.
  - LWC_c relative uncertainty is of ≈50%, based on the publication of Gultepe et al. (2006), from where we obtained the parametrization to calculate LWC as a function of visibility. The critical LWC LWC_c is the LWC associated with a visibility of 1000 m.
  - $\Gamma_{ad}(T,P)$ uncertainty is neglected, since this is a theoretically calculated term ($\Gamma_{ad}(T,P)$ is the inverse of the saturation mixing ratio change with height).
  - The uncertainty of the equivalent adiabaticity $\alpha_{eq}(CTH)$ is estimated as the RMSE of the parametrization with respect to the samples used in its derivation. The results are shown in Fig. 2.7 (a).

- In Fig. 2.7 (a) we can observe that the RMSE is higher for CTH values below 200 m. This likely happens for two reasons. First, when LWP is less than 40 g m^{-2}, its retrieval with the microwave radiometer has an uncertainty of 5-10 g m^{-2} (Marke et al. (2016); Wærsted et al. (2017)). This possibly introduces a significant uncertainty when estimating adiabaticity from closure, for low LWP values (Eq. (6) of Sect. 2.2). Second, this CTH range is associated with the transition phase between shallow radiation and deep adiabatic fog, where adiabaticity may be highly variable due to physical causes. This would increase RMSE, since the parametrization only considers the median behavior.

  For CTH values greater than 200 m, the RMSE decreases sharply. This indicates that adiabaticity is less variable, probably because fog is mostly adiabatic when it reaches this CTH range.

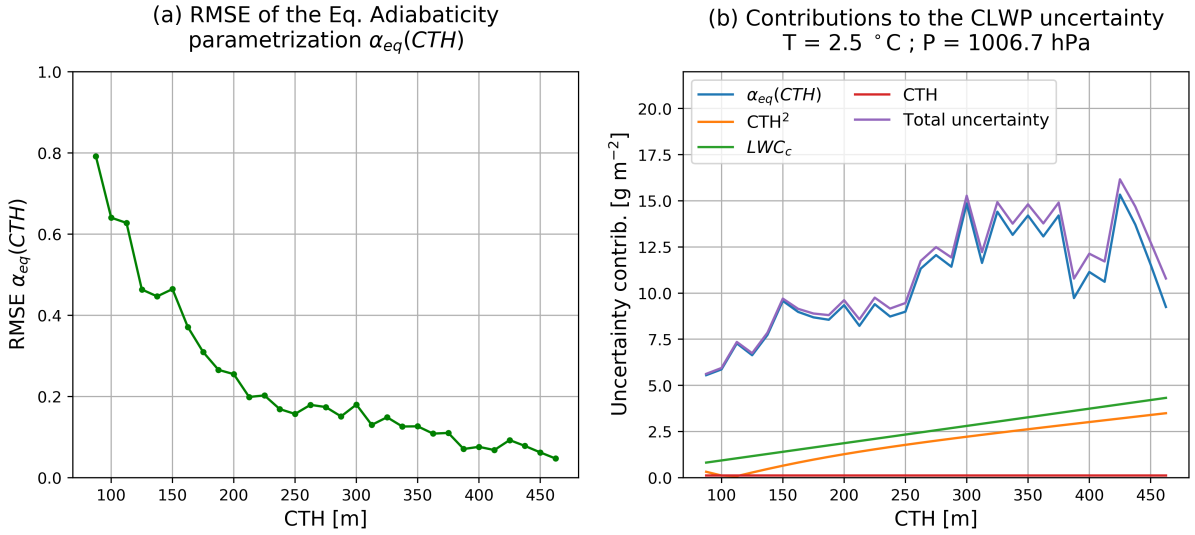

Figure 2.7: (a) RMSE of the adiabaticity parametrization. (b) Uncertainty of the CLWP calculated using error propagation, including the contribution of each term. The uncertainty in the calculation of the theoretical term $\Gamma_{ad}(T, P)$ (inverse of the saturation mixing ratio change with height) is neglected.

- Figure 2.7 (b) shows the contribution of each term to the absolute CLWP uncertainty (uncertainty in CLWP units of g m^{-2}). CLWP is calculated for 2.5 °C of temperature and 1006.7 hPa of pressure, as is done in Fig. 4 of section 2.2. We observe that the adiabaticity parametrization contributes most of the CLWP uncertainty for all CTH ranges. We also observe that the uncertainty of the latter is almost as high as the total uncertainty, reaching values between 5 and 15 g m^{-2}, depending on CTH.

  Another observation is that the uncertainty calculated with error propagation (5-15 g m^{-2}) is consistent with the uncertainty of 10.5 g m^{-2} estimated empirically, from comparisons between predicted and observed LWP (Fig. 5 of Sect. 2.2). The small differences between both results could be caused by possible correlated errors, and because we are comparing a CTH dependent uncertainty with a global result (calculated using all LWP values). However, we can conclude that at present, the uncertainty of conceptual model calculations should be of approximately ±10 g m^{-2}, and that uncertainty is mostly introduced by the adiabaticity parametrization.

- Since a RLWP error of 10 g m^{-2} could have a significant impact on the dissipation probability, it is important to improve the estimation of fog adiabaticity. This could be done, for example, by using cloud radar reflectivity profiles. Reflectivity, paired with other measurements, enable the retrieval of LWC profiles (Boers et al., 2013; Bell et al., 2021). Then, LWC profiles can be used to directly calculate fog adiabaticity. Unfortunately, such retrievals require a reliable calibration of the cloud radar, which is a topic that remains unsolved. This challenge motivates our work on cloud radar calibration, which is addressed in the next two chapters.

Chapter 3

Cloud radar calibration using corner reflectors

3.1 Introduction

The previous chapter addressed the study of fog, with the objective of better understanding the importance of fog top height (CTH) and liquid water path (LWP) on its life cycle. These variables were measured using remote sensing instruments. CTH is retrieved with a cloud radar, and LWP with a microwave radiometer.

The results provided new diagnostic variables that can be used to assess fog dissipation tendency. The main derived variable, which is the reservoir liquid water path (RLWP), depends on fog LWP, CTH, adiabaticity and surface visibility, temperature and pressure. At present, adiabaticity is calculated from a parametrization based on CTH. As is explained in Sect. 2.4, calibrated reflectivity measurements could improve RLWP estimation, by enabling a direct retrieval of the fog adiabaticity profile. Another benefit of calibrated reflectivity measurements is that it would enable comparative studies of data sampled at different fog monitoring stations. This motivates the use of calibrated cloud radars. However, at present there is no methodology that can be applied directly to calibrate a fog monitoring network, with various cloud radars.

This thesis addresses this challenge by developing a two-step calibration strategy. First, to calibrate a reference radar, with a known uncertainty, using corner reflectors. Second, to transfer the reference radar calibration to other radars in the network using clouds as common targets, to calibrate radars located in sites without the needed infrastructure for corner reflector based calibration.

This chapter presents the corner reflector based calibration methodology, developed to calibrate frequency modulated continuous wave cloud radars. In this approach, the radar samples the signal reflected from a corner reflector with a known Radar Cross Section (RCS), mounted on top of a mast. This signal is used as a reference to retrieve the calibration coefficients of the radar.

Calibration experiments were carried out during two calibration campaigns at the SIRTA observatory, using a scanning Basta mini cloud radar. This radar operates in the W band, with a carrier frequency that can be tuned between 94 and 96 GHz. It is equipped with two parallel 30 cm Cassegrain antennas, separated by 35 cm, and a 500 mW transmitter which can emit a chirp with a bandwidth of up to 24 MHz.

In this work we identify and quantify several sources of uncertainty that impacted the calibration results. Specifically, we study the impact of receiver compression, temperature variations inside the radar, frequency dependent losses in the IF of the receiver, environmental clutter and misalignment

of the experimental setup. The methods used to mitigate and quantify uncertainty are presented as a replicable calibration methodology, published in the Atmospheric Measurement Techniques journal (Toledo et al., 2020).

The article and its supplementary material are used to structure this chapter. Section 3.2 presents the article. In this paper, section 2 presents the definition of the calibration terms. Section 3 describes the experimental setup and equipment used. Section 4 presents the calibration methodology, which involved several repetitions of system realignment and sampling of the reflector signal. Section 5 presents all the sources of uncertainty and bias identified in the experiments. Section 6 shows the calibration results, including a table with the contributors to the final uncertainty value. Section 7 presents the conclusions of the article. Additionally, the article appendix A presents a table of symbols, which can be useful for the reader.

Sections 3.3 and 3.4 are based on the article supplementary material. They describe how to calculate the bias introduced by misalignment in the calibration setup, introduced in section 5.6 of the article. Specifically, section 3.3 presents a geometrical model to calculate the effective RCS of a corner reflector for a given incidence angle of the radar beam, considering the antenna lobe shape. Then, section 3.4 uses this model and a monte-carlo like approach to generate the bias probability distribution of the system. This distribution is used to estimate the most likely bias and its uncertainty. Finally, section 3.5 presents a synthesis with the main results.

To facilitate the lecture of this chapter, we recommend reading section 1.6 first. There we provide useful theoretical background on the radar equation and calibration terms.

3.2 Published paper: Absolute calibration method for frequency-modulated continuous wave (FMCW) cloud radars based on corner reflectors

Atmos. Meas. Tech., 13, 6853–6875, 2020
https://doi.org/10.5194/amt-13-6853-2020

Atmospheric Measurement Techniques
Open Access
EGU

Absolute calibration method for frequency-modulated continuous wave (FMCW) cloud radars based on corner reflectors

Felipe Toledo[1], Julien Delanoë[2], Martial Haeffelin[3], Jean-Charles Dupont[4], Susana Jorquera[2], and Christophe Le Gac[2]

[1]Laboratoire de Météorologie Dynamique, Institut Polytechnique de Paris, École Polytechnique, 91128 Palaiseau, France
[2]LATMOS/IPSL, UVSQ Université Paris-Saclay, Sorbonne Université, CNRS, 78280 Guyancourt, France
[3]Institut Pierre-Simon-Laplace, École Polytechnique, CNRS, Institut Polytechnique de Paris, 91128 Palaiseau, France
[4]Institut Pierre-Simon-Laplace, École Polytechnique, UVSQ, Université Paris-Saclay, 91128 Palaiseau, France

Correspondence: Felipe Toledo (ftoledo@lmd.polytechnique.fr)

Received: 24 December 2019 – Discussion started: 14 January 2020
Revised: 28 September 2020 – Accepted: 10 October 2020 – Published: 16 December 2020

Abstract. This article presents a new cloud radar calibration methodology using solid reference reflectors mounted on masts, developed during two field experiments held in 2018 and 2019 at the Site Instrumental de Recherche par Télédétection Atmosphérique (SIRTA) atmospheric observatory, located in Palaiseau, France, in the framework of the Aerosol Clouds Trace gases Research InfraStructure version 2 (ACTRIS-2) research and innovation program.

The experimental setup includes 10 and 20 cm triangular trihedral targets installed at the top of 10 and 20 m masts, respectively. The 10 cm target is mounted on a pan-tilt motor at the top of the 10 m mast to precisely align its boresight with the radar beam. Sources of calibration bias and uncertainty are identified and quantified. Specifically, this work assesses the impact of receiver compression, temperature variations inside the radar, frequency-dependent losses in the receiver's intermediate frequency (IF), clutter and experimental setup misalignment. Setup misalignment is a source of bias, previously undocumented in the literature, that can have an impact of the order of tenths of a decibel in calibration retrievals of W-band radars.

A detailed analysis enabled the quantification of the importance of each uncertainty source to the final cloud radar calibration uncertainty. The dominant uncertainty source comes from the uncharacterized reference target which reached 2 dB. Additionally, the analysis revealed that our 20 m mast setup with an approximate alignment approach is preferred to the 10 m mast setup with the motor-driven alignment system. The calibration uncertainty associated with signal-to-clutter ratio of the former is 10 times smaller than for the latter.

Following the proposed methodology, it is possible to reduce the added contribution from all uncertainty terms, excluding the target characterization, down to 0.4 dB. Therefore, this procedure should enable the achievement of calibration uncertainties under 1 dB when characterized reflectors are available.

Cloud radar calibration results are found to be repeatable when comparing results from a total of 18 independent tests. Once calibrated, the cloud radar provides valid reflectivity values when sampling midtropospheric clouds. Thus, we conclude that the method is repeatable and robust, and that the uncertainties are precisely characterized. The method can be implemented under different configurations as long as the proposed principles are respected. It could be extended to reference reflectors held by other lifting devices such as tethered balloons or unmanned aerial vehicles.

1 Introduction

Clouds remain, to this day, one of the major sources of uncertainty in future climate predictions (Boucher et al., 2013; Myhre et al., 2013; Mülmenstädt and Feingold, 2018). This arises partly from the wide range of scales involved in cloud systems, where a knowledge of cloud microphysics, particularly cloud–aerosol interactions, is critical for predicting

large-scale phenomena such as cloud radiative forcing or precipitation.

To address this and other related issues, the Aerosol Clouds Trace gases Research InfraStructure (ACTRIS) is establishing a state-of-the-art ground-based observation network (Pappalardo, 2018). Within this organization, the Centre for Cloud Remote Sensing (CCRES) is in charge of creating and defining calibration and quality assurance protocols for the observation of cloud properties across the complete network.

One of the key instruments for cloud remote sensing stations is cloud radar. Cloud radars enable retrievals of several relevant parameters for cloud research including, but not limited to, liquid water and ice content profiles, cloud boundaries, cloud fraction, precipitation rate and turbulence (Fox and Illingworth, 1997; Hogan et al., 2001; Wærsted et al., 2017; Dupont et al., 2018; Haynes et al., 2009). Additionally, recent studies revealed the potential of cloud radars to support a better understanding of fog processes (Dupont et al., 2012; Boers et al., 2013; Wærsted et al., 2019).

However, calibration remains a crucial factor in the reliability of radar-retrieved data (Ewald et al., 2019). Systematic differences of 2 dB have already been observed, for example, between the satellite-based radar CloudSat and the Lindenberg microwave radar (MIRA) (Protat et al., 2009). This is a very important issue since calibration errors as small as 1 dB would already introduce uncertainties in liquid water and ice content retrievals of the order of 15 %–20 % (Fox and Illingworth, 1997; Ewald et al., 2019).

Since the objective of the CCRES is to guarantee a network of high-quality observations, it is essential to develop standardized and repeatable calibration methods for its instrumental network.

This paper presents an absolute calibration method for W-band radars. It has been developed based on results from two experimental calibration campaigns performed at the Site Instrumental de Recherche par Télédétection Atmosphérique (SIRTA) atmospheric observatory located in Palaiseau, France (Haeffelin et al., 2005). The SIRTA observatory hosts part of the ACTRIS CCRES infrastructure. For the experiments, we used a BASTA mini W-band frequency-modulated continuous wave (FMCW) radar with scanning capabilities (Delanoë et al., 2016). Nevertheless, the principles, procedures and limitations presented here should be applicable for any radar with similar characteristics, even when operating in another frequency band.

The method consists of an end-to-end calibration approach, which consists of retrieving the radar calibration coefficient by sampling the power reflected from a reference reflector mounted on top of a mast (Chandrasekar et al., 2015). A detailed analysis of uncertainty and bias sources is performed, with the objective of determining how to improve the experiment to reach a calibration uncertainty lower than 1 dB. This low uncertainty in the calibration would not only be useful for high-quality retrievals but would also enable the use of the radar as a reliable reference for calibration transfer to other ground- or space-based cloud radars (Bergada et al., 2001; Protat et al., 2011; Ewald et al., 2019).

The article is structured as follows: Sect. 2 presents the equations and theoretical considerations involved in the calibration exercise. Section 3 shows the experimental setup, complemented by Sect. 4 in which the experimental procedure and data treatment are presented. Section 5 presents an analysis of the sources of uncertainty and bias involved in our calibration experiment. Section 6 presents the final calibration results, the uncertainty budget and an analysis of the variability in the calibration bias correction, followed by the conclusions.

2 Equations used in radar calibration

The absolute calibration of a radar consists of determining the radar cross section (RCS) calibration term C_Γ and the radar equivalent reflectivity calibration term C_Z. They enable the calculation of radar cross section $\Gamma(r)$ (RCS) or radar equivalent reflectivity Z_e, respectively, from the power backscattered by a punctual or distributed target towards the radar (Bringi and Chandrasekar, 2001).

Equation (2a) presents an expression for the RCS calibration term $C_\Gamma(T, F_\mathrm{b})$ of a FMCW radar as a function of its internal parameters. The deduction of this expression is shown in the Supplement. G_t and G_r are the maximum gains of the transmitting and receiving antennas, respectively, and are unitless. λ is the wavelength of the carrier wave in meters, and p_t is the power emitted by the radar in milliwatts.

The gain of solid-state components changes with variations in their temperature. Thus, we make this dependence explicit in the receiver loss budget $L_\mathrm{r}(T, F_\mathrm{b})$ and in the transmitter loss budget $L_\mathrm{t}(T)$. Loss budgets are the product of all losses divided by the gain terms at the end of the receiver or emitter chain and are unitless.

Additionally, a range dependence is included in $L_\mathrm{r}(T, F_\mathrm{b})$ to account for variations in the receiver's intermediate frequency (IF) loss for different beat frequency F_b values. The beat frequency in FMCW radars is proportional to the distance between the instrument and the backscattering element (Delanoë et al., 2016). Thus, changes in the IF loss for different beat frequencies introduce a range-dependent bias. For the 12.5 m resolution mode used in this calibration exercise, F_b ranges between 168 and 180 MHz and can be related to r (in meters) using Eq. (1).

$$r = 500 \cdot (F_\mathrm{b} - 168\,[\mathrm{MHz}])\,. \tag{1}$$

In theory, $C_\Gamma(T, F_\mathrm{b})$ can be calculated by characterizing the gains and losses of every component inside the radar system and adding them. This can be very challenging, depending on the complexity of the radar hardware and the available radio frequency analysis equipment. In addition, with

this procedure it is not possible to quantify losses due to interactions between different components, especially changes in antenna alignment or radome degradation (Anagnostou et al., 2001). This motivates the implementation of an end-to-end calibration, which consists of the characterization of the complete radar system at once by using a reference reflector and Eq. (2b).

$$C_\Gamma(T, F_\mathrm{b}) = 10\log_{10}\left(\frac{L_\mathrm{t}(T) L_\mathrm{r}(T, F_\mathrm{b})(4\pi)^3}{G_\mathrm{t} G_\mathrm{r} \lambda^2 p_\mathrm{t}}\right) \quad (2a)$$

$$\Gamma(r) = C_\Gamma(T, F_\mathrm{b}) + 2L_\mathrm{at}(r) + 40\log_{10}(r) + P_\mathrm{r}(r). \quad (2b)$$

Equation (2b) links the calibration term $C_\Gamma(T, F_\mathrm{b})$ to the RCS $\Gamma(r)$ of a target at a distance r. $\Gamma(r)$ is expressed in units of decibels per square meter (dBsm), $L_\mathrm{at}(r)$ is the atmospheric attenuation between the object and the radar in decibels (dB), which can be calculated using a millimeter-wave attenuation model (e.g., Liebe, 1989). $P_\mathrm{r}(r)$ is the power received from the target in decibel milliwatts (dBm), and $C_\Gamma(T, F_\mathrm{b})$ is the RCS calibration term in $\mathrm{dB(m^{-2}\,mW^{-1})}$. The $\mathrm{dB(m^{-2}\,mW^{-1})}$ unit is the abbreviation of decibels referenced as $1\,\mathrm{m^{-2}\,mW^{-1}}$. The units in the RCS calibration term compensate the radar power units, guaranteeing the retrieval of physical RCS values. The explicit temperature and range dependency of the calibration term has the function of compensating gain changes in $P_\mathrm{r}(r)$ introduced by temperature effects and variations in the IF loss with distance.

This principle can be used in an end-to-end calibration by installing a target with a known RCS Γ_0 at a known distance r_0 and sampling the power $P_\mathrm{r}(r_0)$ reflected back to calculate $C_\Gamma(T, F_\mathrm{b})$. However, some additional considerations must be made to perform this retrieval.

In Eq. (2a), we state that the calibration value has a temperature and a range dependency. Experimental results indicate that the temperature dependency of $C_\Gamma(T, F_\mathrm{b})$ can be approximated by a linear relationship, as shown in Eq. (3). Here n is the temperature dependency term in $\mathrm{dB\,°C^{-1}}$, T the internal radar temperature in °C and T_0 is a reference temperature value in degrees Celsius. More details about the temperature correction can be found in Sect. 5.4.

The range dependence of $C_\Gamma(T, F_\mathrm{b})$ is treated independently by defining a IF loss-correction function, $f_\mathrm{IF}(F_\mathrm{b})$, in decibels. This function is introduced to compensate for relative loss variations at different IF frequencies. The IF loss-correction function is studied in Sect. 5.5.

From the aforementioned observations, we divide $C_\Gamma(T, F_\mathrm{b})$ into three components, as shown in Eq. (3). This separation consists of a constant calibration coefficient C_Γ^0, in $\mathrm{dB(m^{-2}\,mW^{-1})}$, and the two correction functions $n(T - T_0)$ and $f_\mathrm{IF}(F_\mathrm{b})$.

$$C_\Gamma(T, F_\mathrm{b}) = C_\Gamma^0 + n(T - T_0) + f_\mathrm{IF}(F_\mathrm{b}). \quad (3)$$

As $f_\mathrm{IF}(F_\mathrm{b})$ corrects for relative variations in receiver loss with distance, we define $f_\mathrm{IF}(F_0) = 0$ at the IF frequency value F_0, which is associated to the reflector position r_0 (linked by Eq. 1). Using this and Eqs. (2b) and (3), we obtain Eqs. (4a) and (4b).

$$C_\Gamma(T, F_0) = C_\Gamma^0 + n(T - T_0) \quad (4a)$$

$$C_\Gamma(T, F_0) = \Gamma_0 - 40\log(r_0) - 2L_\mathrm{at}(r_0) - P_\mathrm{r}(r_0). \quad (4b)$$

Equation (4a) shows how the calibration term $C_\Gamma(T, F_0)$ at position r_0 is related to the calibration coefficient C_Γ^0 and the temperature correction $n(T - T_0)$. Meanwhile, Eq. (4b) indicates how experimental $P_\mathrm{r}(r_0)$ measurements can be associated with a $C_\Gamma(T, F_0)$ value, using in situ information to calculate $2L_\mathrm{at}(r_0)$. Then, using Eq. (4a), we can compute C_Γ^0 by subtracting the temperature correction function $n(T - T_0)$. This temperature correction is derived independently in Sect. 5.4. Knowing C_Γ^0 and the temperature correction, $C_\Gamma(T, F_\mathrm{b})$ is calculated by adding the IF correction function, which is independently retrieved in Sect. 5.5.

Once $C_\Gamma(T, F_\mathrm{b})$ is known, we can calculate the radar equivalent reflectivity calibration term $C_Z(T, F_\mathrm{b})$, in $\mathrm{dB(mm^6\,m^{-5}\,mW^{-1})}$, with Eq. (5a) (Yau and Rogers, 1996). This relationship assumes that the radar has two identical parallel antennas with a Gaussian-shaped main lobe. θ is the antenna beamwidth in radians, $m\delta r$ is the radar distance resolution in meters, and $|K| = |(\epsilon_\mathrm{r} - 1)/(\epsilon_\mathrm{r} + 2)|$ is the dielectric factor. This factor is related to the relative complex permittivity ϵ_r of the scattering particles and can be calculated, for example, using the results of Meissner and Wentz (2004).

$C_Z(T, F_\mathrm{b})$ enables the calculation of the radar equivalent reflectivity Z_e, in decibels relative to Z (dBZ), of a distributed target located at a distance r by using Eq. (5b). The dBZ unit is usually used to express radar equivalent reflectivity in logarithmic units and is related to the linear units by $1\,\mathrm{dBZ} = 10\log_{10}(1\,\mathrm{mm^6\,m^{-3}})$.

$$C_Z(T, F_\mathrm{b}) = 10\log_{10}\left(\frac{8\ln(2)\lambda^4 10^{18}}{\theta^2 \pi^6 K^2 \delta r}\right) + C_\Gamma(T, r) \quad (5a)$$

$$Z_\mathrm{e}(r) = C_Z(T, F_\mathrm{b}) + 2L_\mathrm{at}(r) + 20\log_{10}(r) + P_\mathrm{r}(r). \quad (5b)$$

3 Experimental setup

Two calibration campaigns that lasted one month each were performed in May–June of 2018 and March–April of 2019 at the SIRTA observatory located in Palaiseau, France (Haeffelin et al., 2005). The observatory has a 500 m long grass field in an area free of buildings, trees or other sources of clutter, making it well suited to the installation of our calibration setup, as shown in Fig. 1.

The instrument used for the calibration experiments is a BASTA mini radar. The BASTA mini is a 95 GHz FMCW radar with scanning capabilities and two parallel Cassegrain antennas (Delanoë et al., 2016). The antennas are separated

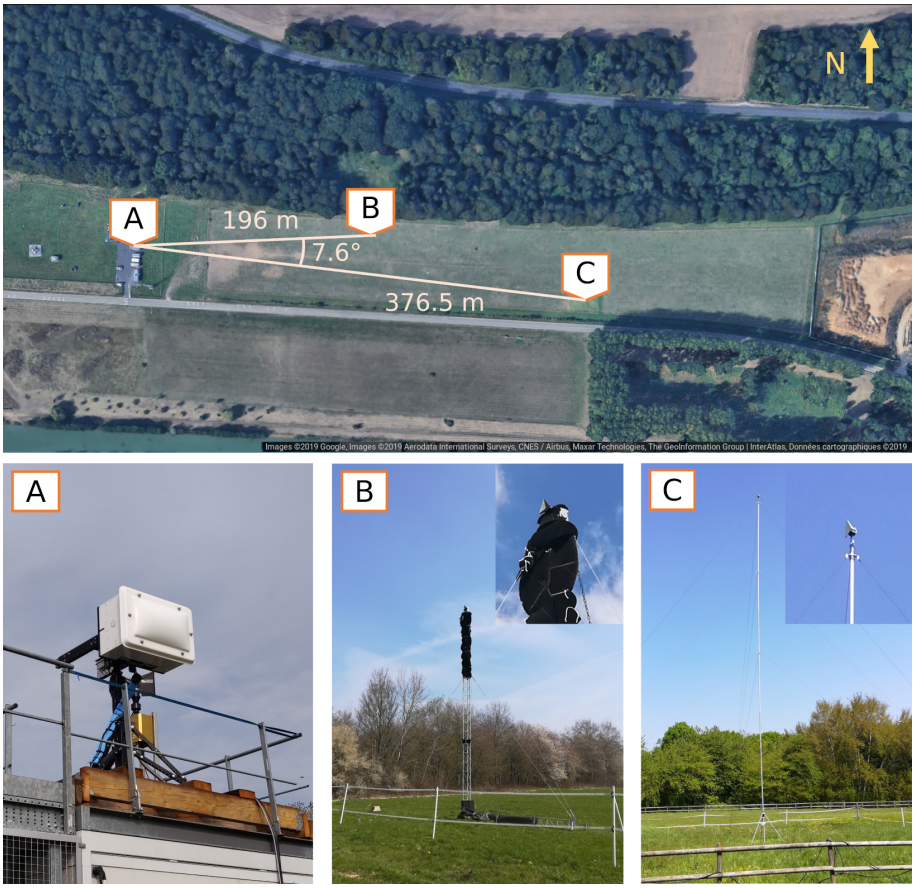

Figure 1. Experimental setup for 2018 and 2019 calibration experiments. (A) Scanning BASTA mini radar located on a reinforced platform 5 m above the ground. (B) A 10 m mast with a 10 cm triangular trihedral target mounted on a pan-tilt motor with an angular resolution and repeatability better than 0.1 °. This mast has microwave-absorbing material wrapped around it to reduce its radar cross section (RCS; clutter). The 10 m mast was only installed in the 2019 calibration campaign. (C) A 20 m mast with a 20 cm triangular trihedral target. The target aiming is fixed relative to the mast. This mast was used in both 2018 and 2019 calibration campaigns. Angular separation between the masts is enough to sample both targets without mutual interference.

by 35 cm and have a Fraunhofer far-field distance of ≈ 50 m, with a Gaussian-shaped main lobe (verified experimentally in Sect. 5.2). Transmitted power is fixed to 500 mW and is under constant monitoring, using a diode with an uncertainty of ≈ 0.4 dB. The diode enables the monitoring of $L_t(T)$ variations, yet our experiments have shown that T is a better indicator for capturing the variability in $C_\Gamma(T, F_b)$. This is likely because internal temperature changes affect both $L_r(T, F_b)$ and $L_t(T)$ simultaneously, and therefore, the information provided by the diode is not sufficient for capturing the behavior of the whole system. The results of the temperature dependency study for our radar are shown in Sect. 5.4.

This radar also includes hardware to enable the tuning of the carrier wave frequency within a range of ≈ 1 GHz, centered at 95 GHz. During the experiments, we fixed the BASTA mini base frequency at 95.64 GHz to avoid any interference with the other two W-band radars operating in parallel at the same site.

Our reference targets are two triangular trihedral reflectors (also known as corner reflectors) composed of three orthogonal triangular conducting plates. Trihedral targets have a large RCS for their size and a low angular variability in RCS around their boresight (Atlas, 2002; Brock and Doerry, 2009; Chandrasekar et al., 2015). One reflector has a size parameter of 10 cm, with a maximum theoretical RCS at our radar operation frequency of 16.30 dBsm. The other is 20 cm, with a maximum theoretical RCS of 28.34 dBsm (Brooker, 2006). These targets were mounted on top of masts B and C in Fig. 1, respectively. Only mast C was used in the 2018 campaign, while both were used in 2019.

To align the system, first, we aim the radar towards the approximate position of the target. Second, we aim the target by slowly changing the pan-tilt angles in the motor on mast B or axially rotating the tube of mast C to maximize the power $P_r(r_0)$ measured at the radar. Third, radar aiming is tuned around the target position until the maximum reflected power

is found. Finally, we repeat the second step, after which we have the system ready to sample $P_r(r_0)$.

It must be mentioned that this procedure does not guarantee a perfect alignment. In fact, it is impossible to have every element perfectly adjusted because of limits in the radar scanner resolution or uncertainties introduced when installing each element. Sections 4 and 5.6 explain how we deal with these limitations.

4 Methodology

This section describes the procedure followed when performing calibration experiments using the setup described in Sect. 3. The methodology has the objective of quantifying and correcting, when possible, all sources of uncertainty to enable a reliable estimation of the calibration terms $C_\Gamma(T, F_b)$ and $C_Z(T, F_b)$.

A challenge we found when using targets mounted on masts to estimate $C_\Gamma(T, F_b)$ is that the value of the target RCS Γ_0 may vary, depending on how components are aligned. Our studies have shown that, for the feasible alignment accuracy we can obtain when installing our setup, this effect is of the order of tenths of a decibel and therefore not negligible. Additionally, we concluded that, if we leave this uncertainty source uncorrected, we would introduce a bias in the calibration result (see Sect. 5.6).

The flow chart of Fig. 2 illustrates the calibration procedure. To quantify the bias introduced by alignment uncertainty, we decided to divide each calibration experiment into N iterations. Each iteration consists of a system realignment, followed by sampling of the target signal $P_r(r_0)$ for at least 1 h. Then, we select the data from the contiguous hour with the lowest variability as the iteration result.

The period chosen to perform the sampling is important because it will have an incidence on how stable the calibration value is. To minimize uncertainty, it is recommended that calibration iterations are performed when the atmosphere is clear, there is no rain and wind speed is under $1\,m\,s^{-1}$. However, these requirements may change, depending on how robust is each setup to atmospheric conditions.

FMCW radars have a discrete distance resolution. Consequently, power measurements vs. distance are resolved in finite discrete points usually named gates. Because of this resolution limitation, the power received from a point target is spread between the gates closer to its position (Doviak and Zrnić, 2006). This phenomena is known as spectral leakage. To reduce leakage, BASTA mini uses a Hann time window (Richardson, 1978; Delanoë et al., 2016).

To correctly assess the total reflected power, we set the radar resolution to 12.5 m (chirp bandwidth of 12 MHz) and its integration time to 0.5 s. This resolution is high enough to accurately identify the reference reflector signal while avoiding the introduction of additional clutter from the trees located behind the mast (see Fig. 3).

To calculate $P_r(r_0)$, we add five gates, namely the target gate plus two before and two after the target position. Adding more contiguous gates increases the power value by less than 0.01 dB; thus, we conclude that these five gates concentrate almost all the power reflected back from the target.

Then $P_r(r_0)$ is corrected considering compression effects and antenna overlap losses (Sect. 5.1 and 5.2). For each corrected $P_r(r_0)$ sample, we proceed to calculate a single C_Γ^0 value with Eq. (4a) and the temperature correction function. This single sample is defined as $C_{\Gamma s}^0$ to differentiate it from the final calibration coefficient C_Γ^0 of Eq. (3). Atmospheric attenuation $L_{at}(r_0)$ is calculated using in situ atmospheric observations and the model published by Liebe (1989).

The target-effective RCS Γ_0 is calculated using a theoretical RCS model, considering the beam incidence angle on the target. Echo chamber measurements have shown that real targets of RCS can be deviated from the theoretical value, depending on the manufacturing precision. Our corner reflectors have an angular manufacturing precision better than 0.1°; therefore, real RCS uncertainty with respect to the model can be roughly estimated to be approximately 2 dB (Garthwaite et al., 2015). Once an experimental characterization of the target becomes available, it can be used to correct any calibration bias and to reduce uncertainty by rectifying the value of Γ_0 used in the calculations.

We performed one calibration experiment with six iterations during the 2018 campaign using the 20 m mast. In the 2019 campaign, we did two experiments, namely one with 10 iterations, using the 10 m mast, and another with two iterations on the 20 m mast (Fig. 1).

The retrieval of the temperature dependency coefficient n and the reference temperature T_0 is done simultaneously with the calibration coefficient experiment by extending the sampling period beyond 1 h when using the 20 m mast. This is done to capture the temperature effect in the variability in $C_{\Gamma s}^0$ by capturing a larger part of the temperature daily cycle. The results of this experiment can be seen in Sect. 5.4. Likewise, the retrieval of the IF correction function $f_{IF}(F_b)$ is an independent experiment based on sampling noise with the radar to obtain the IF amplification curve of the receiver. The details of this experiment are in Sect. 5.5.

From each iteration, we obtain a distribution of resulting $C_{\Gamma s}^0$ values with a small spread introduced by second-order effects. The average value of each iteration i is named $C_{\Gamma i}^0$, and its corresponding standard deviation is named σ_i. With this information, we proceed to calculate the bias-corrected calibration coefficient C_Γ^0 by using Eq. (6). $\tilde{\Lambda}$ is the bias-correction term. The method used to calculate λ relies on simulating the probability distribution of Γ_0 for a given set of uncertainties in the setup parameters. More detail can be found in Sects. 5.6 and S3 in the Supplement.

$$C_\Gamma^0 = \frac{1}{N}\sum_{i=1}^{N} C_{\Gamma i}^0 - \tilde{\Lambda}. \tag{6}$$

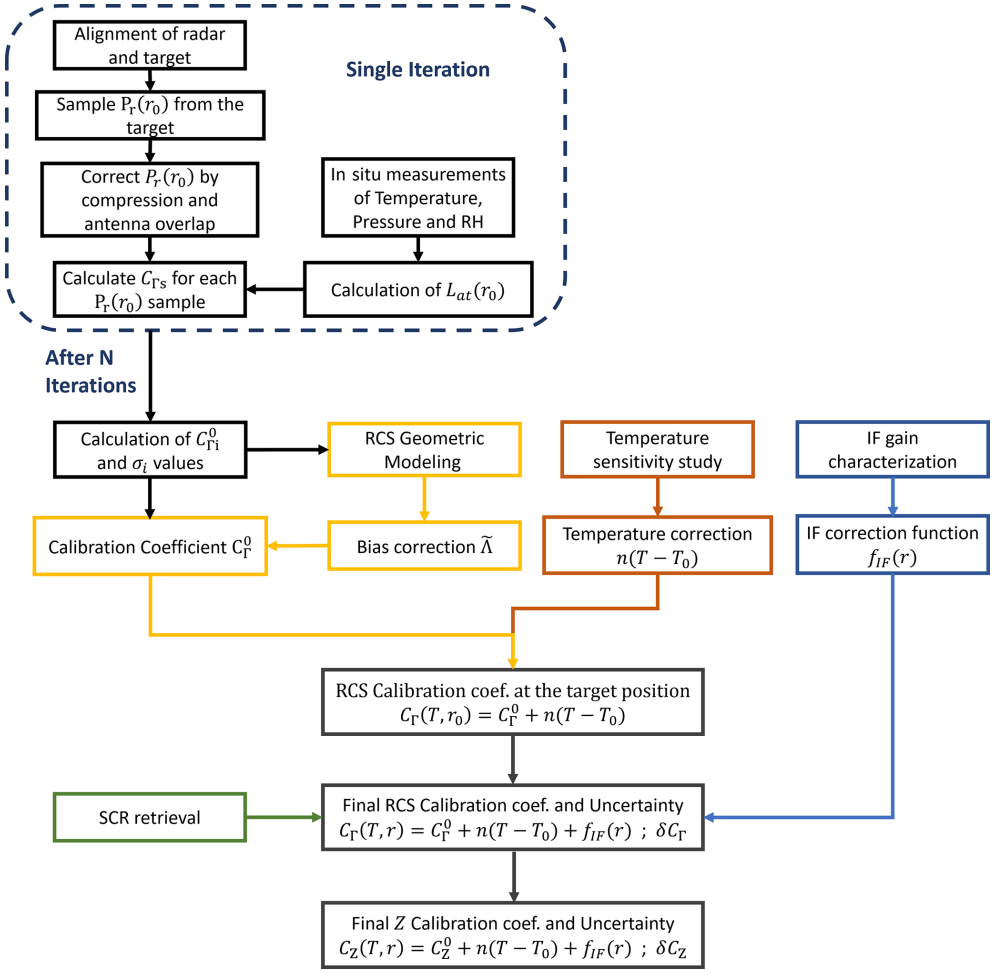

Figure 2. Summary of a complete calibration process. Each calibration requires the repetition of system realignment and sampling steps called iterations. During each iteration, we continuously sample the power reflected from the reference target position for 1 h (power corrections in Sect. 5.1). The retrieval of N iterations enables the estimation of the system bias due to misalignments in the setup (Sect. 5.6). Temperature dependency is retrieved in an independent experiment (Sect. 5.4). Uncertainty introduced by clutter signals at the target location is also included in the total uncertainty budget (Sect. 5.3).

Equations (7a) and (7b) show the uncertainties δC_Γ and δC_Z associated with the estimation of $C_\Gamma(T, F_b)$ and $C_Z(T, F_b)$, respectively.

σ_T is the uncertainty term associated with the temperature correction function $n(T - T_0)$.

σ_{IF} is the uncertainty term associated with the IF loss correction function $f_{IF}(F_b)$.

The term $\sum \sigma_i^2$ comes from the averaging operation in the estimation of $C^0_{\Gamma i}$ (Eq. 6). Since the $C^0_{\Gamma i}$ terms are corrected using the temperature correction function, the uncertainty of the latter must be propagated as well; hence, the term σ_T^2/N appears.

σ_Λ is the uncertainty of the bias correction calculation. It is calculated from the standard deviation σ_i. This procedure is explained in Sect. S3.

σ_{SCR} is the uncertainty introduced by clutter. Clutter is the presence of unwanted echoes, which affect our reading of $P_r(r_0)$, coming from reflections on other objects in the environment. The method of quantifying the uncertainty σ_{SCR} uses a parameter named signal-to-clutter ratio (SCR), which is explained in detail in Sect. 5.3.

σ_{Γ_0} is the uncertainty of the reference target RCS. In this work, we use a theoretical model to calculate the target-effective RCS, which has an uncertainty of approximately 2 dB based on the manufacturing characteristics. The inclusion of an experimental characterization of the target RCS can improve the estimation of C^0_Γ and δC_Γ by reducing this uncertainty term.

σ_K is the uncertainty in the estimation of the backscattering particles dielectric factor. Because our objective is to calculate the calibration term of the radar, we reference this value to $|K| = 0.86$, corresponding to pure water at 5 °C, and neglect the δ_K uncertainty term. However, the value of K and its uncertainty σ_K must be considered when performing

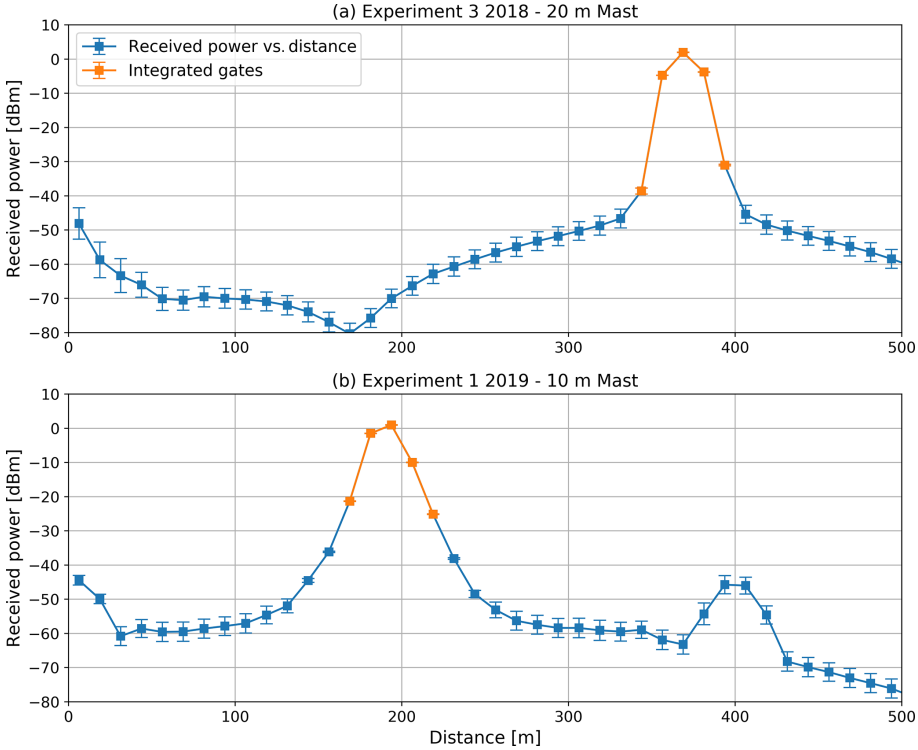

Figure 3. Mean profiles of received power for experiment 5 in 2018, using the 20 m mast **(a)**, and experiment 1 in 2019, using the 10 m mast **(b)**. Standard deviation at each gate is indicated with an error bar. The gates are integrated to calculate the reference reflector, and the backscattered power $P_r(r_0)$ is marked in orange. The secondary peak of panel **(b)**, around 400 m, corresponds to reflections on trees behind the 10 m mast.

radar retrievals (e.g., Sassen, 1987; Liebe et al., 1989; Gaussiat et al., 2003).

σ_A is the uncertainty introduced in the estimation of θ and from parallax errors and deviations from a Gaussian beam shape (Sekelsky and Clothiaux, 2002). For this work, we make the assumption of parallel antennas with a Gaussian beam shape; thus, we neglect this term. This problem is discussed more in depth in Sect. 5.2.

Since both σ_K and σ_A are neglected, we obtain $\delta C_\Gamma \approx \delta C_Z$.

$$\delta C_\Gamma(T, F_b) = \sqrt{\frac{1}{N^2}\sum_{i=1}^{N}\sigma_i^2 + \frac{\sigma_T^2}{N} + \sigma_{IF}^2 + \sigma_T^2 + \sigma_{SCR}^2 + \sigma_\Lambda^2 + \sigma_{\Gamma_0}^2} \quad (7a)$$

$$\delta C_Z(T, F_b) = \sqrt{\delta C_\Gamma^2 + \sigma_K^2 + \sigma_A^2}. \quad (7b)$$

5 Sources of uncertainty and bias in absolute calibration with corner reflectors

In this section, we identify and quantify the uncertainty and bias introduced by several terms in Eq. (2b). Following the recommendations in the work of Chandrasekar et al. (2015), we study the impact of receiver saturation, signal-to-clutter ratio, antenna lobe shape and antenna overlap. Additionally, we consider the impact of temperature fluctuations inside the radar box, loss changes with distance due to uneven amplification at the receiver's IF and the effects of imperfect alignment of the reference target.

5.1 Receiver compression

It is advisable to design calibration experiments which avoid the appearance of compression effects. If this is not possible, compression must be considered in the data treatment so that the retrieved calibration remains valid in the receiver linear regime, where it usually operates during cloud sampling (Scolnik, 2000).

To study how these effects could affect our calibration, we retrieved the radar receiver power transfer curve. Receiver characterization was done by removing the radar antennas and connecting the emitter end to the receiver input with two attenuators in between. The first was a 40 dB fixed attenuator, while the second was a tunable attenuator covering the range between 50 and 1 dB of losses. The adjustable attenuator enabled the retrieval of the power transfer curve by varying the attenuation and sampling the power at the receiver end (digital processing included). Our retrieved power transfer curve is shown in Fig. 4a.

Compression effects must be considered in calibration, or a bias will be introduced. As a consequence, we include com-

pression correction in every sample of reflected power, which consists of projecting their value to the ideal linear response using the power transfer curve.

For example, the power received from the 20 cm target on the 20 m mast returned was 4.1 dBm, on average, before corrections. The power transfer curve shows that, at this power value, we have a loss caused by a compression of ≈ 0.3 dB. After correcting each power sample by compression with the power transfer curve, we obtain a corrected power average value of 4.5 dBm. Meanwhile, for the 10 cm target on the 10 m mast, the average power value before corrections is 3.2 dBm. As this value is lower than what is obtained by the 20 m mast, the associated compression effect is also smaller at ≈ 0.2 dB. After applying this correction to each power sample, we end with a new, corrected power average of 3.4 dBm.

5.2 Antenna properties

Manufacturer specifications indicate that antenna beamwidth should be 0.8°. However, data from an experimental characterization done by the same manufacturer in an anechoic chamber indicate that antenna beam shape is better approximated by a Gaussian function with a half-power beam width (HPBW) of $\theta \approx 0.88°$. The integrated gain difference between the experimentally retrieved curve and the Gaussian function is of ≈ 0.0003 dB in the HPBW region. Therefore, we conclude that the contribution to uncertainty introduced by assuming a Gaussian beam shape is negligible. The antenna beam shape and Gaussian curve are shown in Fig. 4b.

Another source of bias introduced by the antennas is the parallax error. Antenna parallax errors introduce a range-dependent bias determined by the antenna beamwidth and the relative angles of deviation between the antennas' boresight. This bias is usually larger in the first few 100 m closest to the radar. For example, for a deviation of half of the antenna beamwidth, losses would be of the order of 10 dB and would vary significantly over the first hundreds of meters, decreasing with distance to about 1 dB at a approximately 4 km (Sekelsky and Clothiaux, 2002).

To study this effect, we took advantage of our experimental setup and the scanning capabilities of the radar to check if the radar antennas were properly aligned. This was done by using the target on the 20 m mast. Results are shown in Fig. 4b. After analyzing the results, we observed that the aiming uncertainty is of the same order of magnitude as the antennas' beamwidth. Since the correction of the parallax error requires a very precise measurement of antenna alignment, we conclude that it is not possible to directly correct for antenna deviations with this information.

However, the relatively small difference of 0.5 dB in the estimation of C_Γ^0 during the calibration experiments of 2019, obtained using two masts in the most sensitive distance range (placed at a distance of 196 and 376.5 m, respectively), indicate that antennas are unlikely to have a deviation comparable to their beamwidth (calibration results in Sect. 6).

Therefore, for the present version of this calibration methodology, we assume that both antennas are parallel and that they have a Gaussian beam lobe. Once a reliable method for antenna pattern retrieval is developed for W-band radars, it can be directly incorporated into the calibration term by adding an additional correction function $f_A(r)$ to Eq. (3). The uncertainty in this alignment estimation can also be included in the uncertainty budget with the term σ_A of Eq. (7b).

Even if the antennas are parallel, it is necessary to include a correction for the loss $L_o(r)$ caused by incomplete antenna overlap. The correction, shown in Eq. (8), accounts for the loss in power that would be received from a point target compared to a monostatic system (Sekelsky and Clothiaux, 2002). This loss occurs because a point target cannot be in the center of two nonconcentric parallel antenna beams.

$$L_o(r) = \exp\left(\frac{2\arctan(\frac{d}{2r})^2}{0.3606\theta^2}\right). \tag{8}$$

Equation (8) assumes that the radar has two identical, parallel antennas with Gaussian beam lobes. Their main axis is separated by a distance d, and the point target is located at a distance r, facing the geometrical center of the radar, where the gain is maximum. The antenna separation d of BASTA mini is of 35 cm, introducing a loss of 0.08 dB for the target at $r_0 = 196$ m and of 0.02 dB for the target at $r_0 = 376.5$ m.

5.3 Signal-to-clutter ratio

The power sampled from our reference reflector is an addition of the power from the target (signal) and unwanted reflections on other elements in the environment, such as the ground or the mast (clutter). We observed that this clutter dominates above the radar noise, and thus becomes the main source of interference in our calibration signal.

To quantify the impact of clutter, we use the signal-to-clutter ratio (SCR) parameter. It is calculated as the ratio of total power received from the target to the power received from clutter under the same configuration but with the reference reflector removed. SCR enables the uncertainty σ_{SCR} introduced by clutter in the sampled $P_r(r_0)$ values to be computed (Chandrasekar et al., 2015).

Clutter power is sampled and corrected following the same methodology used for reflector $P_r(r_0)$ retrievals but in an scanning pattern mode to capture clutter around the mast area. Figure 5 shows our results from scanning around the 10 and 20 m masts with the targets removed.

We observe that the 10 m mast is more reflective than the 20 m one. This may be caused by its smaller height (more ground clutter) and its larger geometrical cross section. We can also see that the signal at the 10 m mast is stronger where absorbing material is not present (below $\approx 1.5°$ of elevation).

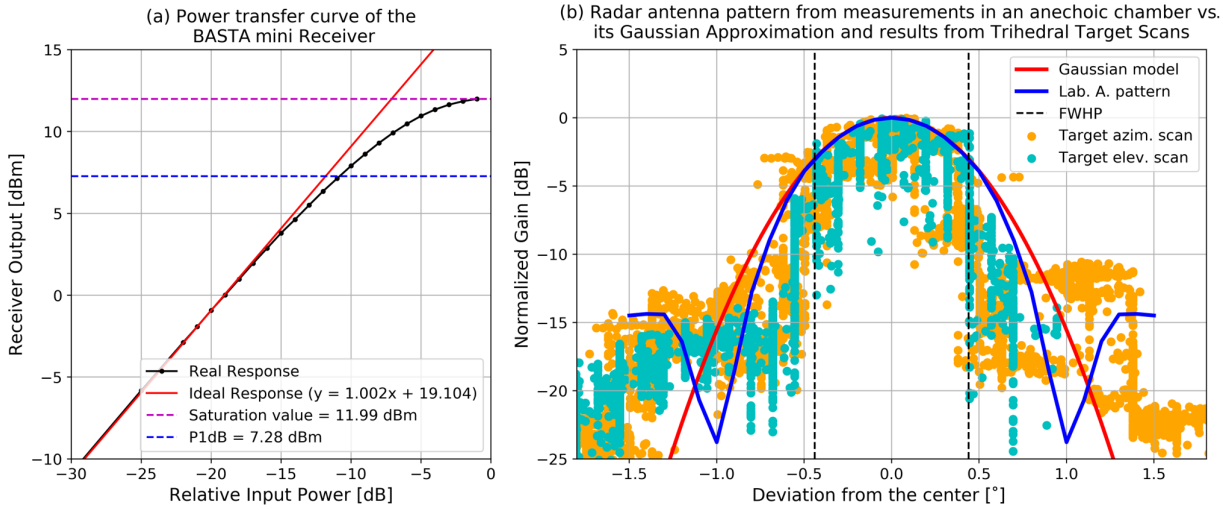

Figure 4. **(a)** Power transfer curve of the BASTA mini receiver. Input power is relative to the minimum attenuation value of the curve characterization experiment. All our signal retrievals from the target are slightly under the 5 dBm line; thus, the correction required due to compression effects is small (< 0.3 dB). **(b)** Normalized antenna pattern of the BASTA mini antennas. We can observe that the Gaussian fit with a beamwidth of $\theta = 0.88°$ is very close to the antenna gain curve measured at the manufacturer's laboratories. This figure also shows the results from mast scans around the target for comparison with the theoretical curves. To enable the comparison with the laboratory antenna pattern, we assume that the gain of both antennas is identical. Then, the received power in decibels per milliwatt is normalized with respect to the maximum measured value and divided by two to represent the gain of a single antenna.

In both cases, we did not detect any signal from the nearby trees close to the target position.

To calculate SCR, we compare the average power received from each target during the calibration experiments with the maximum clutter power observed in a region of 0.125° around the target coordinates, both vertically and horizontally. The value is taken from the radar scanner resolution.

The average power received from the 10 cm target on the 10 m mast is 3.4 dBm. This provides an SCR value of 19.4 dB, which implies a σ_{SCR} uncertainty value of $\approx$ 0.93 dB. From the 20 cm target on the 20 m mast, the average received power is 4.5 dBm. Its SCR equals 40.1 dB, which is translated as an uncertainty contribution of $\sigma_{\mathrm{SCR}} \approx 0.09$ dB. From the results, we see that even if target alignment is better with the 10 m mast, calibration results may not be less uncertain because the motor used for target alignment acts as a big source of clutter.

5.4 Temperature correction

BASTA mini has a regulation system to control temperature fluctuations inside the radar box. However, since the radar is based on solid-state components, even small temperature fluctuations may impact the performance of the transmitter and receiver and, therefore, affect the calibration stability. To account for this effect, we introduced a temperature dependency in the calibration term, as shown in Eq. (3).

During the experiments, we verified the need for this correction by observing that the retrieved calibration term $C_\Gamma(T, F_0)$ has a consistent change, depending on the time of the day, and that this change is strongly correlated to the temperature inside the radar.

Figure 6a, b and c show the results of a representative experiment done in the 2018 campaign. Here we left the radar sampling the target signal for several hours to observe the variability in $C_\Gamma(T, F_0)$ during the day. Figure 6a shows the raw result in the RCS calibration term $C_\Gamma(T, F_0)$. There is a spread of almost 1 dB between the maximum and minimum values during the whole time series. Figure 6b is a Fourier transform of this raw time series. Here we can see that most of the variability happens in the timescale of hours. Figure 6c presents the time series of Fig. 6a but in a daily cycle perspective. Here we plot hourly means of the deviation of $C_\Gamma(T, F_0)$, with respect to the total average, with its hourly standard deviation as error bars. We also superimposed the atmospheric attenuation and the radar amplifier temperature to show that the former has a much smaller impact in calibration variability compared to the latter.

Figure 6d shows the raw results of plotting variations in $C_\Gamma(T, F_0)$ to temperature changes around $T_0 = 26.5\,°\mathrm{C}$. These variations are calculated independently for each iteration by subtracting the constant term of the linear fit of $C_\Gamma(T, F_0)$ with respect to temperature. This operation removes the effect introduced by differences in alignment between the different iterations. The reference T_0 value is chosen because it is approximately the average internal temperature when considering all the experiments.

To maximize the range of temperatures covered, we choose to not limit the sampling period to 1 h. This decision has the drawback of increasing the noise of the data set due

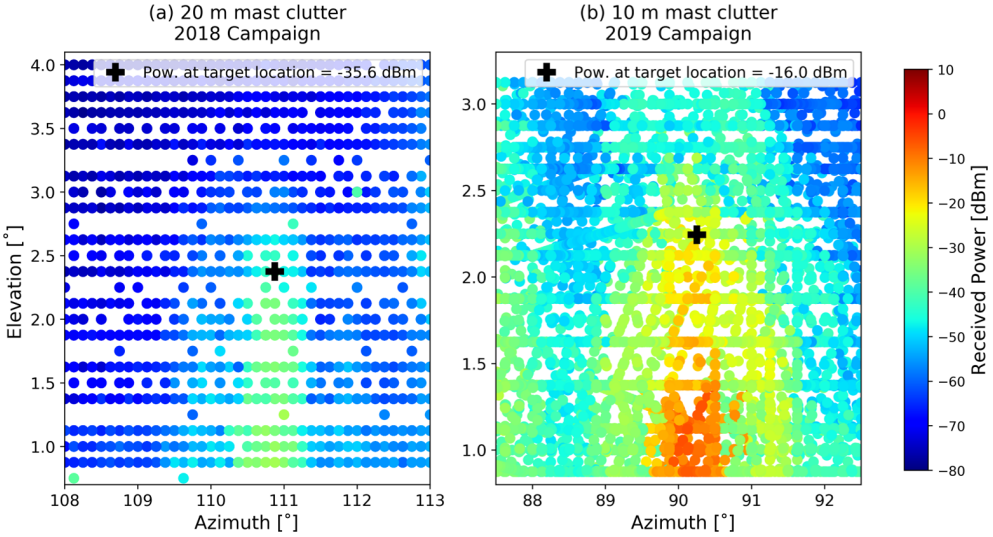

Figure 5. Clutter retrieval from the 10 m **(a)** and 20 m masts **(b)**, respectively. Masts are scanned without the reflectors to measure the clutter signal. The nominal target position is marked with a black cross.

to the inclusion of some data taken under suboptimal conditions, for example, with wind speed velocities above 1 m s^{-1} or with the presence of drizzle. Yet, this step is necessary to enable the retrieval of the temperature correction function for the widest range of temperatures possible.

To retrieve the temperature dependency, we perform a linear regression over the results from all the experiments done in 2018 and 2019, as shown in Fig. 7. The regression shows that the variability in the calibration term has an almost-linear relationship with the internal radar temperature, in the decibel scale, and it is the same for both campaigns. This analysis allows us to estimate the value $n = 0.093\,\mathrm{dB\,°C^{-1}}$ for the temperature correction function of Eq. (3). To estimate the uncertainty of the temperature correction function, we calculate the root mean square error (RMSE) between the linear regression model and the whole data set for each degree of deviation in temperature. The RMSE value for the complete data set is of 0.13 dB, while its value per degree ranges between 0.07 and 0.23 dB for a deviation of 0 and +3 °C, respectively. These results enable us to conclude that the temperature correction function uncertainty σ_T is ≤ 0.23 dB.

5.5 IF loss correction function $f_{\mathrm{IF}}(F_\mathrm{b})$

FMCW radars rely on estimating the beat frequency of the received signal to estimate the distance of an object. This signal may suffer uneven amplification, depending on its frequency, because of a frequency-dependent gain function in the amplifiers of the IF chain of the radar. Since there is a direct relationship between the IF frequency F_b and the target distance r, this dependency on the beat frequency introduces a gain variability with respect to the target distance r. As introduced in Sect. 2, this distance dependency is compensated in the calibration term with a IF correction function $f_{\mathrm{IF}}(F_\mathrm{b})$.

The power $P_\mathrm{r}(r)$ measured by the receiver when no active signal is inputted corresponds to the system noise power $N_\mathrm{s}(F_\mathrm{b})$ plus the environmental noise power N_0 amplified by the radar receiver gain $G_\mathrm{r}(T, F_\mathrm{b})$ (this gain term is equivalent to $L_\mathrm{r}^{-1}(T, F_\mathrm{b})$ of Eq. 2a). Equation (9a) expresses this relationship when $P_\mathrm{r}(r)$ is in decibel milliwatts and N_0 and $N_\mathrm{s}(F_\mathrm{b})$ are expressed in linear units (Pozar, 2009).

The standard way to retrieve each of these terms is to perform a two-point calibration. This requires the use of two noise sources at significantly different and well-known temperatures. Usually, the temperatures of the noise sources are the environmental temperature (298 K) and that of liquid nitrogen (77 K) (Rodríguez Olivos, 2015). The receiver gain versus the frequency retrieved from this two-point calibration could be used to derive the IF correction function directly. However, this approach requires tailored equipment which was not available during the experimentation. Therefore, since the IF correction function is important for removing calibration bias, we follow a different approach when estimating its value.

To estimate the IF correction function, we take advantage of the narrow IF bandwidth of the BASTA mini radar (12 MHz, from 168 to 180 MHz). A calculation done with the Friis formula for the radar system indicates that the system noise $N_\mathrm{s}(F_\mathrm{b})$ should have variations smaller than 0.1 dB in this bandwidth. This can be explained by the large operating bandwidth and the high gain of the receiver low noise amplifier (LNA) of 35 GHz and > 20 dB, respectively, and by the small variation in the mixer conversion loss for the radar bandwidth (< 0.3 dB). To verify the plausibility in the estimation of the noise figure variability, we performed an additional calculation testing the effect of varying the IF noise

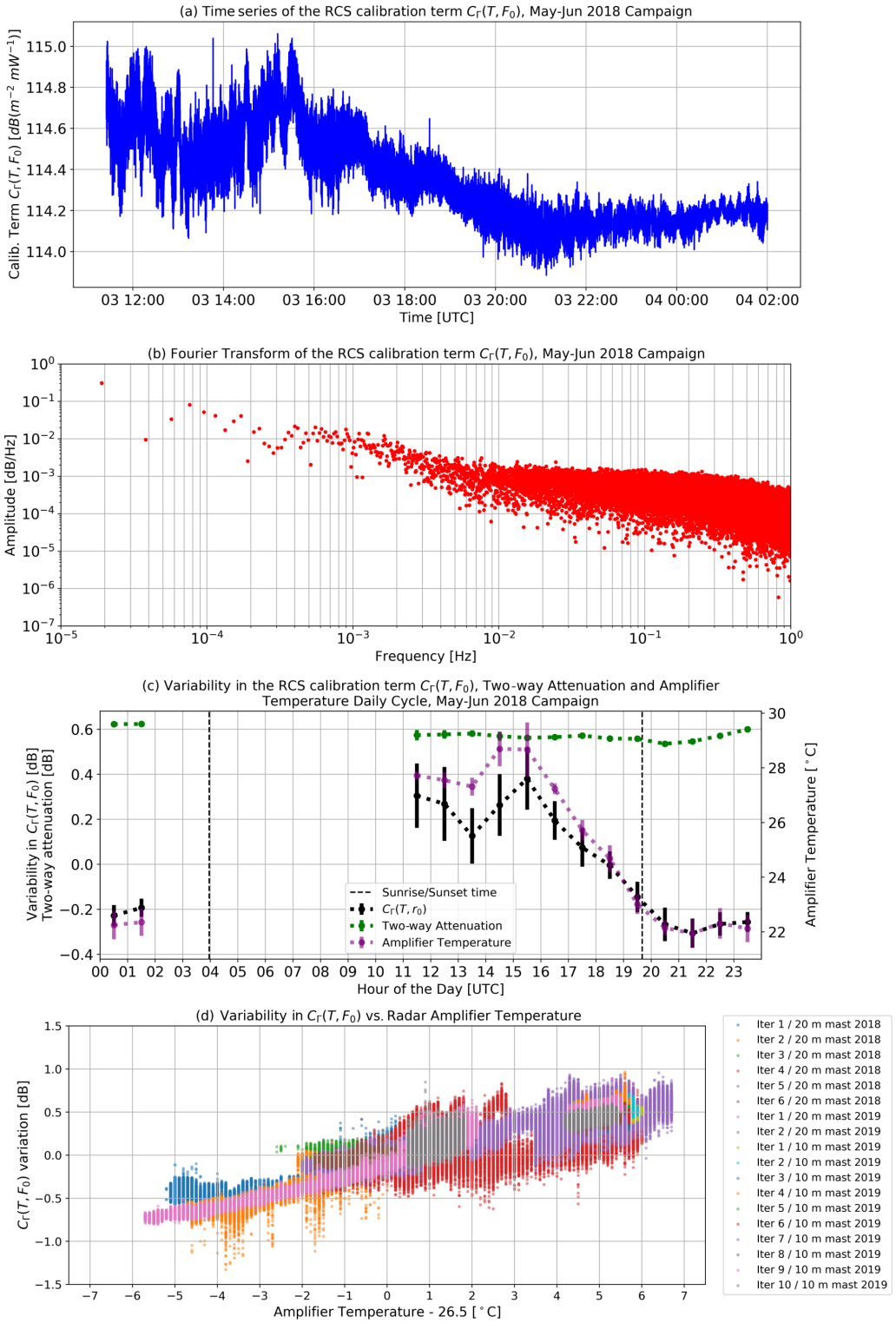

Figure 6. Calibration variability study. Samples from iteration 5 of the 2018 calibration campaign. **(a)** Time series of the RCS calibration term retrieval. **(b)** Fourier transform of the RCS calibration term after subtracting the mean value. **(c)** Calibration variability daily cycle, amplifier temperature and two-way attenuation. Attenuation error bars are too small to be seen at this scale. **(d)** Relative changes in $C_\Gamma(T, F_0)$ versus amplifier temperature plotted using all samples from the 2018 and 2019 campaigns.

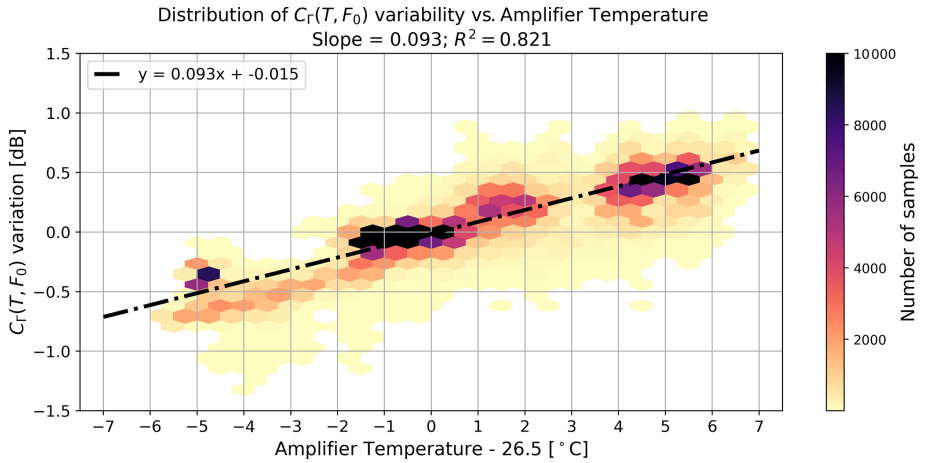

Figure 7. A 2D histogram of the relative changes in $C_\Gamma(T, F_0)$ with respect to changes in the amplifier temperature and its linear least squares fit. The histogram is plotted using all $C_\Gamma(T, F_0)$ samples from the 2018 and 2019 calibration campaigns.

temperature from 0 to 400 K, and in all cases, the system noise variability remained under 0.1 dB.

This low variability enables the retrieval of the IF correction function by assuming a constant noise power density in the IF frequency range (Eq. 9b). The constant noise power term N_c corresponds to the addition of environmental and system noise.

$$P_r(r) \equiv P_r(F_b) = 10\log_{10}\left(G_r(T, F_b) \cdot (N_s(F_b) + N_0)\right) \quad (9a)$$
$$\approx 10\log_{10}\left(G_r(T, F_b) \cdot N_c\right)$$
$$= 10\log_{10}\left(\frac{N_c}{L_r(T, F_b)}\right). \quad (9b)$$

Then, to retrieve the $f_{IF}(F_b)$, we turn off the radar emitter and sample the environmental noise with the radar operating in its calibration configuration (12.5 m distance resolution and 0.5 s integration time). After retrieving a significant amount of noise samples, we calculate the average value of the difference $P_r(F_0) - P_r(F_b)$ for each IF frequency F_b to remove the effect of the unknown noise power density. This operation is done to quantify relative gain variations around the calibrated frequency F_0.

By using Eqs. (2a) and (3), we find that the difference $P_r(F_0) - P_r(F_b)$ is equivalent to the difference between $C_\Gamma(T, F_b)$ and $C_\Gamma(T, F_0)$, and therefore, it is equivalent to the IF correction function $f_{IF}(F_b)$ (Eq. 10). The temperature effect in gain is removed because both $P_r(F_0)$ and $P_r(F_b)$ are sampled simultaneously and, therefore, under the same temperature conditions.

$$\overline{P_r(F_0) - P_r(F_b)} = 10\log_{10}\left(\frac{L_r(T, F_b)}{L_r(T, F_0)}\right)$$
$$= -C_\Gamma(T, F_0) + C_\Gamma(T, F_b) = f_{IF}(F_b). \quad (10)$$

For this experiment only, $P_r(F_0)$ corresponds to the power measured at the gate closer to the reference target position without integrating other gates. This is done because there is no significant leakage and, as the results in Fig. 8 show, $G_r(T, F_b)$ changes are negligible in the five gates used for integration.

Figure 8 shows the results of the IF correction function retrieval referenced to $P_r(F_0)$, using F_0 associated to the target distance $r_0 = 376.5$ m (corresponding to the 20 m mast experimental setup). We can observe that all functions retrieved in 2019 are in close agreement, without significant variations between different dates or times of the day chosen for the plots. The 2018 function is different because the hardware was modified between both calibration campaigns. Additionally, in 2018 the emitter was not turned off to perform the noise sampling. Rather, we resorted to using a sampling period with clear-sky conditions to respect the assumptions of Eq. (9b). To avoid the effect of crosstalk, we only consider gates farther than 200 m from the radar.

A sixth degree polynomial is used to fit $f_{IF}(F_b)$. For both 2018 and all 2019 curves, the fit has a RMSE < 0.03 dB. Furthermore, the standard deviation between the results from the four periods of 2019 has a maximum value of 0.04 dB for any gate. Both results indicate that the uncertainty introduced by the IF correction function is ≤ 0.04 dB. Finally, the IF correction function retrieved for the 10 m mast setup in 2019 (with $r_0 = 196$ m) is almost identical to the 20 m mast results. These functions are presented in Sect. 6. Considering these low RMSE values, we decided to select the uncertainty introduced by assuming a constant system noise as the IF correction function uncertainty; thus, $\sigma_{IF} = 0.1$ dB.

5.6 Misalignment bias

The retrieval of $C_\Gamma(T, F_0)$, using Eq. (4b), requires a precise knowledge of the reference target effective RCS Γ_0. Each decibel per square meter of difference between the theoretical value used in the calculations and the effective target RCS

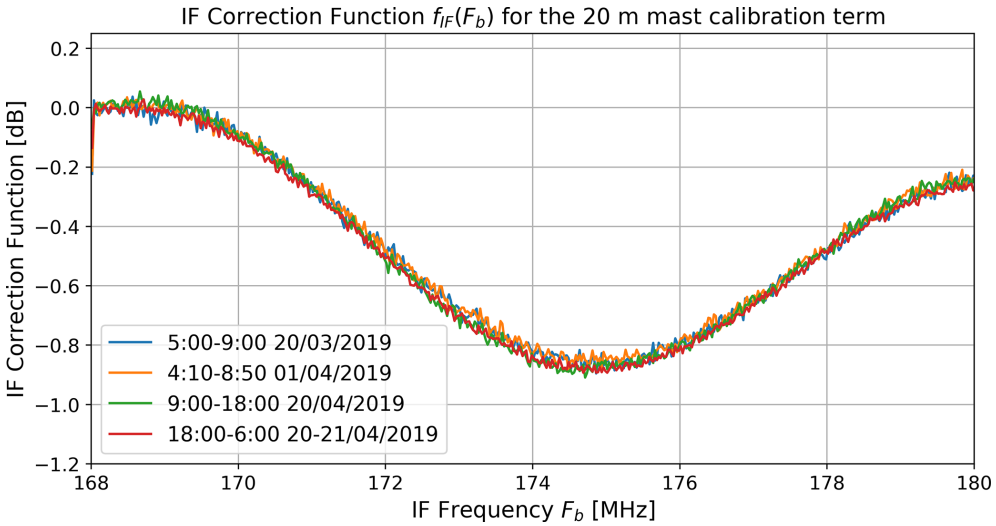

Figure 8. Data used for the IF correction function calculation, retrieved for different periods of the 2019 calibration campaign. The 2018 IF correction function is different from the 2019 results because the hardware was modified between the campaigns (see 2018 IF correction function presented in Sect. 6). The time indicated in the label is in universal coordinated time (UTC).

will introduce a bias of the same magnitude in the estimation of the calibration coefficient C_Γ^0 and, thus, in $C_\Gamma(T, F_0)$.

The effective reflector RCS is the actual physical value that would be measured by a perfectly calibrated radar. It is different from the target-intrinsic RCS which only depends on its physical properties. Effective RCS changes when the experimental setup is modified. For example, if the point target is not exactly in the beam center, the antenna gain will not be maximum, and therefore, the effective RCS will decrease compared to the intrinsic value. Effective RCS also changes when the incidence angle of the radar beam is modified. This latter effect may increase or decrease effective RCS, depending on the original situation.

A common approach in these type of experiments is to set Γ_0 to be the maximum theoretical RCS of the target, assuming misalignment will cause a negligible deviation from this value. This procedure can be refined for cases in which the system default configuration does not have the target boresight aligned with the radar position. In these cases, effective RCS can be calculated using equations derived from geometrical optics (more complex optical calculations may be necessary for other wavelengths or target sizes). For example, we use the equations published by Brock and Doerry (2009) when calculating the effective RCS of our triangular trihedral target on the 20 m mast.

Unfortunately, this approach does not correct the impact of alignment uncertainties. We observed that random errors in the element positioning will statistically impact the effective Γ_0 in a single direction. Thus, simply taking the average of many target sampling iterations would result in a biased estimation of the calibration.

With the objective of quantifying the impact of alignment uncertainties, we developed a geometrical simulator of effective RCS. This simulator receives as input the position of each element in the setup and calculates the effective RCS, considering the beam incidence angle and antenna gain variations when the target is not in the center of the beam. The degrees of freedom included in the simulator are shown in Fig. 9a. It enables the modification of the radar aiming angles, the mast dimensions and the positioning and orientation of the target. The equations used in the simulator can be found in the Supplement.

We now use the simulator to study how uncertainty in alignment can affect the value of Γ_0. For this, we model an example experiment based on the 20 m mast setup. In this model, we separate input variables between known and uncertain. Known terms can be fixed or measured very precisely in the field experiment; hence, they are set as fixed values. Meanwhile, uncertain terms represent the parameters that cannot be fixed or measured very precisely and, for that reason, are better expressed as probability distributions (terms defined in Fig. 9a).

- Known terms, as follows:
  - $x_r = 376.5$ m
  - $h_r = 5.3$ m
  - $\rho = 20$ m
  - $\alpha = 48°$
  - target size $= 20$ cm.
- Variables with uncertainty, as follows:
  - $\theta_r = \mathcal{N}(\theta_r^*, \sigma_{\theta_r}^2)$
  - $\phi_r = \mathcal{N}(\phi_r^*, \sigma_{\phi_r}^2)$

- $\theta = \mathcal{N}(0, \sigma_\theta^2)$
- $\phi = \mathcal{U}([0°, 360°))$
- $\tau = \mathcal{N}(\tau^*, \sigma_\tau^2)$.

In the uncertain variables, $\theta_r^* = 87.82°$, $\phi_r^* = 0°$ and $\tau^* = 0°$ represent the nominal alignment angles, which are the values expected under an ideal field experiment where the radar aims directly at the target and the mast is perfectly vertical. To these nominal values we associate a distribution shape and the uncertainty set of $\sigma_{\theta_r} = 0.075°$, $\sigma_{\phi_r} = 0.075°$, $\sigma_\theta = 1.5°$ and $\sigma_\tau = 5°$. Each term, known and uncertain, is estimated from observations done during the experimental field work.

With these input parameters, we sample the Γ_0 distribution that would arise after a large number of experimental iterations. Figure 9b shows the results from this sampling. The black dashed line shows the effective RCS under our experimental configuration when each element is in its nominal position. We can see that this effect cannot be neglected in our case since its value is 0.8 dB lower than the maximum theoretical RCS.

However, this single correction does not suffice. The results of the model show that the addition of uncertainty into the process induces another bias of ≈ 0.3 dB on average. Since this is within the order of magnitude of our desired uncertainty in the calibration, the example clearly illustrates the need for including a bias correction step in our calibration methodology.

The standard deviation σ_ϵ between N experimental retrievals of $C^0_{\Gamma i}$ cannot be used directly as an estimation of uncertainty because the RCS distribution shape is not Gaussian. The uncertainty introduced by this variability is studied by sampling a large set of possible RCS distributions, based on our experimental configuration, and selecting the candidates matching our observed spread σ_ϵ. This set provides an estimation of the expected bias correction $\tilde{\Lambda}$ and of the effective RCS uncertainty σ_Λ. The uncertainty of the C^0_Γ estimator of Eq. (6) will correspond to the uncertainty of each $C^0_{\Gamma i}$ estimation propagated through the calculation of their average (terms $\sum \sigma_i^2/N^2$ and σ_T^2/N in Eq. 7a) plus the effective RCS uncertainty σ_Λ. The details on how this estimator works and how the RCS distribution sampling is done are fully explained in Sect. S3.

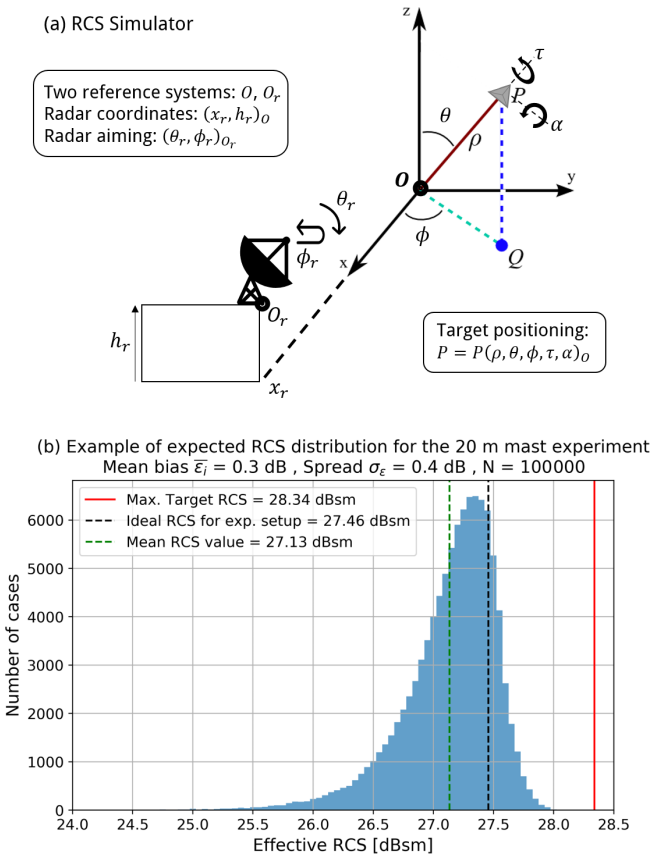

Figure 9. (a) Diagram of the RCS simulator illustrating its degrees of freedom. **(b)** Example of an effective RCS distribution obtained after 100 000 simulations with the uncertainty set specified in the text. The simulations are based on our 20 m mast setup. Bias is calculated by subtracting the ideal RCS from the mean RCS value. The example illustrates how the effective RCS will be, statistically, lower than the result expected from an ideally aligned setup.

6 Results

In 2018 we used the 20 m mast only, performing six iterations. For 2019, we did 10 iterations using the 10 m mast and two iterations with the 20 m mast. The distributions of C^0_Γ obtained in each iteration and experiment are shown in Fig. 10.

The radar hardware changed between the 2018 and 2019 campaigns due to experiments that required retrieving the power transfer curve and performing maintenance operations. This implies that we cannot compare the absolute calibration values between both campaigns. What remains valid is the comparison of the properties, such as the variability, and the results from both experiments in 2019.

In the results, we can notice a difference in the $C^0_{\Gamma i}$ spread when comparing the 10 and 20 m masts. The six iterations of 2018 (Fig. 10a) have a spread of $\sigma_\epsilon = 0.33$ dB, while the spread of the 10 iterations of 2019 is 0.11 dB (Fig. 10b). This happens because the 10 m mast has a motor on top which enables a much finer adjustment of the target position, improving the repeatability of the experiments.

There is also a small difference in the spread of the curves. The $C^0_{\Gamma i}$ values retrieved in experiment (B) have a smaller spread σ_i. This is because we took all the samples during one single night with very clear conditions and an average wind speed below 1 m s^{-1}. A great advantage was the presence of the motor that enables target alignment in ≈ 5 min. Meanwhile, for experiment (A), curves were sampled during different days because the 20 m mast setup requires more time to align (≈ 2 h). The different conditions on each day led to a

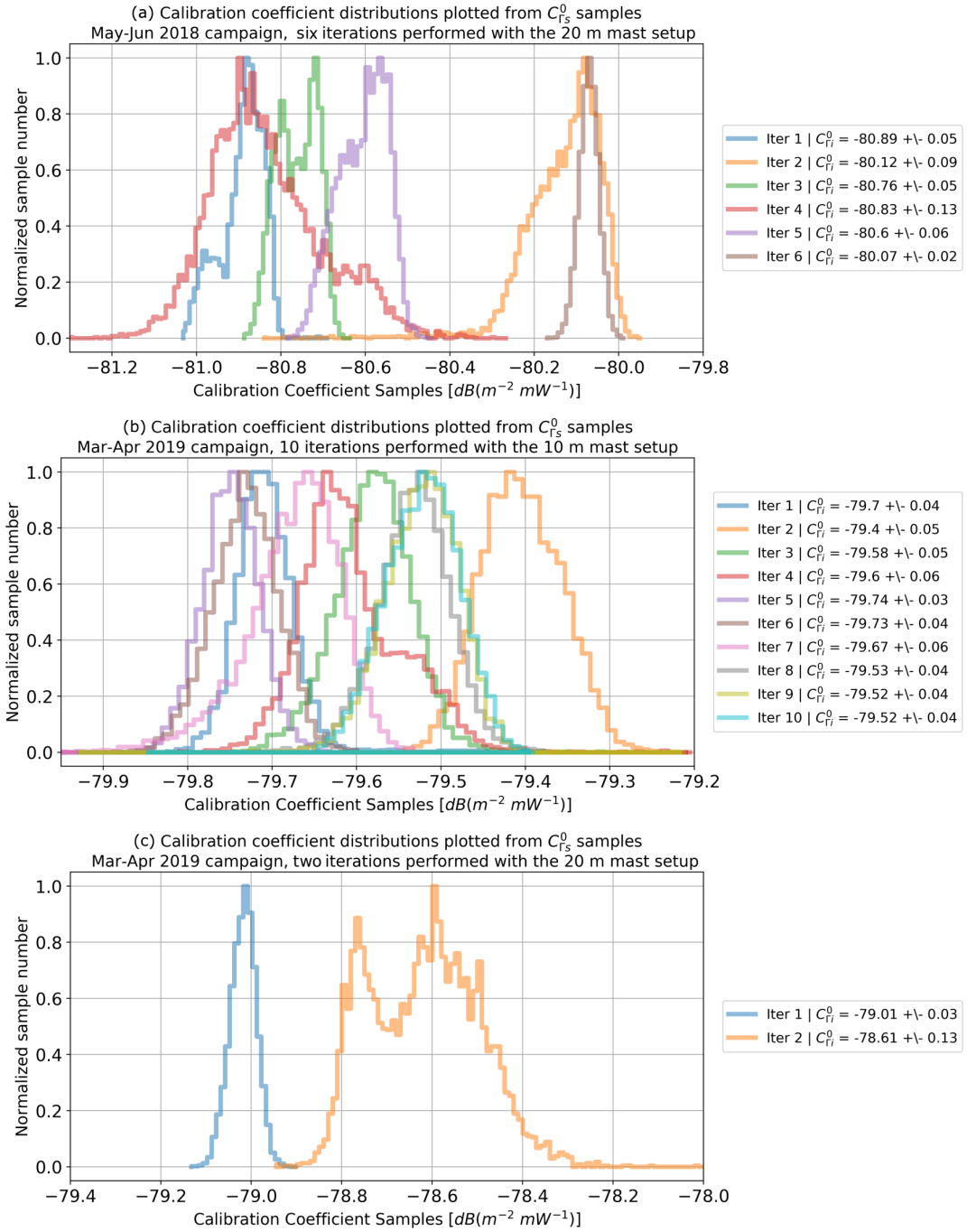

Figure 10. Calibration coefficient distributions obtained for the **(a)** 2018 campaign using the 20 cm target on the 20 m mast, the **(b)** 2019 campaign using the 10 cm target on the 10 m mast and the **(c)** 2019 campaign with the 20 cm target on the 20 m mast.

more varied shape in the retrieved curves. This effect is specially noticeable in experiment (C), where the iterations were performed during daytime when atmospheric conditions are more dynamic, especially the wind speed variability. The introduced variability was not fully compensated by our corrections and, thus, bimodal distributions remained. However, the individual spread is still small, within ≈ 0.1 dB, so we decided to accept these samples for calibration purposes.

To study the dependency of the bias correction on the number of iterations, we calculate the bias correction term $\tilde{\Lambda}$ and its uncertainty σ_Λ for experiments (A) and (B) with different numbers of repetitions. The order of the iterations used in each row matches the sequential order indicated in Fig. 10.

Table 1. Bias correction $\tilde{\Lambda}$ and its uncertainty σ_Λ calculated using a different number of iterations for the experiments of the 2018 and 2019 calibration campaigns (e.g., three iterations means we used iterations 1, 2 and 3 of the experiment). We include the average and spread σ_ϵ between the retrieved $C^0_{\Gamma i}$ for each case. This variability σ_ϵ is introduced in the bias estimation procedure to determine the bias correction $\tilde{\Lambda}$ and its uncertainty σ_Λ.

	No. of iterations	Experimental results		Bias correction	
		$\frac{1}{N}\sum C^0_{\Gamma i}$	σ_ϵ (dB)	$\tilde{\Lambda}$ (dB)	σ_Λ (dB)
Experiment (A) 20 m mast (2018)	2	−80.51	0.38	0.98	1.78
	3	−80.59	0.33	0.65	0.86
	4	−80.65	0.31	0.51	0.50
	5	−80.64	0.28	0.40	0.33
	6	−80.54	0.33	0.44	0.28
Experiment (B) 10 m mast (2019)	2	−79.55	0.15	0.78	1.65
	3	−79.56	0.12	0.42	0.70
	4	−79.57	0.11	0.27	0.34
	5	−79.60	0.12	0.24	0.20
	6	−79.62	0.12	0.22	0.13
	7	−79.63	0.11	0.19	0.10
	8	−79.62	0.11	0.18	0.07
	9	−79.61	0.11	0.17	0.06
	10	−79.60	0.11	0.16	0.05
Experiment (C) 20 m mast (2019)	2	−78.81	–	0.44	0.28

The results are shown in Table 1. For both cases we have the best estimate when we use all the samples available for each experiment, and thus, we use this bias correction and uncertainty when computing the calibration coefficient.

For experiment (C), we followed a different approach. Because we only have two samples, the calculated $\sigma_\epsilon = 0.2$ dB is very likely to be underestimated. Consequently, and because the experimental procedure was identical to what was done in 2018, we assume our parameters σ_ϵ, $\tilde{\Lambda}$ and σ_Λ to be equal to the best estimation of experiment (A). This is possible because in our methodology we assume that the bias probability distribution of a given system is unique, even if it is unknown, and what is done by performing many iterations is successively restricting the possible sets of uncertainties that can generate results consistent with the observations. This latter hypothesis is consistent with the decrease in uncertainty for the bias correction when increasing the number of iterations. Table 2 contains a summary of all known bias corrections and uncertainty contributions, as introduced in Sect. 4. With the aforementioned results, we use Eqs. (6), (3), (7a) and (7b) to estimate the RCS and reflectivity calibration terms $C_\Gamma(T, F_\mathrm{b})$ and $C_Z(T, F_\mathrm{b})$ alongside their uncertainty. Since the term σ_{Γ_0} is much larger than all other uncertainty sources, we calculate a partial calibration uncertainty including all but this term to simplify the comparison of uncertainty contributions between different experimental setups. This term is then added for the calculation of the final result. $C_Z(T, F_\mathrm{b})$ is calculated for the range resolution $\delta r = 12.5$ m, which is the same mode used for target sampling. T is the radar amplifier temperature in degrees Celsius and $f_\mathrm{IF}(F_\mathrm{b})$ is the IF loss correction function.

- Experiment (A), 20 m mast (2018):
  - $C_\Gamma(T, F_\mathrm{b}) = -80.98 + 0.093(T - 26.5) + f_\mathrm{IF}(F_\mathrm{b})[\mathrm{dB(m^{-2}\,mW^{-1})}] \pm 2[\mathrm{dB}]$
  - $C_Z(T, F_\mathrm{b}) = 3.05 + 0.093(T - 26.5) + f_\mathrm{IF}(F_\mathrm{b})\ [\mathrm{dB(mm^6\,m^{-5}\,mW^{-1})}] \pm 2[\mathrm{dB}]$
  - $f_\mathrm{IF}(F_\mathrm{b}) = 7.34 \times 10^{-6} F_\mathrm{b}^6 - 7.70 \times 10^{-3} F_\mathrm{b}^5 + 3.36 F_\mathrm{b}^4 - 7.83 \times 10^2 F_\mathrm{b}^3 + 1.02 \times 10^5 F_\mathrm{b}^2 - 7.15 \times 10^6 F_\mathrm{b} + 2.08 \times 10^8$[dB].
- Experiment (B), 10 m mast (2019):
  - $C_\Gamma(T, F_\mathrm{b}) = -79.76 + 0.093(T - 26.5) + f_\mathrm{IF}(F_\mathrm{b})[\mathrm{dB(m^{-2}\,mW^{-1})}] \pm 2[\mathrm{dB}]$
  - $C_Z(T, F_\mathrm{b}) = 4.28 + 0.093(T - 26.5) + f_\mathrm{IF}(F_\mathrm{b})[\mathrm{dB(mm^6\,m^{-5}\,mW^{-1})}] \pm 2[\mathrm{dB}]$
  - $f_\mathrm{IF}(F_\mathrm{b}) = 7.60 \times 10^{-6} F_\mathrm{b}^6 - 7.97 \times 10^{-3} F_\mathrm{b}^5 + 3.48 F_\mathrm{b}^4 - 8.10 \times 10^2 F_\mathrm{b}^3 + 1.06 \times 10^5 F_\mathrm{b}^2 - 7.40 \times 10^6 F_\mathrm{b} + 2.15 \times 10^8$[dB].
- Experiment (C), 20 m mast (2019):
  - $C_\Gamma(T, F_\mathrm{b}) = -79.25 + 0.093(T - 26.5) + f_\mathrm{IF}(F_\mathrm{b})[\mathrm{dB(m^{-2}\,mW^{-1})}] \pm 2[\mathrm{dB}]$
  - $C_Z(T, r) = 4.79 + 0.093(T - 26.5) + f_\mathrm{IF}(F_\mathrm{b})[\mathrm{dB(mm^6\,m^{-5}\,mW^{-1})}] \pm 2[\mathrm{dB}]$

– $f_{\mathrm{IF}}(F_{\mathrm{b}}) = 7.60 \times 10^{-6} F_{\mathrm{b}}^6 - 7.97 \times 10^{-3} F_{\mathrm{b}}^5 + 3.48 F_{\mathrm{b}}^4 - 8.10 \times 10^2 F_{\mathrm{b}}^3 + 1.06 \times 10^5 F_{\mathrm{b}}^2 - 7.40 \times 10^6 F_{\mathrm{b}} + 2.15 \times 10^8$[dB].

These results enable the analysis of the relative uncertainty contributions from different sources; however, the total calibration uncertainty may be underestimated. As indicated in Sects. 4 and 5, some bias terms remain unknown. Specifically, target physical RCS must be measured in an echo chamber to improve the misalignment bias estimation. In addition, the method for characterizing antenna alignment must be improved to determine if there is a need for an additional distance correction function (Sect. 5.2). The uncertainty of these retrievals will impact the total uncertainty value; however, it is possible to quantify this effect through the terms σ_{Γ_0} and σ_{A} of Eq. (7b).

To finalize, we perform a test of the calibration results by measuring an altostratus cloud in both campaigns (Fig. 11). The sampling was done with a 25 m resolution, and thus, 6 dB had to be subtracted from the $C_Z(T, F_{\mathrm{b}})$ calibration calculated for the 12.5 m resolution. In this correction, 3 dB come from the change in the distance resolution term δr (Eq. 5a), and the other 3 dB are subtracted to compensate for the additional digital gain coming from doubling the number of points in the chirp Fourier transform (Delanoë et al., 2016). A signal-to-noise ratio threshold of 8 dB is used to remove noise samples. We observe that, for both campaigns, the reflectivity measured in an altostratus cloud is within −30 to 0 dBZ, which is typical of the values reported in the literature (Uttal and Kropfli, 2001).

7 Conclusions

This study presents a cloud radar calibration method that is based on a cloud radar power signal backscattered from a reference reflector. We study the validity of the method and variability in the results by performing measurements in two experimental setups and analyzing the associated results. In the first experimental setup, we use a scanning BASTA mini W-band cloud radar that is aimed towards a 20 cm triangular trihedral target installed at the top of a 20 m mast located 376.5 m from the radar. For the second experimental setup, we use the same radar, aimed towards a 10 cm triangular trihedral target mounted on a pan-tilt motor at the top of a 10 m mast. The mast is located 196 m from the radar.

The first consideration in the design of the experimental setup is the need to avoid excessive compression or saturation in the radar receiver. This must be checked before any calibration attempt by comparing the measurements of the radar backscattered power with the radar receiver power transfer curve. In both our setups, we found losses due to compression of the order of $0.2 \sim 0.3$ dB. There is a compensating effect between the target RCS and radar-to-target distance (Eq. 2b). Since the compression effect is small, we correct it using our receiver power transfer curve. However, in cases where the radar is operating close to saturation, or when compression effects are larger than the calibration uncertainty goal, it is advisable to compensate by reducing the target size or by positioning the target farther away from the radar.

Second, the reflector must be positioned far enough from the radar to be outside the antennas' near-field distance and to ensure that the received power has low antenna overlap losses. The BASTA mini cloud radar has a Fraunhofer near-field distance of 50 m. The estimated maximum overlap loss is less than 0.1 dB for the closest (10 m) mast setup. Thus, we conclude that the target positioning is far enough for both setups.

Third, the experimental setup should strive to reduce clutter in the radar measurements. This can be achieved by operating in an open field that is several hundreds of meters in length and free of trees or other signal-inducing obstacles. It is also advisable to perform radar measurements under clear conditions, without fog or rain, with the wind speed below 1 m s^{-1}, and low turbulence.

Next, the proposed calibration method requires performing several iterations in the same setup configuration. In each iteration, the setup is first realigned, followed by approximately 1 h of sampling of the reference reflector's backscattered power. The sampled power is then corrected for compression effects, incomplete antenna overlap, variations in radar gain due to temperature and atmospheric attenuation before being used to estimate a RCS calibration term value. Once all iterations are completed, the final RCS and equivalent reflectivity calibration terms can be computed with their respective uncertainties.

Iterations are necessary because they enable the quantification of bias introduced by inevitable system misalignment. Our experiments indicate that, for our setup, at least five iterations are necessary to reach convergence in the calculation of bias and uncertainty associated with misalignment. We find a bias correction of $\approx 0.4 \pm 0.3$ dB for the 20 m mast and of $\approx 0.2 \pm 0.1$ dB for the 10 m mast. This difference can be explained by the more precise alignment attainable with the pan-tilt motor installed on the 10 m mast.

Calibration is also impacted by changes in the gain of radar components associated with internal temperature variations. For the radar used in our experiment, these changes reach up to ±0.6 dB. Our experiments enabled us to retrieve a correction function for the temperature dependence and to reduce the temperature uncertainty contribution to $\sigma_T = 0.23$ dB. This result indicates that lower calibration uncertainties can be achieved by studying temperature effects, especially for solid-state radars.

Another necessary consideration is the inclusion of gain variations with distance which are introduced by frequency-dependent losses in the IF of the radar receiver. We found calibration variations with distance up to 0.9 dB for the 2019 campaign. Therefore, characterizing the IF loss is a necessary step for validating the calibration results for all ranges.

Table 2. Summary of all known corrections and uncertainty contributions in the calculation of $C_\Gamma(T, F_b)$. The absolute correction terms have a sign associated with the direction in which they impact the final calibration calculation. For the receiver compression correction, we present the average magnitude, and for the temperature correction, we present the range of possible values. The partial calibration uncertainty is the addition of all uncertainty terms except σ_{Γ_0}. This term is later added to calculate the total calibration uncertainty. Note: (A), (B) and (C) refer to the experiments.

	Term (dB)	(A) 20 m mast (2018)	(B) 10 m mast (2019)	(C) 20 m mast (2019)
Absolute corrections				
Compression	Fig. 4a	−0.3 on average	−0.2 on average	−0.3 on average
Partial antenna overlap	$L_o(r_0)$	−0.02	−0.08	−0.02
Temperature correction ($T_0 = 26.5\,°C$)	$n(T - T_0)$	within ±0.6	within ±0.6	within ±0.6
Misalignment bias	$\tilde{\Lambda}$	−0.44	−0.16	−0.44
IF loss correction	$f_{IF}(F_b)$	$\leq \lvert 0.6 \rvert$	$\leq \lvert 0.9 \rvert$	$\leq \lvert 0.9 \rvert$
Uncertainty sources				
$C^0_{\Gamma i}$ estimation	$\sqrt{\frac{1}{N^2}\sum \sigma_i^2}$	0.03	0.01	0.07
Temperature correction – $C^0_{\Gamma i}$ retrievals	$\frac{\sigma_T}{\sqrt{N}}$	0.09	0.07	0.16
Temperature correction – $C_\Gamma(T, F_b)$, $C_Z(T, F_b)$	σ_T	0.23	0.23	0.23
Signal-to-clutter ratio	σ_{SCR}	0.09	0.93	0.09
Bias correction	σ_Λ	0.28	0.05	0.28
IF loss correction	σ_{IF}	0.1	0.1	0.1
Partial calibration uncertainty		0.40	0.97	0.43
Reflector RCS uncertainty	σ_{Γ_0}	2	2	2
Total calibration uncertainty	δC_Γ; δC_Z	2.04	2.22	2.04

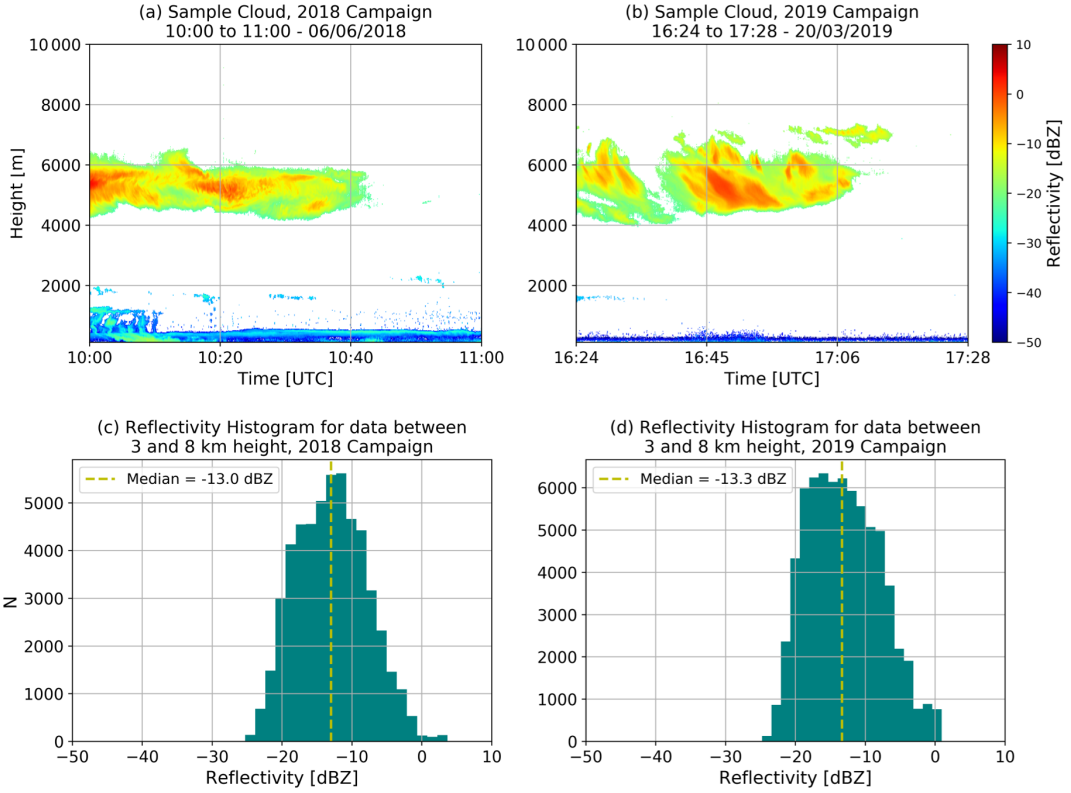

Figure 11. Altostratus cloud sampled during the 2018 **(a)** and 2019 campaigns **(b)**. Lower reflectivities are easier to capture at lower altitudes because of the lower distance and attenuation losses (Eq. 5b). In the altostratus reflectivity histograms **(c, d)** we observe that, for both campaigns, measurements are within the ranges reported in the literature.

Our analyses reveal that the predominant source of uncertainty for all experiments is the reference target RCS, reaching approximately 2 dB due to the use of a theoretical model, instead of an experimental characterization. The next most important contributions to uncertainty come from the levels of clutter and alignment precision. These two effects have different magnitudes in our two experimental setups (10 and 20 m masts). The 20 m mast setup uncertainty is limited by the uncertainty contribution of the alignment bias estimation $\sigma_{\Lambda} = 0.28$ dB. The 10 m mast setup uncertainty is limited by the uncertainty contribution of the signal-to-clutter ratio $\sigma_{\mathrm{SCR}} = 0.9$ dB. This result reveals that there is a tradeoff between better target alignment and additional clutter introduced by the alignment motor.

The complete uncertainty budget enables us to conclude that, to reach a calibration uncertainty under 1 dB, it is necessary to have a target RCS characterization with an uncertainty lower than 0.9 dB, based on the accumulated uncertainty of all terms, except target RCS of 0.4 dB. This uncertainty was obtained using the 20 cm target on the 20 m mast during the 2018 experiment when six target sampling iterations were performed.

Finally, because of cloud radar hardware modifications in the fall of 2018, the calibration coefficients found in May 2018 and March 2019 differ by 1.2 dB. We compare the cloud radar measurements of altostratus clouds performed in May 2018 and March 2019. The reflectivity distributions of the two events are consistent and compatible with values previously registered in the literature. The two distributions yield median values that differ by 0.3 dB.

For future work, we envisage the development of a technological solution to allow target orientation without introducing additional clutter. Another interesting prospect is to improve the accuracy of the radar scanner to enable a direct retrieval of the antenna pattern with the radar, following the method proposed by Garthwaite et al. (2015). This retrieval would improve the bias correction arising from parallax errors, which at present is calculated assuming parallel radar antennas.

We also plan to perform a receiver noise figure characterization, to further reduce uncertainty in the IF correction, and an echo chamber characterization of our reference targets. Target characterization will enable the removal of bias caused by manufacturing imprecision, reduce the RCS uncertainty contribution to total uncertainty and improve the estimation of our system misalignment bias correction.

Furthermore, there is ongoing research on calibration and antenna pattern characterization methods based on reference targets held by unmanned aerial vehicles (UAVs; Duthoit et al., 2017; Yin et al., 2019). Since the underlying principle is the same, most considerations written here should be directly applicable in these new experiments. Here the UAV takes the role of the mast, holding the reflector (usually a sphere), and therefore, it is important to characterize the UAV RCS and verify that it does not interfere with the experiment. The main difference would be in the procedure necessary for estimating bias because the reference target (usually a sphere) will always be moving due to the wind. Here an adaptation of the effective RCS simulator would be necessary to account for the target type and different alignment protocol.

Appendix A: Table of symbols

Symbol	Description	Units
$C_\Gamma(T, F_\mathrm{b})$	RCS calibration term	dB($\mathrm{m}^{-2}\,\mathrm{mW}^{-1}$)
$C_\Gamma(T, F_0)$	RCS calibration term at the IF frequency F_0	dB($\mathrm{m}^{-2}\,\mathrm{mW}^{-1}$)
C_Γ^0	RCS calibration coefficient	dB($\mathrm{m}^{-2}\,\mathrm{mW}^{-1}$)
$C_{\Gamma s}^0$	Single sample of the calibration coefficient C_Γ^0	dB($\mathrm{m}^{-2}\,\mathrm{mW}^{-1}$)
$C_{\Gamma i}^0$	Mean value of all $C_{\Gamma s}^0$ samples retrieved in iteration i,	dB($\mathrm{m}^{-2}\,\mathrm{mW}^{-1}$)
$C_Z(T, F_\mathrm{b})$	Radar equivalent reflectivity calibration term	dB($\mathrm{mm}^6\,\mathrm{m}^{-5}\,\mathrm{mW}^{-1}$)
δC_Γ	RCS calibration uncertainty	dB
δC_Z	Radar equivalent reflectivity calibration uncertainty	dB
F_b	Signal frequency at the radar receiver's IF	MHz
$f_\mathrm{IF}(F_\mathrm{b})$	IF loss correction function	dB
$\Gamma(r)$	Radar cross section of reflections at distance r	dBsm
Γ_0	Radar cross section of the reference target	dBsm
$\tilde{\Lambda}$	Misalignment bias correction	dB
λ	Radar carrier wavelength	m
N	Number of iterations performed in a calibration experiment	
$P_\mathrm{r}(r_0)$	Power received from the target position r_0	dBm
$P_\mathrm{r}(r)$	Power received from distance r	dBm
p_t	Radar transmitted power	mW
r	Distance from the radar	m
r_0	Distance between radar and reference target	m
F_0	IF frequency associated with the target distance	m
σ_A	Calibration uncertainty introduced by antenna properties	dB
σ_ϵ	Standard deviation between all $C_{\Gamma i}^0$ values, used in the estimation of $\tilde{\Lambda}$	dB
σ_{Γ_0}	Uncertainty of the reference target RCS	dB
σ_i	Uncertainty in the estimation of each $C_{\Gamma i}^0$ value	dB
σ_IF	Uncertainty of the IF loss correction function	dB
σ_Λ	Uncertainty of the misalignment bias correction	dB
σ_SCR	Uncertainty introduced by clutter at the target position	dB
σ_T	Uncertainty of the temperature correction function	dB
θ	Antenna beamwidth	rad
Z_e	Radar equivalent reflectivity	dBZ

Data availability. All data related to atmospheric conditions used in this study are hosted by the SIRTA observatory. Data access can be requested free of charge by following the conditions indicated in the SIRTA data policy (https://sirta.ipsl.fr/data_policy.html, last access: 3 December 2020, SIRTA, 2020b). The SIRTA observatory website can be accessed at https://sirta.ipsl.fr/ (last access: 3 December 2020, SIRTA, 2020c), and the data request form can be found at https://sirta.ipsl.fr/data_form.html (last access: 3 December 2020, SIRTA, 2020a). All radar data are distributed by the IPSL with the following identifier: https://doi.org/10.14768/6dd7bbb2-6e0d-4de3-bf03-7d6ead628845 (Toledo et al., 2020).

Supplement. The supplement related to this article is available online at: https://doi.org/10.5194/amt-13-6853-2020-supplement.

Author contributions. All authors contributed to the planning of the campaigns and the design of the calibration experiments. JD was responsible for the radar installation and operation. JCD and FT worked on the preparation, development and operation of the necessary infrastructure for the experiments. JD and FT retrieved the power transfer curve of the radar receiver. Data analysis and the establishment of the calibration methodology presented in the paper were done by FT. MH and FT worked on defining the paper structure and content. FT, SJ and CLG worked on developing the method for retrieving the IF correction function and its calculation. CLG contributed with technical information about the radar. All authors reviewed the paper.

Competing interests. Felipe Toledo has received research funding from Company Meteomodem. The other authors declare that they have no conflict of interest.

Acknowledgements. The authors would like to acknowledge Johan Parra, Patricia Delville, Cristophe Boitel and Marc-Antoine Drouin from the SIRTA atmospheric observatory for their assistance with the execution of the field experiments. This acknowledgement is extended to Razvan Pirloaga and Dragos Ene from the INOE Institute, Romania. We would also like to thank Fabrice Bertrand and Jean-Paul Vinson from the LATMOS Laboratory, France, for their collaboration.

We would like to acknowledge the two reviewers for their expert comments which enabled us to improve the proposed calibration method.

Felipe Toledo acknowledges the French Association Nationale de la Recherche (ANRT) and the company Meteomodem for their contribution to the funding of this work. Finally, we state that this work is part of the ACTRIS-2 project and has received funding from the European Union's Horizon 2020 research and innovation program (grant no. 654109).

Financial support. This research has been supported by the European Union's Horizon 2020 research and innovation program (ACTRIS-2 (grant no. 654109)) and the French Association Nationale de la Recherche (ANRT) and the company Meteomodem. Together, they helped fund the work of coauthor Felipe Toledo.

Review statement. This paper was edited by Stefan Kneifel and reviewed by Alexander Myagkov and one anonymous referee.

References

Anagnostou, E. N., Morales, C. A., and Dinku, T.: The Use of TRMM Precipitation Radar Observations in Determining Ground Radar Calibration Biases, J. Atmos. Ocean. Tech., 18, 616–628, https://doi.org/10.1175/1520-0426(2001)018<0616:TUOTPR>2.0.CO;2, 2001.

Atlas, D.: RADAR CALIBRATION, B. Am. Meteorol. Soc., 83, 1313–1316, https://doi.org/10.1175/1520-0477-83.9.1313, 2002.

Bergada, M., Sekelsky, S. M., and Li, L.: External Calibration of Millimeter-Wave Atmospheric Radar System Using Corner Reflectors and Spheres. Eleventh ARM Science Team Meeting Proceedings, Atlanta, Georgia, 19–23 March 2001.

Boers, R., Baltink, H. K., Hemink, H. J., Bosveld, F. C., and Moerman, M.: Ground-Based Observations and Modeling of the Visibility and Radar Reflectivity in a Radiation Fog Layer, J. Atmos. Ocean. Tech., 30, 288–300, https://doi.org/10.1175/JTECH-D-12-00081.1, 2013.

Boucher, O., Randall, D., Artaxo, P., Bretherton, C., Feingold, G., Forster, P., Kerminen, V.-M., Kondo, Y., Liao, H., Lohmann, U., Rasch, P., Satheesh, S. K., Sherwood, S., Stevens, B., and Zhang, X. Y.: Clouds and Aerosols. In: Climate Change 2013: The Physical Science Basis. Contribution of Working Group I to the Fifth Assessment Report of the Intergovernmental Panel on Climate Change, edited by: Stocker, T. F., Qin, D., Plattner, G.-K., Tignor, M., Allen, S. K., Boschung, J., Nauels, A., Xia, Y., Bex, V., and Midgley, P. M., Cambridge University Press, Cambridge, United Kingdom and New York, NY, USA, 2013.

Bringi, V. N. and Chandrasekar, V.: Polarimetric Doppler weather radar: principles and applications, Cambridge university press, United States of America by Cambridge University Press, New York, 2001.

Brock, B. C. and Doerry, A. W.: Radar cross section of triangular trihedral reflector with extended bottom plate, Sandia National Laboratories Albuquerque, New Mexico 87185 and Livermore, California 94550, United States, Technical Report, Report Nos. SAND2009-2993, TRN: US201016%%1855, 7—22, https://doi.org/10.2172/984946, 2009.

Brooker, G: Introduction to Sensors for Ranging and Imaging, SciTech Publishing Inc, New York, United States, 2008.

Chandrasekar, V., Baldini, L., Bharadwaj, N., and Smith, P. L.: Calibration procedures for global precipitation-measurement ground-validation radars, URSI Radio Science Bulletin, 2015, 45–73, 2015.

Delanoë, J., Protat, A., Vinson, J.-P., Brett, W., Caudoux, C., Bertrand, F., Parent du Chatelet, J., Hallali, R., Barthes, L., Haeffelin, M., and Dupont, J.-C.: Basta: a 95-GHz fmcw doppler radar for cloud and fog studies, J. Atmos. Ocean. Tech., 33, 1023–1038, 2016.

Doviak, R. J. and Zrnić, D. S.: Doppler Radar and Weather Observations, Mineola, Dover Publications, INC, New York, 2006.

Dupont, J.-C., Haeffelin, M., Protat, A., Bouniol, D., Boyouk, N., and Morille, Y.: Stratus–fog formation and dissipation: a 6-day case study, Bound.-Lay. Meteorol.,143, 207–225, 2012.

Dupont, J.-C., Haeffelin, M., Wærsted, E., Delanoë, J., Renard, J.-B., Preissler, J., and O'dowd, C.: Evaluation of Fog and Low Stratus Cloud Microphysical Properties Derived from In Situ Sensor, Cloud Radar and SYRSOC Algorithm, Atmosphere, 9, 169, https://doi.org/10.3390/atmos9050169, 2018.

Duthoit, S., Salazar, J. L., Doyle, W., Segales, A., Wolf, B., Fulton, C., and Chilson, P.: A new approach for in-situ antenna characterization, radome inspection and radar calibration, using an Unmanned Aircraft System (UAS), in: 2017 IEEE Radar Conference (RadarConf), Seattle, WA, USA, 8–12 May 2017, IEEE, 0669–0674, https://doi.org/10.1109/RADAR.2017.7944287, 2017.

Ewald, F., Groß, S., Hagen, M., Hirsch, L., Delanoë, J., and Bauer-Pfundstein, M.: Calibration of a 35 GHz airborne cloud radar: lessons learned and intercomparisons with 94 GHz cloud radars, Atmos. Meas. Tech., 12, 1815–1839, https://doi.org/10.5194/amt-12-1815-2019, 2019.

Fox, N. I. and Illingworth, A. J.: The retrieval of stratocumulus cloud properties by ground-based cloud radar, J. Appl. Meteorol., 36, 485–492, 1997.

Garthwaite, M. C., Nancarrow, S., Hislop, A., Thankappan, M., Dawson, J. H., and Lawrie, S.: The Design of Radar Corner Reflectors for the Australian Geophysical Observing System : A single design suitable for InSAR deformation monitoring and SAR calibration at multiple microwave frequency bands, Record 2015/003, Geoscience Australia, Canberra, https://doi.org/10.11636/Record.2015.003, 2015.

Gaussiat, N., Sauvageot, H., and Illingworth, A. J.: Cloud liquid water and ice content retrieval by multiwavelength radar, J. Atmos. Ocean. Tech., 20, 1264–1275, 2003.

Haeffelin, M., Barthès, L., Bock, O., Boitel, C., Bony, S., Bouniol, D., Chepfer, H., Chiriaco, M., Cuesta, J., Delanoë, J., Drobinski, P., Dufresne, J.-L., Flamant, C., Grall, M., Hodzic, A., Hourdin, F., Lapouge, F., Lemaître, Y., Mathieu, A., Morille, Y., Naud, C., Noël, V., O'Hirok, W., Pelon, J., Pietras, C., Protat, A., Romand, B., Scialom, G., and Vautard, R.: SIRTA, a ground-based atmospheric observatory for cloud and aerosol research, Ann. Geophys., 23, 253–275, https://doi.org/10.5194/angeo-23-253-2005, 2005.

Haynes, J. M., L'Ecuyer, T. S., Stephens, G. L., Miller, S. D., Mitrescu, C., Wood, N. B., and Tanelli, S.: Rainfall retrieval over the ocean with spaceborne W-band radar, J. Geophys. Res., 114, D00A22, https://doi.org/10.1029/2008JD009973, 2009.

Hogan, R. J., Jakob, C., and Illingworth, A. J.: Comparison of ECMWF winter-season cloud fraction with radar-derived values, J. Appl. Meteorol., 40, 513–525, 2001.

Liebe, H. J.: MPM–An atmospheric millimeter-wave propagation model, Int. J. Infrared Milli., 10, 631–650, 1989.

Liebe, H. J., Manabe, T., and Hufford, G. A.: Millimeter-wave attenuation and delay rates due to fog/cloud conditions, IEEE T. Antenn. Propag., 37, 1617–1612, 1989.

Meissner, T. and Wentz, F. J.: The complex dielectric constant of pure and sea water from microwave satellite observations, IEEE T. Geosci.Remote, 42, 1836–1849, https://doi.org/10.1109/TGRS.2004.831888, 2004.

Mülmenstädt, J. and Feingold, G.: The radiative forcing of aerosol–cloud interactions in liquid clouds: wrestling and embracing uncertainty, Current Climate Change Reports, 4, 23–40, 2018.

Myhre, G., Shindell, D., Bréon, F.-M., Collins, W., Fuglestvedt, J., Huang, J., Koch, D., Lamarque, J.-F., Lee, D., Mendoza, B., Nakajima, T., Robock, A., Stephens, G., Takemura, T., and Zhang, H.: Anthropogenic and Natural Radiative Forcing, in: Climate Change 2013: The Physical Science Basis, Contribution of Working Group I to the Fifth Assessment Report of the Intergovernmental Panel on Climate Change, edited by: Stocker, T. F., Qin, D., Plattner, G.-K., Tignor, M., Allen, S. K., Boschung, J., Nauels, A., Xia, Y., Bex, V., and Midgley, P. M., Cambridge University Press, Cambridge, United Kingdom and New York, NY, USA, 2013.

Pappalardo, G.: ACTRIS Aerosol, Clouds and Trace Gases Research Infrastructure, EPJ Web Conf., 176, 09004, https://doi.org/10.1051/epjconf/201817609004, 2018.

Pozar, D. M.: Microwave engineering, John Wiley & Sons, Inc., Hoboken, New Jersey, 2009.

Protat, A., Bouniol, D., Delanoë, J., O'Connor, E., May, P. T., Plana-Fattori, A., Hasson, A., Görsdorf, U., and Heymsfield, A. J.: Assessment of CloudSat reflectivity measurements and ice cloud properties using ground-based and airborne cloud radar observations, J. Atmos. Ocean. Tech., 26, 1717–1741, 2009.

Protat, A., Bouniol, D., O'Connor, E. J., Klein Baltink, H., Verlinde, J., and Widener, K.: CloudSat as a Global Radar Calibrator, J. Atmos. Ocean. Tech., 28, 445–452, https://doi.org/10.1175/2010JTECHA1443.1, 2011.

Richardson, M.: Fundamentals of the discrete fourier transform, Sound and vibration magazine, 12, 40–46, 1978.

Rodríguez Olivos, R.: Design, construction and testing of a 2SB receiver for the southern millimeter-wave telescope, PhD thesis, available at: http://repositorio.uchile.cl/handle/2250/133531 (last access: 3 December 2020), 2015.

Sassen, K.: Ice cloud content from radar reflectivity, J. Clim. Appl. Meteorol., 26, 1050–1053, 1987.

Scolnik, M. I.: Radar Handbook, 3rd edn., McCraw-Hill, New York, 2000.

Sekelsky, S. M. and Clothiaux, E. E.: Parallax Errors and Corrections for Dual-Antenna Millimeter-Wave Cloud Radars, J. Atmos. Ocean. Tech., 19, 478–485, https://doi.org/10.1175/1520-0426(2002)019<0478:PEACFD>2.0.CO;2, 2002.

SIRTA: Data Request Form, SIRTA/IPSL, available at: https://sirta.ipsl.fr/data_form.html, last access: 3 December 2020a.

SIRTA: Data Policy, SIRTA/IPSL, available at: https://sirta.ipsl.fr/data_policy.html, last access: 3 December 2020b.

SIRTA, SIRTA/IPSL, https://sirta.ipsl.fr/, last access: 3 December 2020c.

Toledo, F., Dupont, J.-C., Delanoë, J., Haeffelin, M., Parra, J., Delville, P., Boitel, C., and Le Gac, C.: 2018 and 2019 ACTRIS Cloud Radar Calibration Campaign, Corner Reflectors on Masts Experiment, IPSL, https://doi.org/10.14768/6dd7bbb2-6e0d-4de3-bf03-7d6ead628845, 2020.

Uttal, T. and Kropfli, R. A.: The Effect of Radar Pulse Length on Cloud Reflectivity Statistics, J. Atmos. Ocean. Tech., 18, 947–961, https://doi.org/10.1175/1520-0426(2001)018<0947:TEORPL>2.0.CO;2, 2001.

Wærsted, E. G., Haeffelin, M., Dupont, J.-C., Delanoë, J., and Dubuisson, P.: Radiation in fog: quantification of the impact on fog liquid water based on ground-based remote sensing, Atmos. Chem. Phys., 17, 10811–10835, https://doi.org/10.5194/acp-17-10811-2017, 2017.

Wærsted, E. G., Haeffelin, M., Steeneveld, G.-J., and Dupont, J.-C.: Understanding the dissipation of continental fog by analysing the LWP budget using idealized LES and in situ observations, Q. J. Roy. Meteor. Soc., 145, 784–804, https://doi.org/10.1002/qj.3465, 2019.

Yau, M. K. and Rogers, R. R.: A short course in cloud physics, 3rd edn., Elsevier Science & Technology, Imprint: Butterworth-Heinemann Ltd, Oxford, United Kingdom, 1996.

Yin, J., Hoogeboom, P., Unal, C., Russchenberg, H., Van der Zwan, F., and Oudejans, E.: UAV-Aided Weather Radar Calibration, IEEE T. Geosci. Remote, 57, 10362–10375, https://doi.org/10.1109/TGRS.2019.2933912, 2019.

3.3 Geometrical RCS simulator

This simulator enables the calculation of the perceived RCS of a corner reflector for a given geometrical configuration of the calibration setup. The model includes the effects of imperfect aiming by including antenna pattern calculations and RCS vs incidence angle for the reflector. Regarding the antenna pattern, it is possible to use a Gaussian model, or to input a beam shape manually. In this section we only show how the model works with the gaussian beam lobe. The changes that must be done to equations in order to consider other beam shapes is straightforward.

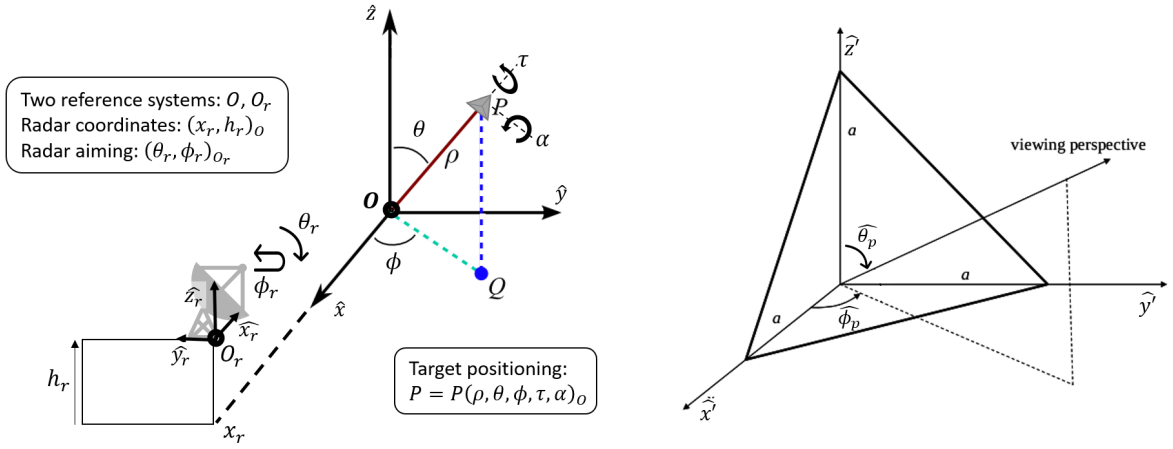

Figure 3.1: Diagram of the geometrical RCS simulator. (Left) shows the coordinate axes and the degrees of freedom of the simulator. (Right) shows the coordinates used to characterize the beam incidence angle on the target. Right figure is adapted from Doerry and Brock (2009).

The input arguments for the RCS simulator are shown in Fig. 3.1 (Left). They are explained as follows:

- Radar position, referenced at the origin O: $\vec{R_O} = (x_r, 0, h_r)$
- Radar aiming angle, referenced at the origin O_r: $\vec{Y_{O_r}} = (1, \theta_r, \phi_r)$
  - θ_r: Azimuth angle of the radar positioner. 0° is vertical aiming.
  - ϕ_r: Azimuth angle of the positioner. The line connecting the radar and the mast base corresponds to $\phi_r = 0°$.
- Target position (in spherical coordinates), referenced at the origin O: $\vec{T_O} = (\rho, \theta, \phi)$
  - τ: Mast twist angle. $\tau = 0°$ when target boresight is parallel to the x axis.
  - α: Target tilt angle. When $\alpha = 0°$ the target z' axis is parallel to $\hat{\rho}$. If $\alpha > 0°$ then the target tilts forward.
- a: Target size parameter (Brooker, 2006).
- λ: Wavelength
- Antenna properties (when using a Gaussian beam lobe):
  - Θ: antenna beamwidth

Output variables:

- Maximum RCS of the target $\Gamma_0[dBsm]$
- RCS of the target for the beam's incidence vector $\hat{r_i}$: $\Gamma(\vec{r_i})[dBsm]$
- Effective RCS of the target considering incidence angle and loss L due to positioning ΔD° away from the antenna beam center: $\Gamma_{eff} = \Gamma(\vec{r_i}) - 2L(\Delta D)[dB]$

In the following sections we list the equations used to calculate each term.

3.3.1 Maximum theoretical RCS of the corner reflector

From Brooker (2006), it can be simply calculated as:

$$\Gamma_0[dBsm] = 10\log_{10}\left(\frac{4\pi a^4}{3\lambda^2}\right) \tag{3.1}$$

3.3.2 Calculation of the corner reflector RCS for a given incidence angle

To calculate the reflector RCS for a given beam incidence angle $\Gamma(\vec{r_i})$, we must first obtain the perspective vector. This is done by changing the coordinate system of the radar aiming vector Y_{O_r}, from O_r to O, and then multiplying by -1 to invert its direction.

$$\vec{r_i} = -1\left(-(\vec{Y_{O_r}}\cdot\hat{x_r})\hat{x} - (\vec{Y_{O_r}}\cdot\hat{y_r})\hat{y} + (\vec{Y_{O_r}}\cdot\hat{z_r})\hat{z_r}\right) \tag{3.2}$$

Target unitary vectors $\hat{x'}$, $\hat{y'}$, $\hat{z'}$ (in Fig. 3.1 (Left)):

$$\begin{aligned}\hat{x'} = \frac{\sqrt{2}}{2}\big[&-\sin(\theta)\cos(\phi)\sin(\alpha)+\cos(\theta)\cos(\phi)(\cos(\alpha)\cos(\tau)+\sin(\tau))-\sin(\phi)(\cos(\alpha)\sin(\tau)-cos(\tau))\big]\hat{x}\\ &+\big[\sin(\theta)\sin(\phi)\sin(\alpha)+\cos(\theta)\sin(\phi)(\cos(\alpha)\cos(\tau)+\sin(\tau))+\cos(\phi)(\cos(\alpha)\sin(\tau)-\cos(\tau))\big]\hat{y}\\ &+\big[-cos(\theta)sin(\alpha)-sin(\theta)(\cos(\alpha)\cos(\tau)+\sin(\tau))\big]\hat{z}\end{aligned} \tag{3.3}$$

$$\begin{aligned}\hat{y'} = \frac{\sqrt{2}}{2}\big[&-\sin(\theta)\cos(\phi)\sin(\alpha)+\cos(\theta)\cos(\phi)(\cos(\alpha)\cos(\tau)-\sin(\tau))-\sin(\phi)(\cos(\alpha)\sin(\tau)+\cos(\tau))\big]\hat{x}\\ &+\big[\sin(\theta)\sin(\phi)\sin(\alpha)+\cos(\theta)\sin(\phi)(\cos(\theta)\cos(\tau)-\sin(\tau))+\cos(\phi)(\cos(\alpha)\sin(\tau)+\cos(\tau))\big]\hat{y}\\ &+\big[-\cos(\theta)\sin(\alpha)-\sin(\theta)(\cos(\alpha)\cos(\tau)-\sin(\tau))\big]\hat{z}\end{aligned} \tag{3.4}$$

$$\begin{aligned}\hat{z'} = &\big[\sin(\theta)\cos(\phi)\cos(\alpha)+\cos(\theta)\cos(\phi)\sin(\alpha)\cos(\tau)-\sin(\phi)\sin(\alpha)\sin(\tau)\big]\hat{x}\\ &+\big[\sin(\theta)\sin(\phi)\cos(\alpha)+\cos(\theta)\sin(\phi)\sin(\alpha)\cos(\tau)+\cos(\phi)\sin(\alpha)\sin(\tau)\big]\hat{y}\\ &+\big[\cos(\theta)\cos(\alpha)-\sin(\theta)\sin(\alpha)\cos(\tau)\big]\hat{z}\end{aligned} \tag{3.5}$$

Project perspective vector to the coordinate system of the target:

$$x_p = \vec{r_i}\cdot\hat{x'} \tag{3.6}$$

$$y_p = \vec{r_i}\cdot\hat{y'} \tag{3.7}$$

$$z_p = \vec{r_i}\cdot\hat{z'} \tag{3.8}$$

Then we can calculate the perspective angles θ_p and ϕ_p:

$$p = \sqrt{x_p^2 + y_p^2 + z_p^2} \tag{3.9}$$

$$\theta_p = \arccos(z_p/p) \tag{3.10}$$

$$\phi_p = \arctan(y_p/x_p) \tag{3.11}$$

$$\tag{3.12}$$

Invalid cases: If θ_p or $\phi_p \notin [0, \frac{\pi}{2}]$, $\Gamma(\vec{r_i})$ is set to Nan (not a number). This avoids invalid results that may happen in configurations where the radar beam does not hit the interior of the reflector.

Finally, we can use valid θ_p and ϕ_p angles and the equations published by Doerry and Brock (2009) to calculate $\Gamma(\vec{r_i})$:

$$\Gamma(\vec{r_i}) = \begin{cases} \frac{4\pi}{\lambda^2} a^4 \left(\frac{4c_1 c_2}{c_1 + c_2 + c_3} \right)^2 & \text{for } c_1 + c_2 \leq c_3 \\ \frac{4\pi}{\lambda^2} a^4 \left(c_1 + c_2 + c_3 - \frac{2}{c_1 + c_2 + c_3} \right)^2 & \text{for } c_1 + c_2 > c_3 \end{cases} \tag{3.13}$$

For c_1, c_2 and c_3, we assign one of the terms indicated below, imposing $c_1 \leq c_2 \leq c_3$.

$$\left.\begin{matrix} c_1 \\ c_2 \\ c_3 \end{matrix}\right\} = \begin{cases} \cos(\theta_p) \\ \sin(\theta_p)\sin(\phi_p) \\ \sin(\theta_p)\cos(\phi_p) \end{cases} \tag{3.14}$$

3.3.3 Calculation of the effective reflector RCS considering antenna pattern

Since we already calculated $\Gamma(\vec{r_i})$ in the previous section, we only have left to estimate the losses $L(\Delta D)$ in the effective RCS introduced when the target is a ΔD angle away from the beam center to obtain the effective RCS Γ_{eff}. Calculations assume an axially symmetric beam, but can be adapted to use beams with other shapes.

First, the vector connecting radar and target position:

$$\vec{\delta_O} = T_O - R_O \tag{3.15}$$

We now change the origin of $\vec{\delta_O}$ from O to O_r:

$$\vec{\delta_{O_r}} = -(\vec{\delta_O} \cdot \hat{x})\hat{x_r} - (\vec{\delta_O} \cdot \hat{y})\hat{y_r} + (\vec{\delta_O} \cdot \hat{z})\hat{z_r} \tag{3.16}$$

With this vector and the radar unitary aiming vector Y_{O_r} we can proceed to calculate the angular deviation ΔD of the target from the center of the beam:

$$\Delta\theta = \arccos\left(\frac{\delta_{O_r} \cdot \hat{z_r}}{\|\delta_{O_r}\|} \right) - \theta_r \tag{3.17}$$

$$\Delta\phi = \arctan\left(\frac{\delta_{O_r} \cdot \hat{y_r}}{\delta_{O_r} \cdot \hat{x_r}} \right) - \phi_r \tag{3.18}$$

$$\Delta D = \sqrt{\Delta\theta^2 + \Delta\phi^2} \tag{3.19}$$

$$\tag{3.20}$$

And the loss, for the Gaussian antenna lobe of beamwidth Θ, is:

$$L(\Delta D) = 10\log_{10}\left(exp\left(\frac{-(2.355\Delta D)^2}{2\Theta^2}\right)\right)[dB] \tag{3.21}$$

Invalid cases: We observed that for our antenna the Gaussian approximation works well if $\Delta D \leq 0.5°$ (Fig. 4 (b) of the article). Thus, we decide that any ΔD larger than $0.5°$ our calculations will return an invalid $L(\Delta D)$ value.

With all these terms and Eq. (3.22) we finally calculate the effective RCS Γ_{eff}:

$$\Gamma_{eff} = \Gamma(\vec{r_i}) - 2L(\Delta D)[dB] \tag{3.22}$$

3.4 Misalignment impact in calibration using corner reflectors

Equation (3.23) is the Radar Cross Section (RCS) calibration constant, obtained when aiming the radar towards a reference reflector of RCS Γ_0 located at a distance r_0. $L_{at}(r_0)$ represents the atmospheric attenuation between the radar and the reflector. $P_r(r_0)$ is the received power from the target position. To be correct, this equation requires a perfect alignment between the target boresight and the axis of the antenna lobe.

The RCS calibration term C_Γ can depend on additional variables, for example on temperature, due to gain changes inside the radar (Eq. (1.8)). For this analysis, however, we neglect these sources of variability in the calibration and assume that $C_\Gamma = C_\Gamma^0$, with C_Γ^0 a constant defined as the calibration coefficient in the article.

$$C_\Gamma^0 = \Gamma_0 - 2L_{at}(r_0) - 40\log_{10}(r_0) - P_r(r_0) \tag{3.23}$$

We define the effective RCS Γ_i as the RCS that will be observed by the radar when the target is off the beam center, or when the target is not in its designed positioning. i.e. the RCS that a perfectly calibrated radar would perceive under a non-ideal alignment.

If we use Eq. (3.23) to calibrate assuming we have an RCS = Γ_0, but in reality we have an effective RCS $\Gamma_i = \Gamma_0 - \epsilon_i$, our estimated calibration term will be biased (Eq. (3.24)). $C_{\Gamma i}^0$ would be the biased, experimentally retrieved calibration coefficient, C_Γ^0 the real value and ϵ_i the calibration bias.

$$C_{\Gamma i}^0 = C_\Gamma^0 + \epsilon_i \tag{3.24}$$

The value of the bias term ϵ_i is difficult to estimate, because it follows an unkown distribution which depends on the alignment uncertainty of the radar, mast and target. In addition, if the average bias $\overline{\epsilon} \neq 0$ (i.e. its distribution is not zero mean), bias will not be canceled by simply averaging $C_{\Gamma i}^0$ values from multiple iterations, as indicated in Eq. (3.24).

$$\frac{1}{N}\sum_{i=1}^{N} C_{\Gamma i}^0 = \frac{1}{N}\sum_{i=1}^{N}(C_\Gamma^0 + \epsilon_i) = C_\Gamma^0 + \overline{\epsilon_i} \tag{3.25}$$

Figure 9 (b) of the article shows one example of a Γ_i distribution obtained from propagating uncertainty in the experiment alingment. We can clearly observe that this distribution is not zero mean. This confirms that, if no further corrections are applied, a calibration coefficient estimated by just using the average of multiple experiments is bound to have a bias $\overline{\epsilon_i}$.

To estimate the value of $\overline{\epsilon_i}$ for our setup, we use the standard deviation σ between the $C_{\Gamma i}^0$ values retrieved in each iteration as an indicator of the underlying bias distribution of the experimental setup

(Eq. (3.26)). It is possible to prove that this σ value is approximately equal to the standard deviation σ_ϵ of the system RCS distribution.

$$\sigma^2 = \frac{1}{N}\sum_{i=1}^{N}(C^0_{\Gamma i} - \overline{C^0_{\Gamma i}})^2 = \sigma_\epsilon^2 \tag{3.26}$$

The problem is that there are many possible uncertainty combinations in the setup that can generate distributions with the same σ_ϵ, but different expected bias $\overline{\epsilon_i}$ values. Nevertheless, by simulating a large amount of RCS distributions we can estimate the most likely bias $\overline{\epsilon_i}$, to a given degree of uncertainty. The procedure for doing this is explained in Sect. 3.4.1.

3.4.1 Estimation of the misalignment bias

In this section we explain how we generate a bias distribution for our setup, to estimate the bias correction term and its uncertainty. This is explained using the 20 m mast setup and the results of the 2018 campaign (Fig. 10 of the article).

We begin by simulating the distribution $f_{\overline{\epsilon_i},\sigma_\epsilon}(\overline{\epsilon_i},\sigma_\epsilon)$. This probability distribution, evaluated at the standard deviation σ observed from repeating N experiments (Eq. (3.26)), provides a probability distribution for the bias.

We define this bias distribution as $\Lambda = f_{\overline{\epsilon_i}|\sigma_\epsilon}(\overline{\epsilon_i} \mid \sigma_\epsilon = \sigma)$.

To simulate $f_{\overline{\epsilon_i},\sigma_\epsilon}(\overline{\epsilon_i},\sigma_\epsilon)$ this we need to generate a large amount of $(\overline{\epsilon_i},\sigma_\epsilon)$ pairs, calculated from experiments of N iterations.

These $(\overline{\epsilon_i},\sigma_\epsilon)$ pairs are generated as follows:

1. We generate a random uncertainty set [1].
2. This uncertainty set is used to generate N random RCS values.
3. The RCS results are used to calculate a single $(\overline{\epsilon_i},\sigma_\epsilon)$ pair.
4. Repeat.

For the **20 m mast setup** we sampled the uncertainty sets used to generate the distribution $f_{\overline{\epsilon_i},\sigma_\epsilon}(\overline{\epsilon_i},\sigma_\epsilon)$ with the following functions[2]:

- $\sigma_{\theta_r} = \mathcal{U}([0°, 0.375°))$
- $\sigma_{\phi_r} = \mathcal{U}([0°, 0.375°))$
- $\sigma_\theta = \mathcal{U}([0°, 5°))$
- $\sigma_\tau = \mathcal{U}([0°, 10°))$

The region where σ_{θ_r} and σ_{ϕ_r} are sampled is within 0 and 3 times the nominal resolution of the radar positioner. For the mast angles θ and τ we have chosen to explore an space much larger than any deviation we observed during the experiments. We found that with these parameters the sampling covers a wide range of σ_ϵ values, large enough to enable a reliable estimation of the bias in our experiment.

Figure 3.2 shows the resulting $f_{\overline{\epsilon_i}|\sigma_\epsilon}(\overline{\epsilon_i},\sigma_\epsilon)$. We can observe that the distribution is very well defined around our results of the calibration experiment of 2018, where we got a value of $\sigma = 0.33$. It only starts to lose density only for relatively large values of $\overline{\epsilon}$ and σ_ϵ.

[1] The uncertainty set is the set of all uncertainties assigned to the system, for example one uncertainty set is described in Sect. 5.6 of the article.

[2] $\mathcal{U}(\cdot)$ is the continous uniform probability distribution.

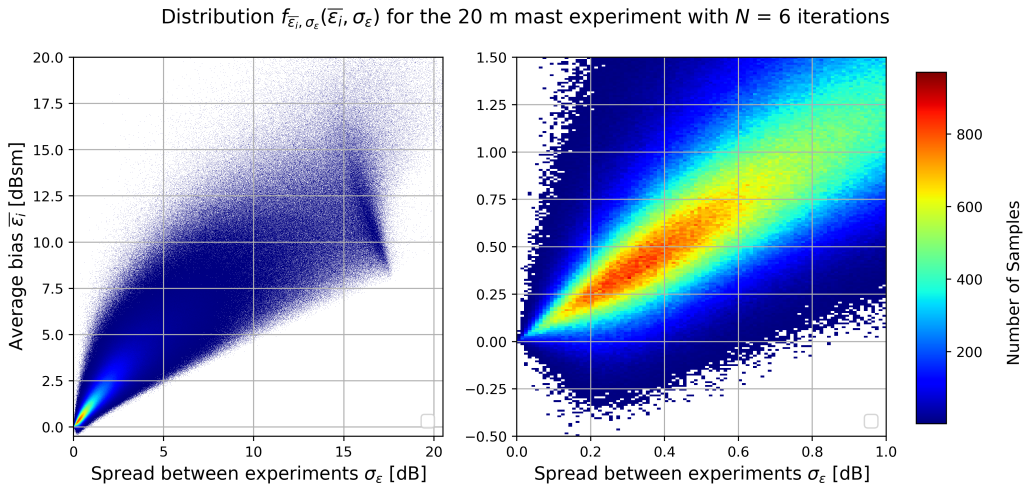

Figure 3.2: Simulation of $f_{\overline{\epsilon_i},\sigma_\epsilon}(\overline{\epsilon_i},\sigma_\epsilon)$. This distribution enables the estimation of the alignment bias distribution Λ by selecting the points with σ_ϵ equal to the experimentally observed σ value.

To avoid problems that could be introduced by the discrete nature of the simulated probability distribution, we estimate the bias distribution Λ as $\Lambda = f_{\overline{\epsilon_i}|\sigma_\epsilon}\left(\overline{\epsilon_i} \mid \sigma_\epsilon = \sigma \pm 5\%\right)$. The bias distribution obtained is shown in Fig. 3.3.

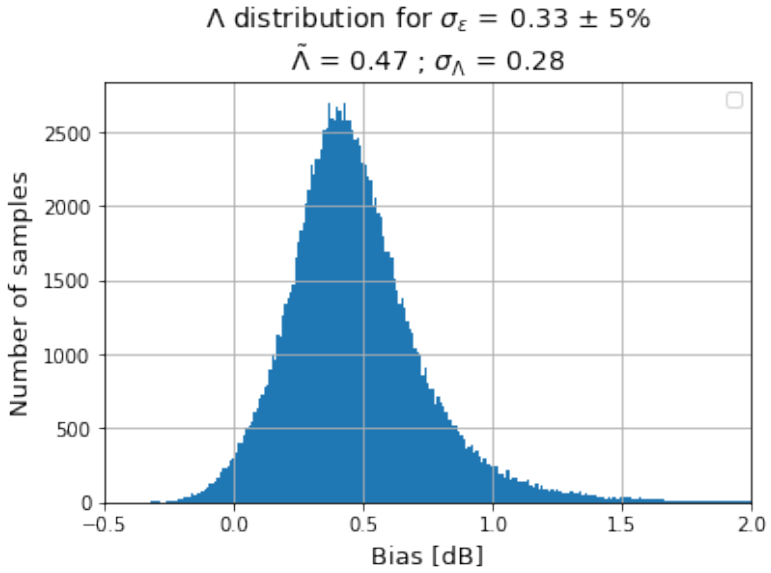

Figure 3.3: Estimated bias distribution Λ for the 20 m mast experiment of 2018.

Since Λ is asymmetric, we use the median $\tilde{\Lambda}$ as the most likely bias for the system, and its RMSE σ_Λ as its uncertainty. This way we can now correct the bias in the calibration experiment with Eq. (3.27). The total uncertainty of this estimator is indicated in Eq. (3.28), with σ_i the uncertainty in the estimation of each $C^0_{\Gamma i}$ value.

$$\hat{C^0_\Gamma} = \frac{1}{N}\sum_{i=1}^{N} C^0_{\Gamma i} - \tilde{\Lambda} \tag{3.27}$$

$$\sigma_{\hat{C^0_\Gamma}} = \sqrt{\frac{1}{N^2}\sum_{i=1}^{N} \sigma_i^2 + \sigma_\Lambda^2} \tag{3.28}$$

Finally, we include the generating functions used for the **10 m mast setup**. The use of a motor to aim the target towards the radar introduced the need of using different generating functions to sample the uncertainty sets. Apart from this the procedure remains the same as the one used for the 20 m mast.

- $\sigma_\alpha = \mathcal{U}(0, 10°)$
- $\sigma_\tau = \mathcal{U}(0, 10°))$
- $\sigma_{\theta_r} = \mathcal{U}(0, 0.375°)$
- $\sigma_{\phi_r} = \mathcal{U}(0, 0.375°)$

3.5 Synthesis

This chapter presented a method to calibrate scanning FMCW cloud radars using corner reflectors, which was developed during two calibration campaigns carried out at the SIRTA atmospheric observatory in 2018 and 2019.

The calibration methodology consists in performing several target sampling iterations. Each iteration begins with a realignment of the experimental setup, followed by approximately one hour of sampling the reflector signal. When all iterations are completed, the final RCS and Equivalent Reflectivity calibration terms can be computed. The calibration methodology includes methods to quantify and correct biases, and to quantify the calibration uncertainty.

The method was applied to calibrate a BASTA-mini radar for two different experimental configurations. The first used a 10 cm corner reflector mounted on a pan-tilt motor, on top of a 10 meter mast, 196 m away from the radar. The second used a 20 cm corner reflector fixed on top of a 20 meter mast, 376.5 m away from the radar. The main results to retain from this chapter are:

- The design of the experimental setup must minimize compression in the radar receiver. Compression can be checked by measuring the power backscattered from the reflector, and comparing it with the power transfer curve of the receiver. In the two experimental setups tested we observed losses due to compression of 0.2-0.3 dB, which were corrected using the receiver power transfer curve. Receiver compression (and receiver saturation) can be reduced by positioning the target farther away from the radar, or by switching the target for another with less RCS.

- The reflector used in calibration must be farther than the radar near-field distance. BASTA-Mini cloud radar has a Fraunhofer near-field distance of 50 m, which is less than the distance used in both experimental setups (distances of 196 and 375.5 m).

- The reflector distance also has to be large enough to minimize loses due to antenna overlap. The estimated maximum overlap loss, assuming parallel antennas, is calculated to be less than 0.1 dB for the closest (10-m) mast setup. This result could not be verified experimentally due to limitations in the precision of the radar scanner. Alternative approaches for estimating this parameter, or for characterizing antenna parallax, should be a focal point of future research.

- Environmental clutter must be minimized in the experimental setup design. It is advisable to perform the calibration experiments in an open field several hundred meters long, free from trees or other obstacles.

  The calibration uncertainty introduced by clutter depends on the signal to clutter ratio. Signal to clutter ratio can be measured by comparing the power received from the target with the power received from the target position after removing the reflector (Chandrasekar et al., 2015). The

impact of signal to clutter ratio in uncertainty can be highly variable, depending on its value. For the 10 m mast setup, signal to clutter ratio introduces an uncertainty of 0.9 dB, while for the 20 m mast setup it introduces 0.09 dB. The likely reason for this difference are the additional clutter from stronger reflections on the pan-tilt motor installed on the 10 m mast.

- To reduce the variability of the reflector signal in each sampling iteration, it is advisable to perform calibration measurements with clear conditions at the surface, without fog or rain. It is also recommended to prefer measurements taken when wind speed is below 1 ms^{-1}, with low turbulence, to minimize mechanical vibration of the experimental setup.

- Calibration is impacted by gain changes of the radar components, caused by temperature variations inside the radar. We found calibration variations of up to $\pm$ 0.6 dB for our radar. This bias was corrected using a temperature correction function, derived with an uncertainty of $\sigma_T = 0.23$ dB. This result indicates that temperature effects must be studied to avoid a temperature dependent bias in the calibration.

- Frequency dependent losses in the IF of the radar receiver cause range dependent gain variations. In this study, IF gain variations reached up to 0.9 dB, implying the need of a IF correction function to avoid the introduction of a range dependent bias in the calibration.

- Iterations are necessary to quantify the bias introduced by unavoidable misalignments in the experimental setup. The variability in the target signal when comparing different iterations can be combined with a geometrical model of the experimental setup, to calculate which sets of positioning uncertainties reproduce the observed results. These sets enable the estimation of the bias and uncertainty introduced by setup misalignment.

  The bias correction for the 20 m mast setup was of $\approx 0.4 \pm 0.3$ dB, with this minimum uncertainty value reached after 5 iterations. Meanwhile for the 10 m mast the bias correction was of $\approx 0.2 \pm 0.1$ dB, reached after 3 iterations only. The difference is explained by the more precise alignment attainable with the pan-tilt motor installed on the 10 m mast.

- The need of iterations may increase the time needed for calibration experiments, depending on the ease of alignment of each setup. Performing 6 iterations with the 20 m mast takes approximately a week, while 10 iterations with the 10 m mast take about 12 hours. This large difference appears because the 20 m mast must be aligned using the ropes that fix its structure to the ground, while the 10 m mast has a remotely controlable pan-tilt motor on top that could be aligned much faster.

- At present, the predominant source of uncertainty is introduced by the reference reflector RCS ($\approx$2 dB). The uncertainty budget indicated that to reach an uncertainty lower than 1 dB, it is necessary to have a target RCS characterization with an uncertainty below 0.9 dB.

- The calibration methodology enabled the quantification of the uncertainty sources for each experimental setup. This information showed, for example, that in the 10 m mast setup the main source of uncertainty, besides the reflector RCS, is clutter (0.9 dB). Meanwhile, in the 20 m mast setup this place is taken by the uncertainty introduced by setup alignment (0.28 dB). The contribution of clutter in this setup is significantly lower (0.09 dB). This analysis shows that the proposed calibration approach allows quantitative comparisons between different experimental setups, providing valuable information to further improve the calibration technique.

Chapter 4

Cloud radar calibration transfer

4.1 Introduction

The first step in of the fog monitoring network calibration strategy is the calibration of a reference radar, with a known uncertainty, using corner reflectors. This work is presented in chapter 3. The second step is the transfer of the reference radar calibration to other radars in the network. The calibration transfer is performed using clouds as common targets, providing a more general calibration solution that does not require a dedicated site with a mast and reference reflectors.

This chapter presents the calibration transfer methodology, developed for the second step of the fog monitoring network calibration strategy. Since its content draws to some extent on the terminology and analyses developed in chapter 4, it is advisable to review the latter before continuing. The method presented in this chapter was developed in collaboration with Susana Jorquera, during her internship at the LMD laboratory (UMR 8539).

The calibration transfer methodology consists of the following steps: first, to transport and install the reference radar next to an uncalibrated instrument. Second, to leave them sampling clouds for several days. Third, to process and then compare the measurements of both instruments, to transfer the calibration. Data processing corrects differences in the sensitivity of the instruments, so it is not necessary that the radars involved be of the same model or manufacturer. However, at present it can only be applied when the involved radars have close operating frequencies, such that differences in the electromagnetic wave absorption of gases and liquid water are negligible.

The proposed solution greatly benefits from the specific capabilities of the BASTA mini radar. First, the instrument can be calibrated reliably and with a known uncertainty using the method described in chapter 3. This method was developed using this radar, so no further modifications are needed. Second, the BASTA mini radar weights just 35 kilograms without the scanner, making it significantly lighter than other radar models (MODEM, 2018). This makes the radar relatively easy and safe to transport. Third, the radar already has a Voltage-Controlled Oscillator (VCO) by default. The VCO allows a 1 GHz tuning range for the carrier wave, enabling the co-location of BASTA next to other radars in its same band without interference problems.

The chapter is structured as follows: Section 4.2 explains the theoretical principle used for calibration transfer, based on the radar equation. Section 4.3 presents the calibration transfer methodology, explained using data gathered during the 2019 ACTRIS Cloud Radar Calibration Campaign. Section 4.4 presents the results of the example calibration transfer experiment. Finally, section 4.5 presents a synthesis with the main results of this chapter.

4.2 Calibration transfer principle

Cloud radars measure the reflectivity of remote hydro-meteors by measuring the power they reflect back. The quantitative calculation is done with the Radar Equation, written in logarithmic units in Eq. (4.1). A more detailed explanation of this equation and of its derivation can be found in Sect. 1.6.

$$Z(r) = C_Z + 2L_{at}(r) + 20\log_{10}(r) + P_r(r) \tag{4.1}$$

The reflectivity $Z(r)$ at a distance r is calculated by adding the received power $P_r(r)$ with the two way atmospheric attenuation $2L_{at}(r)$, the square of the distance in dB scale $20\log_{10}(r)$ and a calibration term C_Z (Bringi and Chandrasekar, 2001; Chandrasekar et al., 2015). Usually, C_Z is considered to be a constant term, however in FMCW radars it may vary depending on other variables. For example, in chapter 3 we observed that C_Z could be separated into a constant calibration coefficient C_{Z0}, a temperature correction function $f_T(T)$ and an intermediate frequency (IF) correction function $f_{IF}(F_b)$ (See Eq. (4.2)).

$$C_Z(T, F_b) = C_{Z0} + f_T(T) + f_{IF}(F_b) \tag{4.2}$$

The calibration coefficient is the reference calibration value of the radar, also known in literature as the radar calibration constant (e.g. Chandrasekar et al. (2015)). The temperature correction function corrects variations in the calibration coefficient due to internal gain changes in the radar caused by temperature variations, and the IF correction function corrects the calibration coefficient, compensating gain variations for power measurements at different distances caused by non ideal filters at each IF frequency F_b. Additional correction functions may be necessary, depending on the radar model. One that could be important for bistatic radars is the correction of range dependent gain variations, caused by errors in antenna parallax (Sekelsky and Clothiaux, 2002). These correction functions are necessary to compensate for variations in gain caused by variations in radar parameters.

In this calibration methodology we have two instruments: a reference radar and an uncalibrated radar. The reference radar is calibrated using an alternative method, such as the one proposed in chapter 3, and thus can measure reflectivity with a known calibration uncertainty. In the next lines, all parameters associated with this radar will have a superscript ^{C} (for example, its reflectivity measurements will be written as Z^C). Meanwhile, the uncalibrated radar performs reflectivity retrievals with unknown bias an uncertainty. Parameters associated with the uncalibrated radar will have a superscript ^{NC} (for example, its reflectivity measurements will be written as Z^{NC}).

Both radars should be installed close to maximize the chance of simultaneously sampling similar cloud sections. The operating frequency of the radars must be different, to avoid interference, but at the same time close enough to neglect atmospheric attenuation differences between the instruments. This is usually feasible because W band radars have relatively narrow bandwidths (in the order of ∼100 MHz) compared to their operation band frequency (≈ 95 GHz). In addition, any correction functions necessary to compensate for changes in internal radar parameters must be obtained independently, and applied during cloud sampling to compensate for gain variations.

The calibration correction is obtained by substracting the reflectivity retrievals of both radars (Eq. (4.3)). The distance and atmospheric attenuation terms of Eq. (4.1) are canceled because samples are retrieved from the same distance, and at very close frequencies. The calibration term correction functions are used to correct power measurements, so that they differ only due to the gain difference between the radars. This constant difference is expressed as a constant term D_C in Eq. (4.4). By adding D_c to the difference between the calibration coefficients (also constant), we get Eq. (4.5). K represents the correction coefficient, which corresponds to the difference between calibrated and uncalibrated measurements.

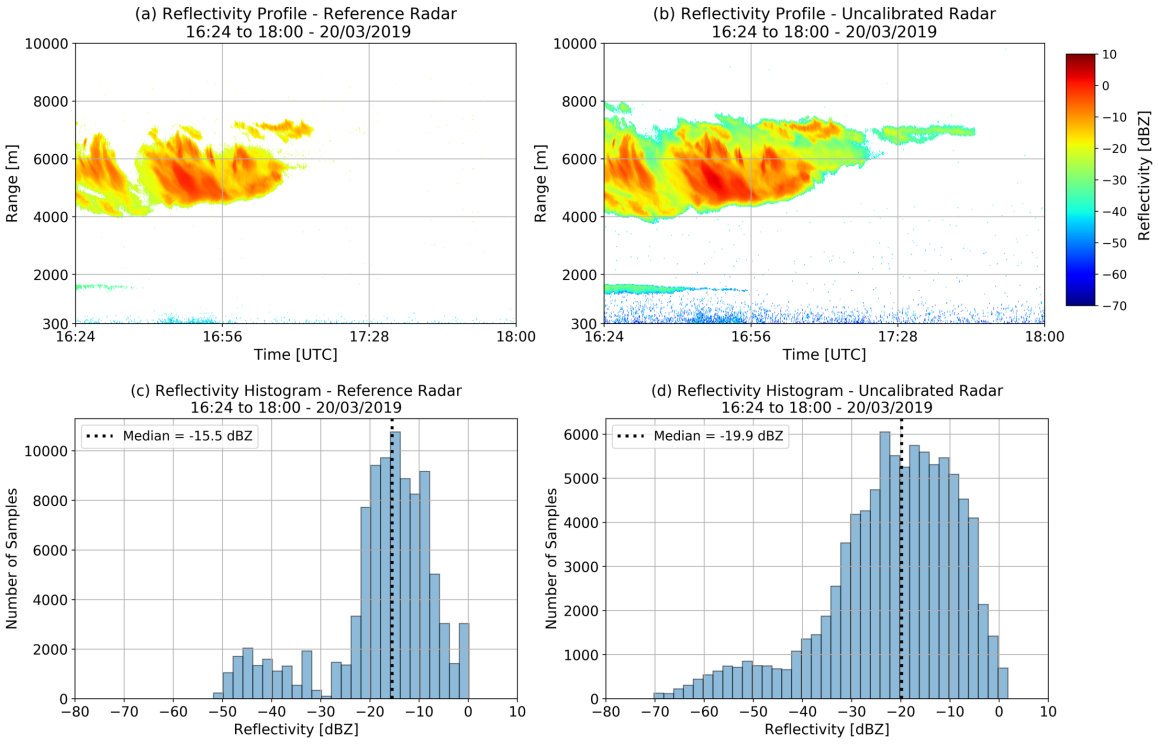

Figure 4.1: (a) Reflectivity of an altostratus cloud, retrieved with the calibrated reference radar. (b) Reflectivity of the same cloud, retrieved with the uncalibrated radar. (c) Histogram of the reflectivity samples shown in panel (a). (d) Histogram of the reflectivity samples shown in panel (b). The differences between the observed data and in the reflectivity distributions come mainly from differences in the sensitivity of the radars.

$$
\begin{aligned}
Z^C(r) - Z^{NC}(r) &= (C_{Z0}^C - C_{Z0}^{NC}) + [P_r^C(r) + f_T^C(T) + f_{IF}^C(F_b)] \\
&\quad - [P_r^{NC}(r) + f_T^{NC}(T) + f_{IF}^{NC}(F_b)] && (4.3)\\
&= (C_{Z0}^C - C_{Z0}^{NC}) + D_c && (4.4)\\
&= K && (4.5)
\end{aligned}
$$

In principle, it should be possible to estimate K just by comparing simultaneous measurements. Yet this is not usually the case, because instruments rarely have the exact same behavior. Figure 4.1 illustrates this problem. There we observe the same cloud sampled by two different radars. In panels (a) and (b) we observe that the reference radar is more noisy and has a lower sensitivity compared with the uncalibrated radar. Panels (c) and (d) show the reflectivity distributions of data in panels (a) and (b) respectively. We can observe that it is not straightforward to estimate K from these distributions. The difference in sensitivity would introduce a bias, since one radar has more low reflectivity samples than the other. Random error is also expected, and may be introduced by radar system noise, and differences in the sampling volume arising from antenna parallax errors or non-perfect vertical pointing (Sekelsky and Clothiaux, 2002).

Thus, the correction coefficient K should be estimated statistically, considering a data processing stage designed to remove asimetric data (reflectivity samples measured by only one of the instruments), and a large number of samples so that random error is minimized. The procedure developed for the estimation of K is presented in Sect. 4.3. After the correction coefficient K is estimated, it is possible

to correct uncalibrated radar measurements using Eq. (4.6).

$$Z^C(r) = Z^{NC}(r) + K \tag{4.6}$$

4.3 Methodology

In Sect. 4.2 we explain what is the calibration correction coefficient K, and how it could be retrieved by comparing measurements between the reference and the uncalibrated radar. We also indicated that a direct comparison may introduce bias due to differences in the radars sensitivity, and random error due to noise, to differences in pointing and to differences on the sampling volume. To mitigate the impact of these bias and uncertainty sources, we developed a calibration transfer protocol with three data processing stages: data selection, data cleansing and calibration transfer.

The experimental setup is presented in Sect. 4.3.1, and the data processing stages are explained in detail in Sects. 4.3.2, 4.3.3 and 4.3.4. The methodology is based on the calbration transfer experiments that took place during the 2018 and 2019 calibration campaigns. Therefore, we illustrate the explanation of each step using data from the calibration transfer experiment of 2019, where a BASTA mini, of the French LATMOS laboratory, transfers its calibration to a 94 GHz RPG cloud radar of the Romanian INOE Institute.

4.3.1 Experimental setup

The reference radar and the uncalibrated radar are placed close to each other, within a few tens of meters. Both radars are vertically aligned using a level tool on their frame. It is recommended to compare doppler velocity profiles to validate the vertical alignment. Then, both radars are setup to the operating modes indicated in Table 4.1. These modes are selected to perform measurements as similar as possible. The RPG radar uses three chirps to measure, and therefore its distance resolution and bandwidth change slightly for different ranges. There is no overlap between both radars operating frequencies. Therefore, no interference between radars was expected. This was later verified when setting up the radars.

Table 4.1: Radar configuration of the BASTA mini radar and the 94 GHz RPG radar, used during the calibration transfer experiment in 2019. BASTA mini is tuned to work in a single operating mode. The RPG radar uses three chirps per sampling period. Each chirp retrieves reflectivity measurements for specific vertical ranges, with independent distance resolutions.

	BASTA mini **Reference**	94 GHz RPG Cloud Radar **Uncalibrated**
Vertical Range (RA) and Distance Resolution (RE)	RA 0-12000 m, RE 15 m	Chirp 1: RA 119-1192 m, RE 29.8 m Chirp 2: RA 1222-4472 m, RE 29.8 m Chirp 3: RA 4531-10971 m, RE 34.1 m
Chirp Bandwidth	12.0 MHz	Chirp 1: 34.1 MHz Chirp 2: 11.0 MHz Chirp 3: 8.0 MHz
Central emission frequency	95.64 GHz	94.00 GHz
Time resolution	3 s	4 s

The IF and Temperature correction functions of BASTA mini were retrieved in chapter 3. Meanwhile, RPG IF correction function is derived using a two point calibration with liquid nitrogen and environmental temperature, following the procedure indicated in its manual (RPG, 2015). The RPG radar has an internal temperature stability within 500 mK, and therefore the use of a temperature correction function is not necessary.

Both radars are left sampling clouds continuously for two weeks. To maximize the time with reliable measurements, an operator on site dried the BASTA mini radome after precipitation events (during working hours). Measurements done when the radome could not be dried are removed in the first data processing stage (Sect. 4.3.2).

4.3.2 Data selection

The objective of this stage is to identify periods with cloud observations that may be used for calibration transfer. The first step is to manually select a time period where cloud formations are detected, for further analysis. An example of detected cloud formations is shown in panel 1 of Fig.4.2.

The second step is to split the time period between single clouds when possible. Cloud selection should be done from earlier to later clouds, because in some cases we may detect precipitation events that could invalidate posterior measurements. In the example of Fig. 4.2, we can identify two separate clouds in the selected time period: the first lasting from 0:00 to 2:30 approximately, and the second from 3:05 to 7:30 UTC. We assign the time period between 0:00 to 3:00 UTC to the first cloud, as shown in panel 2, and then continue with the next step.

In the third step, we study the doppler velocity profile of cloud signals that extend down to the surface. If the samples have a consistently negative doppler velocity, and a relatively strong reflectivity ($>\sim$ 10 dBZ), it is likely that they are associated with precipitation events. If there was no operator to dry the radome after rain, samples taken in the 6 hours after precipitation are discarded. The objective is to remove invalid measurements taken when the radome wet (BASTA mini does not have an active drying mechanism). In panel 3 of Fig. 4.2 we observe a likely precipitation event around 2:20. Thus, we reduce the time span of valid data until just before the first detected rain signal. This makes the final period chosen for this cloud to last from 0:00 to 2:00 UTC, a period which is added to the calibration transfer data pool. On the contrary, since data registered 6 hours after rain is removed, the second cloud period starting at 3:05 UTC is not added to the calibration transfer data pool.

The aforementioned algorithm must be repeated onwards, to cover the complete data time series. Both reference and uncalibrated radar data must be observed in this stage, to guarantee data consistency. All data associated with valid cloud periods pass to the next processing stage, explained in Sect. 4.3.3.

4.3.3 Data cleansing

After selecting cloud period candidates to compare, we perform a data cleansing stage to eliminate possible sources of bias arising from differences between the datasets. These differences could be caused, for example, by noisy measurements, or by differences between the instruments sensitivities.

The proposed methodology assumes that a noise mask has already been applied to the reference radar. In this exercise we used a constant mask of 7 dB above the noise floor level (signal to noise ratio larger than 7 dB).

Data cleansing is done for each selected cloud period and involves five stages:

1. Boundary layer removal: Data below 2500 meters is removed from the comparison. The reason for this is that in the boundary layer cloud radars are sensitive to large aerosols and insects (Wood et al., 2009). The spatial distribution of these targets is highly inhomogeneous spatially and temporally, and therefore is not suitable for intercomparison.

2. 3-sigma filter: The objective is to remove outliers that may bias the intercomparison. For this, we remove all data farther than 3 standard deviations (sigmas) from the mean of the reference and the uncalibrated radar reflectivity distribution.

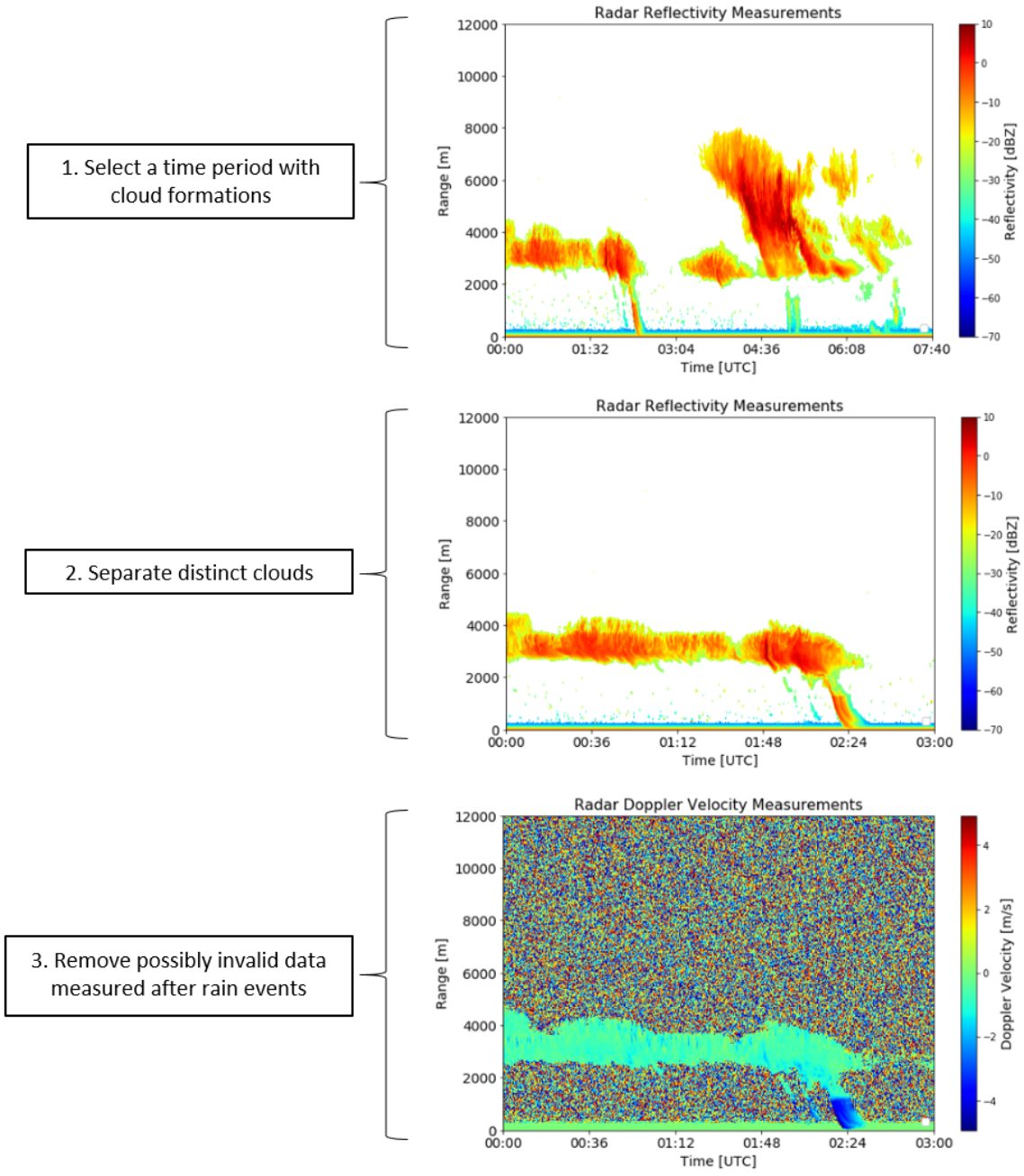

Figure 4.2: Example of the Data Selection stage. First, a time period with cloud formations is identified and delimited for further analysis. Second, we separate this period between distinct cloud formations. Third, we check if there is a likely precipitation event, from earlier to later clouds, to remove data registered with a possibly wet radome (more details in text).

3. Interpolation: The uncalibrated radar reflectivity samples are interpolated to match the reference radar time and range grid.

4. Dynamic range filter: This step removes data that was only measured by one of the two instruments, due to differences in sensitivity. For this, we force the received power dynamic range of both radars to be the same, following the next steps:

   (i) Remove the lower 5% of the less sensitive radar received power samples ($\{P_r\}_{less\ sensitive\ radar}$), to define the lower limit of the dynamic range.

   (ii) Determine the dynamic range Δ of the less sensitive radar. Ouliers were removed in a previous step, so we can calculate it from the received power distribution $\{P_r\}_{less\ sensitive\ radar}$ as: $\Delta = (max\{P_r\} - min\{P_r\})|_{less\ sensitive\ radar}$.

   (iii) Assuming that both radars have sampled the maximum received power from approximately the same physical target, we define the cut-off value $x = max\{P_r\}|_{most\ sensitive\ radar} - \Delta$. Power samples $\geq x$ are in the dynamic range of both radars, and therefore are comparable.

   (iv) Remove from the most sensitive radar all samples with power values $\{P_r\}_{most\ sensitive\ radar} < x$.

5. Correspondence filter: We remove all data points that appear in a single radar only, for each time-range coordinate. After following these steps, the grids of both radars will have the same amount of reflectivity samples, located at the same coordinates.

To illustrate the effect of this procedure, Fig. 4.3 shows the reflectivity profile and reflectivity distribution of the reference and uncalibrated radars before and after data cleansing. On the left, before data cleansing, we can observe the difference in sensitivity on the borders of the high cloud, between 4 and 8 km of height. The uncalibrated radar is more sensitive and therefore it can measure weaker reflectivity values on the borders. This additional data, in addition to boundary layer measurements, make the reflectivity distributions too different to attempt a direct calibration transfer.

After data cleansing we observe that most noisy data-points are removed, and that reflectivity profiles and distributions are much more alike (right panels of Fig. 4.3). The difference between the medians of the distributions changes from 4.4 to -2.7 dB (reference - uncalibrated), hinting that the correction coefficient calculated without data cleansing could be biased by about 6-7 dB.

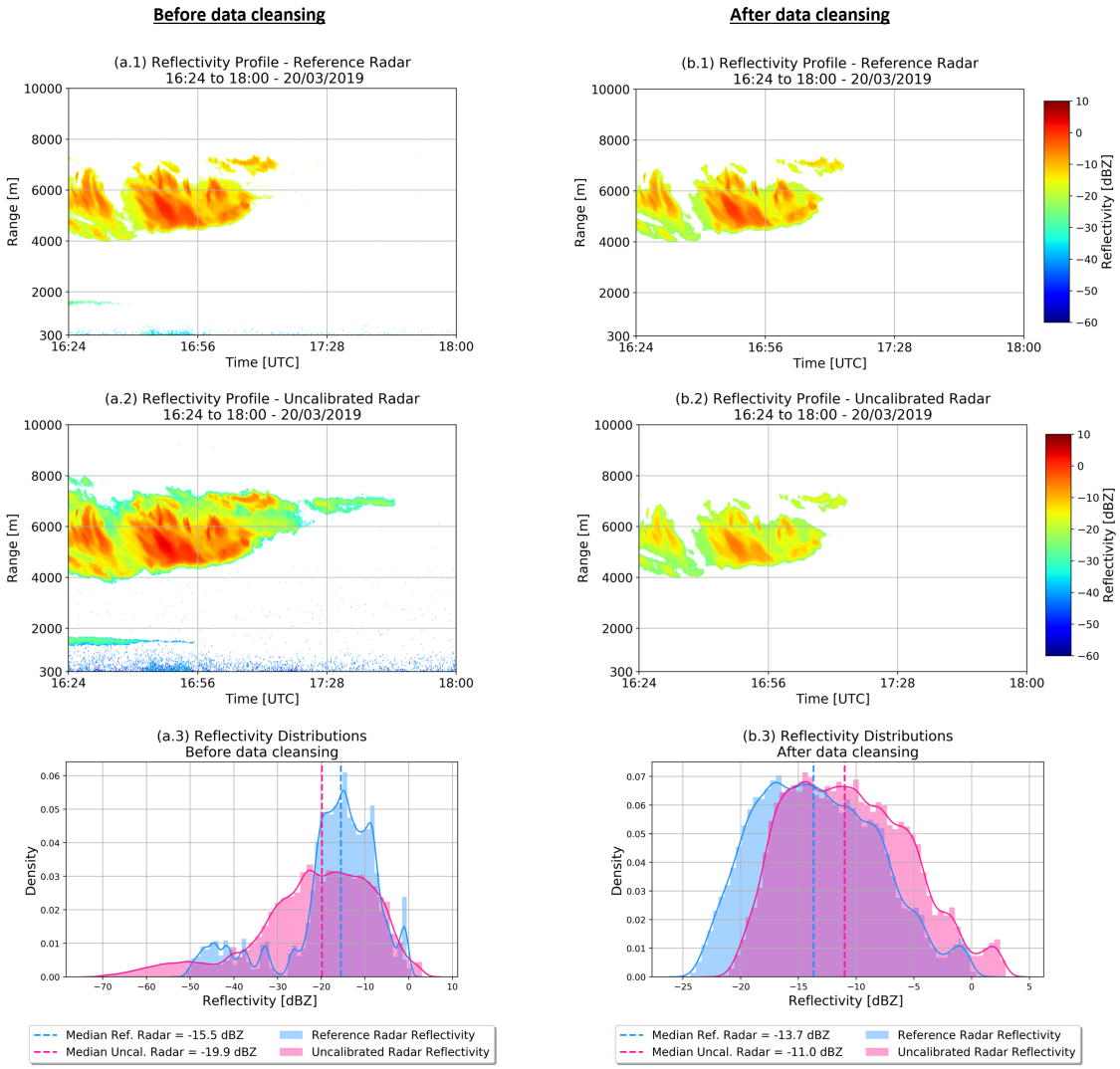

Figure 4.3: Example of a cloud dataset before and after data cleansing. Before data cleansing: (a.1) Reference radar data (a.2) Uncalibrated radar data (a.3) Reflectivity distribution of both radars. After data cleansing: (b.1) Reference radar data (b.2) Uncalibrated radar data (b.3) Reflectivity distribution of both radars.

4.3.4 Calibration transfer

The objective of this stage is to estimate the correction coefficient K, presented in Sect. 4.2, and its uncertainty. As in previous sections, this stage can also be divided in stages:

1. Estimate a correction coefficient K_i for each selected cloud event i. K_i is estimated as the difference between the medians of the reference and the uncalibrated radar reflectivity distributions: $K_i = median(\{Z\}^{ref}_{cloud\ i}) - median(\{Z\}^{uncal}_{cloud\ i})$.

2. Correct the uncalibrated radar reflectivity of each cloud by adding its corresponding correction coefficient K_i to the uncalibrated measurements. Figure 4.4 shows with example how this correction shifts the uncalibrated reflectivity distribution to match the reference radar observations.

3. Compare the reference and corrected distributions of each cloud using a Quantile-Quantile plot (Q-Q plot). If the points behave linearly, and have a R^2 score ≥ 0.8, the K_i value is accepted and used to estimate the correction coefficient K. Figure 4.5 shows, on top, an example of an accepted cloud. We can observe that there is a very good overlap between the reference and corrected reflectivity distributions. This is also reflected in the Q-Q plot, which has an R^2 score of 0.99. On the contrary, the bottom of Fig. 4.5 shows a rejected cloud formation. In this case, even after data cleansing, the corrected reflectivity distribution does not match the shape of the reference radar distribution. This is confirmed by the R^2 value of 0.36. The differences in the distribution shape may be caused by spatial cloud hetereogeneity, or by differences in the radars vertical alignment. Therefore, the K_i value estimated for this time period is rejected (not used in the final calculation of K).

After these steps, we end up with N valid K_i values. These K_i values are used to estimate the final correction coefficient K with Eq. (4.7). As explained in Sect. 4.2, K can be used to correct the previously uncalibrated measurements, to provide calibrated reflectivity retrievals.

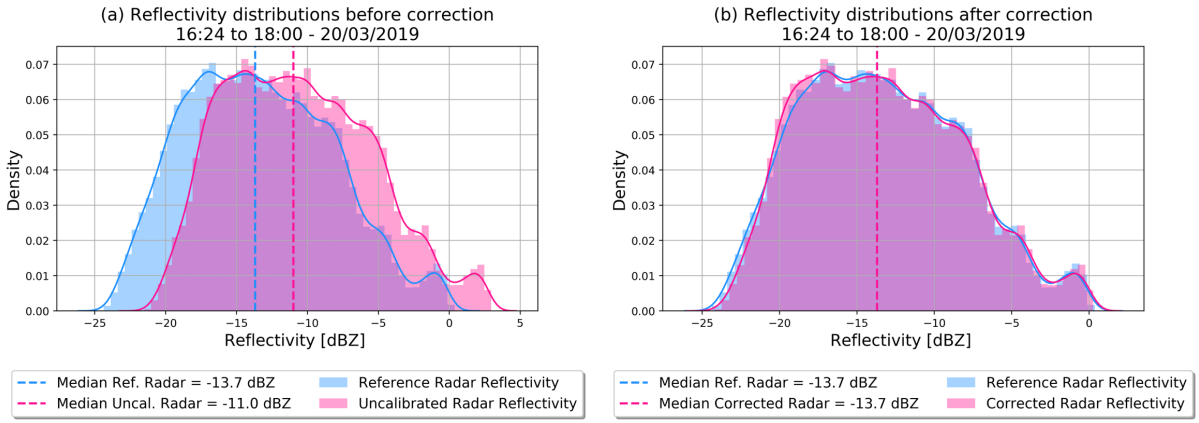

Figure 4.4: Example of the effect of applying the correction coefficient to correct the uncalibrated radar measurements. (a) Reflectivity distributions of the clouds shown in Fig. 4.3 (b.1), (b.2). (b) Reflectivity distributions after correcting the uncalibrated radar measurements.

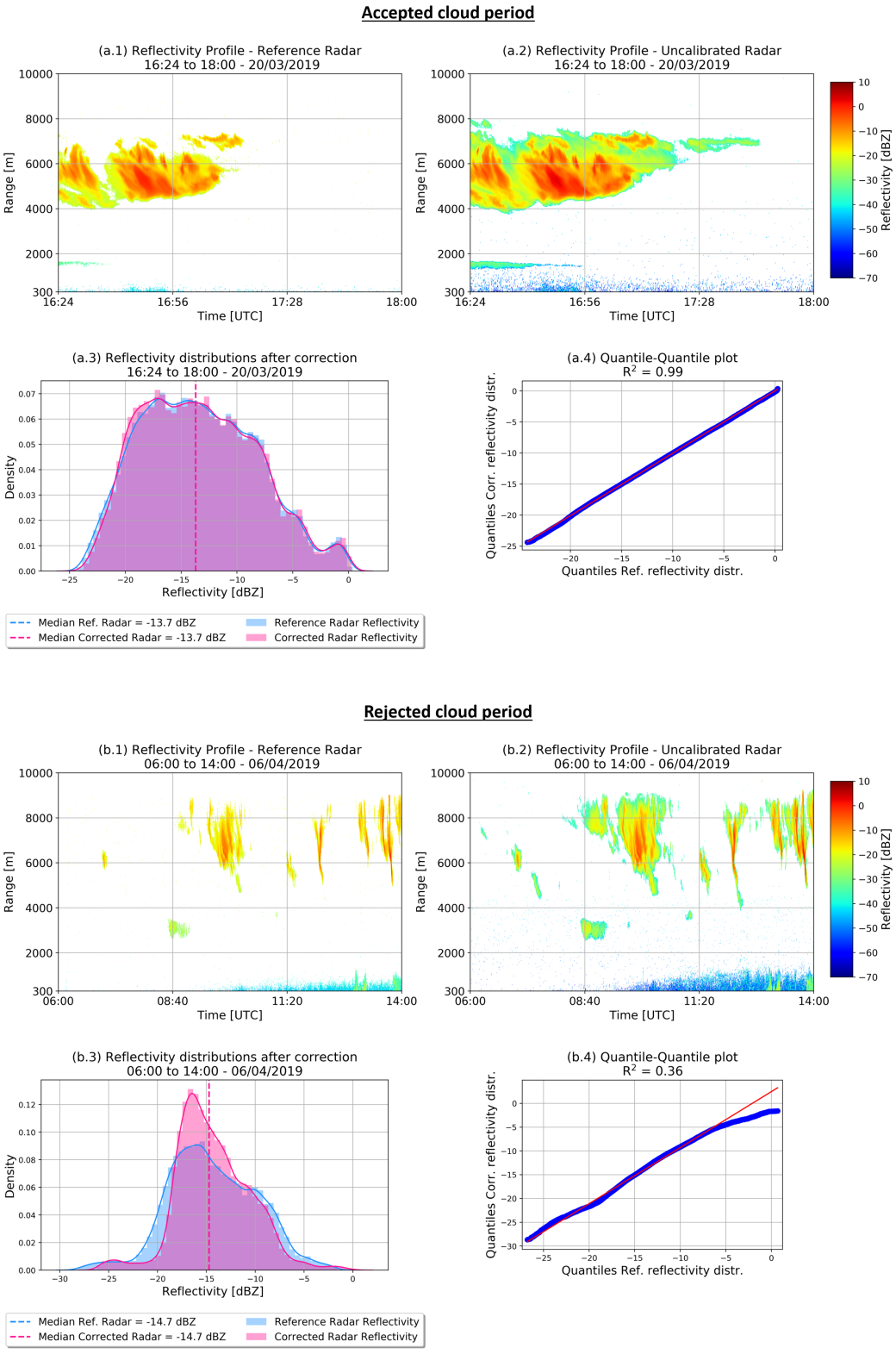

Figure 4.5: On top we observe an example of an accepted cloud period. Panel (a.1) shows the reflectivity profile observed by the reference radar, (a.2) shows the reflectivity profile observed by the uncalibrated radar, (a.3) shows both radars reflectivity distributions after applying the correction coefficient K_i estimated with this cloud data, (a.4) Shows the Q-Q plot of the reference and corrected reflectivity distributions with its R^2 score. The bottom of the figure shows the same plots, but for a rejected cloud event. The difference in the reflectivity distributions is evident in panel (b.3) and in the Q-Q plot of panel (b.4).

The uncertainty of the correction coefficient is calculated with Eq. (4.8). δK is the uncertainty of the correction coefficient K. σ_{ref} is the reference radar calibration uncertainty. σ_K is the standard deviation of the valid K_i values used to calculate K. σ_{K_i} is the uncertainty within each K_i estimation. It is calculated as the RMSE between correction coefficients calculated using each single reflectivity measurement j (Eq. (4.10)), and the cloud global correction coefficient K_i. M_i represents the total amount of valid reflectivity samples of the cloud event i.

$$K = \frac{1}{N}\sum_{i=1}^{N} K_i \tag{4.7}$$

$$\delta K = \sqrt{\sigma_{ref}^2 + \frac{(\sigma_K)^2}{N} + \left(\frac{1}{N^2}\sum_{i=1}^{N}\sigma_{K_i}^2\right)} \tag{4.8}$$

$$\sigma_{K_i} = \sqrt{\frac{1}{M_i}\sum_{j}^{M_i}(K_i^j - K_i)^2} \tag{4.9}$$

$$K_i^j = Z_{cloud\ i}^{ref}(t_j, r_j) - Z_{cloud\ i}^{uncal}(t_j, r_j) \tag{4.10}$$

4.4 Results of the 2019 calibration experiment

This section presents the results from following the steps described in the methodology section, on two weeks of data measured during the calibration experiment of 2019 ACTRIS Cloud Radar Calibration Campaign. As in previous sections, the reference instrument is the BASTA mini radar from the LATMOS laboratory of France, and the uncalibrated instrument is an 94 GHZ RPG Cloud Radar from the INOE institute of Romania.

Figure 4.6 shows the cloud events that were identified in the Data Selection stage (Sect. 4.3.2).

All data in the selected cloud periods were processed following the steps indicated in Sects. 4.3.3 and 4.3.4. The correction coefficients estimated from each cloud, alongside their uncertainty and the R^2 score from each Q-Q plot are shown in Table 4.2. As indicated in Sect. 4.3.4, only cloud events with a R^2 score higher than 0.8 are selected for the calculation of the correction coefficient K and its uncertainty δK.

Table 4.2: Partial calibration transfer results for each cloud identified in the Data Selection stage. K_i is the correction coefficient for cloud i. σ_{K_i} is its uncertainty. As indicated in Sect. 4.3.4, only cloud events with a Q-Q plot R^2 score higher than 0.8 are accepted and used in the final calculation of the correction coefficient K.

Cloud period	K_i [dB]	σ_{K_i} [dB]	Q-Q plot R^2 score	Accepted/Rejected
0	-2.7	0.7	0.99	Accepted
1	-2.6	0.9	0.97	Accepted
2	-2.3	1.4	0.97	Accepted
3	-2.6	3.2	0.88	Accepted
4	-2.4	2.9	0.85	Accepted
5	-3.4	4.7	0.36	Rejected
6	-3.1	2.6	0.87	Accepted
7	-2.6	3.1	0.84	Accepted
8	-2.9	3.6	0.82	Accepted
9	-2.7	4.3	0.76	Rejected
10	-3.0	4.9	0.68	Rejected
11	-2.1	4.0	0.85	Accepted

The calculated correction coefficient K and its uncertainty δK, with the uncertainty contribution

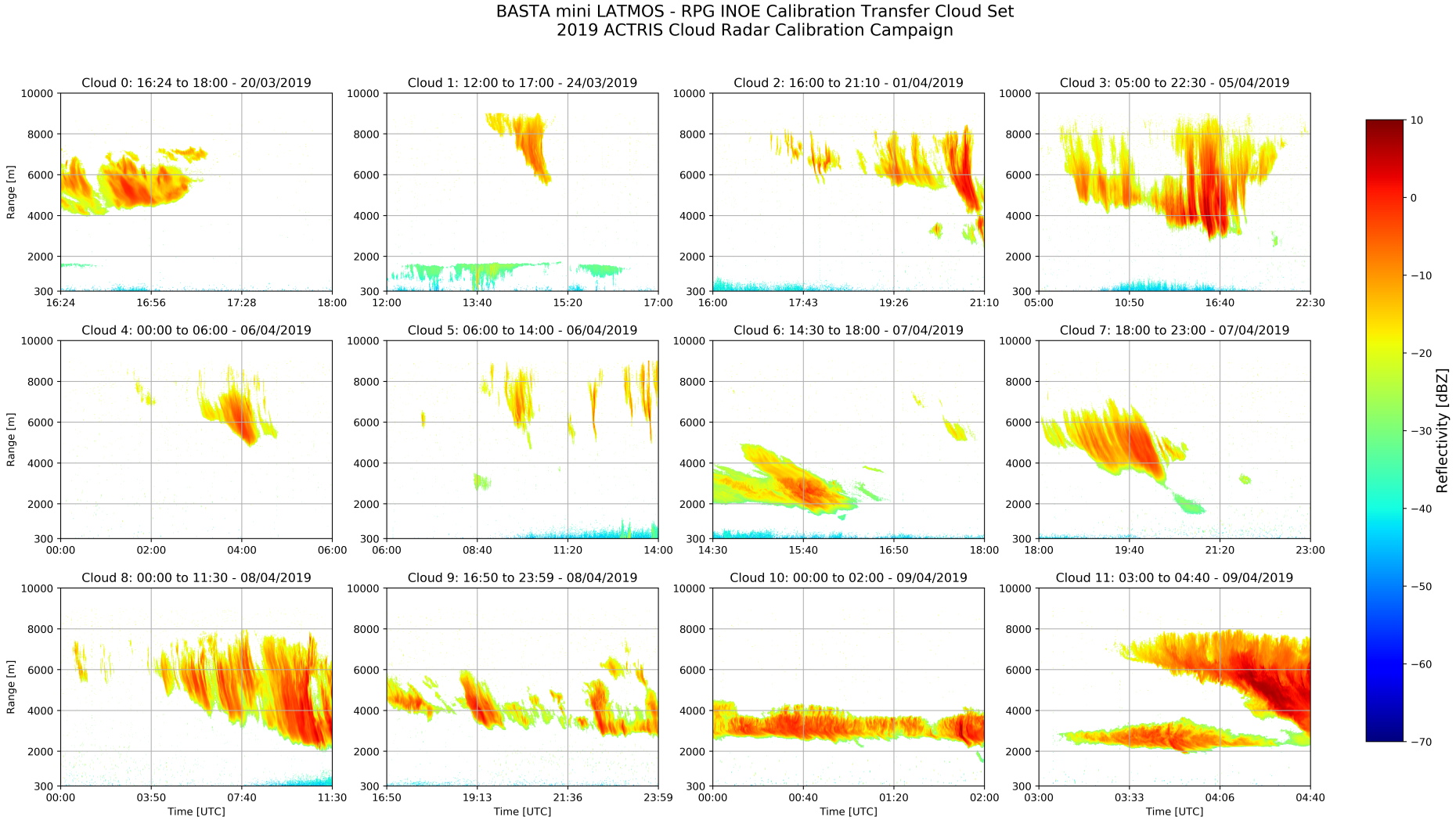

Figure 4.6: Cloud events identified in the Data Selection stage (Sect. 4.3.2). Reflectivity profiles extracted from the reference radar database (BASTA mini radar (Delanoë et al., 2016)).

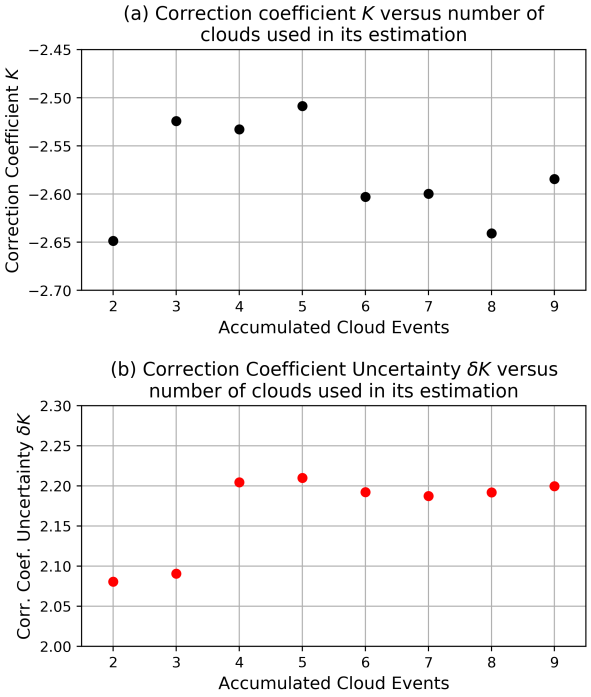

Figure 4.7: (a) Value of the correction coefficient K versus the number of clouds used in its calculation. (b) Uncertainty of the correction coefficient versus the number of clouds used in its calculation. Clouds used are taken from the database of accepted cases.

of each term (Eq. (4.8)), are presented in Table 4.3. We can observe that the main contributor to uncertainty is the reference radar calibration (2 dB). The other two terms related with the calibration transfer process contribute less than 1 dB to total uncertainty.

Table 4.3: Correction coefficient K and its uncertainty calculated using Eqs. (4.7) and (4.8) with the partial results of Table 4.2 (accepted clouds only). Individual uncertainty contributions to δK are detailed.

Correction coefficient K	-2.6 dB
Uncertainty Contributions	
Reference radar calibration uncertainty σ_{ref}	2 dB
Standard error in K estimation $\frac{\sigma_K}{\sqrt{N}}$	0.09 dB
Uncertainty propagation from each K_i estimation $\sqrt{\frac{1}{N^2}\sum_{i=1}^{N}\sigma_{K_i}^2}$	0.91 dB
Correction coefficient uncertainty δK	2.2 dB

From this data, and taking significant figures into account, we conclude that the final Correction Coefficient value is of $K = -3 \pm 2$ dB. When this K value is replaced in Eq. (4.6), we get corrected reflectivity measurements with a calibration uncertainty of $\delta K = 2$ dB.

To study the impact of the number of clouds in the calibration transfer exercise, how K and δK change when they are calculated using an increasing number of clouds, taken from the database of accepted cases (in sequential order). The result is shown in Fig. 4.7. We can observe that the correction coefficient K variations are always smaller than the value of its uncertainty δK, which is a result that indicates that the framework is consistent. The value of K does not change significantly when increasing the amount of cloud events. Meanwhile, its uncertainty δK converges after 4 cloud events. Therefore, results indicate that it may not be necessary to consider more than 4 clouds to obtain the same result. There is further discussion on this result in the conclusions.

4.5 Synthesis

This chapter presented a methodology to transfer the calibration from a reference to an uncalibrated cloud radar. The method was developed and tested using data collected during the 2018 and 2019 ACTRIS Cloud Radar calibration campaigns performed at the SIRTA observatory, France. It consists of using simultaneous cloud measurements to transfer the calibration, correcting the reflectivity of the uncalibrated radar using a constant correction correction coefficient K.

The current version of the method enables the calibration transfer between radars with close operating frequencies (in the same band), and is robust to differences in sensitivity. This enables the use of this method without restrictions on the radar model or manufacturer.

The results of the 2019 campaign are used to illustrate the methodology. In this example we use the BASTA mini radar, calibrated in chapter 3, as the reference instrument. Its calibration is transferred to a 94 GHz RPG Cloud Radar. Both radars are setup separated by a few tens of meters, with similar time and range resolutions. The main results to be retained are:

- The derivation of correction functions for temperature and range dependent gain variations in each radar must be done before the calibration transfer experiment.
- After finding these correction functions, the difference between calibrated and uncalibrated measurements is given by a constant term, defined as the correction coefficient K.
- The correction coefficient can be derived by comparing simultaneous reflectivity measurements done with the reference and the uncalibrated radars. Clouds are a possible source of these reflectivity measurements.
- The first data selection stage is done manually, to avoid periods when wetting of the radome could cause unreliable measurements (during and shortly after rain). The use of doppler velocity proved useful to identify precipitation events.
- The cloud sampling period lasted approximately three weeks, from March 20 to April 9 of 2019. In this time span it was possible to identify 11 cloud periods with valid measurements.
- Differences in the shape of the reflectivity distributions sampled by each radar, for the same clouds, showed the need of performing a data processing stage before the calibration transfer. The processing involved, for each radar: the removal of boundary layer measurements, the removal of outliers, interpolation of the uncalibrated radar data grid to that of the reference radar, and the application of a dynamic range filter and a correspondence filter. The dynamic range filter removed data that could only be measured by the most sensitive radar, to avoid a biased comparison of reflectivity statistics. The correspondence filter removed samples detected by only one of the two radars, by comparing the data grids.

  The data processing stage modified the difference between the medians of the reference and uncalibrated reflectivity distributions of a cloud case example by ~ 6 dB. This is relevant since the difference between the medians is used in the correction coefficient derivation.
- After data processing, a quality control based on Quantil-Quantil plots is applied to each cloud period. Its objective is to determine if the shape of the measured reflectivity distributions is similar enough for calibration transfer. When distributions are not similar, it is not possible to assume that both radars observe the same cloud features, and therefore data is discarded. The quality control rejected 3 of the 11 originally selected cloud periods.

- An estimator of the correction coefficient and of its uncertainty is developed. Uncertainty depends on: 1. The propagation of the uncertainty in the estimation of the correction coefficient value, calculated in each cloud period. 2. On the variability of the correction coefficient values obtained for different cloud periods. 3. On the reference radar calibration uncertainty.

  The 9 valid clouds are used to calculate the correction coefficient of the example. Its estimated value is of $K = -3 \pm 2$ dB is determined. The main source of uncertainty comes from the reference radar calibration (2 dB). Uncertainty source 1 contributed 0.09 dB and uncertainty source 2 contributed 0.91 dB to the final calibration uncertainty of 2.2 dB.

- The correction coefficient value and uncertainty converges when using at least 4 cloud periods. In principle, using more cloud events should decrease uncertainty further, yet at present its value is limited by the reference radar calibration. If the reference radar calibration uncertainty is decreased, it may be possible to further reduce the uncertainty in calibration transfer by increasing the amount of clouds considered.

Chapter 5

Conclusions and Perspectives

The development of a network of fog monitoring stations presents several scientific and technical challenges. There is a need of improving our understanding of the conditions leading to fog dissipation, to improve our capability of forecasting it. This thesis shows how remote sensing can be useful to monitor fog status in real time. Yet the cloud radar, which is a key instrument to observe fog top, has the long-standing need of calibration methodologies, which could also be applied at the scale of an observation network.

This thesis contributed to advances in both topics, through the research of key variables driving the fog life cycle, and of a calibration strategy suitable for cloud radar networks.

The results from our fog research could change the way dissipation is forecasted, by simplifying the problem of forecasting visibility at the surface, which requires the use of complex models with a fine spatial resolution, for the simpler problem of predicting large scale macroscopic variables (LWP, CTH, temperature and pressure). This change of paradigm could contribute to new ways of stating the fog forecasting problem in the future.

Additionally, fog research should benefit from our advances in cloud radar calibration solutions. Harmonized and reliable cloud radar measurements could provide new insights on fog microphysical properties, on its spatial structure and on the processes driving its life cycle.

Radar calibration is a complex issue. To plan and execute a good calibration experiment, it is necessary to consider the specific inner workings of the radar, to have an understanding of remote sensing theory, and to execute highly rigorous technical work. Significant effort has been made on this thesis to develop methods as general as possible (not constrained to a single type of instrument), that could be applied in cloud radar observation networks. This requirement makes it very important to consider existing equipment and logistical limitations.

All of this work was made possible by the existence of the SIRTA atmospheric observatory (Palaiseau, France). Fog research was done using several years of continuous in-situ and remote sensing measurements. These measurements provided enough data to have a statistical view of the fog phenomenon, enabling the identification of general properties and behaviors. Furthermore, the observatory contributed with its outstanding facilities and staff to make possible two cloud radar calibration campaigns. During the experiments, the overlap in objectives with the ACTRIS research infrastructure, which is developing a network of cloud remote sensing stations, also gave place to interesting and enriching international collaborations.

Detailed conclusions and perspectives are presented in the following sections. Section 5.1 concludes on the results and implications of our fog research. Section 5.2 presents the conclusions of the cloud radar calibration research. Finally, section 5.3 presents perspectives for future work.

5.1 The role of LWP and CTH in fog life cycle

Starting from physical principles, and previous work done by Cermak and Bendix (2011); Wærsted (2018), we formulated a new conceptual model that relates the liquid water path (LWP) of fog with its thickness (CTH), surface liquid water content (LWC_0), equivalent adiabaticity (α_{eq}) and surface temperature and pressure. This conceptual model is used to understand the relationship between these meteorological variables, based on data from 80 fog events measured at the SIRTA observatory (section 2.2).

The conceptual model also enabled the identification of two key indicators: the Critical Liquid Water Path (CLWP), and the Reservoir Liquid Water Path (RLWP). The CLWP is the minimum amount of LWP necessary to fill a fog layer of a given thickness. The RLWP is the excess of LWP above the critical value, and quantifies the amount of water that must be removed before fog dissipation can occur at the surface. Both variables are calculated as a function of the conceptual model parameters (LWP, CTH, LWC_0, α_{eq}, surface temperature and pressure). RLWP behavior is studied as a function of the fog life cycle, indicating that it may be used as potential indicator of fog dissipation tendency. This potential is then explored, combining RLWP and surface visibility measurements.

In the following lines we highlight the conclusions from this study:

- **Key instruments:** To study and use the conceptual model formulation, it is necessary to have a specific set of measurements, associated with key instruments: 1.- Fog CTH is retrieved using cloud radar measurements. A suitable cloud radar must be able to detect the upper limit of fog at less than 100 m of vertical height, with a resolution of ∼10 m or finer. 2.- Fog LWP is measured using a microwave radiometer. 3.- Surface visibility is measured using a diffusometer. It enables fog detection and an estimation of LWC_0 using the parametrization of Gultepe et al. (2006). 4.- Temperature and pressure measurements at the surface are used to calculate the saturation mixing ratio change with height, used to calculate the adiabatic LWC profile. 5.- Fog CBH is tracked using a ceilometer, complementing visibility measurements in the formation stage of stratus lowering fog, or during temporary lifting of the fog base.

- **Relationship between LWP and CTH in fog layers:** The equivalent adiabaticity is the parameter that links fog LWP and CTH. In fact, LWP can be split in two different terms: one proportional to fog adiabaticity and the square of the CTH, and another which is the product of surface LWC with fog CTH. The first term is analog to the LWP dependency on thickness for clouds (Braun et al., 2018). The second term is fog-exclussive, and is introduced by an excessive accumulation of water caused by the surface presence, which limits fog vertical development.

- **Fog adiabaticity:** The conceptual model enabled the retrieval of the equivalent adiabaticity α_{eq} of fog profiles. It was found that α_{eq} is highly variable when the LWP is less than 30 g m^{-2}, reaching values between ≈ -1 and 1. Negative adiabaticity values are explained by a decrease in liquid water content (LWC) with height, with respect to the surface value LWC_0, which occurs when radiation fog is at its formation stage (fog is non opaque to infrared radiation and has a stable profile). When LWP increases above 30 g m^{-2}, fog becomes opaque to infrared radiation and adiabaticity converges towards ≈0.6-0.7, matching previous adiabaticity observations of boundary layer clouds (e.g. Braun et al. (2018)). This is explained by a destabilization of the layer caused by localized cooling at the fog top (since fog is opaque), or heating at the fog base (after dawn).

  It was also found that α_{eq} is strongly correlated with fog CTH. This enabled the development of a $\alpha_{eq}(CTH)$ parametrization, which can be used to estimate fog LWP with an uncertainty of ±10.5 g m^{-2}, using the conceptual model plus radar, visibility and weather station measurements.

- **Relationship between CTH, LWP and the fog life cycle:** CTH and LWP are drivers of the fog life cycle, through their impact on the RLWP value.

  Statistically, RLWP is negative before fog formation, reaches 0 g m^{-2} at formation time and increases to possitive values afterwards. The increase in RLWP begins about 50 minutes before formation and persists for other 50 minutes after formation. The rate of change of the RLWP (dRLWP/dt) can reach median values of 10-20 g m^{-2} Hr^{-1} in this stage.

  During the fog mature stage, RLWP is greater than 0 g m^{-2} 90% of the time, and the median rate of change of the RLWP is of -0.2 g m^{-2} Hr^{-1}. The observation of change rates between $\pm$20 g m^{-2} Hr^{-1} during fog mature stage indicate that RLWP can present important oscilations.

  At the fog dissipation stage, RLWP goes from possitive to negative values, passing through 0 at dissipation time. RLWP depletion starts about 60 minutes before dissipation, reaching a median rate of change value of -5 to -20 g m^{-2} Hr^{-1}. The significantly larger depletion rate, with respect to the median value observed in the mature stage, indicates that most of the RLWP is removed in the last stage of the fog life cycle.

- **Impact of LWP and CTH variations on fog RLWP:** The adiabaticity parametrization, and the conceptual model, enable the quantification of the impact that LWP and CTH variations have on the RLWP. The model indicates that increases in LWP will augment the RLWP, while increases in CTH will reduce its value. This opens the possibility of having compensating effects. For example, an increase in LWP could be compensated by CTH development, leading to RLWP depletion and thus fog dissipation. On the contrary, there can be instances where a decrease in LWP is compensated by a reduction of CTH, keeping possitive RLWP values that allow fog to persist. It is also predicted that to have fog dissipation it is necessary that both LWP and CTH time changes have a magnitude that results in a net RLWP decrease. This last property was verified observing LWP and CTH trends for the last 60 minutes of 56 fog cases lasting more than 3 hours.

- **Temporary fog dissipation:** It was found that 45 of the 80 fog events identified in the article (section 2.2) had periods with visibility increases above 1000 meters, lasting for less than 60 minutes within fog events. These transient visibility increases could be caused by the advection of spatial hetereogeneities (Gultepe et al. (2007)), by a temporary LWP depletion caused by drizzle (Dupont et al. (2012)), or by a short-lived lifting of the fog base caused by a transitory RLWP depletion, after a sudden LWP decrease or CTH increase. At present it is not possible to discern if dissipation will be temporary or definitive, based on our diagnostic variables. This would require a forecasting of surface visibility, or of fog RLWP. The second alternative has the advantage of being simpler since its variations can be quantified from real time observations of fog processes, without the need of costly simulations (e.g. Wærsted (2018)).

- **RLWP and visibility as indicators of fog dissipation tendency:** When visibility is less than approximately 600 m, RLWP can range between negative and $\approx$60 g m^{-2}, acting as an independent variable to describe fog status. On the contrary, when visibility is greater than approximately 600 m, the range of possible RLWP values is more restricted and more correlated with visibility. This is due to the RLWP convergence towards 0 g m^{-2} when visibility is increasing towards 1000 m.

  This is consistent with the results of the study on the use of visibility and RLWP as indicators of dissipation probability. Here it was found that RLWP provides additional information of fog dissipation tendency when visibility is below 600 meters. The dissipation probability within 90-180 minutes can vary from 5-20% to 30-60% depending on the RLWP value (for samples in the same visibility range). For visibilities between 600 and 1000 meters the RLWP does not provide

additional information with respect to visibility, probably due to the aforementioned stronger correlation.

5.2 Cloud radar calibration

Radar calibration has been a long-standing challenge. The lack of universal calibration methods introduces the need for continuous research for solutions, tailored for each use case (Süsskind, 1985; Atlas, 2002). Therefore, the calibration of a cloud radar network required a dedicated study which considered its specific characteristics. To address this requirement, we researched and developed a calibration solution based on two steps:

First, to calibrate a cloud radar (BASTA mini), that becomes our reference radar. This is done using corner reflectors mounted on masts, with a comprehensive study of uncertainty sources. Two different experimental setups were tested: one consisting on a 10 m mast with a 10 cm trihedral target on top, that could be aimed using a positioner, at 196 meters of distance. The other consisted on a 20 m mast with a 20 cm trihedral target fixed on top, at 376.5 meters of distance.

Second, to transfer the calibration of the reference instrument to another radar (a 94 GHz RPG radar in our experiment) using clouds as common targets. Experiments to gather data and test the approaches were carried out during two calibration campaings, done in 2018 and 2019 at the SIRTA observatory, in the framework of the ACTRIS infrastructure development.

The conclusions from the first step, about the reference radar calibration, are:

- The proposed calibration method requires performing several iterations in the same setup configuration. In each iteration the setup is first realigned, followed by approximately one hour of sampling the reference reflector signal. Iterations are necessary to quantify the bias introduced by unavoidable misalignments in the experimental setup. The variability in the target signal when comparing different iterations can be combined with a geometrical model of the experimental setup, to calculate which sets of positioning uncertainties reproduce the observed results. These sets enable the estimation of the bias and uncertainty introduced by setup misalignment.

- Calibration can be impacted by changes in the gain of internal radar components. When calibrating BASTA mini we found that temperature introduced systematic variations in the radar gain. This was corrected by deriving a temperature correction function, sampling the calibration value for a wide range of environmental temperatures. It was also found that filters at the IF introduced a range dependent loss term. This was corrected by deriving the IF gain function using the target signal plus noise measurements (section 3.2). Gain variations caused by temperature and the IF filters modified the calibration value of BASTA mini by up to 1 dB. It is advisable to study the radar hardware, to identify possible systematic sources of calibration variability, and to perform experiments to retrieve corrections for these variations.

- The calibration methodology enabled the identification and quantification of the uncertainty sources introduced by different elements of the experimental setup (uncertainty budget). This enabled us, for example, to identify that the main source of uncertainty for both experiments was the reflector RCS (2 dB). Then, the second most importante source of uncertainty for the 10 m mast setup is introduced by clutter (0.9 dB), while in the 20 m mast setup it is introduced by setup alignment (0.28 dB). Clutter contribution on the 20 m mast setup is significantly lower (0.09 dB). This analysis shows that the calibration methodology allows quantitative comparisons between different experimental setups. The results from this study, and the practical experience acquired, enables us

to propose a list of relevant points that should be considered in future reflector-based calibration experiments:

- **Saturation in the radar receiver:** Corner reflectors can produce a strong return signal, that may compress or saturate the receiver of the radar. Excessive compression or saturation must be avoided to have a valid calibration in the linear range of the instrument. To perform this validation it is necessary to know the power transfer curve of the receiver. This curve can also be used to correct small compression effects. For example, it enabled us to detect and correct compression losses of approximately 0.2 dB.

  An excess in the return signal can be mitigated by placing the target farther, or switching it for another with a lower radar cross section (RCS).

- **Near field distance:** The reflector used in calibration must be located farther than the near-field distance of the radar antennas. This near field distance can be estimated using the Fraunhofer distance formula. The Fraunhofer distance calculated for BASTA mini is of 50 m. This distance was greatly surpassed in the two tested experimental setups, where the target was located at 196 and 375.5 meters of distance.

- **Antenna overlap:** The radar equations assumes that the emitting and receiving antennas have superimposed beam lobes. This assumption may not be valid when using bistatic radars, where there may be incomplete antenna overlap. This incomplete antenna overlap happens when the lobe of the emitting and receiving antenna are not completely superimposed, introducing range dependent losses with respect to the behavior predicted by the radar equation. When calibrating bistatic radars using a point target, such as a corner reflector, it is necessary to place it far enough so that losses due to incomplete overlap become neglible. This loss can be calculated as a function of distance, by considering antenna beam width, the separation between the antennas and their parallax. In our calibration experiment, the estimated loss due to incomplete overlap, assuming parallel antennas, was smaller than 0.1 dB for the closest mast setup, at 196 m of distance, and less for farther distances. The parallel antenna assumption could not be verified experimentally due to limitations of the radar positioner accuracy. An alternative approach to estimate the losses caused by antenna parallax errors is proposed in the perspectives section (section 5.3).

- **Clutter:** Clutter, understood as the contribution of unwanted reflections on surrounding objects to radar measurements, may introduce uncertainty when measuring the signal of interest. The magnitude of this contribution depends on the signal to clutter ratio. Signal to clutter ratio can be measured by comparing the power received from the target with the power received from the target position after removing the reflector (Chandrasekar et al., 2015). It is advisable to perform the calibration experiments in an open field several hundred meters long, free from trees or other obstacles, and using a mast as less reflective as possible. The impact of signal to clutter ratio in uncertainty can be highly variable, depending on its value. For one of our experimental setups, signal to clutter ratio introduced an uncertainty of 0.9 dB, while for the other it was just of 0.09 dB.

- **Environmental conditions:** Calibration measurements should be done with clear conditions at the surface, without fog or rain, and a continuous measurement of temperature, pressure and relative humidity nearby to calculate atmospheric attenuation. It is also recommended to monitor wind speed and turbulence, to minimize mechanical vibrations of the experimental setup (on the radar and on the mast holding the target).

– **Experimental setup realignment:** The execution of several iterations of system realignment makes it important to consider the staff and time needed for the experiment. The planning of a good experimental setup can follow one or both of the following strategies: 1.- To have a very precise alignment system, which could reduce the amount of interations necessary to converge in the misalignment bias estimation, or 2.- To have an easy to re-align experimental setup that could enable the execution of a large number of iterations in a short period of time. For all cases, it is advisable to perform experiments to test the setup and study how the misalignment bias converges for an increasing number of iterations.

In addition, the conclusions from the second step, about calibration transfer, are:

- The approach corrects differences between calibrated and uncalibrated measurements using a constant term, defined as the correction coefficient. The correction coefficient can be derived by comparing simultaneous cloud reflectivity measurements done with the reference and the uncalibrated radars.

- The first data selection stage is done manually, to avoid periods when wetting of the radome could introduce unreliable measurements (during and shortly after rain). Doppler velocity measurements can be used to support the identification of precipitation events. In three weeks (from March 20 to April 9 of 2019) it was possible to identify 11 cloud periods with valid measurements.

- Differences in the shape of the reflectivity distributions sampled by each radar, for the same clouds, implied the need of performing a data processing stage before determining the correction coefficient. This processing involved (for each radar): the removal of boundary layer measurements, the removal of outliers, interpolation of the uncalibrated radar data grid to that of the reference radar, and the application of a dynamic range filter and a correspondence filter.

  The dynamic range filter removed data that could only be measured by the most sensitive radar, to avoid a biased comparison of reflectivity statistics (which could have an impact of several dBs). This step is key to enable calibration transfer between radars with different sensitivity.

  The correspondence filter removes data with a given time-range coordinate that is measured by only one of the radars.

- A quality control for each cloud is done using Quantil-Quantil plots. These plots enable a comparison of the shape of the reflectivity distributions from the reference and uncalibrated radar, for each cloud period. When the distributions are not similar, it is not possible to assume that both radars observe the same cloud features, and the cloud period is discarded. The quality control rejected 3 of the 11 originally selected cloud periods.

- Uncertainty in calibration transfer depends on: 1. The propagation of the uncertainty in the estimation of the correction coefficient value, calculated in each cloud period. 2. On the variability of the correction coefficient values obtained for different cloud periods. 3. On the reference radar calibration uncertainty.

  In our calibration transfer excercise, the main source of uncertainty comes from the reference radar calibration (2 dB). Uncertainty source 1 contributed 0.09 dB and uncertainty source 2 contributed 0.91 dB to the final calibration uncertainty of 2.2 dB.

- The correction coefficient value and uncertainty converges when using at least 4 cloud periods. In principle, using more cloud events should decrease uncertainty further, yet at present its value is limited by the reference radar calibration. If the reference radar calibration uncertainty decreases,

it will be possible to further reduce the uncertainty of the calibration transfer by increasing the amount of clouds considered.

5.3 Perspectives

This thesis performed a quantitative study on the relationship between fog LWP and CTH based, and about how they are related with fog evolution, through the development of a new conceptual model for fog and the use of remote sensing measurements. This led to the identification of diagnostic variables that can be used to quantitatively assess fog status.

The thesis also presented the development of tailored methods to calibrate a network of cloud radars, with a comprehensive identification of the uncertainty sources, and identifying remaining challenges.

We believe that it is possible to continue advancing further in both topics. Below we propose some tracks that could be useful for this end:

- **Impact of fog microphysics on RLWP estimation:** The proposed conceptual model integrates fog microphysics implicitly, through the use of experimentally derived parametrizations for the equivalent adiabaticity (section 2.2), and to relate surface LWC with visibility (Gultepe et al., 2006). These parameterizations consider only macroscopic variables in their formulation (CTH or visibility), and therefore represent only first order approximations. In addition, section 2.4 shows that the adiabaticity parametrization is the main source of uncertainty in the CLWP calculation, reaching values of approximately ± 10 g m^{-2}.

  Therefore, it would be interesting to improve the estimation of adiabaticity by including information on fog microphysics, to improve the estimation of the CLWP and RLWP. One approach could be to conduct a sensitivity study, to quantify how conceptual model variables change for different known adiabaticity profiles (observed or simulated).

  This study could be done, for example, by using large eddy simulations (LES). With LES we would get all necessary outputs to calculate conceptual model variables, while having additional information on fog microphysics. For example, Mazoyer et al. (2017) used the Meso-NH model to perform a LES of a fog case measured during the ParisFog campaign, at the SIRTA observatory. In their study they were able to calculate fog LWP and CTH, alongside droplet number concentration and mixing ratio with a 1 m vertical resolution (and a large number of other physical parameters).

  Another complementary approach could be to study conceptual model calculations, based on empirical data, paired with retrievals of fog microphysics. Retrievals of fog microphysics can be obtained using cloud radar reflectivity combined with in-situ instruments, such as granulometers, and data assimilation techniques (e.g. Khain et al. (2008); Dupont et al. (2018); Bell et al. (2021)). This approach would also benefit from the cloud radar calibration improvements developed in this thesis.

- **Improvement of fog LWP retrievals:** Microwave radiometers retrieve the LWP of the complete atmospheric column. This means that what is measured is the addition of the LWP from all liquid clouds in the column. Thus, when clouds are present above the fog layer, it is not possible to retrieve fog LWP from radiometer measurements alone. This limitation is particulary important, because clouds above can reduce LWP generation from radiative cooling by up to 100%, accelerating fog dissipation (Wærsted et al., 2017).

  At present, the conceptual model does not perform calculations when the cloud radar detects clouds above the fog layer, to avoid the use of invalid LWP data. It would be useful to improve this situation by creating a fog LWP product that works when clouds are present above the fog layer.

The conceptual model already enables an estimation of fog LWP with an uncertainty of ±10.5 g m^{-2} based on CTH, visibility, and surface temperature and pressure. This uncertainty, which is mostly introduced by the adiabaticity parametrization (section 2.4), remains important for the estimation of the dissipation probability. However, improvements in this parametrization, or direct observation of fog adiabaticity using calibrated reflectivity measurements, could be used to have a better estimation of fog LWC and LWP, even when clouds are present above this layer (e.g. Khain et al. (2008); Bell et al. (2021)).

- **Differentiation between temporary and definitive fog dissipation:** In section 2.3.2 we observed that fog can dissipate locally for short-time periods, of less than 60 minutes, without implying a definitive dissipation of a fog event (defined as a 60 minute period with visibility > 1000 m).

  We also observed that it is not possible to distinguish temporary from definitive dissipation based on local RLWP and visibility trends only. This requires the use of additional information. One possibity would be to include 3D reflectivity measurements, from a scanning radar, or from a distributed network of cloud radars, to simultaneously observe how conceptual model variables behave at different locations. This would enable the detection of fog regions with local RLWP decreases, which may be caused by hetereogeneities on surface conditions (Gultepe et al., 2007), that could advect and cause temporary dissipation downwind.

  The observation of fog physical processes could also provide valuable information. The thesis done by Wærsted (2018), which is part of this project, and other authors, researched how observations of local fog processes can be used to quantify LWP and CTH variations. This information can be used to predict the short-term evolution of RLWP, and may enable the differentiation between dissipation ocurring under conditions that systematically lead to RLWP depletion, from non-lasting LWP and CTH perturbations caused by horizontal advection.

  Finally, the use of forecasting tools could also be considered, such as data asimilation techniques and numerical weather prediction (NWP) simulations (e.g. Román-Cascón et al. (2016a)). Here the advantage of the conceptual model is that it simplifies the problem of predicting surface visibility (which requires a fine vertical resolution and cloud microphysics), for the simpler problem of predicting large scale macroscopic variables (LWP, CTH, temperature and pressure).

- **Study the generality of the fog conceptual model:** The conceptual model has been developed with data from the SIRTA observatory, located near Paris, in France. Temporal variability is well captured, by the use of 7 years of fog measurements. However, it is not known to which extent the results obtained are applicable to other sites.

  The term that is most likely to vary between different sites is the adiabaticity parametrization. Even though its value is consistent with previous observations from other sites when fog is in its adiabatic stage (e.g. Cermak and Bendix (2011); Braun et al. (2018)), its parametrization as a function of CTH could change for sites with different terrain, climate or fog types (the SIRTA observatory is mostly affected by continental radiation fog and continental stratus lowering fog). Therefore, it would be interesting to research how our parametrization compares with observations done in other observatories. The use of data from other sites is also interesting to improve fog dissipation diagnostics, which are partially based on statistics. This issue reinforces the need of fog observation networks, which are essential to reach more universal conclusions on fog properties, and to have a better assessment and forecasting of fog dissipation tendency.

  Fortunately, work is being done to have a homogeneized cloud monitoring network. The european ACTRIS infrastructure already has 15 sites with cloud radar and microwave radiometer observa-

tions, and therefore is a good place to start looking for stations with suitable fog measurements to perform conceptual model calculations.

- **Improvement of the reference radar calibration:** At present, the predominant source of uncertainty in the reference radar calibration is introduced by the reflector RCS (2 dB). The uncertainty in the reference radar calibration also limits the performance of calibration transfer when using this instrument. Using the uncertainty budget, we found that to reach a calibration uncertainty below 1 dB, it is necessary to characterize the target RCS with an uncertainty of less than 0.9 dB. This characterization could be done by measuring the target RCS as a function of the beam incidence angle in anechoic chambers, or other suitable facilities (e.g. Thankappan et al. (2013); Jayasri et al. (2018)). A study on the uncertainty of the RCS measurement should also be conducted.

- **Characterization of the impact of antenna parallax errors:** At present, calibration is retrieved assuming that the radar antennas are parallel. However, errors in antenna parallax are possible and could have a non neglibile impact on gain for different distances, specially for cloud radars with narrow beams (Sekelsky and Clothiaux, 2002). Thus, it is important to detect and correct gain variations introduced by non ideal parallax. This could be done by using our calibration method with the same target, but at different distances. Since all other sources of variability are corrected, changes in the retrieved calibration coefficient would be produced by gain variations, arising from imperfect antenna parallax. These variations could be compared with the results of a forward model to estimate the most likelly antenna pointing angles, using a monte-carlo approach analogous to what is used to estimate misalignment bias. A bistatic version of the RCS simulator of section 3.3 could be used as this forward model, after adding new parameters to represent the separation between the center of the antennas, and azimuth and elevation angles to indicate their pointing direction.

- **Use of UAVs for cloud radar calibration:** There is ongoing research on weather radar calibration and antenna pattern characterization based on reference reflectors held by Unmanned Aerial Vehicles (UAVs) (Duthoit et al., 2017; Yin et al., 2019). It would be interesting for the cloud radar comunity to adapt these methods for cloud radars. Since the underlying principle is the same of calibration using reflectors on masts, most of our recommendations are valid for this approach. The main difficulty should arise from the narrower beam widths of cloud radars, which should increase the precision required in the UAV positioning. It would also be necessary to develop a tailored geometrical model and to study how does misalignment bias change with the amount of experimental iterations.

- **Calibration transfer for radars operating on different frequency bands:** It would be useful to improve the calibration transfer method, to enable calibration transfer between radars that operate in different frequency bands. This requires the addition of atmospheric attenuation calculations for each radar. Additionally, the data selecton stage should consider aditional steps to guarantee that compared data is in the Rayleigh scattering regime for both radars (Doerry and Brock (2009)), and to avoid the use of measurements that could be attenuated by liquid water presence in the beam path. The reason for the latter is that liquid water attenuation changes depending on the radar frequency band, and is difficult to estimate precisely because it depends on cloud LWC (LWC estimation would introduce an additional uncertainty term in the calculation).

These proposals may help us to further improve our understanding of fog, our capacity to perform short-range forecast of fog dissipation, and the development of a new generation of cloud radar calibration techniques with a complete characterization of their uncertainty.

Bibliography

Abdel-Aty, M., Ekram, A.-A., Huang, H., and Choi, K.: A study on crashes related to visibility obstruction due to fog and smoke, Accident Analysis & Prevention, 43, 1730 – 1737, https://doi.org/https://doi.org/10.1016/j.aap.2011.04.003, URL http://www.sciencedirect.com/science/article/pii/S0001457511000844, 2011.

Aguirre, R., Toledo, F., Rodríguez, R., Rondanelli, R., Reyes, N., and Díaz, M.: Low-Cost Ka-Band Cloud Radar System for Distributed Measurements within the Atmospheric Boundary Layer, Remote Sensing, 12, https://doi.org/10.3390/rs12233965, URL https://www.mdpi.com/2072-4292/12/23/3965, 2020.

Albrecht, B. A., Fairall, C. W., Thomson, D. W., White, A. B., Snider, J. B., and Schubert, W. H.: Surface-based remote sensing of the observed and the Adiabatic liquid water content of stratocumulus clouds, Geophysical Research Letters, 17, 89–92, https://doi.org/10.1029/GL017i001p00089, URL https://agupubs.onlinelibrary.wiley.com/doi/abs/10.1029/GL017i001p00089, 1990.

American Meteorological Society: Glossary of Meteorology: Fog, Size Parameter, URL http://glossary.ametsoc.org/wiki/Fog, 2012.

Anagnostou, E. N., Morales, C. A., and Dinku, T.: The Use of TRMM Precipitation Radar Observations in Determining Ground Radar Calibration Biases, Journal of Atmospheric and Oceanic Technology, 18, 616–628, https://doi.org/10.1175/1520-0426(2001)018<0616:TUOTPR>2.0.CO;2, URL https://doi.org/10.1175/1520-0426(2001)018<0616:TUOTPR>2.0.CO;2, 2001.

Atlas, D.: Radar Calibration, Bulletin of the American Meteorological Society, 83, 1313–1316, https://doi.org/10.1175/1520-0477-83.9.1313, URL https://doi.org/10.1175/1520-0477-83.9.1313, 2002.

Atlas, D. and Mossop, S. C.: Calibration of a Weather Radar by Using a Standard Target, Bulletin of the American Meteorological Society, 41, 377 – 382, https://doi.org/10.1175/1520-0477-41.7.377, URL https://journals.ametsoc.org/view/journals/bams/41/7/1520-0477-41_7_377.xml, 1960.

Balanis, C. A.: Antenna theory: analysis and design, John wiley & sons, 2016.

Bell, A., Martinet, P., Caumont, O., Vié, B., Delanoë, J., Dupont, J.-C., and Borderies, M.: W-band Radar Observations for Fog Forecast Improvement: an Analysis of Model and Forward Operator Errors, Atmospheric Measurement Techniques Discussions, 2021, 1–27, https://doi.org/10.5194/amt-2020-468, URL https://amt.copernicus.org/preprints/amt-2020-468/, 2021.

Bergada, M., Sekelsky, S. M., and Li, L.: External calibration of millimeter-wave atmospheric radar systems using corner reflectors and spheres, cal, 3, 6, 2001.

Bergot, T.: Small-scale structure of radiation fog: a large-eddy simulation study, Quarterly Journal of the Royal Meteorological Society, 139, 1099–1112, 2013.

Bergot, T., Escobar, J., and Masson, V.: Effect of small-scale surface heterogeneities and buildings on radiation fog: Large-eddy simulation study at Paris–Charles de Gaulle airport, Quarterly Journal of the Royal Meteorological Society, 141, 285–298, https://doi.org/https://doi.org/10.1002/qj.2358, URL https://rmets.onlinelibrary.wiley.com/doi/abs/10.1002/qj.2358, 2015.

Boers, R., Baltink, H. K., Hemink, H. J., Bosveld, F. C., and Moerman, M.: Ground-Based Observations and Modeling of the Visibility and Radar Reflectivity in a Radiation Fog Layer, Journal of Atmospheric and Oceanic Technology, 30, 288–300, https://doi.org/10.1175/JTECH-D-12-00081.1, URL https://doi.org/10.1175/JTECH-D-12-00081.1, 2013.

Boneh, T., Weymouth, G. T., Newham, P., Potts, R., Bally, J., Nicholson, A. E., and Korb, K. B.: Fog Forecasting for Melbourne Airport Using a Bayesian Decision Network, Weather and Forecasting, 30, 1218 – 1233, https://doi.org/10.1175/WAF-D-15-0005.1, URL https://journals.ametsoc.org/view/journals/wefo/30/5/waf-d-15-0005_1.xml, 01 Oct. 2015.

Braun, R. A., Dadashazar, H., MacDonald, A. B., Crosbie, E., Jonsson, H. H., Woods, R. K., Flagan, R. C., Seinfeld, J. H., and Sorooshian, A.: Cloud Adiabaticity and Its Relationship to Marine Stratocumulus Characteristics Over the Northeast Pacific Ocean, Journal of Geophysical Research: Atmospheres, 123, 13,790–13,806, https://doi.org/10.1029/2018JD029287, URL https://agupubs.onlinelibrary.wiley.com/doi/abs/10.1029/2018JD029287, 2018.

Bringi, V. N. and Chandrasekar, V.: Polarimetric Doppler weather radar: principles and applications, Cambridge university press, 2001.

Britannica, E.: Attenuation: attenuation of electromagnetic energy in the atmosphere, URL https://www.britannica.com/topic/telecommunications-media?oasmId=3696, accessed: 2021-01-26, 2017.

Brooker, G.: Sensors and signals, Citeseer, Australian Centre for Field Robotics, Rose St Building (J04), University of Sydney, Australia, 2006.

Brooker, G. M.: Understanding millimetre wave FMCW radars, in: 1st international Conference on Sensing Technology, pp. 152–157, 2005.

Brunfeldt, D. R. and Ulaby, F. T.: Active Reflector for Radar Calibration, IEEE Transactions on Geoscience and Remote Sensing, GE-22, 165–169, https://doi.org/10.1109/TGRS.1984.350610, 1984.

Cadeddu, M. P., Peckham, G. E., and Gaffard, C.: The vertical resolution of ground-based microwave radiometers analyzed through a multiresolution wavelet technique, IEEE Transactions on Geoscience and Remote Sensing, 40, 531–540, https://doi.org/10.1109/TGRS.2002.1000313, 2002.

Cermak, J. and Bendix, J.: Detecting ground fog from space – a microphysics-based approach, International Journal of Remote Sensing, 32, 3345–3371, https://doi.org/10.1080/01431161003747505, URL https://doi.org/10.1080/01431161003747505, 2011.

Chandrasekar, V., Baldini, L., Bharadwaj, N., and Smith, P. L.: Calibration procedures for global precipitation-measurement ground-validation radars, URSI Radio Science Bulletin, 2015, 45–73, https://doi.org/10.23919/URSIRSB.2015.7909473, 2015.

Costa-Surós, M., Calbó, J., González, J., and Martin-Vide, J.: Behavior of cloud base height from ceilometer measurements, Atmospheric Research, 127, 64–76, https://doi.org/https://doi.org/10.1016/j.atmosres.2013.02.005, URL https://www.sciencedirect.com/science/article/pii/S0169809513000665, 2013.

Croft, P. J., Darbe, D. L., and Garmon, J. F.: Forecasting significant fog in southern Alabama, National Weather Digest, pp. 10–16, 1995.

Croft, P. J., Pfost, R. L., Medlin, J. M., and Johnson, G. A.: Fog Forecasting for the Southern Region: A Conceptual Model Approach, Weather and Forecasting, 12, 545 – 556, https://doi.org/10.1175/1520-0434(1997)012<0545:FFFTSR>2.0.CO;2, URL https://journals.ametsoc.org/view/journals/wefo/12/3/1520-0434_1997_012_0545_ffftsr_2_0_co_2.xml, 1997.

Delanoë, J., Protat, A., Vinson, J.-P., Brett, W., Caudoux, C., Bertrand, F., Parent du Chatelet, J., Hallali, R., Barthes, L., Haeffelin, M., et al.: Basta: a 95-GHz fmcw doppler radar for cloud and fog studies, Journal of Atmospheric and Oceanic Technology, 33, 1023–1038, 2016.

Doerry, A. W. and Brock, B. C.: Radar cross section of triangular trihedral reflector with extended bottom plate, Sandia Report, Sandia National Laboratory, 2009.

Duntley, S. Q.: The Reduction of Apparent Contrast by the Atmosphere, J. Opt. Soc. Am., 38, 179–191, https://doi.org/10.1364/JOSA.38.000179, URL http://www.osapublishing.org/abstract.cfm?URI=josa-38-2-179, 1948.

Dupont, J., Haeffelin, M., Stolaki, S., and Elias, T.: Analysis of dynamical and thermal processes driving fog and quasi-fog life cycles using the 2010–2013 ParisFog dataset, Pure and Applied Geophysics, 173, 1337–1358, 2016.

Dupont, J.-C., Haeffelin, M., Protat, A., Bouniol, D., Boyouk, N., and Morille, Y.: Stratus–fog formation and dissipation: a 6-day case study, Boundary-layer meteorology, 143, 207–225, 2012.

Dupont, J.-C., Haeffelin, M., Wærsted, E., Delanoë, J., Renard, J.-B., Preissler, J., and O'dowd, C.: Evaluation of Fog and Low Stratus Cloud Microphysical Properties Derived from In Situ Sensor, Cloud Radar and SYRSOC Algorithm, Atmosphere, 9, 169, 2018.

Duthoit, S., Salazar, J. L., Doyle, W., Segales, A., Wolf, B., Fulton, C., and Chilson, P.: A new approach for in-situ antenna characterization, radome inspection and radar calibration, using an Unmanned Aircraft System (UAS), in: 2017 IEEE Radar Conference (RadarConf), pp. 0669–0674, 2017.

Ela, E., Diakov, V., Ibanez, E., and Heaney, M.: Impacts of variability and uncertainty in solar photovoltaic generation at multiple timescales, Tech. rep., National Renewable Energy Lab.(NREL), Golden, CO (United States), 2013.

Ewald, F., Groß, S., Hagen, M., Hirsch, L., Delanoë, J., and Bauer-Pfundstein, M.: Calibration of a 35 GHz airborne cloud radar: lessons learned and intercomparisons with 94 GHz cloud radars, Atmospheric Measurement Techniques, 12, 1815–1839, https://doi.org/10.5194/amt-12-1815-2019, URL https://www.atmos-meas-tech.net/12/1815/2019/, 2019.

Fox, N. I. and Illingworth, A. J.: The Retrieval of Stratocumulus Cloud Properties by Ground-Based Cloud Radar, Journal of Applied Meteorology, 36, 485 – 492, https://doi.org/10.1175/1520-0450(1997)036<0485:TROSCP>2.0.CO;2, URL https://journals.ametsoc.org/view/journals/apme/36/5/1520-0450_1997_036_0485_troscp_2.0.co_2.xml, 1997.

Frisch, A. S., Feingold, G., Fairall, C. W., Uttal, T., and Snider, J. B.: On cloud radar and microwave radiometer measurements of stratus cloud liquid water profiles, Journal of Geophysical Research: Atmospheres, 103, 23 195–23 197, https://doi.org/https://doi.org/10.1029/98JD01827, URL https://agupubs.onlinelibrary.wiley.com/doi/abs/10.1029/98JD01827, 1998.

Garthwaite, M. C., Nancarrow, S., Hislop, A., Thankappan, M., Dawson, J. H., and Lawrie, S.: Design of radar corner reflectors for the Australian Geophysical Observing System, Geoscience Australia, 3, 2015.

Gultepe, I., Müller, M. D., and Boybeyi, Z.: A New Visibility Parameterization for Warm-Fog Applications in Numerical Weather Prediction Models, Journal of Applied Meteorology and Climatology, 45, 1469–1480, https://doi.org/10.1175/JAM2423.1, URL https://doi.org/10.1175/JAM2423.1, 2006.

Gultepe, I., Tardif, R., Michaelides, S., Cermak, J., Bott, A., Bendix, J., Müller, M. D., Pagowski, M., Hansen, B., Ellrod, G., et al.: Fog research: A review of past achievements and future perspectives, Pure and applied geophysics, 164, 1121–1159, 2007.

Haeffelin, M., Barthès, L., Bock, O., Boitel, C., Bony, S., Bouniol, D., Chepfer, H., Chiriaco, M., Cuesta, J., Delanoë, J., et al.: SIRTA, a ground-based atmospheric observatory for cloud and aerosol research, in: Annales Geophysicae, vol. 23, pp. 253–275, 2005.

Haeffelin, M., Bergot, T., Elias, T., Tardif, R., Carrer, D., Chazette, P., Colomb, M., Drobinski, P., Dupont, E., Dupont, J.-C., et al.: PARISFOG: Shedding new light on fog physical processes, Bulletin of the American Meteorological Society, 91, 767–783, 2010.

Haeffelin, M., Dupont, J.-C., Boyouk, N., Baumgardner, D., Gomes, L., Roberts, G., and Elias, T.: A comparative study of radiation fog and quasi-fog formation processes during the ParisFog field experiment 2007, Pure and Applied Geophysics, 170, 2283–2303, 2013.

Haeffelin, M., Crewell, S., Illingworth, A. J., Pappalardo, G., Russchenberg, H., Chiriaco, M., Ebell, K., Hogan, R. J., and Madonna, F.: Parallel Developments and Formal Collaboration between European Atmospheric Profiling Observatories and the U.S. ARM Research Program, Meteorological Monographs, 57, 29.1 – 29.34, https://doi.org/10.1175/AMSMONOGRAPHS-D-15-0045.1, URL https://journals.ametsoc.org/view/journals/amsm/57/1/amsmonographs-d-15-0045.1.xml, 2016a.

Haeffelin, M., Laffineur, Q., Bravo-Aranda, J.-A., Drouin, M.-A., Casquero-Vera, J.-A., Dupont, J.-C., and De Backer, H.: Radiation fog formation alerts using attenuated backscatter power from automatic lidars and ceilometers, Atmospheric Measurement Techniques, 9, 5347, 2016b.

Hautiere, N., Labayrade, R., and Aubert, D.: Real-time disparity contrast combination for onboard estimation of the visibility distance, IEEE Transactions on Intelligent Transportation Systems, 7, 201–212, https://doi.org/10.1109/TITS.2006.874682, 2006.

Hogan, R. J., Bouniol, D., Ladd, D. N., O'Connor, E. J., and Illingworth, A. J.: Absolute calibration of 94/95-GHz radars using rain, Journal of Atmospheric and Oceanic Technology, 20, 572–580, 2003.

Horvath, H.: On the applicability of the koschmieder visibility formula, Atmospheric Environment (1967), 5, 177 – 184, https://doi.org/https://doi.org/10.1016/0004-6981(71)90081-3, URL http://www.sciencedirect.com/science/article/pii/0004698171900813, 1971.

Hudson, J. G. and Yum, S. S.: Droplet Spectral Broadening in Marine Stratus, Journal of the Atmospheric Sciences, 54, 2642 – 2654, https://doi.org/10.1175/1520-0469(1997)054<2642:DSBIMS>2.0.CO;2, URL https://journals.ametsoc.org/view/journals/atsc/54/22/1520-0469_1997_054_2642_dsbims_2.0.co_2.xml, 1997.

Illingworth, A. J., Hogan, R. J., O'Connor, E., Bouniol, D., Brooks, M. E., Delanoé, J., Donovan, D. P., Eastment, J. D., Gaussiat, N., Goddard, J. W. F., Haeffelin, M., Baltink, H. K., Krasnov, O. A., Pelon, J., Piriou, J.-M., Protat, A., Russchenberg, H. W. J., Seifert, A., Tompkins, A. M.,

van Zadelhoff, G.-J., Vinit, F., Willén, U., Wilson, D. R., and Wrench, C. L.: Cloudnet: Continuous Evaluation of Cloud Profiles in Seven Operational Models Using Ground-Based Observations, Bulletin of the American Meteorological Society, 88, 883 – 898, https://doi.org/10.1175/BAMS-88-6-883, URL https://journals.ametsoc.org/view/journals/bams/88/6/bams-88-6-883.xml, 2007.

Jayasri, P., Niharika, K., Yedukondalu, K., Kumari, E. S., and Prasad, A.: Radar cross section characterization of corner reflectors in different frequency bands and polarizations, International Archives of the Photogrammetry, Remote Sensing and Spatial Information Sciences, 42, 5, 2018.

Katata, G.: Fogwater deposition modeling for terrestrial ecosystems: A review of developments and measurements, Journal of Geophysical Research: Atmospheres, 119, 8137–8159, https://doi.org/https://doi.org/10.1002/2014JD021669, URL https://agupubs.onlinelibrary.wiley.com/doi/abs/10.1002/2014JD021669, 2014.

Kato, S., Mace, G. G., Clothiaux, E. E., Liljegren, J. C., and Austin, R. T.: Doppler Cloud Radar Derived Drop Size Distributions in Liquid Water Stratus Clouds, Journal of the Atmospheric Sciences, 58, 2895 – 2911, https://doi.org/10.1175/1520-0469(2001)058<2895:DCRDDS>2.0.CO;2, URL https://journals.ametsoc.org/view/journals/atsc/58/19/1520-0469_2001_058_2895_dcrdds_2.0.co_2.xml, 2001.

Kazama, S., Rose, T., Zimmermann, R., and Zimmermann, R.: A Precision Autocalibrating 7 Channel Radiometer for Environmental Research Applications, Journal of the Remote Sensing Society of Japan, 19, 265–273, https://doi.org/10.11440/rssj1981.19.265, 1999.

Khain, A., Pinsky, M., Magaritz, L., Krasnov, O., and Russchenberg, H. W. J.: Combined Observational and Model Investigations of the Z–LWC Relationship in Stratocumulus Clouds, Journal of Applied Meteorology and Climatology, 47, 591 – 606, https://doi.org/10.1175/2007JAMC1701.1, URL https://journals.ametsoc.org/view/journals/apme/47/2/2007jamc1701.1.xml, 2008.

Koračin, D., Lewis, J., Thompson, W. T., Dorman, C. E., and Businger, J. A.: Transition of Stratus into Fog along the California Coast: Observations and Modeling, Journal of the Atmospheric Sciences, 58, 1714 – 1731, https://doi.org/10.1175/1520-0469(2001)058<1714:TOSIFA>2.0.CO;2, URL https://journals.ametsoc.org/view/journals/atsc/58/13/1520-0469_2001_058_1714_tosifa_2.0.co_2.xml, 2001.

Kotthaus, S., O'Connor, E., Münkel, C., Charlton-Perez, C., Haeffelin, M., Gabey, A. M., and Grimmond, C. S. B.: Recommendations for processing atmospheric attenuated backscatter profiles from Vaisala CL31 ceilometers, Atmospheric Measurement Techniques, 9, 3769–3791, https://doi.org/10.5194/amt-9-3769-2016, URL https://amt.copernicus.org/articles/9/3769/2016/, 2016.

Liebe, H. J.: MPM—An atmospheric millimeter-wave propagation model, International Journal of Infrared and millimeter waves, 10, 631–650, 1989.

Löhnert, U., Crewell, S., Simmer, C., and Macke, A.: Profiling Cloud Liquid Water by Combining Active and Passive Microwave Measurements with Cloud Model Statistics, Journal of Atmospheric and Oceanic Technology, 18, 1354 – 1366, https://doi.org/10.1175/1520-0426(2001)018<1354:PCLWBC>2.0.CO;2, URL https://journals.ametsoc.org/view/journals/atot/18/8/1520-0426_2001_018_1354_pclwbc_2_0_co_2.xml, 2001.

Marke, T., Ebell, K., Löhnert, U., and Turner, D. D.: Statistical retrieval of thin liquid cloud microphysical properties using ground-based infrared and microwave observations, Journal of Geophysical Research: Atmospheres, 121, 14,558–14,573, https://doi.org/10.1002/2016JD025667, URL https://agupubs.onlinelibrary.wiley.com/doi/abs/10.1002/2016JD025667, 2016.

Martucci, G. and O'Dowd, C. D.: Ground-based retrieval of continental and marine warm cloud microphysics, Atmospheric Measurement Techniques, 4, 2749–2765, https://doi.org/10.5194/amt-4-2749-2011, URL https://amt.copernicus.org/articles/4/2749/2011/, 2011.

Mazoyer, M., Lac, C., Thouron, O., Bergot, T., Masson, V., and Musson-Genon, L.: Large eddy simulation of radiation fog: impact of dynamics on the fog life cycle, Atmospheric Chemistry and Physics, 17, 13 017–13 035, https://doi.org/10.5194/acp-17-13017-2017, URL https://acp.copernicus.org/articles/17/13017/2017/, 2017.

Merk, D., Deneke, H., Pospichal, B., and Seifert, P.: Investigation of the adiabatic assumption for estimating cloud micro- and macrophysical properties from satellite and ground observations, Atmospheric Chemistry and Physics, 16, 933–952, https://doi.org/10.5194/acp-16-933-2016, URL https://acp.copernicus.org/articles/16/933/2016/, 2016.

MODEM: BASTA Leaflet, URL http://www.meteomodem.com/docs/en/Leaflet-basta.pdf, 2018.

Myagkov, A., Kneifel, S., and Rose, T.: Evaluation of the reflectivity calibration of W-band radars based on observations in rain, Atmospheric Measurement Techniques, 13, 5799–5825, https://doi.org/10.5194/amt-13-5799-2020, URL https://amt.copernicus.org/articles/13/5799/2020/, 2020.

Nakanishi, M.: Large-eddy simulation of radiation fog, Boundary-layer meteorology, 94, 461–493, 2000.

Nilo, S. T., Cimini, D., Di Paola, F., Gallucci, D., Gentile, S., Geraldi, E., Larosa, S., Ricciardelli, E., Ripepi, E., Viggiano, M., and et al.: Fog Forecast Using WRF Model Output for Solar Energy Applications, Energies, 13, 6140, https://doi.org/10.3390/en13226140, URL http://dx.doi.org/10.3390/en13226140, 2020.

Pappalardo, G.: ACTRIS Aerosol, Clouds and Trace Gases Research Infrastructure, EPJ Web Conf., 176, 09 004, https://doi.org/10.1051/epjconf/201817609004, URL https://doi.org/10.1051/epjconf/201817609004, 2018.

Porson, A., Price, J., Lock, A., and Clark, P.: Radiation fog. Part II: Large-eddy simulations in very stable conditions, Boundary-layer meteorology, 139, 193–224, 2011.

Price, J.: Radiation fog. Part I: observations of stability and drop size distributions, Boundary-layer meteorology, 139, 167–191, 2011.

Protat, A., Delanoë, J., Bouniol, D., Heymsfield, A. J., Bansemer, A., and Brown, P.: Evaluation of Ice Water Content Retrievals from Cloud Radar Reflectivity and Temperature Using a Large Airborne In Situ Microphysical Database, Journal of Applied Meteorology and Climatology, 46, 557 – 572, https://doi.org/10.1175/JAM2488.1, URL https://journals.ametsoc.org/view/journals/apme/46/5/jam2488.1.xml, 2007.

Protat, A., Bouniol, D., Delanoë, J., O'Connor, E., May, P. T., Plana-Fattori, A., Hasson, A., Görsdorf, U., and Heymsfield, A. J.: Assessment of CloudSat reflectivity measurements and ice cloud properties using ground-based and airborne cloud radar observations, Journal of Atmospheric and Oceanic Technology, 26, 1717–1741, 2009.

Román-Cascón, C., Steeneveld, G. J., Yagüe, C., Sastre, M., Arrillaga, J. A., and Maqueda, G.: Forecasting radiation fog at climatologically contrasting sites: evaluation of statistical methods and WRF, Quarterly Journal of the Royal Meteorological Society, 142, 1048–1063, https://doi.org/https://doi.org/10.1002/qj.2708, URL https://rmets.onlinelibrary.wiley.com/doi/abs/10.1002/qj.2708, 2016a.

Román-Cascón, C., Yagüe, C., Steeneveld, G.-J., Sastre, M., Arrillaga, J. A., and Maqueda, G.: Estimating fog-top height through near-surface micrometeorological measurements, Atmospheric Research, 170, 76–86, https://doi.org/https://doi.org/10.1016/j.atmosres.2015.11.016, URL https://www.sciencedirect.com/science/article/pii/S0169809515003877, 2016b.

Rose, T., Crewell, S., Löhnert, U., and Simmer, C.: A network suitable microwave radiometer for operational monitoring of the cloudy atmosphere, Atmospheric Research, 75, 183–200, https://doi.org/https://doi.org/10.1016/j.atmosres.2004.12.005, URL https://www.sciencedirect.com/science/article/pii/S0169809505000189, cLIWA-NET: Observation and Modelling of Liquid Water Clouds, 2005.

RPG: RPG-FMCW-94-SP/DP 94 GHz W-band Cloud Doppler Radar Instrument Installation, Operation and Software Guide (Version 2.10-1), URL http://www.radiometer-physics.de/downloadftp/pub/PDF/Cloud%20Radar/RPG-FMCW-Instrument_Manual.pdf, 2015.

Ryzhkov, A. V., Giangrande, S. E., Melnikov, V. M., and Schuur, T. J.: Calibration Issues of Dual-Polarization Radar Measurements, Journal of Atmospheric and Oceanic Technology, 22, 1138 – 1155, https://doi.org/10.1175/JTECH1772.1, URL https://journals.ametsoc.org/view/journals/atot/22/8/jtech1772_1.xml, 2005.

Sassen, K.: Ice cloud content from radar reflectivity, Journal of climate and applied meteorology, 26, 1050–1053, 1987.

Sekelsky, S. M. and Clothiaux, E. E.: Parallax Errors and Corrections for Dual-Antenna Millimeter-Wave Cloud Radars, Journal of Atmospheric and Oceanic Technology, 19, 478–485, https://doi.org/10.1175/1520-0426(2002)019<0478:PEACFD>2.0.CO;2, URL https://doi.org/10.1175/1520-0426(2002)019<0478:PEACFD>2.0.CO;2, 2002.

Sekelsky, S. M. and McIntosh, R. E.: Cloud observations with a polarimetric 33 GHz and 95 GHz radar, Meteorology and Atmospheric Physics, 59, 123–140, 1996.

Skolnik, M. I.: Radar Handbook, Mc Craw-Hill, 3 edn., 2000.

Slingo, A., Brown, R., and Wrench, C.: A field study of nocturnal stratocumulus; III. High resolution radiative and microphysical observations, Quarterly Journal of the Royal Meteorological Society, 108, 145–165, 1982.

Smith, D. K. E., Renfrew, I. A., Price, J. D., and Dorling, S. R.: Numerical modelling of the evolution of the boundary layer during a radiation fog event, Weather, 73, 310–316, https://doi.org/https://doi.org/10.1002/wea.3305, URL https://rmets.onlinelibrary.wiley.com/doi/abs/10.1002/wea.3305, 2018.

Solheim, F., Godwin, J. R., Westwater, E. R., Han, Y., Keihm, S. J., Marsh, K., and Ware, R.: Radiometric profiling of temperature, water vapor and cloud liquid water using various inversion methods, Radio Science, 33, 393–404, https://doi.org/https://doi.org/10.1029/97RS03656, URL https://agupubs.onlinelibrary.wiley.com/doi/abs/10.1029/97RS03656, 1998.

Steeneveld, G., Ronda, R., and Holtslag, A.: The challenge of forecasting the onset and development of radiation fog using mesoscale atmospheric models, Boundary-Layer Meteorology, 154, 265–289, 2015.

Suleymanov, S.: Design and Implementation of an FMCW Radar Signal Processing Module for Automotive Applications, Master's thesis, University of Twente, 2016.

Süsskind, C.: Who invented radar?, Endeavour, 9, 92 – 96, https://doi.org/https://doi.org/10.1016/0160-9327(85)90043-2, URL http://www.sciencedirect.com/science/article/pii/0160932785900432, 1985.

Tardif, R. and Rasmussen, R. M.: Event-based climatology and typology of fog in the New York City region, Journal of applied meteorology and climatology, 46, 1141–1168, 2007.

Thankappan, M., Garthwaite, M. C., Williams, M. L., Hislop, A., Nancarrow, S., and Dawson, J.: Characterisation of Corner Reflectors for the Australian Geophysical Observing System to Support SAR Calibration, Powder Coat, 1, 37–9222, 2013.

Toledo, F., Delanoë, J., Haeffelin, M., Dupont, J.-C., Jorquera, S., and Le Gac, C.: Absolute calibration method for frequency-modulated continuous wave (FMCW) cloud radars based on corner reflectors, Atmospheric Measurement Techniques, 13, 6853–6875, https://doi.org/10.5194/amt-13-6853-2020, URL https://amt.copernicus.org/articles/13/6853/2020/, 2020.

Toledo, F., Haeffelin, M., Wærsted, E., and Dupont, J.-C.: A New Conceptual Model for Adiabatic Fog, Atmospheric Chemistry and Physics Discussions, 2021, 1–32, https://doi.org/10.5194/acp-2020-1314, URL https://acp.copernicus.org/preprints/acp-2020-1314/, 2021.

Veljović, K., Vujović, D., Lazić, L., and Vučković, V.: An analysis of fog events at Belgrade International Airport, Theoretical and Applied Climatology, 119, 13–24, 2015.

Wærsted, E.: Description of physical processes driving the life cycle of radiation fog and fog–stratus transitions based on conceptual models, Ph.D. thesis, Paris Saclay, 2018.

Wærsted, E. G., Haeffelin, M., Dupont, J.-C., Delanoë, J., and Dubuisson, P.: Radiation in fog: quantification of the impact on fog liquid water based on ground-based remote sensing, Atmospheric Chemistry and Physics, 17, 10 811–10 835, https://doi.org/10.5194/acp-17-10811-2017, URL https://www.atmos-chem-phys.net/17/10811/2017/, 2017.

Wærsted, E. G., Haeffelin, M., Steeneveld, G.-J., and Dupont, J.-C.: Understanding the dissipation of continental fog by analysing the LWP budget using idealized LES and in situ observations, Quarterly Journal of the Royal Meteorological Society, 145, 784–804, https://doi.org/10.1002/qj.3465, URL https://rmets.onlinelibrary.wiley.com/doi/abs/10.1002/qj.3465, 2019.

Wallace, J. M. and Hobbs, P. V.: Atmospheric science: an introductory survey, vol. 92, Elsevier, 2006.

Ware, R., Carpenter, R., Güldner, J., Liljegren, J., Nehrkorn, T., Solheim, F., and Vandenberghe, F.: A multichannel radiometric profiler of temperature, humidity, and cloud liquid, Radio Science, 38, https://doi.org/https://doi.org/10.1029/2002RS002856, URL https://agupubs.onlinelibrary.wiley.com/doi/abs/10.1029/2002RS002856, 2003.

Wood, C. R., O'Connor, E. J., Hurley, R. A., Reynolds, D. R., and Illingworth, A. J.: Cloud-radar observations of insects in the UK convective boundary layer, Meteorological Applications, 16, 491–500, https://doi.org/https://doi.org/10.1002/met.146, URL https://rmets.onlinelibrary.wiley.com/doi/abs/10.1002/met.146, 2009.

Yao, W., Zhang, C., Hao, H., Wang, X., and Li, X.: A support vector machine approach to estimate global solar radiation with the influence of fog and haze, Renewable Energy, 128, 155 – 162, https://doi.org/https://doi.org/10.1016/j.renene.2018.05.069, URL http://www.sciencedirect.com/science/article/pii/S0960148118305901, 2018.

Yau, M. K. and Rogers, R. R.: A short course in cloud physics, Elsevier, 1996.

Yin, J., Hoogeboom, P., Unal, C., Russchenberg, H., Van der Zwan, F., and Oudejans, E.: UAV-Aided Weather Radar Calibration, IEEE Transactions on Geoscience and Remote Sensing, 57, 10 362–10 375, https://doi.org/10.1109/TGRS.2019.2933912, 2019.

Zhou, B. and Ferrier, B. S.: Asymptotic analysis of equilibrium in radiation fog, Journal of Applied Meteorology and Climatology, 47, 1704–1722, 2008.

ECOLE DOCTORALE

Titre : Amélioration des produits radar nuage pour les réseaux de surveillance du brouillard : Analyses du cycle de vie du brouillard et méthodologies de calibration

Mots clés : Brouillard, Cycle de vie du brouillard, Télédétection du brouillard, Radar nuage, Étalonnage de radars

Résumé : La réduction de la visibilité occasionnée par le brouillard a un impact significatif sur les activités humaines. De plus, le brouillard est un phénomène complexe dont l'évolution dépend de l'équilibre délicat de plusieurs processus physiques. Des développements récents montrent que les radars nuage sont des instruments clés pour améliorer l'observation des processus pilotant le cycle de vie des brouillards. Ceci, associé à de nouveaux développements réduisant leur coût, ouvre la possibilité d'établir des réseaux de stations de surveillance du brouillard. Pourtant, il y a des défis à relever pour garantir la valeur de ces réseaux :
1.- Les processus qui pilotent le cycle de vie du brouillard se produisent dans une épaisseur d'atmosphère de plusieurs centaines de mètres, en particulier à sa limite inférieure où elle interagit avec le sol, et à son sommet où elle interagit avec l'air insaturé au-dessus. Les capteurs in-situ sont bien adaptés pour surveiller les variables clés dans la limite la plus basse. Les instruments de télédétection, y compris les radars nuage, peuvent surveiller l'état de la couche de brouillard et les processus se produisant à son sommet. Le contenu intégré en eau liquide (LWP) et l'altitude du sommet du brouillard sont montrés comme deux variables de télédétection importantes qui pilotent l'évolution temporelle du brouillard tout au long de son cycle de vie.
Pour réussir à évaluer la tendance à la dissipation du brouillard, la thèse propose une nouvelle approche qui repose sur des variables détectées à distance combinées à un nouveau modèle conceptuel. L'approche fournit deux variables de diagnostic : le LWP Critique (CLWP) et le LWP de Réservoir (RLWP). CLWP est la quantité minimale de LWP nécessaire pour maintenir une couche de brouillard d'une épaisseur donnée. Le RLWP est l'excès d'eau qui doit être épuisé avant que la dissipation du brouillard puisse se produire à la surface. Le modèle conceptuel établit un nouveau paradigme basé sur l'observation de la colonne de brouillard afin d'évaluer sa tendance à la dissipation.
2.- L'étalonnage des radars nuage est un problème non résolu qui entrave la performance des réseaux d'observation du brouillard, en limitant la fiabilité des mesures microphysiques et des études comparatives entre sites d'observation. Cette thèse étudie une stratégie d'étalonnage qui pourrait être appliquée sur un réseau de surveillance du brouillard, à partir des résultats de deux campagnes d'étalonnage qui ont eu lieu à l'observatoire SIRTA, dans le cadre du développement de l'infrastructure ACTRIS.
La stratégie comprend deux étapes : d'une part calibrer un radar de référence avec une estimation fiable de l'incertitude et d'autre part transférer l'étalonnage à d'autres radars, en comparant ses mesures de réflectivité. Le radar de référence (95 GHz BASTA mini) est étalonné avec une nouvelle méthode, basée sur des réflecteurs trièdres. Les sources de biais et d'incertitude sont discutées et quantifiées. Actuellement, l'incertitude de la méthode est de 2 dB, limitée par l'utilisation d'un modèle théorique pour calculer la section efficace du radar du réflecteur. Pourtant, les calculs indiquent que l'incertitude pourrait atteindre un minimum théorique de 0.4 dB, en fonction de l'incertitude de caractérisation du réflecteur et du montage expérimental. La méthodologie de transfert d'étalonnage est basée sur l'analyse de mesures simultanées de nuages. En utilisant deux semaines d'observations, il a permis le transfert d'étalonnage vers un radar nuage RPG de 94 GHz, avec une incertitude ajoutée de 0.9 dB par rapport à l'étalonnage du radar de référence. Les travaux techniques et scientifiques réalisés dans cette thèse contribuent à améliorer notre capacité à surveiller les variables clés qui contribuent à une meilleure compréhension de l'évolution du cycle de vie du brouillard.

Title : Improvement of cloud radar products for fog surveillance networks: fog life cycle analyses and calibration methodologies.

Keywords : Fog, Fog life cycle, Fog remote sensing, Cloud radar, Radar calibration

Abstract : Visibility reduction caused by fog has a significant impact on human activities. In addition, fog is a complex phenomenon whose evolution depends on the delicate balance of several physical processes. Recent developments show that cloud radars are key instruments to improve observation of key fog processes. This, paired with new developments reducing their cost, opens the possibility of establishing networks of fog surveillance stations. Yet, some challenges must be addressed to secure the value of such networks:
1.- Processes that drive fog life cycle occur throughout the fog layer, in particular at its lower boundary where the fog layer interacts with the soil, and at the top where it interacts with the unsaturated air above. In-situ sensors are well suited to monitor key variables in the lowest boundary. Remote sensing instruments, including cloud radars, can monitor the state of the fog layer and processes occurring at fog top. Fog Liquid Water Path (LWP) and fog top height are shown to be remotely sensed variables that are key drivers of fog temporal evolution throughout its life cycles.
To address the challenge of assessing fog dissipation tendencies, the thesis proposes a novel approach that relies on remotely sensed variables combined with a new conceptual model. The approach provides two diagnostic variables: the Critical Liquid Water Path (CLWP), and the Reservoir Liquid Water Path (RLWP). CLWP is the minimum amount of LWP necessary to maintain a fog layer of a given thickness. RLWP is the excess of water that must be removed before fog dissipation at the surface can occur. The conceptual model establishes a new paradigm based on the observation of the fog column to assess its dissipation tendency.
2.- Cloud radar calibration is an unsolved issue that hampers the performance of fog observation networks, by limiting the reliability of microphysical retrievals and of comparative studies between observation sites. This thesis researches a calibration strategy that could be applied on a fog surveillance network, based on the results of two calibration campaigns that took place at the SIRTA observatory, as part of ACTRIS infrastructure developments.
The strategy consists of two steps: First, to calibrate a reference radar with a reliable estimation of uncertainty. Second, to transfer the calibration to other radars, by comparing reflectivity measurements. The reference radar (95 GHz BASTA mini) is calibrated using a new method, based on corner reflectors. Bias and uncertainty sources are discussed and quantified. At present, the method uncertainty is of 2 dB, limited by the use of a theoretical model to calculate the reflector radar cross section. Yet, calculations indicate that uncertainty could reach a theoretical minimum of 0.4 dB, depending on the characterization uncertainty of the reflector and on the experimental setup. The calibration transfer methodology is based on the analysis of simultaneous cloud measurements. Using two weeks of observations, it enabled the calibration transfer from the reference to a 94 GHz RPG cloud radar, with an added uncertainty of 0.9 dB with respect to the reference radar calibration.
The technical and scientific work carried out in this thesis contribute to improving our capacity to monitor key variables that contribute to a better understanding of fog life cycle evolution.

Institut Polytechnique de Paris
91120 Palaiseau, France